High Reynolds Number Turbulent Boundary Layer Flow over Small Forward Facing Steps

Manuj Awasthi

Thesis submitted to the faculty of the Virginia Polytechnic Institute and State University
in partial fulfillment of the requirements for the degree of

Master of Science

in

Aerospace Engineering

William J. Devenport

Kevin T. Lowe

Stewart A.L. Glegg

06/29/2012

Blacksburg, Virginia

Keywords: turbulent boundary layer, forward facing steps, wall pressure fluctuations, separating-reattaching Flow, velocity fluctuation

High Reynolds Number Turbulent Boundary Layer Flow over Small Forward Facing Steps

Manuj Awasthi

ABSTRACT

Measurements were made on three forward steps with step height to boundary layer ratio of approximately 3.8%, 15% and 60% and Reynolds number based on step height ranging from 6640 to 213,000. The measurements included mean wall pressure, single and 2 point wall pressure fluctuations, single and 2 point velocity fluctuations and, oil flow visualization. Pressure fluctuation measurements were made 5 boundary layer thicknesses upstream of step to 22 boundary layer thickness (or 600 step heights for smallest step size) downstream of the step. The results show that the steps remarkably enhance the wall pressure fluctuations that scale on the step height in the vicinity of the step and far downstream of the step. The decay of wall pressure fluctuations post reattachment is a slow process and elevated levels can be seen as far as 150 step heights downstream for the mid step size. The enhanced pressure fluctuations come from the unsteady reattachment region on top face of the step which was found to be a strong function of flow geometry and flow parameters such as Reynolds number. The 2 point pressure and velocity space-time correlations show a quasi-periodic structure which begins to develop close to the reattachment and grows in intensity and scale further downstream of reattachment and is responsible for the elevated pressure fluctuations downstream of the step. However, the velocity correlations lack in scale reflecting the fact that large scales reflected in pressure are masked by smaller scales that exist within them.

Acknowledgements

I would like to begin by thanking my academic adviser and my mentor Dr. William J. Devenport. I owe a huge thank you to him for not only teaching me the basics of research but also helping me develop a researcher's attitude. This work would not have been possible without his support and encouragement and I look forward to being mentored by him in future.

Next, I would like to thank my committee members Dr. Stewart Glegg and Dr. Todd Lowe for their insights and assistance in my research. I would like to thank the Office of Naval Research, in particular Dr. Ron Joslin, for their support under grant N00014-09-1-0315. I also wish to thank Dr. Ki-Han-Kim for providing support in velocity correlation measurements through ONR grant N00014-10-1-0908.

I would also like to thank all the people in Lab-7 who have helped me with my research over the past two years. I would like to thank Jonathan Forest for all his hard work on the microphones including calibrations and microphone holder designing. I would also like to thank Dr. Aurelien Borgoltz for teaching me and helping me with single hot wire and quad hot wire measurements even if it meant coming in the middle of the night to help with the measurements in the wind tunnel. I would also like to thank Michael Morton for the quad hot wire calibrations and measurements he made over the forward step flows. A big thank you also to Matthew Rasnik, Ryan Throckmorton, Timothy Meyers, Jacques Li and Nathan Alexander for their help with installing the false wall, contraction and setting up forward steps among many other tasks.

I would also like to thank the staff at the AOE machine shop, James Lambert and Scott Patrick for helping me with modification of the panels and the forward step. A special thanks to Bill Oetjens for helping with the wind tunnel operation and dealing with numerous issues that arose during the experiments.

I would also like to thank my friends back in India, Apurva Singh and Manish Upreti for always being supportive and treating my family like their own while I was away from home. My friends in Blacksburg Siddhartha Sharma, Rupinder Paul, Aniruddha Chaudhary for making me feel at home.

Finally, I would like to thank my family. Rajmitra and Sadhna Awasthi for giving birth to me and helping me become what I am today. Thank you for letting me pursue my dream and being strong while I was thousands of miles away. I would also like to thank my younger brother Tanuj Awasthi for being there when I needed him the most and for taking care of things back home in absence of my father. I would also like to thank my younger sister Megha Awasthi for being supportive and understanding that I cannot be home due to my education and work for a while. I owe a huge thank you to my Uncle Dr. Sanjay Awasthi, my Aunt Dr. Sangeeta Awasthi and their children Meenakshi Awasthi, Arjun Awasthi, Ishaani Awasthi and Raaghav Awasthi for giving me a home away from home and supporting my every endeavor.

Again, I thank you all for your help and support.

Manuj Awasthi

Blacksburg, VA

June, 2012

Table of Contents

Nomenclature

Roman

a_n	Coefficients for Proper Orthogonal Decomposition (POD)
$B(s)$	n^{th} degree polynomial
C_f	Skin friction coefficient
C_p	Mean wall pressure coefficient
f	Frequency
$f(t),g(t)$	Time domain representation of a continuous signal
$F(\omega),G(\omega)$	Frequency domain representation of a signal
G_{pp}	Autocorrelation of a signal
$H(s)$	Transfer function of a system
h	Forward step height
i	Complex number
k	Index notation
N	Length of a discrete signal
p	Pressure
R	Correlation coefficient
t	time scale
T	time period
U	Mean streamwise velocity component
$u+$	Non dimensional mean streamwise velocity within the boundary layer
u	streamwise velocity component
v	spanwise velocity component
w	Normal to the wall velocity component
x	Streamwise coordinate
$x(t)$	Time dependent discrete signal
$X(k)$	Frequency domain representation of discrete signal
y	Spanwise coordinate
$y+$	Non dimensional normal to the wall coordinate for law of the wall
z	Normal to the wall coordinate

Greek

δ	Boundary layer thickness
Δ	Spatial or temporal separation
δ^*	Boundary layer displacement thickness
δ_{nm}	Dirac Delta function
θ	Boundary layer momentum thickness
λ	Eigen value
υ	Kinematic viscosity
ρ	Free stream air density
τ	Time delay
τ'_{ij}	Reynolds stress tensor
ϕ_{pp}	Wall pressure fluctuation spectral density
φ_n	Real basis function
ω	Frequency

Abbreviations and Symbols

$\langle \quad \rangle$	Time averaged quantity
∇	Gradient
B&K	Brüel & Kjær
F&C	Authors Farabee and Casarella
J&W	Authors Ji and Wang
Re	Reynolds number based on step height
r.m.s	Root mean square value of a quantity

Superscripts and Subscripts

*	Conjugate of a signal in frequency domain
∞	Free stream quantities
δ	Boundary layer thickness
θ	Boundary layer momentum thickness
$'$	Fluctuating quantities
a,b,c	Pressure fluctuation measurement locations along test wall
e	Quantity at the edge of boundary layer

h	Step height
i,j,k	Tensor notation
M	Measured signal
N	Signal due to noise
S	Subtracted signal
T	Signal due to turbulence
wall	quantity measured at the wall

List of Figures

List of Tables

1. Introduction

1.1 *Motivation*

The problem of turbulent boundary layer flow over discontinuities present on surface of aerodynamic and hydrodynamic vehicles is important from the standpoint of designing an efficient low noise vehicle. Forward steps are a common form of discontinuity found of vehicle surface. Forwards steps on a vehicle surface are inevitable due to panel mismatches, joints, ribs, surface mounted instruments etc. The presence of forward steps on smooth surface separates the incoming boundary layer which reattaches at some downstream distance. This separating-reattaching type flow modifies the incoming equilibrium turbulent boundary layer and induces turbulence activity far greater than what is observed in a surface without steps (Farabee & Zoccola, 1998). This increased turbulence activity causes wall pressure fluctuations that are significantly elevated compared to smooth wall. The elevated pressure fluctuations cause surface vibration which results in undesired acoustic radiation (Hudy, Naguib, & Humphreys Jr., 2003). Moreover, these vibrations induced by the wall pressure fluctuations can also adversely affect a structure's fatigue life (Hubbard, 1956). In addition, the presence of forward steps on vehicle surfaces can also corrupt data from surface mounted instrumentations (Awasthi, Forest, Morton, Devenport, & Glegg, 2011).

It is important to gain a good understanding of surface pressure fluctuations due to small forward steps to provide design criteria which minimizes the aforementioned undesired effects. In addition to this, an advantage of studying forward steps is that their separation and reattachment are well defined but at the same time they produce flow field that are found in more complex separated-reattached flow fields. Thus, studying forward step geometry provides an opportunity to understand complex separated-reattached flows without the added complication of complex geometries. Moreover, since pressure fluctuations are induced by the boundary layer velocity fluctuations, understanding pressure fluctuations offers a non-intrusive way of determining the flow structure associated with a flow (Farabee & Casarella, 1986).

The goal of the present work is to further the understanding of forward step flows by measurement and study of wall pressure fluctuations, separation-reattachment lengths, boundary layer velocity and turbulence, and flow structure associated with the forward step flow. It is expected that the present work, besides providing new insights into separated-reattached flows, will also help establish a design criteria in future for low noise aerodynamic and hydrodynamic vehicles.

1.2 *General Background of Flow over Forward Steps*

In the past there have been numerous studies (experimental, computational and theoretical) dealing with separated-reattached flow over a backward step. However, there are very few studies dealing with forward steps. A possible reason might be that compared to backward steps, which contain only one separation-reattachment region, forward step flow are more complex as they contain two separation-reattachment regions. As an equilibrium turbulent boundary layer (zero wall pressure gradient) approaches a forward step of height '*h*', it separates

upstream of the step and then reattaches to the face of the step. This separation of boundary layer creates a recirculation bubble just upstream of the step with near stagnant flow. The upstream separation point is not fixed but it has been found to be independent or very weak function of Reynolds number. Fiorentini *et al*. (2007) who performed PIV over forward facing steps for Reynolds number based on step height (Re_h) ranging from 4400-26,300 found that upstream separation is independent of Re_h and occurs at about 1 step height upstream. They found that the reattachment on the face of step occurs at about half the vertical height. A similar result was obtained by Camussi *et al*. (2008) who also studied forward facing steps for $8800 \leq Re_h \leq 26{,}300$. Leclercq *et al.* (2009) who studied flow over a pair of forward facing and backward facing step in a wind tunnel found a shorter upstream separation length of about 0.8*h* and slightly larger vertical reattachment length of 0.6*h*. Addad *et al*. (2003) who performed Large Eddy Simulation (LES) on forward-backward step also reported a separation length of 1.2*h* and vertical reattachment length of 0.6*h*. All these studies seem to indicate upstream separation and vertical reattachment lengths that lie within a narrow band and are independent of the Reynolds number variation.

After reattaching to the vertical face of the step, the flow again separates at the corner of the step. This separation leads to the formation of another recirculation bubble with near stagnant flow on the top face of the step. The formation of the two recirculation bubbles and a faster moving shear layer on top of them upstream and downstream of the step create a free mixing shear layer. This phenomenon has been depicted in Figure 1 (figures shown at the end of the text). After passing over the step, this shear layer then reattaches to the surface at some downstream location called reattachment point. The reattached shear layer is quite energized and undergoes a relaxation phase downstream of the step before developing into an equilibrium turbulent boundary layer (Aglenichaab & Tachie, 2008). In this relaxation phase, the shear layer is quite different from a mixing layer of a thin shear layer as observed by Bradshaw and Wong (1972). This separation bubble and reattachment on the top face of the steps is highly unsteady in nature as observed by many studies in the past (e.g. (Camussi, Felli, Pereira, Aloisio, & Di Marco, 2008)). Unlike upstream separation lengths and vertical reattachment length, the downstream reattachment region is not well understood and often yields contradictory results between different studies. For example, Leclercq *et al.* (2009) who performed experiments over forward facing steps with $h/\delta = 1.43$ and $Re_h = 170{,}000$ report a reattachment length of 3.2*h* from their forward step experiment while Addad *et al*. (2003) who performed LES over the same step height but much lower Reynolds number of $Re_h = 17{,}000$ report a reattachment length of 4.7*h*. Moss and Baker (1980) who studied forward steps with same h/δ but a higher Re_h of 50,000 also reported reattachment length of 4.7*h*. On the other hand, Gasset, *et al*. (2005)who studied atmospheric boundary layer flow over a cliff with similar height as above mentioned studies ($h/\delta \approx 1.43$) and Re_h same as Moss and Baker (1980) found the reattachment further downstream at 5 step heights. Zhang (1994) who computed flow over forward steps of similar height ($h/\delta = 1.43$) found reattachment length to be about 4 step heights downstream of the step.

(Farabee & Casarella, 1986) ($h/\delta = 0.417$, $Re_h = 21{,}000$) found reattachment length close to 3 step heights downstream of step. Camussi, *et al.* (2008) made PIV measurements in flow over forward facing steps ($h/\delta = 0.2$, $8800 \leq Re_h \leq 26{,}300$) and found that the downstream reattachment length is unsteady and a strong function of Reynolds number and varies from 1.5*h*-2.1*h* for lowest to highest Reh. Castro and Dianat (1983) studied small forward steps with $h/\delta = 0.192$ which is similar to that of Camussi, *et al.* (2008) and $Re_h = 50{,}000$ and found the

reattachment to be further upstream at 1.4*h*. Sherry *et al.* (2009) conducted PIV experiment on small and large forward steps for a range of Reynolds number (h/δ = 1.11-0.25, 2000 ≤ Re_h ≤ 20,000) and found reattachment length to vary between 1.1 to 4 step heights. On the other hand, Aglenichaab and Tachie (2008) studied even smaller forward steps and low Reynolds number (h/δ = 0.107, Re_h = 1920) and found reattachment far downstream at 4.1 step heights.

Taking the reattachment lengths as criteria and based on the previous findings mentioned above, the study of forward steps can be divided into two broad categories: one where the step height is larger or comparable to the incoming boundary layer thickness (large forward steps) and the other where it is less than the boundary layer thickness (small forward steps). The main difference between these two categories as shown by the previous studies seems to be the dependence of the downstream reattachment on the step height to boundary layer ratio. For small forward steps reattachment length has been shown to be a strong function of step height to boundary layer ratio while large forward steps seem to be weakly effected by this ratio Sherry *et al.* (2009). This is an important distinction since the downstream reattachment length and the region preceding it have been shown to contain the highest levels of wall pressure fluctuations and turbulence activity in the past (Farabee & Casarella, 1986). Since small forward steps are a more common feature of the flow field and come in variety of sizes that are established by structural requirements a thorough knowledge of flow field associated with them is important. However, there have been very few forward step studies in the past that have dealt with steps smaller than the incoming boundary layer thickness. The present study aims to extend the work already done on small forward steps and enhance the available knowledge of flow field that develops due to presence of these steps.

The formation of a free shear layer between the slower moving fluid close to the wall due to separation-reattachment in forward steps and faster moving free stream increases turbulence mixing and elevates the turbulence activity within the boundary layer. This results in higher velocity fluctuations, which in turn, results in elevated pressure fluctuations (compared to equilibrium ZPG boundary layer) in the vicinity of the step. In the region upstream of the step, the wall pressure fluctuations are elevated due to the presence of adverse pressure gradient caused by the separation of boundary layer. These elevated pressure fluctuations and their reach upstream of the step have been found to be significant by many studies in the past. Efimtsov *et al.* (1999) conducted wind tunnel experiments on small forward facing steps and measured pressure fluctuations upstream of the step with an aim to identify potential acoustic source of aircraft cabin noise. They studied forward steps with step size to boundary layer ratios ranging from 1% to 20% of the incoming boundary layer thickness and momentum thickness Reynolds number ranging from 2800 to 300,000. They found that the elevated wall pressure fluctuations extended as far as 100 step heights upstream of the step, a remarkable reach for a small step. They also determined that the extent of smaller steps was greater in terms of step heights upstream of the step. They found that in the upstream separation region the wall pressure fluctuations can exceed the smooth wall values by about 30 dB and for very small steps the pressure fluctuations are still about 10 dB higher at 12 step heights. Farabee and Casarella (1986) measured wall pressure fluctuations upstream and downstream of forward steps that were about 41% of the incoming boundary layer thickness with Re_h = 21,000. They found that in the upstream vicinity of the step the wall pressure fluctuations were about 20 dB higher than the smooth wall values. However, in their case the wall pressure fluctuations at about 16 step heights upstream of the step had settled down to equilibrium values. This reach of step is far less than

that found by Efimtsov *et al.* (1999) possibly due to their step size being much smaller than Farabee and Casarella (1986). Their results also show that upstream of the step, the pressure fluctuations are dominated by low frequency while the higher frequency content is lower than the equilibrium flow. They also found that closer to the step, in the separation region; the convection velocities were much lower than the equilibrium boundary layer. This indicates presence of large, slower moving eddies in the separation region. Their results also show a decrease in coherence as the flow approaches the step. This coherence is limited to lower frequencies and shows that although the separation causes large pressure fluctuations upstream of the step there is no single coherent source of pressure.

Downstream of the step, the separation and subsequent reattachment of the shear layer on solid surface is a highly unsteady process accompanied by irregular and sometimes large scale shedding of vorticity which causes high velocity fluctuations, and in turn, high pressure fluctuations in the reattachment region Cherry et al. (1984). The behavior of these large scale vortices not only cause high pressure fluctuations in the separation bubble but also effect the pressure fluctuations in the relaxation phase downstream of the reattachment. The elevated pressure and velocity fluctuations within the reattachment region have been observed by many authors in past. However, the post reattachment downstream extent to which these fluctuations can last is not clearly known. Farabee and Casarella (1986) found that the pressure fluctuation levels reach maximum around 3 step heights downstream indicating reattachment of the shear layer. They found pressure levels to be elevated compared to smooth wall across all frequencies indicating presence of both large and smaller structures in the near wall region. This is in contrast with the upstream separation bubble flow where the pressure fluctuations were elevated only at lower frequencies indicating lifting of smaller structure away from the wall. At this reattachment location (3 step heights downstream) they found that the wall pressure fluctuations exceeded the smooth wall values by about 30 dB. Moreover, they were about twice the value of pressure fluctuation induced by a backward step at reattachment. A similar observation was made by Greshilov *et al.* (1969) who found the wall pressure fluctuations to be about 26 dB higher than smooth wall near reattachment. Fricke and Stevenson (1968) studied separated flow behind a fence mounted normal to the wall and found that the highest pressure fluctuations occurred at the reattachment position. They observed that at reattachment the pressure fluctuations were about eight times the smooth wall values. A similar result was obtained by Largeau and Moriniere (2007) where they found that the highest root mean square pressure occurred at the reattachment point. They also found that the maximum value of the root mean square of streamwise velocity fluctuations and Reynolds shear stress also occurs near the reattachment. Farabee and Casarella (1986) also found that downstream of reattachment the pressure fluctuations in the relaxation phase do not quite return to their smooth wall levels even at 36 step heights downstream of step. At 36 step heights they found pressure fluctuations at lower frequencies to be about 10 dB higher than smooth wall values. They measured the coherence of wall pressure fluctuations and found that in vicinity of step (at 2 and 4 step heights, reattachment at 3 step heights) within the separation bubble the pressure fluctuations were coherent only at lower frequencies. A similar result was also obtained by Leclercq *et al.* (2009) (at 5.8 step heights, reattachment at 3.2 step heights). The coherence downstream as found by Farabee and Casarella (1986) was high as far as 24 step height downstream and there was a rise in convection velocity indicating an organized motion in post reattachment region which they attributed to the process of separation in front of forward step into a free shear layer.

Recently, Ji and Wang (2010, 2010a) performed Large Eddy Simulation (LES) on forward steps whose size ranged from 0.83% to 53% of the incoming turbulent boundary layer thickness. Their momentum thickness Reynolds number was 4100 and the Reynolds number based on step height ranged from 400 to 26,000. The present work was designed to closely match their work so as to form a good comparison platform between measurement and computation. Their results show that the maximum root mean square pressure occurs in the reattachment region except for their two smallest step sizes (h/δ = 0.83%, 3.3%) for which the highest r.m.s pressure actually occurs upstream of the step due to the disappearance of the separation bubble from the top face of the step. They also found that upstream of the step at 6 step heights only the small steps influence the pressure fluctuation which is similar to the observation made by Efimtsov *et.al* (1999) that smaller steps have greater extent upstream of step in terms of step heights. At 1 step height upstream they found that the pressure fluctuations for all steps show similar levels except for their largest step size which is actually displays lower spectral levels than the rest of the steps. Downstream of the step, they found that the two largest steps with a recirculation bubble present on the top face of the step show highest magnitudes at all frequencies. Their downstream spectra also shows a faster decay in spectral levels for larger step sizes as one moves further downstream from the step. Ji and Wang (2010) also studied the relaxation of reattached shear layer downstream of the step and found spectral levels were 10% above the smooth wall at about 100 step heights downstream of the step. They also studied the space time pressure correlations to determine the flow structure due to the presence of forward steps and its effects on the wall pressure fluctuations. They found large slow moving well correlated structures in the reattachment region downstream of the step and less coherent structures downstream of the reattachment region. Downstream of reattachment, however, the structures were well correlated with those further downstream. These results indicate that the unsteady process of reattachment serves to de-correlate pressure fluctuations across it.

In summary, many previous studies dealing with forward facing steps in a turbulent boundary layer have shown that the separation upstream of the step is a weak function of Reynolds number. On the other hand, the downstream reattachment is unsteady and a strong function of flow parameters (Reynolds number) and step geometry. Previous studies have found the downstream recirculation bubble (on top face of the step) just upstream of the reattachment region to be the most efficient region in terms of wall pressure fluctuations. Some studies have shown that the recovery of flow after the reattachment is a slow process and have indicated that pressure fluctuations can persist far downstream of the step. However, the behavior of these flows is not well understood especially for step heights that are smaller than the incoming boundary layer thickness. The dependence of reattachment on flow parameters and geometry is not well understood. The pressure fluctuations that are induced due to the unsteady reattachment of the flow are thought to persist far downstream of the step. However, due to lack of information on pressure fluctuations far downstream of the step, the exact extent of these pressure fluctuations is not known. The extent of the modified reattached boundary layer downstream of the step also remains unclear. The wall pressure-velocity fluctuations relationship within the reattached and energized boundary layer and the flow structure also remain ambiguous in small forward step flows. The present work was performed keeping in mind these shortcomings and the objectives of the work have been outlined in the following section.

1.3 *Objectives*

In light of relatively few studies on forward steps summarized here, the present work attempts to further the knowledge of turbulent boundary layer flows over small forward steps.

The objectives of the work were:

- Extend the knowledge of separated-reattaching turbulent boundary layer flows that are a common feature in flows over aerodynamic/hydrodynamic vehicles, wind turbines etc. and are a source of interior noise, panel vibrations and reduced fatigue life.
- Determine the effect of the step geometry (step height) and flow parameters (boundary layer thickness and Reynolds number) on the wall pressure fluctuations in the vicinity, upstream and far downstream of the step.
- Reveal the scaling of wall pressure fluctuations in forward step flows.
- Determine the flow structure in forward step flows non-intrusively through the use of spatial-temporal characteristics of wall pressure fluctuations.
- Determine how the presence of forward step modifies the attached equilibrium turbulent boundary layer velocity characteristics.
- Relate the spatial-temporal wall pressure fluctuations to the velocity fluctuations to find a possible pressure-velocity relation in forward step flows.

To achieve these objectives, measurements of quantities such as mean wall pressure, wall pressure fluctuations, velocity fluctuations, single point and two point pressure characteristics, single point and two point velocity fluctuations, separation/reattachment lengths in non-equilibrium, small forward step flows were made at Virginia Tech Stability Wind Tunnel. Due to its large test section (7.3 m × 1.85 m × 1.85 m), high Reynolds number flows with small h/δ geometry are easily achievable. Moreover, the quite operation of the wind tunnel due to its unique semi-anechoic/anechoic configuration enables measurement of wall-pressure fluctuations/acoustics with minimum acoustic contamination from the facility noise.

2. Experimental Setup and Instrumentation

2.1 *Virginia Tech Stability Wind Tunnel*

The measurements for the present study were performed in Virginia Tech Stability Wind Tunnel which was originally built in 1940 at NACA Langley Aeronautical laboratory. The goal of the tunnel was to measure the dynamic stability derivatives for a fixed model in position, hence the name. The wind tunnel was acquired by Virginia Polytechnic Institute (VPI) in 1959 and became operational in 1961 after calibration of the tunnel. In the year 1994 the fan motor was completely overhauled and windings were reinsulated. This was followed by installation of a new fan increasing the overall efficiency of the tunnel. The tunnel has a rectangular test section measuring 7.3 m × 1.85 m × 1.85 m which is removable and thus provides both aerodynamic and acoustic testing capability. The tunnel is a single return subsonic type and the air flow is provided by a 4.3-m propeller which can run up to 600 RPM. The propeller is powered by a 0.5-MW variable speed DC motor. The maximum speed that can be attained in the tunnel is 80 m/s with Reynolds number per meter up to about 5,000,000. The free stream velocity is monitored using a reference pitot static tube which for the present work was located at (x, y, z) = (-0.44m, -0.59m, 1.25m)[*]. An air exchange tower which is located downstream of the fan and motor assembly provides temperature stabilization in the tunnel. The air flows from the exchange tower to a settling chamber measuring 5.5 m × 5.5 m consisting of seven turbulence-reducing screens. The settling chamber is followed by a 9:1 contraction nozzle which further reduces the turbulence levels and the flow is then directed to the test section. The use of the screens and contraction nozzle provides uniform flow in the test section with low turbulence levels of 0.024% and 0.031% at 30 m/s and 57 m/s respectively. Due to the unique capability of having a removable test section; the wind tunnel can be operated in both aerodynamic and acoustic configurations. In its acoustic configuration, the wind tunnel is the largest university operated anechoic tunnel in the United States. The acoustic test section is lined with sound absorbent Kevlar panels on the floor and ceiling and two Kevlar windows on either side that are associated with two large anechoic chambers. These anechoic chambers consist of foam wedges that eliminate any acoustic reflection for frequencies above 190 Hz. A schematic of the wind tunnel with the location of fan, acoustic test section with anechoic chambers on both sides and the air exchange tower has been shown at the top of Figure 2. The acoustic chambers and their dimensions have been shown in a zoomed in view at the bottom left of the figure. In order to create the step one of the Kevlar windows was replaced with a false test wall. The test section was modified slightly to accommodate this test wall by replacing the Kevlar panels close to the wall by aluminum panels. This configuration has been shown at the bottom right of the figure. The custom made fan of the Stability Tunnel manufactured by Prince Aircraft Company has been shown in Figure 3. The modification of the acoustic test section to create forward steps will now be described in detail.

[*] Coordinate system defined in section 2.2

2.2 *Test Wall and Forward Step Setup*

To create the forward steps a false wall was installed in place of one of the acoustic Kevlar window. This false wall was designed such that it was capable of moving inward towards the test section and outwards from it. This false wall was made of 6 Lexan panels which covered the entire height (1.85 m) and spanned the entire length (7.32 m) of the test section. In order to provide a smooth transition between the wind tunnel contraction and the test wall a contraction fairing was installed upstream of the test wall. At the upstream end of this contraction a 9.5 mm L-shaped beam was installed to trip the incoming boundary layer. The trip was located 1.36 m upstream of the test section entrance providing a total length of 8.7 m to grow a turbulent boundary layer. Figure 4 shows the entire stretch of the contraction fairing and Lexan test wall inside the test section with flow from left to right. The dimension of the contraction and test section, location of trip are also shown. The top left of the figure shows the 9.5 mm boundary layer trip in the inset. Each of the 6 Lexan panel used to create the false wall were 48.0 in. wide and 72.0 in. high. The panels were created by bracing a Lexan sheet with 10 series Aluminum 80/20 beams on the rear side to create a frame. This frame consisted of two longitudinal beams of square cross section measuring 2.0 in. on upstream and downstream side. A cross sectional view of one of these beams has been shown on the right in Figure 5 (b). The top and bottom edges of the panels were braced with Aluminum 80/20 beams running parallel to the floor and ceiling of the test section and measuring 2.0 in. × 1.0 in. in cross section. To provide buckling strength to the panels another 2.0 in. × 1.0 in. 80/20 beam running longitudinally was attached to the center of the frame. The cross section view of one of these beams has been shown on the left in Figure 5 (a). Figure 6 shows a schematic of one of the Lexan panels along with an actual panel and the entire support system consisting of the 80/20 beams. It should be noted that the longitudinal beams on the upstream and downstream side of the panels are not aligned with edge of the Lexan sheet and there is an offset of 0.5 in. (12.7 mm) on either side.

In order to attach the panels to the floor and ceiling of the test section the slotted cross section of the 80/20 beams was used. The 80/20 beams have a slotted cross section (as seen in Figure 5 (a) and (b)) through which a pair of screws and wing nuts can be slid. The ceiling and floor are fitted with 24 (4 for each panel) 80/20 pieces each with cross section profiles similar to that of the panels support beams. The laterally running beams at the top and bottom of the panels were fitted with brackets consisting of wing-nuts and screws that can slide into the 80/20 pieces attached to the floor and ceiling of the test section. The top and bottom beams were slid into these pieces attached to the floor and ceiling and were fastened down. The space between the 80/20 pieces attached on the floor and ceiling was padded with spacers made of hardboard to ensure no outflow of air from the test section. The top left of Figure 7 shows this entire mechanism and the setup. The figure shows the Lexan panel fastened to the floor of the test section with the help of the wing-nuts slid into the 80/20 pieces attached on the floor. The bottom right of Figure 7 shows the same setup without a Lexan panel inside the test section.

For the present work, first all six panels were installed by attaching them to the floor and ceiling of the test section using the mechanism described above. Next, these panels were adjusted to obtain an equilibrium position for these panels. The equilibrium position was the position of each of the panels at which zero mean wall pressure gradient was obtained. To create a forward step the first 3 upstream panels were kept fixed at their zero pressure gradient positions while the 3 downstream panels were moved inwards by distance '*h*' corresponding to the step size to be

tested. The gap created between the 3rd and 4th panel due to the movement of the last 3 panels was filled by installing a 12.7 mm thick Lexan sheet to form the face of the step. This Lexan step was installed behind the 4th panel in the 12.7 mm space offered by the overlaying Lexan sheet. Any gaps around the face of the step were sealed using a caulking method and proper care was taken to ensure there was no flow leakage. Figure 8 shows the movement of the last 3 panels to create forward step and the Lexan sheet used to create the step. The acoustic chamber which was used for instrumentation has also been shown. The bottom of the figure shows a zoomed in view in *x*-*z* plane (or top view) of panels 3 and 4 to show the mechanism through which the 12.7 mm thick Lexan was attached between panels 3 and 4. The coordinate system used throughout the wind tunnel measurements and data analysis have has also been shown in Figure 8. The streamwise coordinate is '*x*' with origin at the face of the step and downstream of the step being the positive direction. The spanwise coordinate is '*y*' with origin at the mid height of the test section. The normal to the wall coordinate is '*z*' with the origin always at the wall (i.e. for both upstream and downstream of the step the origin is at the wall). The actual setup of the step in the test section has been shown in Figure 9. On the right a zoomed in view of the forward step and the rear side of the 4th panel with Lexan step in place has also been shown.

Using the mechanism described above 3 forward steps of height 3.65 mm, 14.6 mm and 58.4 mm were tested for the present work. These step heights are separated by a factor of 4 i.e. the largest step size is 16 times the smallest step and 4 times the medium step size. These sizes were deliberately chosen to match Ji and Wang's (2010, 2010a) step height to boundary layer thickness ratios in order to provide a good comparison platform between experimental and computational work. Due to the large size of the test section, the step sizes mentioned here generated large aspect ratios (step height to spanwise tunnel dimension ratio) of 500, 125, and 31.3 for small, medium and large step size respectively. Cherry *et al.* (1984) observed that for a forward step flow with endplates a certain minimum aspect ratio was required to achieve spanwise uniformity in the flow. They observed that for forward steps flow that do not meet the aspect ratio criteria the mean reattachment line curves across the span and the flow is not free from 3 dimensional effects. When they compared their reattachment length with some other past works with different aspect ratios they found that the reattachment lengths reach asymptotic values at aspect ratios in the range of 10-15. The aspect ratios for the present work are much larger than this range and ensure spanwise uniformity of the flow.

2.3 *Mean Wall Pressure*

Mean wall pressure along the wall was measured using pressure taps at several streamwise and spanwise locations along the wall, both upstream and downstream of the step. This was done to study the effect of separation and reattachment process on the mean wall pressure and to establish two dimensionality of the flow. In addition, several pressure taps were installed on floor and ceiling panels of the test section to establish the zero pressure gradient line. The pressure taps used to measure the mean wall pressure were manufactured using an Objet Alaris 30 3D prototyping machine. The outside port diameter on the flow side was 1.5 mm and the inside diameter (sensing area) was about 0.5 mm. The head of these pressure taps measured 13 mm same as thickness of the Lexan sheet in which these taps could be inserted. The pressure taps were connected to 1/8th in. (3.17 mm) thick Tygon tubing connected to a scanivalve connector which was in turn connected to an Esterline NetScanner Model 98RK to measure the pressure signal. A schematic of this entire setup has been shown in Figure 10. The figure shows a

single pressure tap inserted in the 13 mm thick Lexan sheet routed through Tygon tubing to the pressure scanner. Also shown in the figure are the rapid prototyped pressure taps, scanivalve connectors and the pressure scanner. The reference free stream pressure and velocity needed to calculate the wall pressure coefficient was measured using a reference pitot located at (x, y, z) = (-0.44m, -0.59m, 1.25m).

2.4 *Wall Pressure Fluctuations*

The wall pressure fluctuations from forward steps immersed in turbulent boundary layer were measured at several upstream and downstream locations using microphones. The measurement locations for wall pressure fluctuations were designed to meet the following criteria

- Measurements far downstream from the step for all 3 step sizes to determine the streamwise influence of the step on pressure fluctuations.
- Large spanwise extent of measurement stations to satisfy the two dimensionality of the flow and to enable spanwise space time pressure correlations to identify the spanwise flow structure.
- Common streamwise distance of measurement stations in terms of step height from the step for all 3 step sizes to determine any possibility of flow scaling on step height

To measure the wall pressure fluctuations induced due to forward steps Senheiser KE4-211 microphones were used initially. However, post measurement analysis showed that the pressure fluctuations from steps exceeded the dynamic range (130 dB) of these microphones. Due to these over range issues, B&K 4138, 1/8 inch pressure field microphones were used in the second phase of testing to measure surface pressure fluctuations. These microphones have a higher dynamic range and wider frequency range compared to the Senheiser microphones. B&K 4138 microphones have a maximum SPL of about 168 dB compared to 130dB of Senheiser and therefore these microphones were an ideal solution to the dynamic range issue. Moreover, these microphones provide a wider range of frequency resolution (6.5 Hz to 140 kHz) so the pressure fluctuations at lower frequency could be better resolved with these microphones. The sensitivity of the microphones was 1.0 mV/Pa and a diameter of 3.175 mm ($1/8^{th}$ inch). These microphones originally came with a salt and pepper shaker cap which was replaced by ½ mm pinhole caps custom manufactured by B&K which Devenport *et al*. (2011) showed to be sufficiently small to resolve pressure fluctuations up to 20 KHz. Original salt and pepper shaker cap and custom manufactured ½ mm pinhole cap have been shown in Figure 11.

Although these microphones are better equipped to deal with the high pressure fluctuation signals as seen in the step flow, there were two major issues that had to be dealt with before they could be used for final testing. Firstly, in order to thoroughly understand the nature of pressure fluctuations and their far downstream extent induced by forward steps a large number of microphones spanning across the test wall had to be placed. However, there were only 7 B&K microphones available. To overcome the deficit between the measurement locations and available microphones a new microphone movement system had to be adopted where the available microphones would be used to measure pressure fluctuations at a particular speed and step setting. Once a particular location was measured, the tunnel would be stopped and the microphones would be moved over to a new location. However, placing the B&K microphones directly into the wall and then moving them over and over again would put them at high risk of

breaking since these microphones are extremely delicate. To overcome these issues, a microphone holder system was designed and manufactured. The microphone holders consisted of sleeves manufactured using Alaris 30 3D prototyping machine. These sleeves were then inserted into slots that were machined into the Lexan panel. The slots were carefully machined so that the sleeves would sit tight in these slots and would prevent the microphones from breaking while keeping the microphone surface flush with the test wall. There were two different microphone holders that were designed to hold the 7 B&K microphones available for measurement. The first holder was a 152 mm long bloc to hold 5 microphones together and two single microphone holders one of which was used for the cancellation microphone. For a particular step size or smooth wall these holders were inserted into particular slots on the test wall covering 6 or 7 measurement locations (since 1 microphone suffered failure during testing) at a time and measurements were taken for 30 and 60 m/s. Figure 12 (a) and (b) show the flow side view of a 5 microphone holder and a single microphone holder respectively. The dimensions showing the separations of each of the microphone from the farthest microphone within the 5 microphone holder have also been shown. The size of the holder bloc exposed to the flow has also been shown for both holders. Figure 13 shows the rear view of these 5 and single microphone holders inserted into the test wall. After taking measurements for 6 locations on the wall for 30 and 60 m/s the tunnel was turned off and then these holders were inserted into slots corresponding to 6 other measurement and cancellation locations. The slots that corresponded to locations not being measured on the test wall were covered by inserting slot covers in them. These slot covers were similar to microphone holders but without sleeves in them. A test wall view with measurement holders and the holder covering slots in the test wall has been shown in Figure 14. Despite of the care taken in ensuring that the microphone holders were flush against the test wall a small step was inevitably present at the edge of these holders. These steps, however small they might be may corrupt the pressure signals since the microphones in the holders are fairly close to these edges. To find the effects of these steps the pressure signals acquired with microphone holder flush against the wall was compared to the pressure signals acquired with microphone holder slightly offset. The two results were compared and showed no difference thus establishing the fact that the step at the edge was too small to corrupt the signals acquired by the microphones.

Figure 15 shows the front view (x-z plane) of panels 3, 4 and 5 which contained all the pressure fluctuation measurement locations. The test section floor and ceiling have also been shown in the figure along with the height of the test section. The figure shows the 5 microphone slots and single microphone slots as they were machined in the test wall for all measurement locations. The 5 microphone slots were created in both a streamwise and spanwise arrangement along with a number of single microphone slots in the same arrangement. This kind of arrangement helps to measure the streamwise extent of the pressure fluctuations as well as ascertain the two dimensionality of the flow by measuring spanwise pressure fluctuations. Additionally, this setup helps to measure the streamwise and spanwise space time characteristics of pressure fluctuations. From the figure it can be seen that there were 4 primary spanwise measurement arrays, one upstream of the step and three downstream. The streamwise distance of each of the 4 primary spanwise measurement array has been shown on the figure. At the bottom of each spanwise array the three numbers show the streamwise distance of a particular spanwise array in terms of step height for all 3 step sizes. The number on the top is for the smallest step size, the number in middle for the medium step size and the number at bottom is for the largest step size. From the figure it can be seen that the last spanwise array is at 576, 144, 36 step

heights for the small, medium and largest step size respectively. These streamwise distances extend farther downstream than any other measurements taken in the past for forward steps. It should also be noted that the downstream location of the spanwise arrays was designed so as to provide common measurement stations in terms of step height distance for each step size. These spanwise arrays were determined keeping in mind a factor of 4 between the 3 step sizes. For example, the second spanwise array is 4 times the distance of the first spanwise array and the third spanwise array four times the distance of the second one. Also seen in the figure are two rows of streamwise measurement locations and their distance from the floor of the test section. The top row of the microphones was designed to provide streamwise pressure fluctuation measurements for the 3 step sizes such that there were common step height distance for the three step sizes for the purpose of streamwise pressure fluctuation scaling. The bottom row in the figure that runs along the streamwise direction was used for acoustic cancellation where a microphone without a pinhole was to be placed during each measurement.

The addition of custom made ½ mm pinholes for greater spatial resolution changes the response of the microphones, so the B&K microphones were calibrated using a comparison calibration method. The microphones with pinholes along with a reference B&K 4138 microphone without a pinhole were both subjected to white noise source inside an acoustically treated chamber. Their responses were then compared to yield the sensitivity and phase response of microphones with pinholes. The calibration of the microphones was performed using the same technique as described by Alexander (2009) in which the microphone calibration is simply given by the response of the microphone divided by the response of the reference B&K microphone. Once the calibration is known then it can be multiplied with the known sensitivity of the reference microphone to yield the absolute sensitivity of the microphone. The calibration was performed both before and after the test to account for any changes in the frequency response of the microphones due to exposure to flow and handling during the test. An Agilent VXI data acquisition system was used to create white noise using a University sound IDC60C8 speaker and acquire frequency response from the microphones. Figure 16 shows the calibration setup inside the acoustic chamber with the reference microphone mounted on the stand facing the white noise source. The figure also shows amplifiers used for B&K microphones and the white noise source. The frequency response for all 7 microphones i.e. 6 microphones with pinholes and a 7th reference microphone without the pinhole were recorded up to 25 KHz using this setup.

Once the calibrations for all microphones were performed, it was found that the microphone calibrations can be modeled as a 2nd order dynamical system with the transfer function given by

$$H(s) = \frac{B(s)}{a_1 s^2 + a_2 s + a_3} \qquad \text{(Eq.1)}$$

B(s) is a polynomial of degree less than the order of the system. The denominator of the above transfer function describes the behavior of the system. The coefficients a1 and a3 control the resonant frequency while the coefficient a2 controls the damping frequency. A sample phase and magnitude calibration along with the fitted curve has been shown in Figure 17.

The pressure fluctuation signals from the microphones in the actual tunnel measurements were acquired through the pulse analyzer platform developed and manufactured by B&K. The pulse system consists of a multichannel data acquisition hardware called LAN-XI which allows hardware to PC interfacing and pulse analyzer platform software. A LAN-XI setup with

microphones connected has been shown in Figure 18. Using the pulse system, the un-calibrated raw spectra for pressure fluctuations was acquired at a sampling rate of 65536 Hz. The pulse analyzer platform implicitly converts the data in volts to Pascal using the sensitivities determined by the amplitude calibrations and thus could be viewed in real time to watch for any discrepancies. The amplitude calibrations were performed daily for each microphone using a 250 Hz Pistonphone. The frequency calibrations done in the acoustic chamber were applied to the raw spectral data post measurement.

During testing, the spectra of pressure fluctuations revealed that the response of the microphone with pinhole was a function of flow speed. This phenomenon is clearly visible in Figure 19 where the measured boundary layer spectra for microphones clearly show a resonant peak around 10 kHz after applying calibrations. The reason for this is that when the there is no flow over the microphones, the Reynolds number of the microphones is very low but as the flow speed is increased and the Reynolds number increases the effective viscous effects on the pinhole-microphone system reduces. This leads to a reduction in viscous damping. The effects of viscous damping due to pinhole attachment were taken into account during the post processing of data by optimizing the calibrations. In the optimization process both the damping and resonant frequency of the 2^{nd} order system were optimized for each flow speed by finding a combination of damping and frequency multipliers which would yield minimum r.m.s level for the derivative of calibrated spectrum. Figure 20 shows the optimization contour displaying the effects of damping and frequency multipliers on the R.M.S levels for the derivative of the calibrated spectra for 60 m/s flow speed case. Following this approach it was found that the damping multiplier significantly reduces with the flow speed while the frequency multiplier shows little deviation. For example, at 60 m/s the damping reduces by about 40% and the frequency by about 4%. The correction factors found using this approach were then implemented to the calibration fit and calibration was applied to the raw data. Figure 21 shows the raw i.e. un-calibrated spectra and calibrated spectra found using this approach along with the magnitude of calibration itself. It can be seen from Figure 21 that taking into account the changes in the system response of microphone-pinhole combination due to flow speed variation the calibrated spectrum no longer shows the spikes seen in Figure 19.

2.5 *Hot Wire Anemometry*

An Auspex AHWU-100 constant temperature single wire probe was used to measure the mean velocity and turbulent intensity within the boundary layer for steps and smooth wall at 30 m/s. A single hot wire consists of two probe prongs that are connected through a thin wire of known resistance. For the AHWU-100 anemometer the probe prong length is 15 mm. The prongs are separated by a distance of 1.2 mm and are connected via a Tungsten wire of diameter 5 μm. The probe prongs are attached to a 38 mm long shaft with outside diameter of 3.175 mm. The entire prong-shaft setup sits in a C-shaped block about 25 mm long. The tubing is attached to the C shaped block through a set screw. The entire setup itself sits inside another C-shaped metal block that is attached to the tunnel traverse. The entire setup with dimensions of the prongs, tubing and the C-shaped holder has been shown in Figure 22.

The electrical input power through the probe wire is equal to the convective heat transfer from the hotwire. Thus, if the resistance of the wire is known and the fluid temperature is nearly constant then the fluid velocity can be found by using the convective heat transfer coefficient and

the current (or the voltage) passed through the wire. In order to find the relation between the voltage and the fluid velocity the probe was calibrated based on king's law. To calibrate the anemometer, it was placed in the free stream away from the boundary layer (roughly at the center of the tunnel) and then calibrations were performed by acquiring voltages for speeds in increments of 5 m/s beginning from 15 m/s up to 65 m/s. A Dantec Dynamics 90C10 Streamline CTA system was used to operate the probe and anemometer signals were recorded using a 64 channel 16-bit Agilent E1432 digitizer and signal analyzer. The temperature in the tunnel was monitored using a temperature probe attached to the test wall and the probe was recalibrated if the temperature deviation was more than 5 degrees Fahrenheit than the measurement temperature.

The single hot wire anemometer was used to measure the mean velocity and turbulence profiles for the smooth wall and for medium forward step (14.6 mm) at 30 m/s. For the forward step case, a number of profiles were taken at different streamwise locations by traversing the probe on a tunnel traverse system through the boundary layer. The probe was traversed from outside the boundary layer to ½ mm away from the wall. The absolute position of probe relative to the wall was determined using a contact resistance method. In this method, a wire of known thickness was taped to the measurement location on the wall. Another wire was taped on the probe holder itself and both were then connected to a voltmeter. As the probe holder touched the tape on the test wall the circuit was complete and voltmeter registered a resistance. With the thickness of the tape known, the exact position of probe from the wall was known. A hotwire probe setup with dimensions and a foil tape used for the contact resistance method have been shown in Figure 22.

The mean velocity and streamwise velocity fluctuation profiles (streamwise turbulence intensity) were measured for the smooth wall 152 mm upstream of the location of the step at 30 m/s. These profiles were also acquired at 30 m/s for the medium step (h = 14.6 mm) at one upstream location and 8 downstream locations from the step. Table 1 shows the absolute streamwise locations in mm as well as the corresponding measurement locations in terms of step height from the step. The negative sign in the first row indicates upstream location of measurement. The mean velocity at these locations was measured at a sampling rate of 6400 Hz. Streamwise velocity autospectra within the boundary layer was also measured at a sampling rate of 51200 Hz. Looking at Table 1 it can be seen that the velocity measurements were made as far as 148 step heights downstream from the step. In order to analyze the pressure-velocity relationship in step flows measurements were made close to the 3 downstream spanwise microphone measurement array locations of 9, 37 and 148 step heights.

Table 1. Streamwise Anemometry Measurement Locations for Medium Step (h = 14.6 mm)

x (mm)	*x/h*
-152.0	*-10.6*
22.0	*1.5*
132.8	*9.2*
333.0	*23.3*
532.9	*37.0*
1066.8	*74.2*
1600.2	*111.3*
2132.8	*148.0*

Dr. Aurelien Borgoltz and Mr. Michael Morton used a quad hotwire probe to measure the boundary layer velocity characteristics of smooth wall flow along the present test wall at 60 m/s. However, due to the tunnel blockage by the 3D traverse system speeds of only 55 m/s could be achieved in these measurements. Thus, all the boundary layer velocity data for smooth wall shown in the text for high Reynolds number case is at 55 m/s. Some 2 point velocity measurements using two quad hotwire anemometers were also made for the smooth wall and for medium step height at x/h =9 and 36 by Dr. Aurelien Borgoltz and Mr. Michael Morton. The measurements included measurements of velocity fluctuations in both spanwise and normal to the wall direction using two three component quad hotwire anemometers. One of these anemometers was the fixed anemometer which was allowed to move only in normal to the wall direction and the other was mounted on a 3D tunnel traverse system capable of moving in all 3 dimensions. This setup was used to obtain the 3 component single point profiles as well as 2 point velocity data. The details of the setup, hotwire calibration and, data acquisition can therefore be found in Morton *et al.* (2012).

2.6 *Oil Flow Visualization*

Oil Flow visualization was done to visualize the flow around the step as well as to measure the separation and reattachment lengths for step flow. Oil flow visualization was done at speeds of 30 m/s and 60 m/s for all 3 step sizes to determine possible effects of step size and Reynolds number on the reattachment locations. In order to perform the flow visualization black contact paper with a mix of oil were pasted upstream and downstream of the step. The oil mixture consisted of 5 parts of Titanium Dioxide (TiO_2), 1 part of Oleic Acid ($C_{18}H_{34}O_2$) and 15 parts of Kerosene. Once the flow is turned on, the solution on the contact paper flows to reveal a

mean separation and reattachment lines on the contact paper due to recirculation bubbles upstream and downstream of the step. A sample oil flow visualization done of the upstream region for the largest step (h = 58.4 mm) has been shown in Figure 23.

3. Experimental Results and Analysis

The experimental results obtained in the present work are presented and discussed in the following sections. The mean wall pressure and boundary layer velocity measurements for the equilibrium setting (no step) will be discussed first. This will be followed by a discussion on the mean wall pressure and the mean separation and reattachment lengths due to presence of forward steps in the flow. Next, the fluctuating wall pressure will due to forward steps will be discussed in forms of r.m.s wall pressure and pressure frequency autospectra. The scaling of pressure spectra will then be discussed followed by a presentation on the 2 point space-time pressure measurements. Thereafter, switching gears, the text will turn to the single point and two point velocity measurements obtained for the medium step size.

3.1 Equilibrium Mean Wall Pressure Gradient

Mean wall pressure was measured using the pressure taps installed on the wall. It was important to establish a zero pressure gradient line to get the equilibrium setting for the false wall. In total there were 60 streamwise wall pressure taps that were used to measure the mean wall pressure. The free stream mean pressure was measured using the reference Pitot tube. The wall pressure coefficient then is given by

$$C_p = \frac{p_{wall} - p_\infty}{\frac{1}{2}\rho_\infty U_\infty^2} \qquad (Eq.2)$$

Figure 24 shows the streamwise mean wall pressure coefficient for the no-step case at both low and high Reynolds number. The Reynolds number per meter is also shown on the figure, it can be seen that Reynolds number per meter of about 6 million was achieved in this test. The step location has also been shown in the figure; note that the origin of the coordinate system is the step location. So, the negative x locations show the upstream pressure coefficient. It can be seen from the figure that a good zero wall pressure gradient was achieved for both the cases. For both the cases the mean wall pressure coefficient stays between 0 and -0.03 throughout the entire stretch of the test wall. The reason it is not zero is due to the inevitable presence of minor discontinuities such as the seam of the panels in the flow field.

Mean wall pressure was also used to establish the two dimensionality of the flow in the tunnel. To do this, mean wall pressure was also measured in the spanwise direction using the pressure taps at two different streamwise locations for both speeds. The spanwise mean wall pressure coefficient at two streamwise locations for both Reynolds number has been shown in Figure 25. Looking at the spanwise pressure it can be seen that it is a near horizontal line showing spanwise homogeneity of the flow and indicating a two dimensional flow along the test wall.

3.2 Equilibrium Boundary Layer Velocity Statistics

In order to test the turbulent boundary layer flow over small steps, one of the first objectives was to grow and establish the equilibrium boundary layer thicknesses for the two different Reynolds number cases. As mentioned in the previous section, a 9.5 mm trip (shown at

the top left corner of Figure 4) upstream of the test wall was used to grow boundary layers for speeds of 30 and 60 m/s. However, due to the blockage created by the 3D Traverse system installed in the test section, free stream velocity up to 55 m/s could only be obtained. It is assumed that the parameters measured at this speed are same as those for 60 m/s and were used throughout the analysis and plotting for forward steps presented in this text. The boundary layer profiles were measured 152 mm upstream of the step location (4.87 m downstream of the 9.5 mm trip). For the 30 m/s case, the smooth wall profile was measured using a single hotwire probe. Additionally, the profile at 30 m/s for the same smooth wall configuration as present case were measured using a quad hotwire probe in both single point and two point configurations by Mr. Michael Morton and Dr. Aurelien Borgoltz. Forest (2010) also measured the smooth wall profile at the same location and same configuration as the present case using a Flat Head Pitot. The smooth wall profile at 60 m/s on the present test configuration (or 55 m/s due to tunnel blockage) was measured using a quad hotwire probe by Dr. Aurelien Borgoltz and Mr. Michael Morton.

These profiles were plotted on a log scale along with the theoretical law of the wall profile to establish their correctness. Law of the wall relates the velocity within the boundary layer by dividing the entire turbulent boundary layer into four different regions: viscous sublayer, buffer layer, log-law region and the outer layer. The theoretical law of the wall profile along with the present and past measured profiles for 30 m/s has been shown in Figure 26. The smooth wall profile at 55 m/s measured using a quad hotwire probe along with the law of the wall profile has been shown in Figure 27. Figure 26 and Figure 27 also show the four different regions within the boundary layer defined by the law of the wall. The vertical axis is the velocity parallel to the wall non-dimensionalized by the wall shear stress and is given by

$$u^+ = u\sqrt{\frac{2}{C_f}} \qquad (Eq.3)$$

Since no measurements were made for the skin friction coefficient it was found through a fitting algorithm where a range of values for C_f were chosen and the profiles were plotted against the law of the wall for these values. The best fit C_f value was then chosen to be the true value. These C_f values were found to be 0.0025 and 0.00245 for 30m/s and 55m/s respectively and have been shown at the top Figure 26 and Figure 27. The horizontal axis shows the normal to the wall coordinate non-dimensionalized by the wall shear stress and is given by

$$y^+ = \frac{z\sqrt{C_f}U_\infty}{\sqrt{2}\upsilon} \qquad (Eq.4)$$

As seen in Figure 26 and Figure 27 the profiles are in good agreement with each other and the law of the wall. It can also be seen that single hotwire profile reaches closest to the wall and has a few data points within the buffer region while all the other profiles are contained within the log-law and outer region.

The boundary layer thickness was calculated using linear interpolation to find the normal to the wall distance where the streamwise turbulence intensity reaches to about 2%. Two important boundary layer parameters that can be calculated once the mean velocity boundary layer data is available are displacement thickness and momentum thickness. Displacement

thickness is defined as the distance the wall would have to be moved normal to the flow in inviscid flow to obtain the same solution outside the boundary layer as the boundary layer equations would yield. The displacement thickness is found by integrating the velocity defect across the boundary layer thickness and is given by:

$$\delta^* = \int_0^{\delta} \left(1 - \frac{U}{U_e}\right) dz \qquad (Eq. 5)$$

Momentum thickness is similar to displacement thickness and is the amount wall would have to shift in inviscid flow so as to give the same momentum as in the real viscous fluid. The momentum thickness is given by:

$$\theta = \int_0^{\delta} \left(1 - \frac{U}{U_e}\right) \frac{U}{U_e} dz \qquad (Eq. 6)$$

Note that the above equations need to be integrated from the wall to the boundary layer thickness. However, in measurements there is a certain restriction on how close to the wall data can be obtain and integrating above equations just with the measured data points would yield incorrect results. Thus, the measurement points need to be extrapolated to provide points closer to the wall. The extrapolation process was carried out by taking the fitted law of the wall single hotwire data points and then extrapolating them to the wall. The measured and extrapolated velocity data was then used to compute the momentum and displacement thicknesses. The measured and calculated boundary layer parameters for the present work are shown in Table 2 where they are compared with the step sizes tested in present work. The boundary layer parameters for Farabee and Casarella's (1986) experiment and Ji and Wang's (2010, 2010a) LES simulation have been shown in row 2 and 3 of Table 2 respectively for the sake of comparison. Looking at Table 2 it can be seen that the current measurement conditions have a wide range of step height to boundary layer ratio and Reynolds numbers. The step height to boundary layer ratios (h/δ) range from as low as 3% for smallest step to as high as 60% for largest step indicating the relative small size of the step compared to the boundary layer. Comparing the Re_h for large step at 60 m/s with that of Farabee and Casarella (1986) we see that it is about 10 times higher. Moreover, there is a much larger range of h/δ in the current work and the lowest ratio is about $1/10^{th}$ of Farabee and Casarella (1986). Comparing the statistics with LES simulation conditions we see similar h/δ ratios but much larger Reynolds number (about 4 times) in the present work. As mentioned in section 1.2 and 1.3 the h/δ ratios for the present work were purposely designed to match Ji and Wang's (2010, 2010a) work so as to provide a comparison platform between the present experimental work and past LES simulation.

Table 2. Equilibrium Boundary Layer Parameters for Present and Past Works[†]

U_∞ (m/s)	δ (mm)	θ (mm)	δ^*	Re_δ	Re_θ	C_f	h (mm)	h/δ	Re_h
Present									
60	*95*	*7.3*	*8.8*	*346,000*	*26,600*	*0.0023*	*3.65*	*3.8%*	*13,300*
							14.6	*15.4%*	*53,200*
							58.4	*61.5%*	*213,000*
30	*97*	*8.5*	*10.8*	*177,000*	*15,500*	*0.0025*	*3.65*	*3.8%*	*6,640*
							14.6	*15.1%*	*26,600*
							58.4	*60.1%*	*106,000*
Farabee & Casarella (1986)									
25	*30.5*	-	-	-	*4079*	-	*12.7*	*41.70%*	*21,000*
Ji &Wang (2010)									
-	-	-	-	-	*4100*	-	-	*0.80%*	*400*
								3.30%	*1600*
								13.00%	*6400*
								53.00%	*26,000*

In turbulent flow the velocity at any instant is comprised of the mean component and the fluctuating part. So, the velocity in any one dimension, say x direction can be written as

[†] The BL parameters presented here for 60 m/s were actually measured at 55 m/s because the maximum free stream velocity in the test section was limited by the blockage created by the 3D tunnel traverse system. However, it is assumed that these parameters are same at 60 m/s and were thus used in the pressure fluctuation analysis.

$$u = \langle U \rangle + u' \qquad (Eq.7)$$

The velocity in the two other directions can be written similarly. The fluctuating term in *Eq. 7* is also referred to as the turbulent intensity. The root mean square values of the streamwise velocity fluctuation for 30 and 55 m/s have been shown in Figure 28. It can be seen that for both the cases the velocity fluctuations peak close to the wall indicating higher velocity fluctuations (or turbulence) there. As one moves out of the wall towards free stream the turbulence intensity approaches zero and this can be seen in Figure 28.

Another quantity of interest within a turbulent boundary layer is the Reynolds shear stress which is a tensor and is defined as the product of averaged fluctuations in velocities. The i^{th} and j^{th} term of the tensor can be written as

$$\tau'_{ij} = \rho \, \overline{u'_i u'_j} \qquad (Eq.8)$$

Where, the bar over the fluctuating terms denotes averaged values. Reynolds shear stress is often just written without the density term since for incompressible flow density is just constant. The Reynolds shear stress is a symmetric tensor and consists of 6 quantities out of which 3 are independent. Figure 29 shows these 3 independent shear stresses normalized with the density for smooth wall at 30 and 55 m/s. It can be seen that as expected the shear stresses are higher within the boundary layer (they peak around $z/\delta \approx 15\%$) and approach zero outside the boundary layer. Comparing the shear stresses on 3 different planes we see that the shear stresses in the *x*-*z* plane which is the perpendicular to the wall and has a higher stress compared to the other two planes. This is expected because the velocity gradient within the boundary layer close to the wall in the normal to the wall direction is significantly high giving rise to high shear stresses in that direction. Figure 29 can also be used to approximate wall skin friction coefficient and it is given by

$$C_f = \frac{\overline{u'_i u'_j}}{0.5 U_\infty^2} \qquad (Eq.9)$$

The skin friction coefficients found in this manner have been shown in Figure 29 for 30 and 55 m/s. It can be seen that the skin friction coefficients obtained this way are close to the values found by adjusting mean velocity profiles to the law of the wall in Figure 26 and Figure 27.

3.3 Forward Steps Mean Wall Pressure and Separation-Reattachment Regions

The separation and reattachment regions are the most interesting aspects of the step flows. The determination of the lengths of these regions is important in characterizing the flow structure of step flows and these lengths can also have an influence on the length scale of turbulence due to step. To characterize the flow around the step location, the mean wall pressure and oil flow visualization techniques were used.

Figure 30 (a) shows the streamwise mean wall pressure coefficient as defined in *Eq.2* for all 3 step sizes along with the smooth wall mean pressure at 30 and 60 m/s. The black symbols in the figure correspond to 30 m/s while the blue symbols represent 60 m/s. It should be noted that the streamwise distance here is in meters and the vertical line indicates the step location. Looking

at the figure it can be seen that as the flow approaches the step, for all cases there is a sudden rise in the mean wall pressure just upstream of the step. This rise in mean pressure can be associated with the flow separation since the separation leads to formation of separation bubbles which have a much lower velocity compared to the mean wall flow. The pressure continues to rise and reaches a maximum at the face of the step.

Looking downstream of the step, the mean pressure for all steps and cases is much lower than the smooth wall pressure. This is due to the fact that the presence of the step tends to accelerate the flow locally downstream and thus lower the pressure. The pressure then starts rising due to the reattachment of the flow and approaches a constant value for all the cases. This constant value for small and medium step size is same as the smooth wall pressure. However, for the largest step size this value is slightly lower than the smooth wall case for both speeds. This can be attributed to the fact that the small and medium steps are about 0.19% and 0.77% of the tests section width and do not act as significant contractions. However, the largest step size is about 3% of the test section width in size and does act as a contraction in the test section thereby reducing pressure slightly. Figure 30 (a) also shows the influence of Reynolds number on the mean wall pressure. Upstream of the step there is a slight effect of Reynolds number on the mean pressure and the mean pressure is higher for higher Reynolds number. However, downstream of the step in the reattachment region, the effect of Reynolds number is not as significant and the pressure at both speeds is nearly the same for all 3 step sizes. Figure 30 (b) shows the spanwise mean wall pressure for all steps and smooth wall at both speeds. As seen in the figure, the pressure is constant in the spanwise direction for all cases indicating the two dimensionality of the step flow which is to be expected due to the large aspect ratio of the step.

Figure 30 (c) shows the mean pressure for all the step sizes now plotted against step height on the x-axis. Also shown in Figure 30 (c) is the mean wall pressure measured by Farabee and Casarella (1986) (h/δ = 41%, Re_h = 21,000) in their experiment and mean wall pressure calculated by Ji and Wang (2010, 2010a) for their h/δ = 13%, Re_h = 6400 case. Upstream of the step, all the three results follow the same general pattern with the present results lying roughly in between the previous experiment and LES mean pressure

Downstream of the step however, there are some noteworthy differences between the present and past results. Consider Farabee and Casarella's mean pressure first, their mean pressure recovers to smooth wall values much quicker than any of the current mean pressure measurements. Ji and Wang's mean pressure recovers slower than Farabee and Casarella's but is still quicker compared to the present measurements. Their Reynolds number is very similar to that of the small step size at 30 m/s (Re_h = 6640) and as seen in Figure 30 (c) this is the only present case which seems to agree with Ji and Wang's recovery. The mean pressure for the medium step size (h/δ = 15.1 and 15.4%) recovers much later than Ji and Wang's pressure despite of the step size similarity possibly due to much higher Reynolds number in present case. This shows a clear dependence of the downstream mean pressure on the Reynolds number.

Table 3 shows the separation and reattachment lengths measured using oil flow visualization along with the step height to boundary layer ratio and step Reynolds number for each case. The separation length for the low Reynolds number largest step size is missing due to corrupted oil flow visualization for this particular case. Looking at the separation lengths it is clear that the separation lengths do not fluctuate much with the step size or the Reynolds number and stay within 1.5h to 1.9h upstream of the step.

. Column four shows the downstream reattachment lengths as measured by oil flow visualization results. It is worthwhile mentioning here that reading the oil flow visualization for the smallest step cases was extremely difficult due to high uncertainties caused by small separation bubble at the top of the step. To avoid this, the reattachment lengths for small step (both Reynolds number) was obtained by using the low uncertainty reattachment lengths of largest step and the mean wall pressure associated with them. For the largest step, the mean wall pressure coefficients for low and high Reynolds number cases are -0.24 and -0.25 respectively at the reattachment points of x/h = 4.1 and x/h = 4.2. Assuming the same reattachment length to mean wall pressure coefficient for the medium step one obtains reattachment lengths of x/h = 3.6 and x/h = 3.8 for 30m/s and 60m/s respectively which are fairly close to the lengths obtained from oil flow visualization. Extension of this method to the smallest step case yields reattachment lengths of x/h = 1.6 and x/h = 3.2 for 30m/s and 60m/s respectively. Looking at Table 3 it can be see that as opposed to the upstream separation length which does not vary much with Reynolds number based on step height (Re_h), the downstream reattachment length is a strong function of the Reynolds number based on step height (Re_h). This reattachment length variation is particularly large for the smallest step where it almost doubles with Reynolds number. For the medium and large step cases the variation with Reynolds number is not significant.

A similar result was obtained by Camussi *et al.* (2008) where they studied separation and reattachment locations using 2D PIV on flow over forward steps. Their results show that the separation position stays nearly constant at x/h = -1 for different Re_h while the downstream reattachment location ranges from x/h =1.5 to 2.1 for a Reynolds number ranging from 8800-26,300. For present case if we look at Re_h for small and medium step for 30 m/s the range for which is close to that of Camussi *et al.* (2008) then we find that that the separation stays constant at x/h = 1.9 while we see larger variation in downstream reattachment length, furthermore if we look at the 60 m/s case then also we see minor variation in separation length for all three steps while larger variation in reattachment length. Similarly, Fiorentini *et.al* (2007) who studied forward steps of size $h/\delta^*=2.0$ with Reynolds number range of 4400-26,300 also found that separation is independent of the Reynolds number and stays around x/h = 1. On the other hand, their reattachment length varied from 2h-3h from lowest to highest Reynolds number. This is consistent with the present measurement if we consider the low Reynolds number medium step ($h/\delta^*=1.4$) for which the Reynolds number matches closely with theirs.

Farabee and Casarella (1986) found reattachment lengths for their case (Re_h = 21,000) to vary between 3h-4h downstream of the step which is consistent with present measurements. Ji and Wang (2010) found separation and reattachment lengths for their largest step size (h/δ = 53.0%, Re_h = 26,000) to be about 0.6h and 3h respectively. They also found that their separation-reattachment lengths grow and shrink according to step size and for their small step size (h/δ=3.3%, Re_h=1600) the separation bubble on top of the step disappears completely. These results disagree with the present measurements and a possible reason for this is the Reynolds number difference between the computation and experiment.

Table 3. Separation and reattachment lengths

U_∞ (m/s)	h/δ	Reh	x_s/h	x_r/h
30	3.80%	6,640	-1.9	1.6
	15.10%	26,600	-1.9	3.6
	60.10%	106,000	-	4.1
60	3.80%	13,300	-1.5	3.2
	15.40%	53,200	-1.7	3.8
	61.50%	213,000	-1.5	4.2

The separation and reattachment lengths have been plotted as a function of Reynolds number in Figure 31. Let us consider the separation length variation with Reynolds number first. It can be seen that the separation length shows little or no variation with Reynolds number and this is in agreement with previous studies (e.g. Sherry *et al.* (2009)). Looking at the reattachment length variation with Reynolds number there are clearly two regimes that exist. The first regime is for Re_h less than about 30,000. In this regime the reattachment lengths are a strong function of the Reynolds number. However, for higher Re_h the reattachment lengths seem to be weakly influenced by Reynolds number.

Figure 32 shows the reattachment lengths for the present work and those for LES simulations by Ji and Wang as a function of Reynolds number and step height to boundary layer ratio. It can be clearly seen that the reattachment lengths collapse very well when plotted as a function of step height Reynolds number. While when plotted as a function of step height to boundary layer ratio there is a very poor correlation. This further highlights the fact that reattachment lengths are a strong function of Reynolds number while the boundary layer seems to have a secondary effect on the reattachment process.

3.4 Forward Steps Root Mean Square Pressure

Root mean square of wall pressure was calculated in the frequency domain. In frequency domain the r.m.s pressure is given by

$$P_{rms} = \sqrt{\int_0^f \phi_{pp}\, df} \qquad (Eq.10)$$

ϕ_{pp} is the single-sided autospectral density of the pressure signal per circular frequency *f*. The root mean square pressure for all step sizes at 30m/s and 60m/s are plotted against the streamwise distance in terms of step height in Figure 33 and Figure 34 respectively. The step location has been shown in both the figures along with the smooth wall r.m.s pressure levels for the two Reynolds numbers. The r.m.s Pressure has been normalized on the incoming dynamic head. The pressure in all the cases follows similar trends in that as the flow approaches the step and the separation region the r.m.s pressure begins to rise indicating incipient separation of the flow. The highest values of r.m.s pressure are observed just downstream of the step near the reattachment region. In this region the maximum value for large and medium step size at high Reynolds number are about 14 times those of smooth wall. The high values of r.m.s pressure are due to the impingement of highly turbulent boundary layer on the surface. Downstream of the reattachment, the r.m.s values of pressure begin to decay due to the boundary layer relaxation process following reattachment region and settle down to the smooth wall values. This can be observed in Figure 33 and Figure 34 and it can be seen that for the smallest step the values of r.m.s pressure downstream have settled to the smooth wall values by about 200 step heights. However, a remarkable observation here is that a memory of the step's presence in the flow can still be seen at about 150 step heights downstream where the r.m.s values of pressure are still slightly elevated than smooth wall for at least the small and medium step. The values of r.m.s pressure for largest step are not available at far downstream distances because the last measurement station for the largest step was 36 step heights downstream.

A noteworthy feature of the step flow shown by the r.m.s values of wall pressure fluctuations is the nature of separation and reattachment regions and their dependence on the step size and Reynolds number. Figure 35 shows a zoomed in view of the r.m.s pressure in and near the separation-reattachment region for medium and large step (since small step only has measurements at locations $x/h > 24$ it is not shown on this plot) at both Reynolds number. Recall that the oil flow visualization and mean wall pressure discussed in previous section showed that the upstream separation length was independent of Reynolds number and step height while the downstream reattachment length was a strong function of these parameters. This fact can also be seen in the r.m.s pressure near the step. Upstream of the step there is a negligible difference between the r.m.s pressure for the two Reynolds number and rising r.m.s value being indicators of flow separation suggests that the separation is independent of Reynolds number and step height. On the other hand, the pressure fluctuation peaks downstream of the step are different for the two Reynolds number and the peaks in r.m.s values occur at different locations. The r.m.s pressure results re-establish the mean pressure and oil flow results which show that the separation length is near constant and does not vary with Reynolds number or step height while the reattachment length is a strong function of these parameters.

A comparison of the pressure fluctuation r.m.s values with the previous works of Farabee and Casarella (1986) and Ji and Wang (2010, 2010a) has been shown in Figure 36. For the present case only the r.m.s values for the medium step size for 30m/s have been shown since Re_h for this case is similar to the past experiment and study. Comparing the overall trend of the pressure fluctuations it can be seen that all the results follow the same general trend as discussed

earlier. Upstream of the step the pressure fluctuations agree closely with past results despite of the difference in step size to boundary layer ratio and the Reynolds number. Downstream of the step, however, the pressure fluctuation recovery to smooth wall values is much slower for the present work. Looking at Figure 36 it can be seen that even though the peak pressure near reattachment is approximately same for the lower Reynolds number case and past work, the present work pressure peak occurs farther downstream. For the past work cases, the pressure relaxes to smooth wall values around x/h = 30. However, for the present work this relaxation occurs around x/h = 80. One reason for this difference might be the fact that the present pressure measurements have a much wider frequency range than either of the past works. This difference might cause the r.m.s pressure level to differ since calculating it requires integrating the pressure levels across the frequency range.

3.5 Wall Pressure Autospectra

As highlighted under the objectives, the primary goal of the present work was to determine the character and the extent of the wall pressure fluctuations due to the presence of forward steps. The wall pressure fluctuations were obtained for the 3 forward step sizes upstream and far downstream of the step. The measurements included both pressure autospectra and two point pressure fluctuations. The mathematical procedure used to obtain these results has been outlined in Appendix A.

As mentioned in chapter 2 for a particular wall pressure fluctuation measurement a single microphone without ½ mm pinhole was used for acoustic cancellation to remove any contamination from the background facility noise. The acoustic cancellation procedure has been discussed in Appendix B.

3.5.1 Smooth Wall Autospectrum

The pressure fluctuations resolved up to 25 kHz were obtained in spectral form after applying calibrations and acoustic subtraction. The equilibrium turbulent boundary layer pressure spectrum can broadly be divided into three different regions: firstly there is a flat low frequency region with high pressure fluctuations, secondly there is an overlap region in mid frequency region with a slope less than 1 and lastly there is the steep roll off at higher frequency. Figure 37 shows the smooth wall pressure spectrum measured 165 mm upstream of the step for both Reynolds numbers. The spectral levels are non-dimensionalized by the free stream velocity, dynamic head and, the incoming boundary layer thickness measured 152 mm upstream of step. The frequency of the spectrum is non-dimensionalized by the free stream velocity and the incoming boundary layer thickness. Spectra are only plotted where the uncertainty in acoustic subtraction was less than 3 *dB*. This is the reason why the present measured spectra for the low and high Reynolds numbers have different low-frequency limits.

The spectrum in both cases displays a typical zero pressure gradient boundary layer behavior in that we see a flat low frequency region followed by an overlap region of slope of -0.8 which is succeeded by a steep roll off high frequency region with slope close to -5 which is only seen in the spectrum for 30 m/s. The pressure spectra for both the speeds are similar except for some fluctuations at low frequencies at 60 m/s. The figure also shows the smooth wall spectra as measured by Farabee and Casarella (1986) and calculated by Ji and Wang (2010,

2010a) for comparison. The spectra exhibit similar spectral levels as the present results for lower frequencies. However, at mid to high frequencies the spectra of Ji and Wang (2010, 2010a) decay at lower frequency values compared to both the present case and Farabee and Casarella (1986). Another interesting feature of the LES smooth wall spectra is that it does not contains the mid frequency slope close to 1. Instead, it has only the flat low frequency region followed by high frequency roll off. It should be noted however, that Ji and Wang (2010, 2010a) performed LES simulation which is unable to resolve the smaller structures, or higher frequencies. For this reason the discussion of LES autospectra in this text is limited to the non-dimensional frequencies ($f\delta/U_\infty$) below 1.

3.5.2 Forward Steps Pressure Spectra

The pressure fluctuation pressure frequency spectra measured at several upstream and downstream locations are shown and discussed in the following sections. The discussion will begin with the upstream pressure spectra followed by a discussion on the downstream pressure spectra. Finally, a comparison between the present case, experiments of Farabee and Casarella (1986) and LES calculations of Ji and Wang (2010, 2010a) will be presented and discussed.

3.5.2.1 Upstream Pressure Spectra

This section describes the pressure spectra obtained upstream of the step location for both the low and high Reynolds number case. Figure 38 (a) and Figure 38 (b) show the spectra for 30 m/s and 60 m/s respectively for the smallest step. For the purpose of discussion, we will first consider the low Reynolds number spectra since those for high Reynolds number are quantitatively similar. The spectral magnitude has been non-dimensionalized on the free stream velocity, smooth wall boundary layer thickness and the dynamic head. The frequencies have been non-dimensionalized with the incoming boundary layer thickness and free stream velocity. It should be noted that the incoming boundary layer thickness was measured 152 mm upstream of the step for the equilibrium (smooth wall) case using a single hot wire. The figure also shows that the farthest upstream measurement location for this step size was about 157 step heights upstream. The smooth wall pressure fluctuation spectra have been shown as a bold thick line. The pressure levels far upstream of the step are same as the smooth wall with negligible differences at all frequencies. However, as the flow approaches the step a rise in pressure levels at low frequencies is seen. These elevated pressure levels are first seen at about 18 step heights upstream of the step where the pressure levels are about half a decade larger than the smooth wall pressure levels up to about non-dimensionalized frequencies of 0.1. Although, this seems like a large distance for a step size of less than 4 mm, however, it should be noted that 18 step heights is still smaller than the boundary layer thickness ($x/\delta \approx 67\%$) and thus is less than the size of the largest eddies within the boundary layer. As the flow moves closer to the step and approaches separation a large rise in low frequency pressure levels associated with large turbulent scales is seen and at about 9 step heights upstream the pressure is more than a decade larger than the smooth wall levels. At higher frequencies, the pressure levels are slightly below the smooth wall pressure. This indicates that the separation of the flow upstream of the step tends to lift the smaller eddies away from the wall while there is a presence of larger eddies close to the wall as shown by the high pressure levels at low frequencies. Figure 38 also shows the

overlap region slope for the small step case which is similar to the smooth wall and at mid and high frequencies there is none or very little deviation from the smooth wall values.

Now consider the high Reynolds number spectra shown in Figure 38 (b) measured at 60 m/s. The spectra shows no qualitative differences compared to the low Reynolds number spectra. Quantitatively, the high Reynolds number spectra shows elevated magnitudes at low frequencies for locations close to the step but as one moves further upstream these differences also disappear. Thus, it can be said that the Reynolds number has no significant effect on the pressure fluctuations. It should be noted that the spectra shown for the higher Reynolds number cuts off at higher frequencies (non-dimensional frequency of about 3) and no data is shown for the steep roll off region. This is due to the Nyquist limit.

Figure 39 (a) shows the upstream spectra at 30 m/s for the medium step (h/δ = 15%). The spectra have very similar trends as the small step upstream spectra; however, the magnitude of the pressure levels is much larger. At about 11 step heights upstream of the step the spectra is undistinguishable from the smooth wall. The spectral levels at low frequencies begin to rise at about 6 step heights upstream of the step indicating incipient separation of the boundary layer. The spectral levels at x/h = -2.3 (just upstream of the separation location x_s/h = -1.9) are about 100 times those of the smooth wall at lower frequencies. At higher frequencies the upstream spectra are below the smooth wall levels due to lifting of smaller structures by the separation process. A noticeable difference between the small and medium step upstream spectra is seen in the mid frequency overlap region. The slope of this region gets steeper for the medium step size and has increases to about -3/2 from -0.8 for small step case.

Comparing the spectra in Figure 39 (a) with the upstream spectra for small step in Figure 38 (a) we see a larger pressure rise at about 11 step heights upstream of the smallest step as compared to the medium step at same distance in terms of step height. This can be explained using the fact that for medium step, 11 step height in terms of boundary layer thickness is about 1.6δ, while for smaller step it is about 0.4δ. Thus, for medium step case 11 step heights is greater than the boundary layer thickness and also the size of largest scales of the flow and so we see very little variation from the smooth wall at this location. However, if we look at Figure 38 (a) we can see that even at 22 step heights for small step ($x/\delta \approx 85\%$) there is a trace of presence of step upstream. This result is similar to observation made by Efimtsov *et al.* (1999) that upstream of the step the smaller the step larger is its extent upstream in terms of step height. The extents of medium and small steps upstream also suggest that in separation region the pressure fluctuations are a function of the incoming boundary layer thickness.

Figure 40 (a) shows the upstream spectra for the large step size. Qualitatively the spectra are similar to those seen for small and medium step. Quantitatively, however, large step shows an even larger magnification of pressure fluctuations at low frequencies. Close to separation for the large step size, the spectral levels at lower frequencies are about 400 times (about 25 dB) that of smooth wall. The higher frequency show a further decrease in magnitude compared to small and medium step size. The mid frequency slope continues to get steeper and as shown in Figure 40 has a value of -5/2.

*3.5.2.2 **Downstream Pressure Spectra***

The downstream pressure spectra for small step at 30 m/s and 60 m/s are shown in Figure 41 (a) and (b) respectively. The separation-reattachment process due to forward step leads to the formation of a free turbulent shear layer which enhances turbulence mixing and wall pressure fluctuations in the reattachment region on the top face of the step. The recirculation bubble downstream of the step has been found to be an efficient source of wall pressure fluctuations in the past (e.g. Camussi *et al.* (2008)). Post reattachment the reattached boundary layer undergoes a relaxation process where it is unlike the incoming equilibrium boundary layer and experiences increased turbulent activity and wall pressure fluctuations levels. Thus, the region downstream of the step is critical in terms of wall pressure fluctuations and will be discussed in this section.

Figure 41(a) and (b) show the downstream spectra for the small step at 30m/s and 60m/s respectively. We will consider the lower Reynolds number spectra first for all 3 step sizes for the sake of qualitative and quantitative comparison. Consider the downstream spectra for the small step at 30 m/s shown in Figure 41(a) first. At the closest measurement station downstream of the step, about 24 step heights, a flat high energy region at low frequencies can be seen. This is followed by a roll off with a slope close to -5/2. Compared to smooth wall, the slope of the equilibrium region is much sharper indicating a faster energy transfer in this region due to the step. Finally, one can see a steep roll off at high frequencies similar to the smooth wall. As one moves downstream of the first measurement station, similar trends in spectra are observed. The traces of the reattachment of the flow can be seen as far as 600 step heights downstream of the step especially at lower frequencies. This is a remarkable reach for a step which is only about 4% of the boundary layer thickness.

Figure 42 and Figure 43 show the downstream pressure spectra for the medium and largest step sizes respectively. Quantitatively these spectra are similar to the ones shown for the small step size and appear in some ways as amplified versions of the small step spectra. Possibly, the most notable and striking feature shown by these spectra is the level of pressure fluctuations present at lower frequencies compared to smooth wall. For the medium step, at locations ranging from 5 to about 9 step heights which is just downstream of the reattachment (x_r/h = 3.6), the pressure levels are elevated at all frequencies but particularly at low to mid frequencies where the pressure is more than 2 orders of magnitudes (or 20 dB) larger than smooth wall. The elevation of spectral levels all frequencies at and near reattachment region suggests the presence of both large and small energetic turbulent structures in the near wall region. Downstream of the reattachment, the spectrum begins to decay in magnitude and recover its smooth wall form. The higher frequency part of the spectrum ($f\delta/U_\infty > 10$) has recovered by about 22 step heights downstream. The low to mid frequency parts, however, experience a very slow decay process. At x/h = 36 the low frequency content ($f\delta/U_\infty < 0.3$) is still about 10-15 dB higher than smooth wall. Moving further downstream at x/h = 151.7 (the last measurement station for this step size) one can see that the low frequency content is still clearly about 5 dB higher than smooth wall. This shows the remarkable reach of a small step far downstream of the step and suggests that the boundary layer has yet not recovered from the separation-reattachment induced by the step. The slope of roll off at mid frequencies for medium step is close to -5/2 as shown in Figure 42. This roll-off is steeper than what was seen in the upstream spectra and suggests a faster energy transfer process in this region.

Figure 43 (a) shows the downstream spectra for the large step at 30 m/s. The spectra for large step is qualitatively similar to the two smaller steps in that it consists of an amplified low to frequency region due to separation-reattachment process which is followed by a mid-frequency roll off with slope of -5/2. Quantitatively, however, it is very different from the smaller steps and shows a large magnification of low frequency pressure fluctuations in the recirculation bubble and downstream from the reattachment. The pressure levels near reattachment and in the recirculation bubble ($x/h < 4$) are about 3 orders of magnitude higher than the smooth wall at low frequencies. The high frequency content recovers by about 10 step heights; however, the low frequencies are still elevated by about 15 dB at 36 step heights downstream of the step.

The feature of downstream spectra which is most striking and common regardless of the step size or Reynolds number is the presence of a ridge at mid frequencies. The frequency values for this ridge at $x/h = 36$ normalized both on incoming boundary layer thickness and step height for each case have been shown in a box on Figure 41-43. Comparing the normalization of ridge frequencies at the same x/h location for all 3 step sizes for low Reynolds number we see that when normalized on the step height (fh/U_∞) the ridge frequencies for the 3 steps are 0.05, 0.05 and 0.09 for small, medium and large steps respectively. For higher Reynolds number these values are .044, .098 and .09. When normalizing ridge frequency on the boundary layer thickness ($f\delta/U_\infty$), at lower Reynolds number these values are 1.2, 0.35 and 0.15 for small, medium and large steps respectively. At higher Reynolds number these values are 1.2, 0.65 and .15. Therefore, one sees that ridge frequencies scale more closely on the step height than the incoming boundary layer thickness. This gives a very good indication that the step flow disturbance as a whole might scale on the step size rather than the boundary layer parameters. The presence of this ridge makes the spectra look self-similar and give motivation to attempt scaling of pressure spectra. This fact can be utilized to perform scaling of step flows and will be discussed in a later section in this text.

Comparing the spectra for two different Reynolds number shown in Figure 41-43 (a) and (b) one can see that there is no qualitative difference between the spectra except for the medium step case in Figure 42 (a) and (b) where the higher Reynolds number shows a longer low frequency plateau. This difference is also reflected in the ridge frequencies and the ridge frequency values are higher for the high Reynolds number due to elongation of the low frequency region. The reason for this difference is not clear and may be a Reynolds number effect. However, as we will see later in this text, this difference does not emerge as an issue when we consider the scaling and self-similarity of the spectra.

Before moving on to the next section, a note on the differences between the upstream and downstream pressure fluctuations is necessary. Comparing the upstream and downstream spectra for forward steps one comes across some qualitative as well as quantitative differences. The most striking difference is the extent of the spectra in the two cases. Let us consider the low Reynolds number medium step for this illustration as it is clearer than the small step and has more measurement stations than the large step. Upstream of the step, the effect of the step does not seem to affect the region upstream of 11 step heights while downstream the effect can be felt as far as 151 step heights. Upstream of the step within the upstream recirculation bubble, the wall pressure is about 100 times the smooth wall pressure. On the other hand, downstream of the step the pressure is much higher and is about 400 times the smooth wall in the recirculation bubble. This shows that the downstream reattachment is more energetic than the upstream separation in

terms of pressure fluctuation. Another difference is the fact that the high frequency pressure upstream of the step falls below the smooth wall while in the downstream region the pressure is elevated at all frequencies. This suggests that while separation forces small structures away from the wall, the unsteady reattachment contains both small and large scale structures. Finally, the mid-frequency roll off upstream of the step seems to be a strong function of the step height and increases with increasing step height. On the other hand, the roll-off slopes for the downstream spectra are nearly independent of step height or the Reynolds number and approach -5/2 in all cases.

The comparison of the upstream and downstream spectra for the present work with past experiments of Farabee and Casarella (1986) and LES of Ji and Wang (2010, 2010a) will now be discussed in the following section.

*3.5.2.3 **Comparison of Pressure Autospectra with Past Work***

Figure 44 shows the upstream pressure spectra comparison between the present work, Farabee and Casarella (1986) and Ji and Wang (2010, 2010a). The step size to boundary layer thickness ratio for the present work shown in this comparison is much smaller than the other two cases shown, but the Reynolds number based on the step height are fairly close. Looking at the overall shape of the upstream spectra closely it can be seen that the shape of the spectra is the same for present and past work. The spectra from the measurements and calculations display three distinct regions: low frequency high energy region, an equilibrium region where the energy is still higher than the smooth wall and finally a steep roll off at higher frequencies with energy lower than the smooth wall. These three regions are more visible in the present work than the past calculation or measurement due to the larger frequency resolution in the present case.

Figure 44 (a) shows the pressure spectra upstream of the low Reynolds number medium step size for the present case on the left. Also shown are the upstream pressure spectra measured by Farabee and Casarella (1986) and calculated by Ji and Wang (2010, 2010a) in Figure 44 (b) and Figure 44 (c) respectively. Comparing the spectra in Figure 44 (b) and Figure 44 (c) one sees that they are in very good agreement and show similar spectral levels at x/h = -6 and x/h = -1. However, when looking at the present and past measurement spectra at about x/h = -2 it can be seen that the spectral levels at lower frequencies are about 20 *dB* higher than the smooth wall for the present case while they are about 10 *dB* higher than smooth wall for the past measurement. Similarly if one compares the present spectra at x/h = -5.7 with the past measurement and LES spectra at x/h = -6 it can be seen that spectral levels for the present case are much more elevated than either of the two cases. This discrepancy in the magnitude of the pressure fluctuations might be due to the much smaller step size for the present case despite of the similar Reynolds number. This phenomenon was also observed by Efimtsov *et.al* (1999) where they found that lower the size of the step higher was its influence upstream on pressure fluctuations in terms of step height.

Figure 45 (a), (b) and (c) shows a comparison of downstream pressure spectra for medium step with those of Farabee and Casarella (1986) and Ji and Wang (2010, 2010a) respectively. Looking at the smooth wall spectra for their work and present work we see that they are similar in shape and spectral levels. Farabee and Casarella's (1986) pressure spectra are resolved between non-dimensional frequency ranges of about 0.01-20 while the present spectra are resolved between frequency ranges of .006-90. Their measurements go much closer to the step compared to present measurements and they also have measurements on the face of the step

(x/h = 0). On the other hand, the current measurements go far beyond their farthest downstream station which is x/h = 36. Qualitatively, the spectra from the present work are similar to those of Farabee and Casarella (1986). They both have a low frequency high magnitude region followed by equilibrium mid frequency power law decay region with the same slope of -5/2 and finally a steep high frequency roll off. Quantitatively however, there are some differences. If we look at spectra within the reattachment region, which for their work is 3*h*-4*h*, their spectra behaves similar to current spectra and shows similar spectral levels. However, further downstream from the reattachment at x/h = 6 current spectral levels are about 5-7 dB higher than theirs. Moving further downstream of reattachment the spectra for current work at x/h = 14.8 is still slightly higher than their spectra at x/h = 12. Further downstream from that at x/h = 36 the spectra is roughly the same as current spectra for x/h = 54. One noticeable difference between the two spectra is that for the current work the effect of reattachment seems to last longer on the spectra than the past experiment. This is evident in the fact that for the current work the spectra for x/h = 5 to x/h = 9 are grouped together while in Farabee and Casarella's (1986) work this effect only seems to last up to about x/h = 6 and further downstream from that the spectra falls beneath the levels of current work. This difference, though not significant might be due to the difference in Reynolds number between the current and past experiment. Another noticeable fact in Farabee and Casarella's (1986) spectra is the fact that it also shows formation of a ridge which is centered at $f\delta/U_\infty$= 0.3 similar to the current results.

Moving on to Ji and Wang's (2010, 2010a) LES results over forward step we see that their step height to boundary layer ratio is more than 3 times the present case but the Reynolds number based on step height is very close to the current case. Since, the smallest scales or the higher frequencies are not resolved in LES results we will limit our discussion to non-dimensional frequencies less than 1. Quantitatively, their spectra behave similar to both the current and past experiment results and have the same slope of about -5/2 in the equilibrium region. Quantitatively however, there are some significant differences when one observes the spectra closely. Within their reattachment region which is about 3h downstream of step their spectra shows levels similar to the current spectra within the reattachment region. However, past that their spectra also falls in magnitude compared to present work and at about 10 step heights downstream of the step the current spectra is about 7 dB higher compared to the calculation. Further downstream their spectra at x/h = 16 is still about 5 *dB* lower than the current spectra at x/h = 14.8.

In order to further explore the interplay of Reynolds number and step height consider the downstream spectra for the present largest step at 30 m/s, medium step at 30 m/s, and Ji and Wang's largest step size shown in Figure 46 (a), (b) and (c) respectively. The step height for the largest step of current work is much closer to the computation as compared to the medium step. However, the Reynolds number is about 4 times that of the computational work. Observing the large step size spectra and LES spectra in Figure 46, it can be seen that despite of comparable sizes, the increased step based Reynolds number serves to further slowdown the decay process. The pressure fluctuations within the reattachment region for present work (x_r = 4.1) have now become larger due to increased Reynolds number than both the medium step case and LES results. Further downstream at x/h = 36 the spectral levels for the present case is same as found at x/h = 16 for the computation. Thus, increasing the step size (or the Reynolds number) only serves to further slowdown the spectral decay process compared to similar Reynolds number case.

Although not significant, but the reason for the slower decay of spectral levels in comparable Reynolds number spectra is not known. However, it is assumed that some underlying presumption in the experiment or computation is responsible for this difference.

3.6 Pressure Spectra Scaling

The downstream pressure spectra for forward steps discussed in section 3.5.2.2 show some qualitative similarity for different locations, step heights and Reynolds numbers. This provided motivation for an attempt to scale the pressure spectra based on a single set of parameters. As discussed in the previous section, the spectral ridge was found to scale approximately on the step height rather than boundary layer thickness. Since the spectra for all steps at both Reynolds number show this feature, scaling the spectra based on this parameter was the most logical step. Moreover, the downstream spectra were elevated from their smooth wall levels across the entire frequency range. This suggests that the presence of step serves to add to the wall pressure fluctuations induced by an equilibrium turbulent boundary layer.

Following these observations, the approach to scale the spectra consisted of three steps. The first step was to subtract the smooth wall spectra from the steps spectra so that only the disturbance to the pressure fluctuations due to steps was obtained. The forward step spectra were subtracted from the smooth wall spectra only for locations where the difference between the two was greater than 1dB. Figure 47 shows the subtracted autospectra for all the steps at 30 m/s, the legend for each subtracted spectra has been shown underneath the spectra themselves. The subtracted spectra show a remarkably similar qualitative trend for all the step sizes. All the spectra have a similar flat low frequency region followed by a roll off after the ridge at slope of about -7/3 for all the cases.

Figure 48 shows the subtracted pressure spectra for all steps at 60 m/s. Note that the legend for this figure is same as that for Figure 47. The subtracted spectra at higher Reynolds number shows the same qualitative features as shown by the lower Reynolds number subtracted spectra. An important feature is the fact that the mid frequency roll off slope for these spectra is also close to -7/3. The ridge in the spectra also behaves in the similar manner as that for lower Reynolds number in that the ridge frequency (normalized on boundary layer thickness) lies in close vicinity for all the streamwise x/h locations. However, the ridge spectral levels vary across the x/h location spectrum. This is especially visible in the subtracted spectra for the medium step case for both the Reynolds number.

The second step in pressure spectra scaling was to identify the ridge frequency and spectral magnitudes for all cases at all downstream locations. Finally, the third step was to normalize each disturbance spectrum on the corresponding ridge frequencies and spectral values. Figure 49 and Figure 50 show the normalize disturbance spectra for 30m/s and 60m/s respectively. It is worthwhile mentioning here that the normalization on ridge values was done only for locations that clearly show a presence of ridge. This excludes primarily, the spectra at $x/h > 150$ for small step size because the ridges could not be identified clearly at these locations. It can be seen that normalization of spectrum on ridge values provides a good collapse in all cases at mid to high frequencies. However, at low frequencies this normalization fans out the spectra by almost a decade. This fanning out of spectra at lower frequencies is because at $x/h < 8$ locations the unsteady reattachment region dominates the pressure fluctuations and this unsteadiness increases the uncertainty in the spectra, especially at lower frequencies. Therefore

the spectra were normalized only for $x/h > 8$. Figure 51 and Figure 52 show the disturbance spectra for all steps normalized on ridge values only for streamwise stations downstream from $x/h = 8$ for 30m/s and 60m/s respectively. Looking at these spectra it can be seen that leaving out the stations upstream of 8 step heights provides a good collapse of the spectra in all cases.

Figure 53 (a) and Figure 53 (b) show the pressure disturbance spectra scaled with ridge values for all step sizes at both Reynolds number on the same plot for all streamwise measurement stations and for $x/h > 8$ respectively. It can be seen from the plot that one obtains a good collapse of data using this normalization scheme. This means that the downstream disturbance spectra for forward steps has a self-similar form which in turn means that regardless of the Reynolds number or the step size, the disturbance spectra at a particular downstream x/h location should have the same form.

To confirm the self-similarity of the disturbance spectra, the subtracted spectra normalized both on step height and incoming boundary layer thickness at $x/h = 36$ have been shown in Figure 56 (a) and Figure 56 (b). It can be seen that in case of step height normalization the spectra has the same form while upon normalization with boundary layer thickness it is no longer self-similar. Another noticeable fact is that the subtracted spectra for the medium step at 30 m/s (h/δ=15.1%) is an outlier when looking at Figure 56 (a). The reason for this anomaly is unknown; however, this anomaly is also clearly visible in the ridge frequency and spectral values where this particular case (shown as black circles in Figure 54 and Figure 55) clearly is off the curve. Again, the reason for this anomaly is presently unknown. However, when subtracted and normalized on ridge values the spectra for this particular case still collapses well.

The collapse of the disturbance spectra on ridge values proves that the spectra has a self-similar form but it remains to be seen how this form is dependent on step geometry and flow parameters. Figure 54 (a) and Figure 54 (b) shows the ridge frequencies normalized on boundary layer thickness and step height respectively. Looking at Figure 54 it is clear that the ridge frequencies for different cases collapse well when normalized on step height rather than boundary layer thickness. The ridge spectral levels normalized on boundary layer thickness and step height have been shown in Figure 55 (a) and (b) respectively. The ridge spectral levels show a different behavior than the ridge frequencies. The spectral levels for medium and large step sizes are similar when normalized on both boundary layer thickness and step height. However, the small step falls of the curve when normalized on boundary layer thickness but collapses well when normalized on step height. Another noteworthy aspect of the ridge spectral levels is the fact that close to the step at about $x/h < 8$ (the locations within or near the downstream reattachment region) the spectral levels are a near constant and do not follow the decaying trend shown by the locations downstream. This is obvious when looking at the autospectra for medium and large step size (small step does not have any measurements in this region) which show large and similar spectral levels till about $x/h = 8$.

The behavior of ridge frequencies and spectral levels mentioned above shows that regardless of the step height or Reynolds number, the self similarity of pressure disturbance due to step is only a function of x/h location when scaled on step height. On the other hand, when this behavior is not observed when ridge values are scaled on boundary layer thickness showing wall pressure in step flow scales on step height rather than boundary layer thickness.

3.7 Pressure Space Time Correlations

The space time correlation of pressure signals were computed using the cross spectra measured at the 4 major spanwise array locations in both streamwise and spanwise directions. The microphones that were placed in the 5 microphone block as shown in Figure 15 produced 10 unique separations in both positive and negative directions. The presence of an additional microphone produced another 5 different separation in either direction thus producing a total of 30 different separations. The space time correlation was obtained by inverse transforming the cross spectra and obtaining the cross correlation coefficient. The space time correlation coefficient was plotted as a contour plot with horizontal and vertical axes showing the temporal and spatial separations respectively.

3.7.1 Smooth Wall Pressure Space Time Correlation

The streamwise pressure space time correlation was obtained from pressure cross spectra measured by placing the 5 microphone bloc at 4 different locations along the wall, 1 upstream of the step and 3 downstream of the step. The streamwise pressure correlations have been shown at these locations for 30 m/s and 60 m/s case in Figure 57 (a) and Figure 57 (b) respectively. The correlations shown were obtained from the cross spectra measured at separations up to 23 boundary layer thicknesses from the step location. The spatial separation between the microphones has been normalized with the boundary layer thickness. It should be noted that the boundary layer thickness is not the local value but it is the one measured at 152mm upstream of the step using a single hot wire probe as discussed in the section 3.2. This location corresponds to 1.57 and 1.6 boundary layer thicknesses upstream of the step for 30 and 60 m/s respectively. The temporal dimension in the space time correlations has been normalized with the free stream velocity and upstream boundary layer thickness. The scale for the contour map has been shown at the bottom right corner of the figure. The correlation contours have been shown as if flow was from left to right and the location of the step has been also shown with a bold black line. It should be noted that the spatial and temporal scales in these contour maps have a 1:1 ratio so that the spatial and temporal scales are comparable. The correlation contours immediately downstream of the step (spatial separation of about 0.8δ -2.2δ) look spurious compared to the correlation at other locations. The reason for this anomaly is not known, however, it is speculated that this might be due to an uneven seam created at the junction of the two panels that were used to create steps. Since the microphone array used to measure these correlations was immediately downstream of this junction, this uneven seam might have corrupted the data.

Looking at the streamwise correlations for smooth wall there seems to be no significant qualitative difference between the two Reynolds numbers. In all the correlation maps, a presence of convective ridge can clearly be seen. Using Taylor's hypothesis the slope of this convective ridge can be used to determine the convection velocity of the turbulent structures. For the present smooth wall case the convection velocity was found to be about 80% of the free stream velocity and has been shown in Figure 57. The correlations at small streamwise separations have a slightly lower slope compared to the correlations at larger separations i.e. the smaller separations have a lower convection velocity. This is because the larger structures that are away from the wall are convected at a higher velocity than the smaller structures and thus produce higher pressure fluctuations that are seen at lower frequencies in the pressure Autospectra. A similar observation was made by Willmarth and Woolridge (1962) who reported convection velocities

ranging from 0.56 to 0.83 times the free stream velocity for a smooth wall 5 inch thick turbulent boundary layer. The lower end being associated with smaller separations i.e. when high frequency pressure fluctuations are correlated and the higher end associated with larger separation or when low frequency pressure fluctuations are correlated. The reason for this is that large structures that are associated with lower frequencies are carried by the outer, fast moving layer while the smaller structures associated with high frequencies move slowly. Blake (1970) also reported a convection velocity of 80% of the free stream value for their largest structures.

The spanwise correlations were obtained by placing the 5 microphone block and the reference acoustic cancellation microphone in a spanwise orientation at 4 streamwise locations (1 upstream of step and 3 downstream of the step). The spanwise pressure correlation maps at the four measurement locations along the wall for 30 and 60 m/s have been shown in Figure 58 (a) and Figure 58 (b) respectively. The location of the step has been shown with a bold black line with flow from left to right. At the top of each map the streamwise distance of the measurement station in terms of boundary layer thickness has been shown for each case. The contour map scale has been shown at the bottom right corner. The horizontal and vertical axis of each of the map represents temporal and spatial scales respectively. The temporal dimension has been non-dimensionalized with the free stream velocity and δ and the spatial separation has been non-dimensionalized with δ. Looking at the two Reynolds number cases (30 m/s and 60 m/s) it can be seen that there is no qualitative difference between the two cases so we will focus our discussion just on the high Reynolds number case. It can be seen that as one moves downstream the spanwise spatial correlation gets slightly stronger and thus elongating the map in the vertical direction due to the presence of larger wake like structures downstream. The maps at all the measurement stations are oval in shape with elongation occurring in spatial direction and temporal direction is smaller. For example, if one looks at the map for $x = 5.61\delta$ the correlation reaches to about 5% at a spatial dimension of $\Delta y/\delta = 0.5$ while in temporal direction it reaches at $U_\infty t/\delta < 0.5$. This oval structure occurs due to the fact that the convection velocity of eddies is smaller than the free stream velocity and thus causes this distortion and oval shape. Thus, these types of oval structures in space time dimension actually indicate an almost isotropic turbulence.

In order to show a comparison of the space time correlation for forward steps and smooth wall the contour maps were distorted to fit them on the same page. The contour maps were distorted so that the temporal axis was stretched about 3 times as much as the spatial axis. Figure 59 shows the distorted and undistorted view of both spanwise and streamwise space time correlations.

3.7.2 Forward Steps Pressure Space Time Correlations

The spanwise pressure space time pressure correlations for steps were obtained from the measured cross-spectra at the same locations as the smooth wall pressure correlation. First let us consider the spanwise correlations for steps and smooth wall at 30 m/s since those for 60 m/s are qualitatively similar. Figure 60 (a) shows the spanwise correlations at the four spanwise array locations for the small step at 30 m/s along with the position of the step with flow being from left to right. The streamwise *x/h* locations have been shown on each of the contour maps in the top left corner and the streamwise locations x/δ have also shown on the top. The vertical and horizontal axes show the spatial and temporal separations respectively non-dimensionalized with the boundary layer thickness. Figure 60 (b) shows the spanwise correlations for smooth wall at

the same streamwise array locations for comparison. Looking upstream of the small step it can be seen that the correlations are enhanced by about 50% in spanwise direction and to about 100% in temporal direction compared to smooth wall case. This means that the separation of the flow upstream of the step is accompanied by a strong spanwise organization and the large structures that are responsible for the enhanced low frequency pressure fluctuations seen in the pressure autospectra. Moving downstream of the step, at 36 step heights from the step, the spanwise correlation for the step is reduced in the spatial dimension. This indicates the presence of smaller structures in the flow at this location and the enhanced pressure fluctuations downstream of the step are primarily due to smaller structures. This fact is reflected well in the pressure Autospectra downstream of the small step in Figure 41 where the mid frequency pressure fluctuations are quite significant compared to smooth wall. Moving further downstream to 146 step heights the spanwise correlations seem to return to smooth wall form but with a slight stretch in the spanwise direction and by 584 step heights the correlations have returned to their smooth wall form.

Figure 61 (a) and Figure 61 (b) show the spanwise correlations for the medium step and smooth wall respectively at 30 m/s. The layout of the figure is similar to that of Figure 60. Looking at the correlations upstream of the step a strong spanwise and temporal organization associated with the separation can be seen. In this case the extent of correlations is further enhanced in spatial and temporal directions compared to small step. This is due to the fact that this streamwise location (x/h = -2.26) is within the separation region as was determined using oil flow results for the medium step. In this separation region there is a presence of large, slow moving structures and hence, the enhanced space time correlations. Moving downstream of the medium step, at x/h = 9.1 the spanwise correlations begin to look like the smooth wall correlations with the exception of emergence of two lobes of negative correlation on either side. The spanwise extent of the correlations is also slightly stretched than the smooth wall and explains the elevated low frequency fluctuations associated with large structures seen in the pressure autospectra at this location. At this point one would expect the correlations to return to their smooth wall form further downstream. However, at x/h = 36.5 the correlation map for medium step has taken an entirely different form with strong spanwise organization and strengthening of the negative lobes seen at x/h = 9.1. At this location the correlation in the spanwise direction extends to about 2-3 times and in temporal direction to about an order of magnitude compared to the smooth wall. The temporal scales of the correlations at this location is about $2.8\delta/U_\infty$ (or $19h/U_\infty$) which closely matches the ridge frequency of $0.35\delta/U_\infty$ (or $0.05h/U_\infty$) seen in the pressure autospectra at this location. Moving further downstream to x/h = 146 the correlations have still not returned to their smooth wall form and show a strong spanwise organization compared to the smooth wall. The negative lobes at this location have reduced in intensity but have grown in scale. The temporal scale of this structure has grown to about $4\delta/U_\infty$ (or $26h/U_\infty$) which matches the ridge frequency of $0.3\delta/U_\infty$ (or $0.05h/U_\infty$) seen in pressure autospectra at this location. This oscillatory motion can best be classified as a quasi-periodic motion and is possibly responsible for elevated pressure fluctuations seen far downstream of the step.

Figure 62 (a) shows the spanwise correlations for the large step at 30 m/s along with the smooth wall spanwise correlations in Figure 62 (b). The correlations for large step show a magnified version of the features seen in the medium step case due to the large size of the step. Upstream of the step a large correlation in spanwise and temporal direction is seen due to

presence of the slower moving large structures in the separation region. Downstream of the step, the presence of large spanwise organization as well as the presence of negative lobes can be seen. At x/h = 9.1 the oscillatory nature of the flow is very clear and the correlations in temporal direction are several order of magnitude larger than the smooth wall. At the last measurement station (x/h = 36) the reach of spanwise correlations exceed the measurement range.

Figure 63 through Figure 65 show the streamwise pressure space time correlation for small, medium and large step size respectively. The correlation map for smooth wall is also shown in each figure for comparison. Upstream of the step in the separation region we see elongated correlations in both space and time for all the step sizes similar to the spanwise correlation maps. These elongated correlations are due to slow moving nearly stagnant structures. These features are clearer in medium and large step case than the small step case. As flow moves past the step we see a developing quasi-periodic structure as we saw in the spanwise correlations. The negative lobes can be clearly seen in the medium and large step cases and the presence of step creates a totally new kind of flow as these lobes have strengthened in spatial and temporal directions at about 4 boundary layer thicknesses downstream of the step. The presence of these negative lobes is far reaching and is present even 22 boundary layer thicknesses (or 148 step heights) downstream of the step for medium step case. For the large step the correlations extend far beyond the measurement scales and the correlations maps show enhanced version of correlations seen for the medium step. Another interesting modification that the step makes to the streamwise correlations is the gradual decay along the convective ridge. For the smooth wall case, the slope of this ridge which is indicative of the fact that convection velocity was about 80% of the free stream velocity. However, for the large step size, the convective ridge seen in Figure 65 (a) for correlations from x/δ = 0.86 to 2.22 (or x/h = 1.44 to 3.7) shows a convective velocity of about 40% of the free stream velocity. This gradual decay of the ridge in step flows imply longer lasting turbulence compared to smooth wall flow.

3.8 Boundary Layer Velocity Statistics for Medium Size Forward Step

3.8.1 Single Point Velocity Statistics

The pressure space-time correlations discussed in section 3.7 show the presence of an entirely different flow structure downstream of the step as far as x/h = 148. This is a new discovery and means that post downstream reattachment the recovery of the shear layer to its equilibrium form is a gradual process. In light of these results, mean velocity and turbulence intensity profiles for the TBL flow over medium size step at 30 m/s (h/δ = 15.1%) were also measured at several streamwise locations along the wall to explore the effect of step far downstream. The profiles were measured for the medium step case since the quasi-periodic phenomenon is much clearer in it than small step and large step does not provide far enough measurement locations. These profiles were measured and then compared with the smooth wall profiles that were measured 152 mm upstream of the step. The profiles were measured at 8 (1 upstream and 7 downstream of the step) streamwise locations using a single hotwire probe as far as 148 step heights downstream of the step. Figure 66 (a) and (b) show the mean velocity BL profiles (u/U_∞) and streamwise turbulence intensity (u'^2/U_∞^2) respectively at several streamwise locations for the medium step at 30 m/s. The profiles are plotted so that the vertical axis shows the normal to the wall distance 'z' normalized with the smooth wall boundary layer thickness measured 152 mm (x/h = -10.6 for medium step) upstream of step location. The

horizontal axis is the streamwise distance along the wall with flow being from left to right. The scale of the mean velocity and turbulence intensities has been shown as a blue arrow on the profiles immediately downstream of the step. The streamwise *x/h* location at which a specific profile was measured has been shown in red immediately to the left of each profile. The smooth wall profiles have been shown at *x/h* = -10.6, 9.2, 37 and 148 with a blue dotted line for comparison.

First looking at the profile upstream of the step, a slight velocity defect can be seen in the step profile. This defect is due to the slower moving fluid in and near the separation region. The mean wall pressure coefficient at this location was about .07 and the pressure Autospectra shows almost no variation from the smooth wall spectra. These facts are reflected well in the mean velocity profile in that there is only about 3.5% deceleration of the flow at this point. The streamwise turbulence intensity at this location (shown at the bottom of Figure 66) is slightly higher than the smooth wall and shows little effect of step at this location.

Now consider mean velocity and turbulence intensity profiles downstream of the step at *x/h* = 1.5. It should be noted that this location is within the downstream separation bubble on top face of the step and is upstream of the reattachment position (x_r/h = 3.6). The profiles here show the effects of presence of a free turbulent shear layer in that near the wall to about 20% there is a big velocity defect due to slowing down of the fluid within the separation bubble. On the other hand for locations $z>0.2\delta$ the step accelerates the flow and a flat mean velocity profile is seen from there on. The turbulent mixing that takes place due to the free shear layer can also be seen in the turbulence intensity profile where large streamwise velocity fluctuations are seen in near wall region below z/δ = 20%. Moving further downstream to *x/h* = 9.2 the effect of the separation and unsteady reattachment can clearly be seen. At this location though the mean velocity defect and turbulence intensity have decreased, their extent normal to wall has increased to about 40%. The peak turbulence intensity at this location is about 4 times the smooth wall and occurs at $z/\delta \approx 12\%$. Note that this location also corresponds to where the negative lobes first appear in the spanwise space-time pressure correlations. Moving further downstream to *x/h* = 37 the mean velocity defect and turbulence intensity have decreased but now the boundary layer region that the downstream reattachment effects has increased from bottom 40% to bottom 70% of the boundary layer. The corresponding spanwise pressure space-time correlation at this location are shown in Figure 61 show strengthening of the negative lobes that developed around reattachment as well as a stronger correlation in the spanwise direction than the smooth wall. Moving to the farthest streamwise measurement station at *x/h* = 148, the mean velocity defect and turbulence intensity have further decreased, however, now their extent has further increased and the entire boundary layer except for the bottom 10% seems to effected by the reattachment process and the reattached boundary layer is not like the equilibrium boundary layer upstream of the step. This is an interesting result and shows that flow recovery downstream of a step is a very slow process. The spanwise space-time pressure correlations at this streamwise location show a large increase in spanwise organization that extends to about 10 step heights in the spanwise direction and the negative lobes, though weak, can still be seen at this location.

The 3 component statistical and spectral profiles were also obtained for the medium step case using a quad hot wire probe at 9 and 36 step heights downstream of the step. Note that these measurements were made by Mr. Michael Morton and Dr. Aurelien Borgoltz.

Figure 67 shows the 3 (or 6 assuming symmetry) shear stress components for the medium step and smooth wall at *x/h* = 9 and 36. At *x/h* = 9 all 3 shear components are elevated compared to smooth wall with the principal component $\overline{u'w'}$ being the highest as expected. These stresses fall back to the smooth wall values at about 20% of the boundary layer thickness due to the presence of decaying shear layer. At *x/h* = 36 the shear stresses, though, small in magnitude are extended in the normal to wall direction due to the reduction of intensity and growth of turbulence scale post reattachment process.

First let us consider the frequency spectra of the streamwise velocity fluctuation component (u') at different normal to wall locations normalized with the smooth wall boundary layer thickness measured 152 mm upstream of step at 30 m/s. The spectra at 9 and 36 step heights downstream of medium step have been shown in Figure 68 for z/δ approximately equal to 4%, 15% and 50%. Looking at the spectra at *x/h* = 9 close to the wall at 4% of boundary layer thickness the unsteady reattachment causes elevation of the streamwise fluctuation spectra at all frequencies. Moving further to 15% of boundary layer thickness the spectra shows no change but away from the wall at 50% of boundary layer thickness it drops significantly and is only slightly higher compared to the smooth wall spectra. This reflects the trend that was observed in mean velocity and turbulence intensity profiles and indicates growth of turbulence scales post reattachment process. A similar trend is observed in spectra of streamwise velocity at *x/h* = 36 except that at z/δ = *50%* the spectra is higher than what was observed at *x/h = 9*. This is to be expected because as shown by the turbulence intensity profiles, the normal to wall extent of the effects of reattachment increases as one moves further downstream from the reattachment.

Now consider the velocity spectra of normal to the wall velocity fluctuation component (w') shown in Figure 69 for *x/h* = 9 and 36 at approximately 4%, 15% and 50% of the boundary layer thickness locations. The spectra for normal to the wall velocity fluctuations shows the same trend as seen for the streamwise velocity fluctuation spectra except that closer to the wall at z/δ = 4% and 15%, the difference between the spectra at 9 and 36 step heights is slightly more in low to mid frequency region than what was seen in streamwise velocity fluctuations.

3.8.2 2 Point Velocity Statistics

The 2 point spanwise and normal to the wall measurements were made at U_∞= 30 m/s for smooth wall and medium step by Morton *et al.* (2012). The measurements were made 0.152 m upstream of step for the smooth wall and at *x/h* = 9 and *x/h* = 36 for the medium step. The results presented in this section were adapted from the 2 point velocity data reduction done by Dr. William J. Devenport[*].

The 2 point measurements were made using two quad hotwire probes with one of them having only a single degree of freedom in the normal to the wall or 'z' direction and will be referred to as the fixed probe. The other probe was mounted on a 3 dimensional tunnel traverse system and was capable of moving in all 3 spatial dimensions. This probe will be referred to as the moving probe in this text. The two probes were used to obtain measurements on a spatial grid of 35x35 points in the normal to the wall directions at *x/h* = 9 and *x/h* = 36. In the spanwise

[*] Professor, Aerospace and Ocean Engineering Department at Virginia Polytechnic Institute and State University

direction the measurements were obtain on a grid of 15x15 and 13x15 spatial points (first index being that for fixed probe) for *x/h* = 9 and *x/h* = 36 respectively. The details of the experimental setup, data acquisition, processing and reduction can be found in Morton *et al.* (2012).

The velocity fluctuations in turbulent flow can be related to the pressure fluctuations observed on the wall through the Poisson's equation given by

$$\frac{1}{\rho}\nabla^2 p' = -2\frac{\partial < U_i >}{\partial x_j}\frac{\partial u_j}{\partial x_i} - \frac{\partial^2}{\partial x_i \partial x_j}\left(u_i u_j - < u_i u_j >\right) \qquad (Eq.11)$$

In the above equation the right hand side contains two source terms, the first term as defined by Pope (2000) is the rapid pressure $p^{(r)}$ and the second term is the slow pressure $p^{(s)}$. There is also a third contribution to the overall pressure field called the harmonic pressure and it satisfies Laplace's equation: $\nabla^2 p^{(h)} = 0$. The rapid pressure contribution is significant only in mean velocity gradients while the slow pressure is significant in most cases. The harmonic pressure is zero in homogenous turbulence and is important only in near wall regions.

Since step flows experiences mean velocity gradients and the present study is concerned with studying the boundary layer all the three pressures contribute to the wall pressure fluctuations. Solving *Eq.11* for step flows can therefore be a tedious task. Another better way to understand the relationship between the wall pressure fluctuations and velocity fluctuations is two point velocity space-time correlations and two point pressure space-time correlations. Therefore, in this section we turn to these spatial-temporal results to better understand the flow structure and the pressure-velocity relationship in forward step flows.

Since, the maximum contribution to the fluctuating velocity field comes from normal to wall and streamwise velocity fluctuation components (as shown by the shear stress profiles in Figure 69) the space time correlations of these two components will be discussed in this section. Consider first the spanwise space-time correlation of the normal to the wall velocity fluctuation (*w'*) at $z/\delta \approx 15\%$ for smooth wall and medium step at *x/h* = 9 and *x/h* = 36 shown in the first row of Figure 70. The bottom row of the figure shows the spanwise pressure space-time correlation map for smooth wall and same streamwise locations. Although, the spanwise correlations were measured at several normal to wall locations, this particular z/δ location was chosen since the velocity spectra shown in Figure 68 and Figure 69 clearly show these fluctuations to be higher than smooth wall and in the turbulence intensity profiles seen in Figure 66 a peak in turbulence intensity can be seen around this location.

Looking at the spanwise correlation of (w') for smooth wall it can be seen that it has a similar structure to the spanwise pressure correlation for smooth wall. However, the pressure is much more elongated in the spatial dimension and is well correlated to about a boundary layer thickness in spanwise direction. The velocity correlations however show length scales that are about $1/10^{th}$ of those shown by the pressure. However, the velocity correlations have much larger time scale compared to pressure correlations. This suggests that the smaller scale structures that are closer to and are moving slower are reflected in the velocity correlations. On the other hand, larger structures that are moving away from the wall and moving faster seem to affect the wall pressure fluctuations. A similar observation was made by Corcos (1964) who studied the wall pressure fluctuations in a turbulent boundary layer on a smooth wall.

The spanwise normal to the wall velocity correlations and the spanwise pressure correlations at $x/h = 9$ can be seen in the 2nd column of Figure 70. Looking at the correlations of w' at this location it can be seen that it is elongated in the spatial dimension (to about 0.2δ) and is compressed in the temporal dimension compared to its smooth wall form. This indicates faster moving and slightly larger structures in the near wall region downstream of the step. Another interesting feature is the emergence of two negative correlation lobes on either side in these correlations. This is similar to what was observed in spanwise pressure correlations seen also seen at the bottom of the figure and thus suggest a quasi-periodic motion as suggested by the pressure correlations. The velocity correlations at $x/h = 9$ have the same form as the spanwise pressure correlations; however, they are compressed in both temporal and spatial direction at this location. The reason for this might be that post reattachment the larger structures have within them smaller eddies that are uncorrelated over large distances and are reflected in the velocity correlations. While, the larger eddies moving over them are seen by the pressure correlations. It can thus be concluded that in the near wall region the velocity fluctuations are unable to affect the wall pressure fluctuations.

The third column of Figure 70 which shows the w' and pressure space-time correlations at $x/h = 36$ and $z/\delta \approx 15\%$. The velocity correlation at this location seems to return to their smooth wall form shows reduced spatial-temporal scales. The two negative lobes that were seen at $x/h = 9$ have also disappeared at this location. On the other hand, the pressure fluctuation correlations at this location have a larger spatial-temporal scale and also show the strengthening of the negative lobes.

Figure 71 shows the normal to wall space-time correlation of normal to wall velocity fluctuation component for smooth wall, $x/h = 9$ and, $x/h = 36$. The layout of the figure is similar to that of Figure 70. The normal to the wall correlations display the exact same behavior as was seen in the spanwise velocity correlations. For the smooth wall case, the normal to wall velocity fluctuation is well correlated throughout the boundary layer and the spanwise pressure fluctuations also extend about a boundary layer thickness. At $x/h = 9$ the length scale has increased to 0.6δ and this increase in length scale is accompanied by a reduced temporal scale indicating faster moving structures. The negative lobes as seen in the spanwise pressure correlations and velocity correlations are also observed in the correlations. Further downstream, at $x/h = 36$, the correlations seem to return to their smooth wall form. However, the temporal scale of correlations is much shorter suggesting faster moving large eddies in this region of the flow.

Now consider the spanwise space time correlation of the streamwise velocity fluctuation component shown in Figure 72 for smooth wall, $x/h = 9$ and $x/h = 36$. The layout of the figure is same as that of Figure 70 and Figure 71. Looking at the smooth wall correlation for u' at the top left corner of the figure one can see a much more intense correlation than seen in w' correlations earlier. In the spanwise direction the streamwise velocity fluctuation has a strong positive correlation up to 0.25δ. However, beyond that to about distance equal to a boundary layer thickness a negative correlation can be seen. This interesting correlation shows that a stripy spanwise organization develops in the near wall turbulent boundary layer. This '*stripiness*' is caused by alternating low and high speed structure organization in the spanwise direction.

Now consider the spanwise correlations of u' for the medium step height at $z/\delta = 15\%$ for $x/h = 9$ and 36 shown in the 1st row and 2nd and 3rd column of Figure 72. Looking at 9 step

heights correlations one can see that the reattachment (at x_r/h = 3.6) serves to reduce both the spatial and temporal scale of correlations downstream of the reattachment. This is possibly due to the vortex shedding from the step and shows the presence of smaller faster moving structures at 9 step heights downstream. The negative lobes seen in smooth wall correlations have decayed in intensity and length scale as well at this location. Further downstream at x/h = 36, the correlations have increased in spatial-temporal scale and are larger compared to those seen in smooth wall.

Now consider the normal to wall correlations of streamwise velocity fluctuations for medium step at x/h = 9 and 36 seen in Figure 73. The smooth wall correlations show a large spatial correlation that lasts up to almost a boundary layer thickness and shows an elongated time scale as seen in the spanwise correlations in Figure 72. Consider now the medium step correlations downstream at x/h = 9 and 36 step heights seen in the 2nd and 3rd column of first row respectively. It can be seen that at 9 step heights, the correlations have reduced in spatial-temporal scale similar to the spanwise correlations seen earlier. In normal to the wall direction the correlations extend to about 0.8δ and the time scale has reduced to about half of its smooth wall value. Further downstream at x/h = 36 the correlations seem to return to their smooth wall form and extend about a boundary layer thickness in spatial dimension. However, in the temporal direction the intensity is much less than the smooth wall values and indicates large faster moving structures at this location.

To summarize the velocity 2 point correlations it can be said that the effects of velocity fluctuations on the wall pressure are suppressed by the fact that there are smaller less coherent eddies in the near wall region which are picked up by the hotwire probes and are reflected in the velocity correlations. On the other hand, the wall pressure fluctuations are effected by larger eddies which blanket these smaller eddies. Therefore, it is hard to determine a relationship between the pressure and velocity fluctuations by just looking at the correlations. However, the velocity space time correlations do confirm the presence of quasi-periodic structures at x/h = 9 for the medium step suggesting that it actually is a flow feature of forward step flows.

3.8.3 Proper Orthogonal Decomposition (POD)

The non-linear nature of Navier-Stokes equations makes it difficult to solve them and extract information about turbulence. Proper orthogonal decomposition is a technique which allows a quantitative and qualitative analysis of the turbulent structures without the complications of non-linearity. It was pioneered by Lumley (1967) and serves to extract coherent structures from a turbulent flow field through the use of two point velocity correlation measurements. POD is a technique which decomposes the velocity field into proper orthogonal modes and identifies the motions which, on average, contain the most energy (Pope, 2000). Thus, using POD one can identify the structures that dominate a flow field and deduce general behavior of a particular flow.

To better understand the velocity field and flow structure in forward step flows the two point correlations presented in previous section were used to perform a proper orthogonal decomposition of the velocity field. The theory and methodology behind POD will be described in this section followed by the results that were obtained.

The orthogonal decomposition of the fluctuating velocity field $u(x,t)$ is given by

$$u(x,t) = \sum_{n=1}^{\infty} a_n(t)\varphi_n(x) \qquad (Eq.12)$$

a_n represents the coefficients that are random functions of time while φ_n are the real basis functions that are only a function of space and non-random and 'n' is the mode number. The basis functions satisfy the following orthonormality condition

$$\frac{1}{\mathcal{L}}\int_0^{\mathcal{L}} \varphi_n(x)\varphi_m(x)\,dx = \delta_{nm} \qquad (Eq.13)$$

Where δ_{nm} is the delta function and $\mathcal{L}$ is some length scale such that$0 \le x \le \mathcal{L}$. The choice of the basis function used for the decomposition is arbitrary and is valid as long as the above condition is satisfied. The average mean energy of the velocity fluctuations as shown by (Pope, 2000) is given by

$$\bar{E} = \sum_{n=1}^{\infty} \frac{1}{2}\langle a_n^2 \rangle \qquad (Eq.14)$$

Where $\langle\ \rangle$ indicates a time averaged quantity. Thus, the term $\frac{1}{2} < a_n^2 >$ is the contribution to the energy from the nth mode and summing the above equation over N modes gives the contribution to the mean energy from the 1st N modes. The defining basis of the POD is that the basis function φ_n is chosen such that it leads to maximum energy in first N modes than any other orthogonal decomposition. Holmes *et al.* (1996) showed that the basis functions needed for POD can be determined by just using the two point velocity correlation. To do this one needs to perform the eigenvector decomposition of the zero time delay correlations in effect solving the equation

$$\frac{1}{\mathcal{L}}\int_0^{\mathcal{L}} \langle u(x)u(y)\rangle \varphi_n(y)\,dy = \lambda_n \varphi_n(x) \qquad (Eq.15)$$

The term $\langle u(x)u(y)\rangle$ represents the zero time delay correlation coefficient. Or, in terms of the present nomenclature with 'z' representing the normal to the wall location of fixed probe, 'z'' representing the normal to the wall location of fixed probe, R_{ij} (0, z, z$'$) representing the zero time delay correlation coefficient between the velocity components, i and j representing the index of fixed and moving probes, *Eq.15* can be written as

$$\frac{1}{\mathcal{L}}\int_0^{\mathcal{L}} R_{ij}(0,z,z')\varphi_n^j(z')dz' = \lambda_n \varphi_n^i(z) \qquad (Eq.16)$$

Solving above equation requires finding the eigenvalues and eigenvectors of a matrix that consists of the zero time delay correlation coefficients over the entire spatial measurement grid for all the velocity components. This matrix essentially is a matrix that has all the Reynolds shear stress correlations. A contour map of the normal to wall zero time delay correlations for smooth wall and the medium step at 9 and 36 step heights has been shown in Figure 74 where the main diagonal clearly shows the normal stress correlations ($\overline{u_i'^2}$) and the off diagonals show the shear stress correlations ($\overline{u_i' u_j'}$) with the upper right hand corner and lower left hand corner showing the $\overline{u'w'}$ correlation.

The eigenvalues of this matrix when arranged in decreasing order ($\lambda_1 > \lambda_2 > \cdots \lambda_N$) then represent the average energy contained in the first N modes. A distribution of the mean turbulent energy by modes has been shown in Figure 75 which shows the contribution of first 5, first 10 and first 20 modes to the total average energy for the smooth wall and the medium step at 9 and 36 step heights. Looking at the figure it can be seen that for all 3 cases the first 5 modes contribute to about 50% of the total energy, first 10 modes contribute about 65% and the first 20 modes about 80%. It should also be noted that the contribution of the lower modes increase by about 4 % at x/h = 9 and by about 1-2% at x/h = 36 compared to the smooth wall. This fact is further illustrated in Figure 76 which shows the eigenvalue spectrum as well as the cumulative eigenvalue spectrum for all cases and modes and also shows a magnified view of the first 20 modes at the bottom of the figure. Since, the first 5 modes were found to provide a significant contribution to the turbulent energy these modes were picked for further detailed analysis to reveal the compact eddy structure in the normal to the wall direction within the boundary layer.

Figure 77 shows the product of the mode magnitude and the eigenfunctions of all 3 components of the velocity for the first 5 modes for smooth wall and the medium step at x/h = 9 and 36. The representation of the modes in this manner provides both the amplitude and shape of modes. Looking at the figure it can be seen that for all the case, the 1st, 2nd and the 4th mode are dominated by the streamwise velocity fluctuations (u') and the normal to the wall velocity component (w') while the 3rd and 5th mode see contribution by the spanwise fluctuating component (v'). The 1st mode on the top left corner shows that the presence of the step in the flow field increases the mode amplitude but the overall mode shape is preserved. The shapes of the two dominant velocity fluctuation components (u' and w') are similar and just differ in the magnitude. The 2nd mode also shows that the overall shape is preserved, however, in this case the magnitude of the streamwise fluctuating velocity goes from negative to positive moving away from the wall while the magnitude of normal to the wall component goes from positive to negative moving away from the wall. The 4th mode displays similar qualitative behavior as the 2nd mode just with reduced magnitude. The 3rd and 5th modes are dominated by the spanwise fluctuating component with similar qualitative behavior as the other modes. In essence, Figure 77 shows that the step only serves to redistribute the energy within the boundary layer without causing any qualitative changes.

3.8.4 Compact Eddy Structures (CES)

Applying POD to flows that are homogenous in at least one direction requires a large number of modes to describe the flow (Glegg & Devenport, 2001). An alternative approach to find the structures that dominate a particular flow field is the Linear Stochastic Estimate or LSE. This approach, however, cannot be used to create a time representation of the flow since the modes obtained from LSE are time averaged. They can however be used in combination with the POD to create what are called Compact Eddy Structures (CES). In this approach the POD is applied to directions in which flow is inhomogeneous and LSE to homogenous direction. In this manner, one can obtain the time history of the flow without being concerned about the homogeneity of the flow.

CES are obtained from correlations by projecting the zero time delay correlations over the time domain. This is done by taking the inner product of the eigenfunctions for a particular mode with the time delayed correlation at each moving and fixed probe locations. This process

then gives the instantaneous velocity components for each time delay over the entire spatial domain which can then be combined to produce the velocity vectors. Figure 78 shows the CES for the smooth wall for the first 5 modes normalized on the eigenvalues. The velocity vectors obtained by combining the streamwise and normal to the wall velocities have been shown as blue arrows and the spanwise velocity component has been shown as a contour map in the background. Looking at the 5 modes of the smooth wall one can see that similar to POD modes the 3rd and 5th modes are dominated by spanwise velocity fluctuation component while the rest of the modes contain the other two components. The first mode contains 'u-w' velocity vectors with lower slope and elongated temporal scale in the near wall region than the vectors that lie away from the wall. This shows the presence of larger faster moving eddies away from the wall that shroud the slower moving smaller eddies in the near wall region as suggested by the velocity correlations. Looking at the 2nd mode for smooth wall one can see the presence of

Figure 79 shows the CES for the medium step at x/h = 9 for the first 5 modes. The first mode shows velocity vectors elongated in temporal dimension indicating presence of large structures in the near wall region. The left pointing velocity vectors indicate lower mean velocity than the local instantaneous value indicating slower moving fluid rushing away from the wall or faster moving fluid rushing towards the wall (since the sign is arbitrary). This region with large structures lasts up to about 40% of the boundary layer thickness which is reflected in the streamwise turbulence intensity profile shown in Figure 66 at x/h = 9 and the turbulence spectrum which shows elevated velocity frequency spectra at this location up to about 50% of boundary layer thickness. The 2nd mode shows a conventional spanwise eddy motion centered at about 10-20% of the boundary layer thickness. The 4th mode shows a fast moving flow which is angled at about 45 degrees towards the wall and centered at about 10% of the boundary layer thickness. The 3rd and 5th modes show larger contours of the spanwise velocity components since these modes were dominated by this component as seen earlier.

Moving on to x/h = 36, the CES for the 5 modes have been shown in Figure 80. Modes 1 and 2 at this location do not show significant difference from the smooth wall structures and seem to return to that form. However, mode 4 shows the same feature as seen for x/h = 9, only the motion has increased in intensity and extent. The fluid from outer region seems to rush in at much a steeper angle than seen at x/h = 9 and almost perpendicular to the wall. Modes 3 and 5 that contain the spanwise velocity component intensify further at this location.

4. Conclusions

Measurements were made on forward facing steps of three different sizes immersed in a turbulent boundary layer for two different Reynolds number. The step sizes were about 3.8%, 15% and 60% of the incoming boundary layer thickness and the Reynolds number based on step height ranged from 6640 to 213,000. The measurements were made upstream, in the vicinity and, far downstream of the step location. Measurements included mean wall pressure, single and two point streamwise and spanwise wall pressure fluctuations, single and two point spanwise and normal to the wall 3 component velocity fluctuations and, oil flow visualization near the step to determine separation-reattachment lengths. Following are the major observations made in the present work:

Separation-Reattachment Region Features

- Forward steps serve to separate the incoming equilibrium (ZPG) turbulent boundary layer creating a strong adverse pressure gradient recirculating flow region just upstream of the step. The mean wall pressure begins to rise near the separation and continues to rise until the face of the step is reached where the flow reattaches. In this separation region the pressure is weakly dependent upon the Reynolds number and the flow geometry (step height to boundary layer ratio). The separation length for different Reynolds number and step height to boundary layer ratios determined through oil flow visualization also reflect this fact. The separation lengths stay between 1.5 to 1.9 step heights upstream for all 3 step sizes or all 6 Reynolds number.
- After reattachment on the face of the step, the flow again separates at the edge of the step (a fixed separation point) and then reattaches some distance downstream. The separation of boundary layer at the edge of the step accelerates the flow and as a result the pressure immediately downstream of the step is much lower than free stream. The mean pressure then recovers slowly to a constant value near the reattachment. The flow separation and reattachment process forms two regions within the boundary layer: slow moving recirculation region near the wall and faster moving free shear layer away from the wall. The formation of this shear layer enhances turbulence mixing within the boundary layer and causes high velocity and pressure fluctuation levels. These features are well reflected in the mean velocity and turbulence profiles which clearly show a large velocity defect and high turbulence intensity within about 20% of boundary layer thickness away from the wall.
- As opposed to the separation length, the downstream reattachment length was found to be a strong function of the Reynolds number and ranged from 1.6 to 4.2 step heights downstream for Reynolds numbers ranging from 6640 to 213,000. The reattachment length for medium step (Re_h = 26,600) is about 3.6 step heights which is fairly close to that of Farabee and Casarella (1986) and the difference can be attributed to the Reynolds number. Reynolds number affects the small step reattachment length significantly (it doubles with Reynolds number) while the reattachment lengths for medium and large step sizes are weakly affected by variation in Reynolds number. Thus, it can be concluded from the present results that the reattachment length is a strong function of Reynolds number for small forward facing steps.

Wall Pressure Fluctuations, Velocity Fluctuations and Flow Structure

As noted earlier, the separation-reattachment process due to presence of forward steps modifies the incoming equilibrium turbulent boundary layer by adding turbulence to it. The added turbulence causes elevated velocity and wall pressure fluctuations in the vicinity as well as upstream and downstream of the step. The observations made from pressure and velocity measurements have been summarized below

- Upstream of the step, the pressure fluctuations were found to be highest around separation point. For medium step size ($h/\delta \approx 15\%$) the pressure fluctuations are about 100 times the smooth wall just upstream of separation at lower frequencies. And, for large step size ($h/\delta \approx 60\%$), they are about 400 times the smooth wall values just downstream of separation at lower frequencies. The higher frequencies on the other hand, were found to dip below the smooth wall for all steps. This suggests that separation lifts the smaller structure away from the wall. The pressure space-time correlations upstream of the step show an increase in spatial and temporal scales showing the presence of large, nearly stagnant structures in this region. Similar to observation made by Efimtsov *et al.* (1999), the upstream extent of the pressure fluctuations is a function of step size and is larger for smaller steps in terms of step height. The velocity measurements for the medium size step show that at about 10 step heights upstream of the step there is a very slight velocity defect an increase in streamwise turbulence intensity.

- Downstream of the step, the pressure fluctuations are the highest at and near the reattachment location at all frequencies. For the medium step, the pressure fluctuations exceed the smooth wall by about 25 dB and for the large step by more than 30 dB near the reattachment location. The downstream extend of pressure fluctuation was also found to be remarkable. For the small step size, the presence of steps can be felt as far as 600 step heights for small step size and 152 step heights for medium step size suggesting that the reattached shear layer has not quite returned to its smooth wall form even after travelling such large distances. The mean velocity and turbulence profiles at $x/h = 148$ also reflect this fact and a velocity defect along with increased streamwise velocity fluctuations from $z/\delta = 10\%$ to the edge of boundary layer can be seen in these profiles.

- The downstream pressure spectra for all 3 steps and 6 Reynolds number show a common feature which is the presence of a ridge that is centered at mid frequencies. When subtracted from the smooth wall (no step) spectrum and normalized on these ridge values for $x/h > 8$ locations, the downstream spectra collapse well for all step sizes and Reynolds number. The ridge frequencies and spectral magnitudes for $x/h > 8$ collapse well when normalized on step height rather than the boundary layer thickness. This shows that the disturbance spectra due to the step downstream of step are self-similar regardless of the step height or the boundary layer thickness. Moreover, the disturbance pressure field due to a forward step is only a function of the x/h location when scaled on step height.

- The pressure space-time correlations show the presence of an organized quasi-periodic structure for medium and large size steps with temporal scale matching the ridge frequencies seen in pressure autospectra. For medium step size, the structure appears at about 9 step heights downstream of the step and by 37 step heights it has grown in intensity and scale.

Further downstream at 152 step heights this structure has decayed in intensity but has grown in scale. For large step size, this structure begins to appear at 2.3 step heights, just upstream of reattachment in the recirculation bubble and completely dominates the correlations by 37 step heights downstream. The presence of these organized structures downstream of the step suggests regular formation of large eddies in the separation bubble just downstream of the step and explains the large scale pressure fluctuations seen downstream of the steps.

- Comparisons of steps pressure spectra with that of Farabee and Casarella (1986) and Ji and Wang (2010, 2010a) shows that while qualitatively the spectra behave the same, decay of magnitude of spectra post reattachment is much slower in the present work. This fact is also reflected in the root mean square pressure results and appears to be a Reynolds number effect.
- 2 point normal to wall and spanwise velocity correlations from the measurements made downstream of medium size step also show a presence of quasi-periodic structure seen in the pressure correlations. This structure begins to appear at 9 step heights downstream of the step in both normal to wall and spanwise velocity correlations. However, the scale and intensity of this structure is much lower than what was seen in pressure correlations and by 37 step heights it has disappeared. The reason for this is that the large scale structures that affect the pressure correlations are masked by the small structures that are present within them and are reflected in velocity measurements.
- Proper Orthogonal Decomposition (POD) shows that first 5 modes of velocity fluctuations contribute about 50% of the overall turbulent energy present. The presence of step only serves to redistribute the mode shapes in the boundary layer while preserving the qualitative mode shapes.

References

Addad, Y., Laurence, D., Talotte, C., & Jacob, M. C. (2003). Large Eddy Simulation of a Forward-Backward Facing Step for Acoustic Source Identification. *International Journal of Heat and Fluid Flow*, 562-571.

Aglenichaab, M., & Tachie, M. F. (2008). PIV Study of Separated and Reattached Open Channel Flow Over Surface Mounted Blocks. *Journal of Fluid Engineering*, vol.130, pp.1-9.

Alexander, W. N. (2009). *Normalization of Roughness Noise on the Near-Field Wall Pressure Spectrum.* M.S Thesis, Blacksburg, VA: Aerospace and Ocean Engineering Department at Virginia Polytechnic Institute and State University.

Awasthi, M., Forest, J. B., Morton, M. A., Devenport, W. J., & Glegg, S. A. (2011). The Disturbance of a High Reynolds Number Turbulent Boundary Layer by Small Forward Steps. *17th AIAA/CEAS Aeroacoustics Conference.* Portland, OR: AIAA.

Blake, W. K. (1970). Turbulent boundary layer wall-pressure fluctuations on smooth and rough walls. *Journal of Fluid Mechanics*, vol.44, pp.637-660.

Bradshaw , P., & Wong, F. Y. (1972). The Reattachment and Relaxation of a Turbulent Shear Layer. *Journal of Fluid Mechanics*, vol.52, pp.113-135.

Camussi, R., Felli, M., Pereira, F., Aloisio, G., & Di Marco, A. (2008). Statistical Properties of Wall Pressure Fluctuations over a Forward Facing Step. *Physics of Fluids*, vol.294, pp.177-204.

Castro, I. P., & Dianat, M. (1983). Surface flow patterns on rectangular bodies in thick boundary layer. *Journal of Fluid Mechanics*, vol.11, pp.107-119.

Cherry, N. J., Hillier, R., & Latour, M. E. (1984). Unsteady measurements in a separated and reattaching flows. *Journal of Fluid Mechanics*, vol.144, pp 13-46.

Corcos, G. M. (1964). The Structure of Turbulent Pressure Field in Boundary-Layer Flows. *Journal of Fluid Mechanics*, vol.18, pp.353-378.

Devenport, W. J., Grissom, D. L., Alexander, W. N., Smith, B. S., & Glegg, S. A. (2011). Measurements of Roughness Noise. *Journal of Sound and Vibration*, published online, doi:10.1016/j.jsv.2011.03.017.

Efimtsov, B. M., Kozlov, N. M., Kravchenko, S. V., & Andersson, A. O. (1999). Wall pressure fluctuation spectra at small forward-facing steps. *AIAA Paper*, 99-1964, 1999.

Farabee, T. M., & Casarella, M. J. (1986). Measurement of fluctuating wall pressure for separated/reattached boundary layer flows. *Journal of Vibration, Acoustics, Stress, and Reliability in Design*, vol.108, pp.301-307.

Farabee, T. M., & Zoccola, P. J. (1998). Experimental Evaluation of Noise Due to Flow Over Surface Steps. *ASME Noise Control and Acoustics Division.* Anaheim, CA: ASME.

Fiorentini, E., Felli, M., Pareira, F., Camussi, R., & Di Marco, A. (2007). Wall Pressure Fluctuations Over a Forward-Facing Step. *13th AIAA/CEAS Aeroacoustics Conference* (pp. 1-10). Rome: AIAA.

Forest, J. B. (2012). *The Wall Pressure Spectrum of High Reynolds Number Rough-Wall Turbulent Boundary Layer.* M.S Thesis, Blacksburg, VA: Aerospace and Ocean Engineering Department at Virginia Polytechnic Institute and State University.

Fricke, F. R., & Stevenson, D. C. (1968). Pressure fluctuations in a separated flow region. *Journal of Acoustical Society of America*, vol.44, pp.1189-1200.

Gasset, N., Poitras, G. J., Gagnon, Y., & Brothers, C. (2005). Study of atmospheric boundary layer flow over a coastal cliff. *Wind Engineering*, vol.29-1, pp.3-24.

Glegg, S. A., & Devenport, W. J. (2001). Proper Orthogonal Decomposition of Turbulent Flow for Aeroacoustic and Hydroacoustic Applications. *Journal of Sound and Vibration*, vol.239, pp.767-784.

Greshilov, E. M., Evtuchenko, A. V., & Lyamshev, L. M. (1969). Spectral characteristics of the wall pressure fluctuations associated with boundary layer behind a projection on a smooth wall. *Soviet Physics-Acoustics*, pp.29-34.

Holmes, P., Lumley , J. L., & Berkooz, G. (1996). *Turbulence, Coherent Structures, Dynamical Systems, and Symmetry.* New York: Cambridge University Press.

Horne, M. P. (1990). *Physical and Computational Investigation of Pressure Fluctuations in Channel Flow.* Washington D.C: Naval Research Laboratory.

Hubbard. (1956). Some experiments related to noise from boundary layer. *Acoustical Society of America*, vol.28, pp.331-334.

Hudy, L. M., Naguib, A. M., & Humphreys Jr., W. M. (2003). Wall-Pressure-Array Measurements Beneath a Separating/Reattaching Flow Region. *Physics of Fluid*, vol.15, pp.706-717.

Ji, M., & Wang, M. (2010). Aeroacoustics of turbulent boundary-layer flow over small steps. *48th AIAA Aerospace Sciences Meeting Including the New Horizons Forum and Aerospace Exposition.* Orlando: AIAA.

Ji, M., & Wang, M. (2010a). Sound generation by turbulent boundary-layer flow over small steps. *Journal of Fluid Mechanics*, vol.654, pp.161-193.

Largeau, J. F., & Moriniere, V. (2007). Wall Pressure Fluctuations and Topology in Separated Flow Over A Forward Facing Steps. *Experiment in Fluids*, vol.42, pp.21-40.

Leclercq, D. J., Jacob, M. C., Louisot, A., & Talotte, C. (2009). Forward-Backward facing step pair: Aerodynamic flow, wall pressure and acoustic characterization. *Proceedings of the 7th AIAA/CEAS Aeroacoustics Conference* (pp. 075113-1 075113-13). Seoul: AIAA.

Lumley, J. L. (1967). The structure of inhomogeneous turbulent Flows. *In Atmospheric Turbulence and Radio Wave Propagation*, pp.166-178.

Morton, M., Devenport, W., Alexander, W. N., Glegg, S. A., & Borgoltz, A. (2012). Rotor Inflow Noise Caused by a Boundary Layer: Inflow Measurements and Noise Prediction. *18th AIAA/CEAS Aeroacoustics Conference* (pp. 1-15). Colorado Springs, CO: AIAA.

Moss, W. D., & Baker, S. (1980). Recirculating Flows Associated With Two Dimensional Steps. *Aeronautical Quarterly*, pp.151-172.

Pope, S. B. (2000). *Turbulent Flows.* Cambridge: Press Syndicate of the University of Cambridge.

Sherry, M. J., Jacono, D. L., Sheridan, J., Mathis, R., & Marusic, I. (2009). Flow separation characterisation of a forward facing step immersed in a turbulent boundary layer. *Sixth International Symposium on Turbulence and Shear Flow Phenomena*, (pp. 1325-1330). Seoul.

Willmarth, W. W., & Woolridge, C. E. (1962). Measurement of fluctuating pressure at the wall beneath a thick turbulent boundary layer. *Journal of Fluid Mechanics*, vol.14, pp.187-210.

Zhang, C. X. (1994). Numerical prediction of recirculating turbulent flow with k-e model. *Journal of Wind Engineering and Industrial Aerodynamics*, vol.51, pp.177-201.

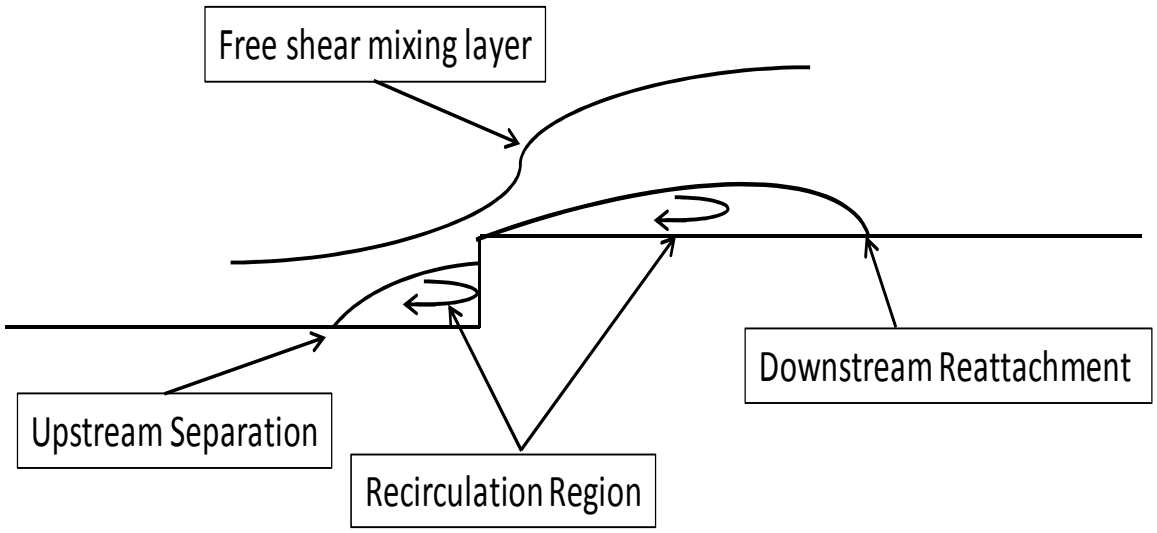

Figure 1. Separation Reattachment of Flow Over Forward Step

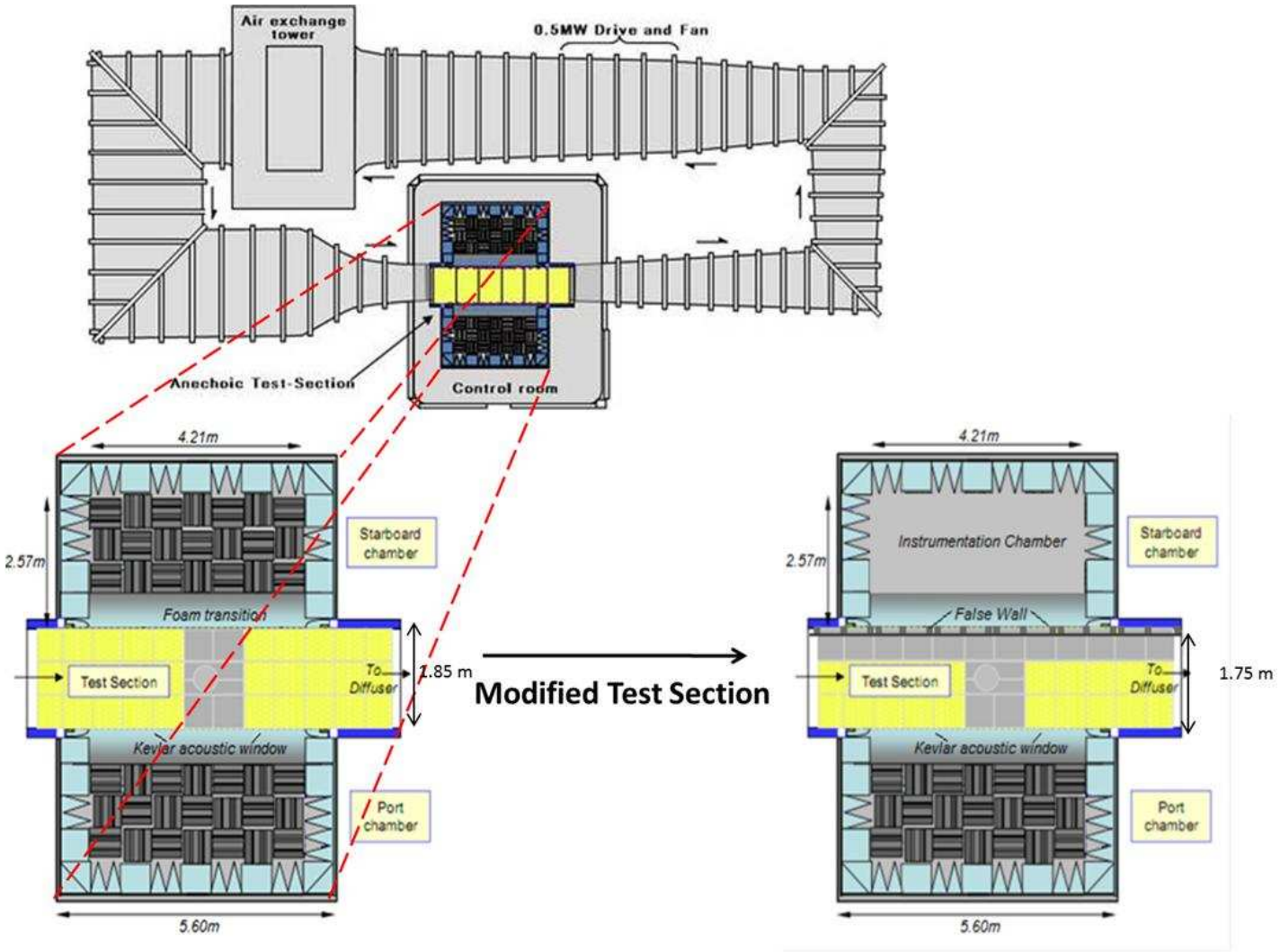

Figure 2 Design Layout of Virginia Tech Stability Wind Tunnel, Acoustic Test Section, Modified Test Section for Present Work (Used with permission of Dr. William J. Devenport (2012))

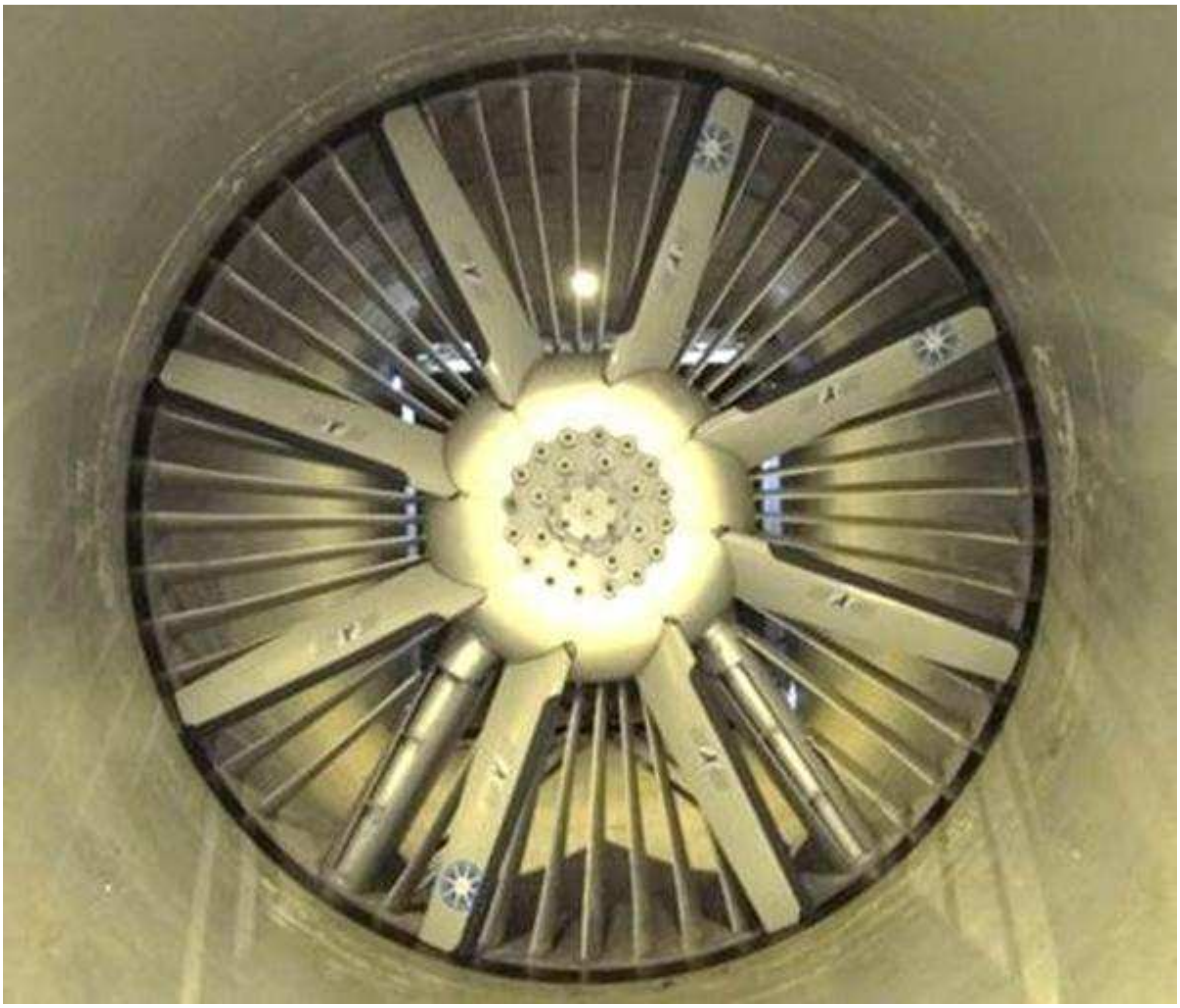

Figure 3. Virginia Tech Stability Tunnel Fan (Used with permission of Dr. William J. Devenport (2012))

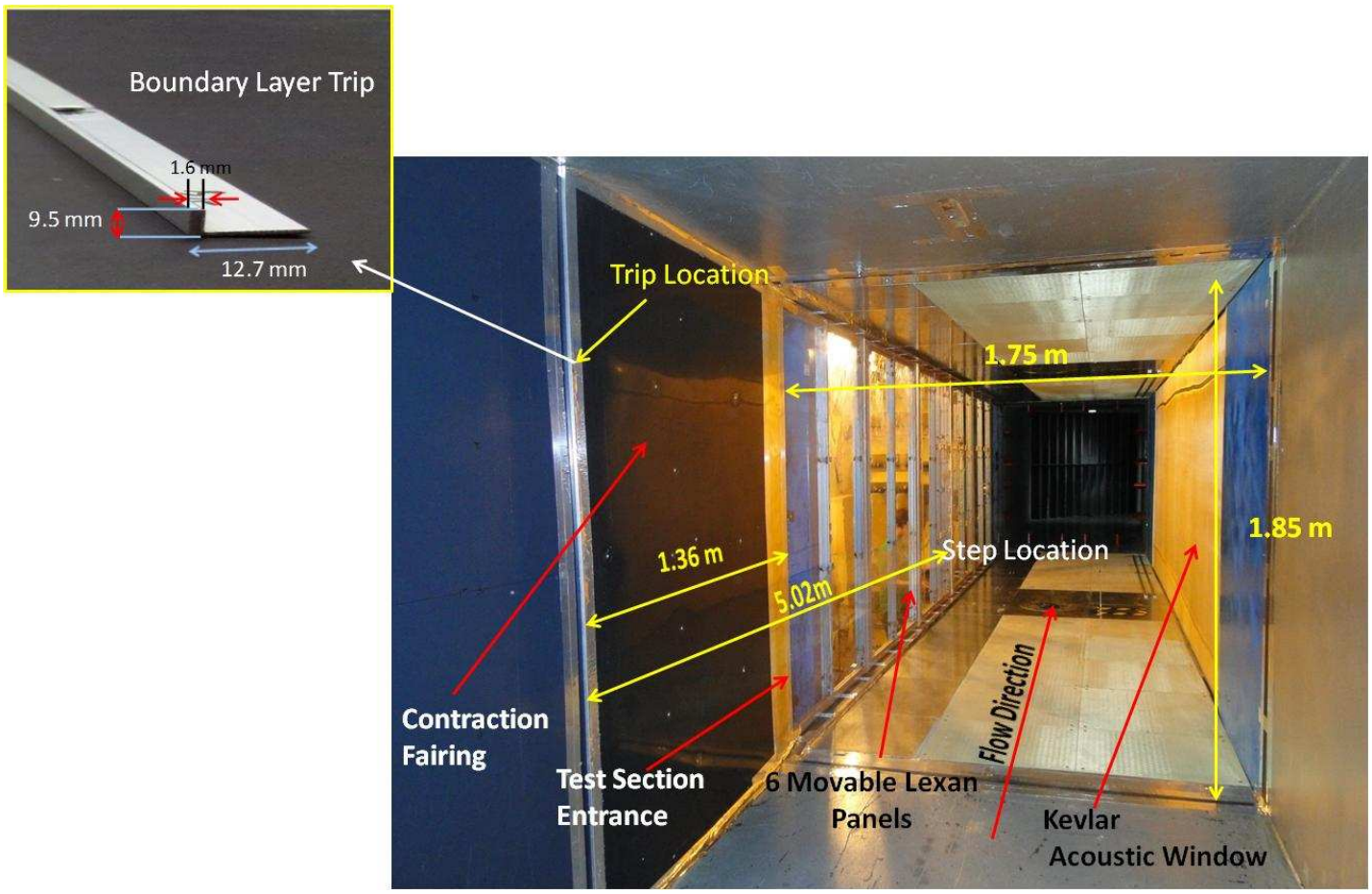

Figure 4. Test Wall/Contraction Area view (9.5 mm boundary layer trip shown in inset on top left (Used with permission of Jonathan B. Forest (2012))

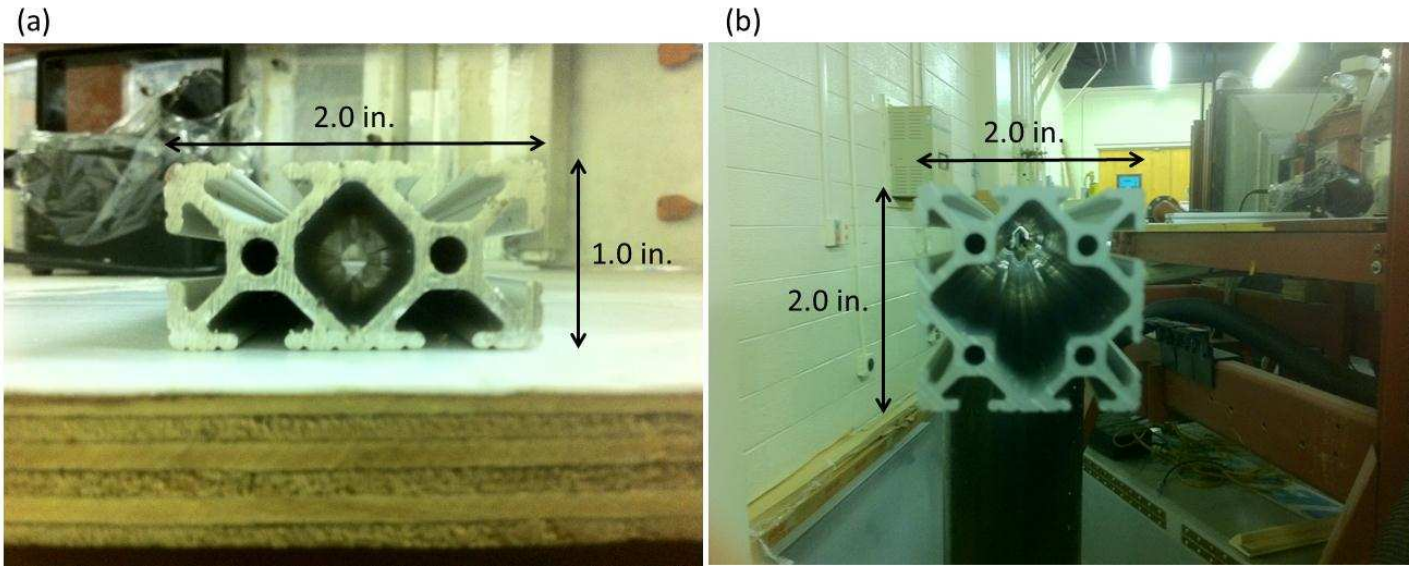

Figure 5. Cross sectional view of a typical 80/20 beam used to brace the Lexan panels and attached to floor and ceiling of test section. (a) Beams used on top, bottom and on the centerline of the panel, (b) Beam used on the sides of the panels

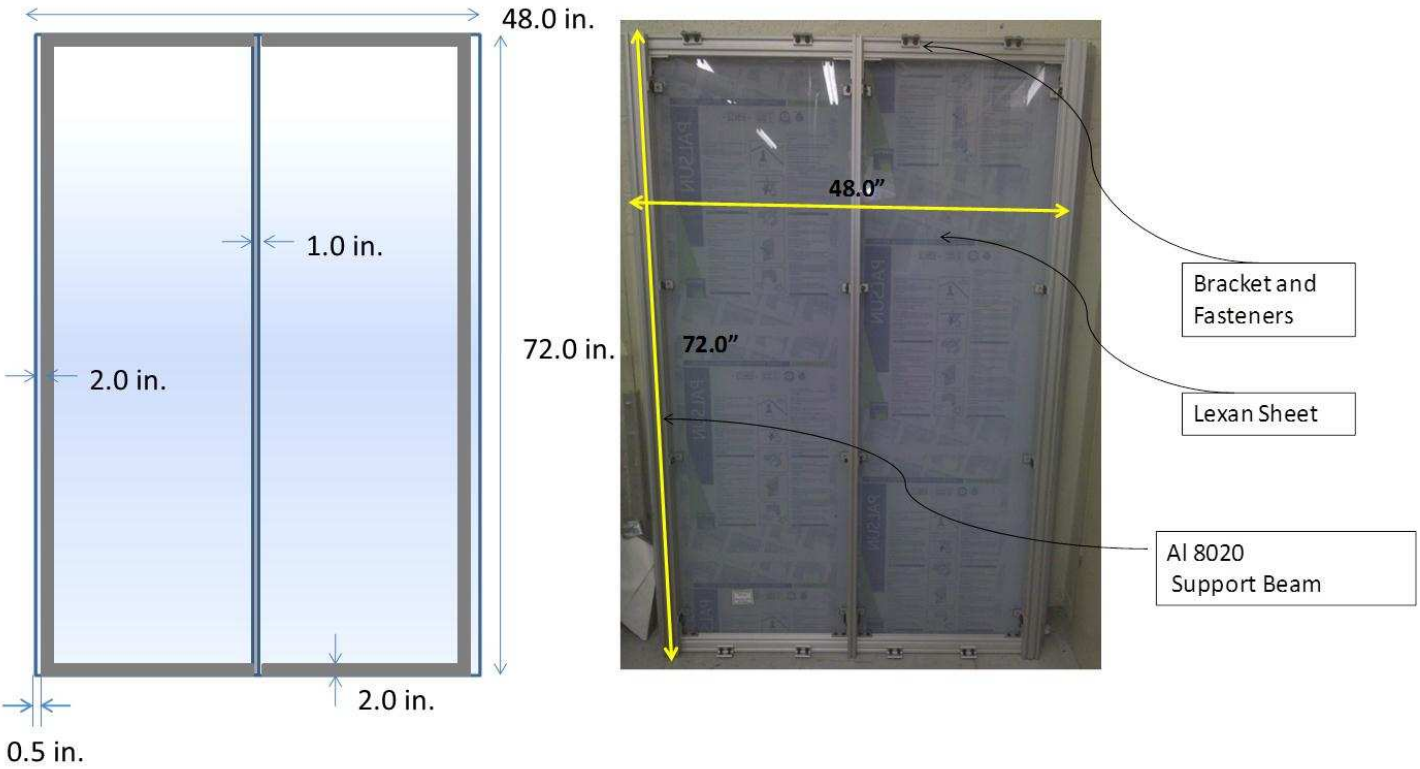

Figure 6. Layout of Lexan panel used for false wall

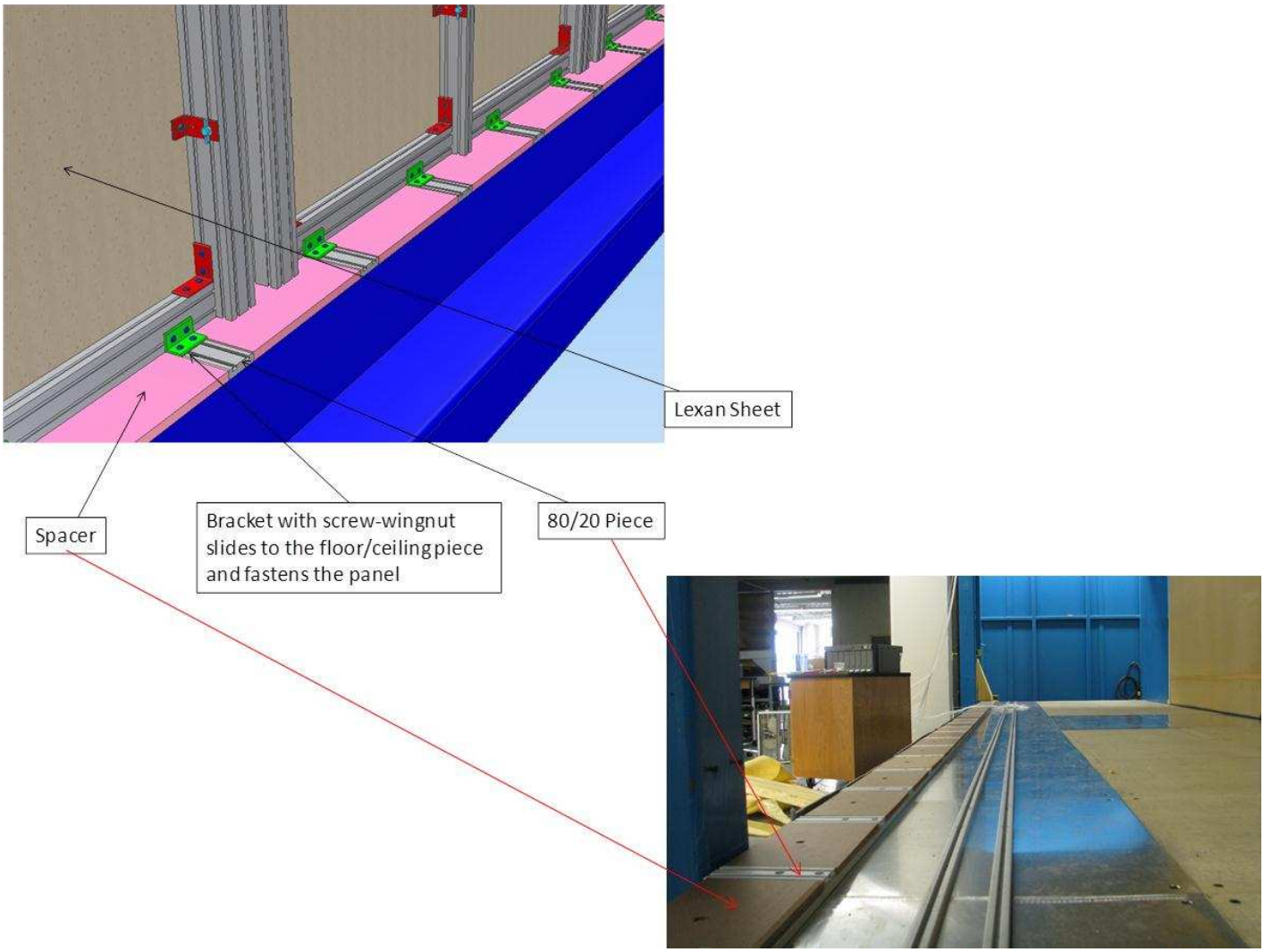

Figure 7. Test wall to test section attachment mechanism (Used with permission of Jonathan B. Forest (2012))

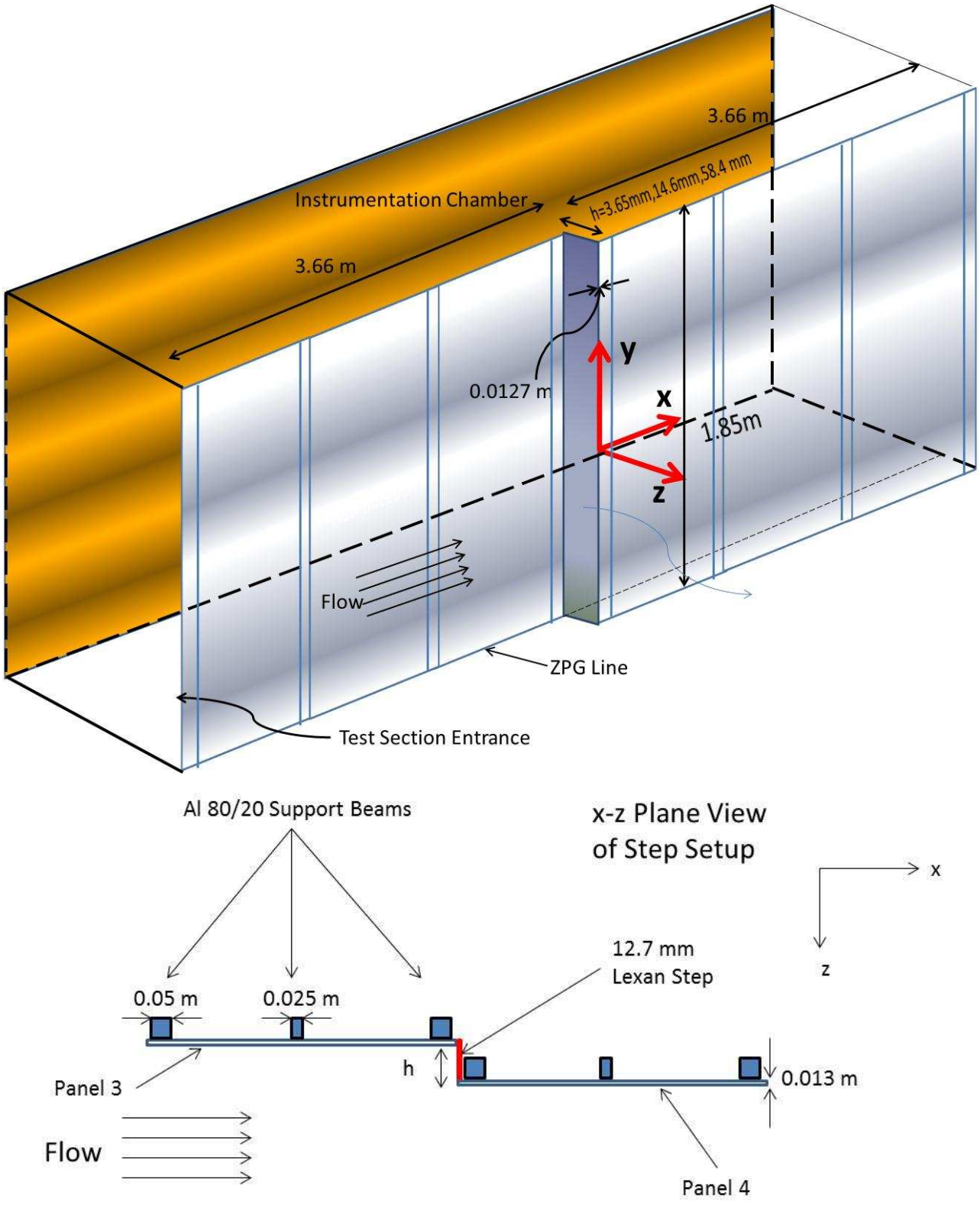

Figure 8. Movement of panels and forward step setup

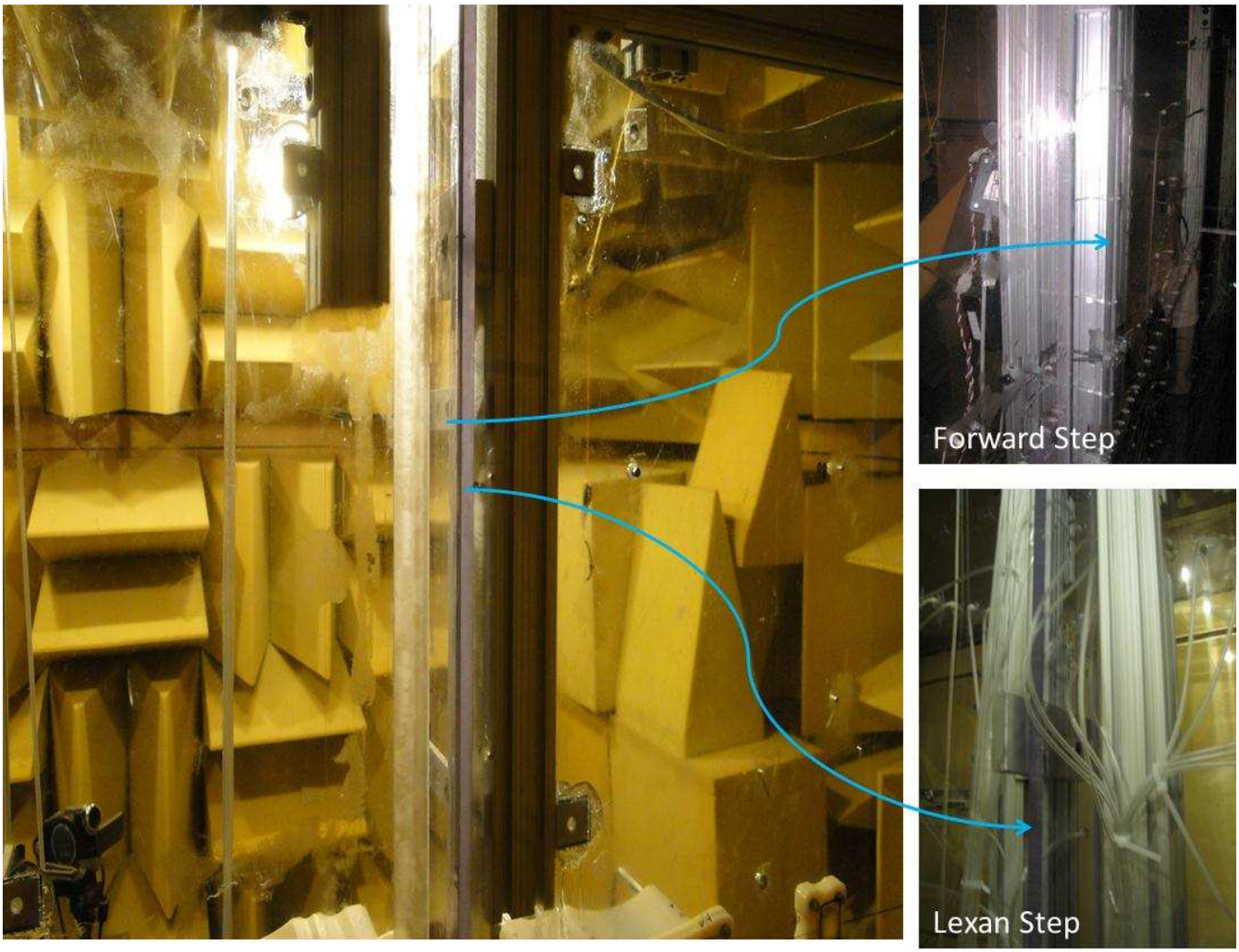

Figure 9. Forward step in position inside test section

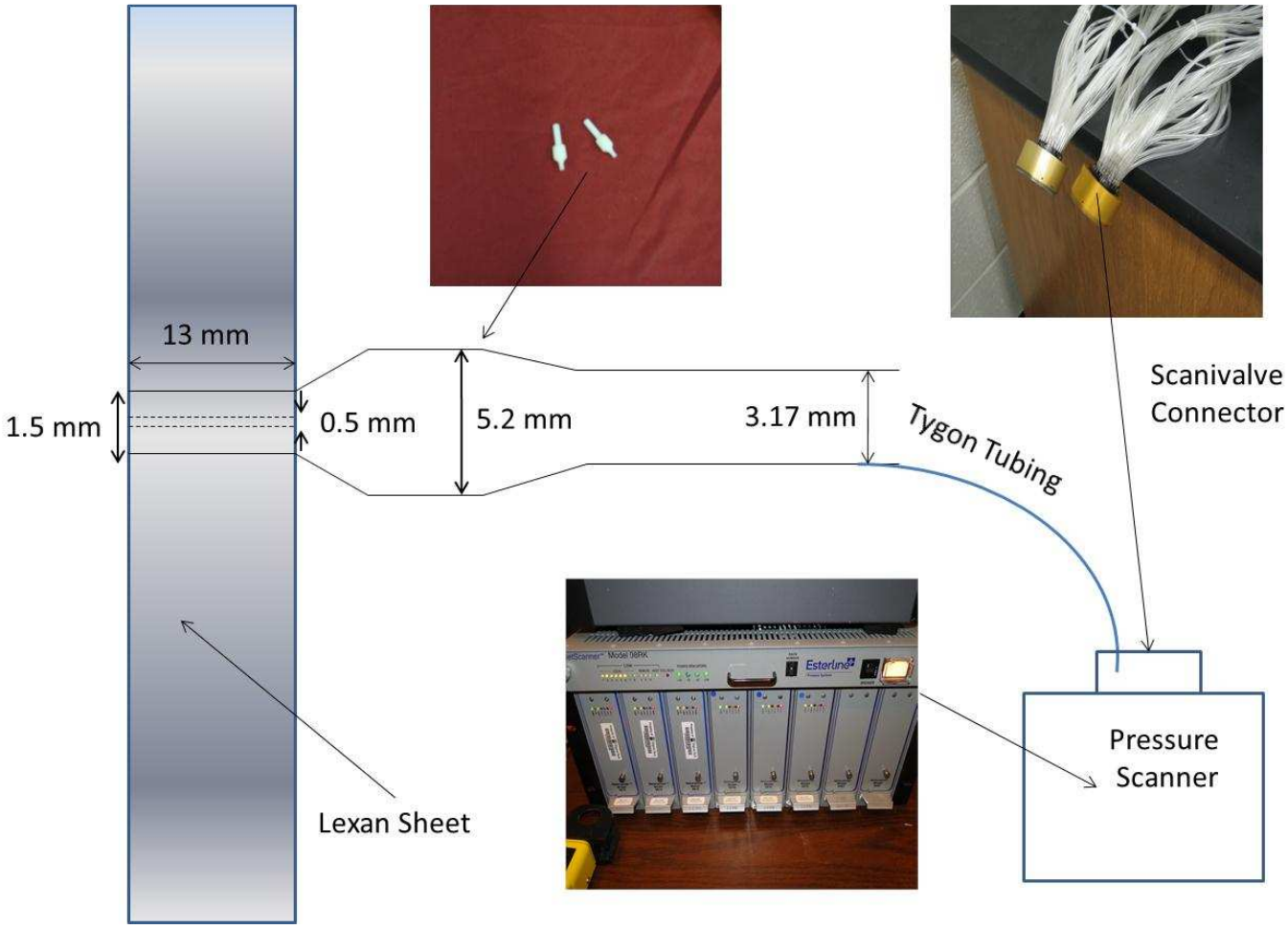

Figure 10. Mean Wall Pressure Measurement System Layout

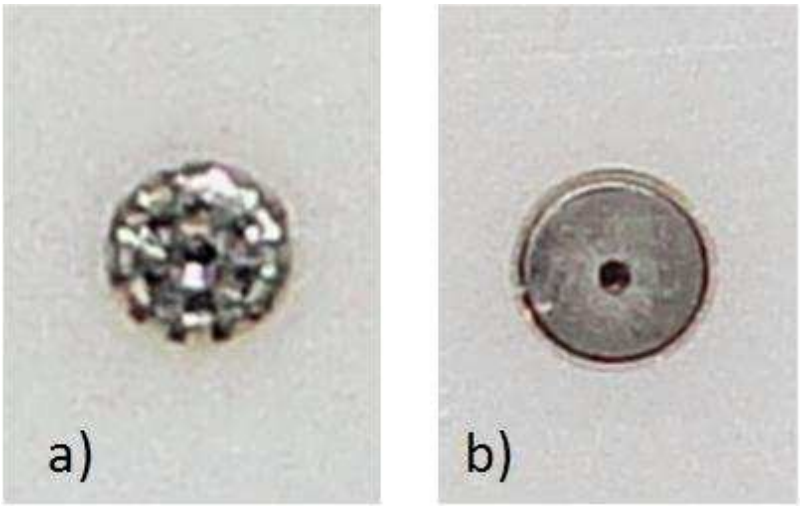

Figure 11. a) Salt and pepper shaker cap b) Custom manufactured ½ mm pinhole

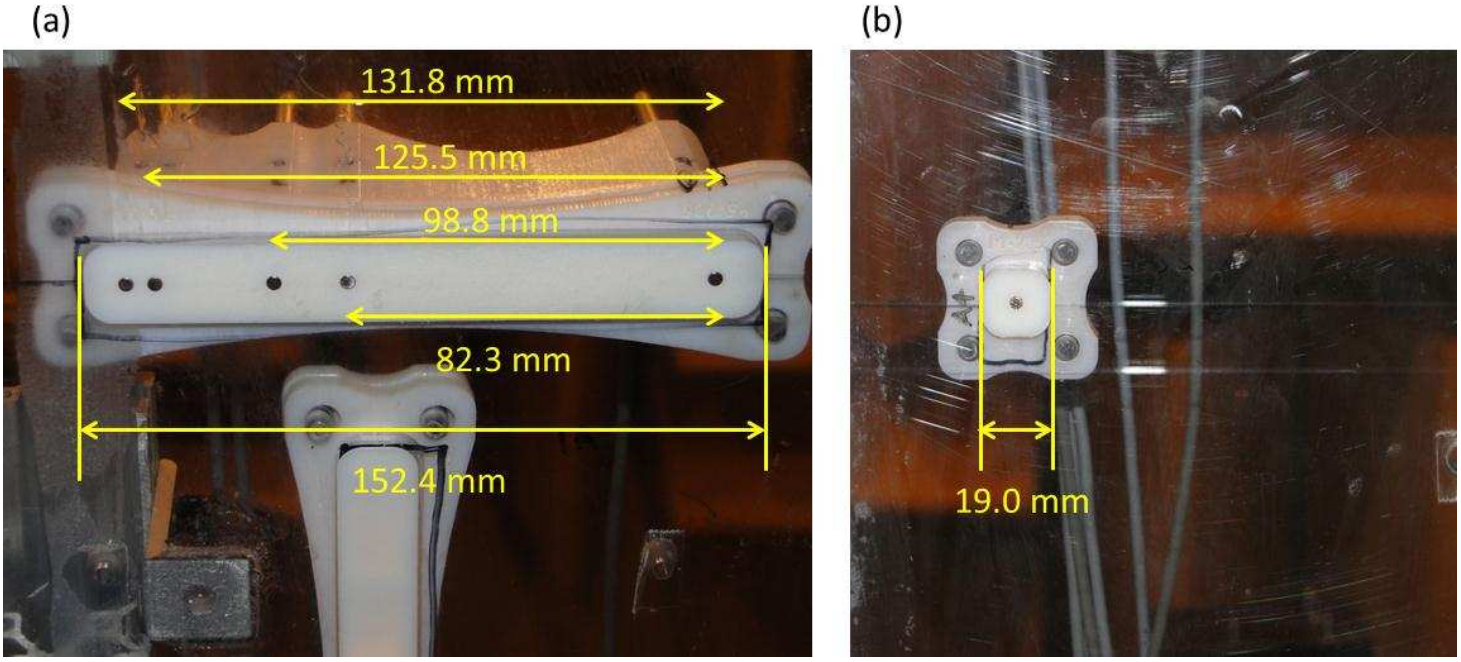

Figure 12. B&K Microphone Holders inserted into test wall. (a) 5 Microphone holder (b) 1 Microphone holder

Figure 13. Rear view of the microphone holders

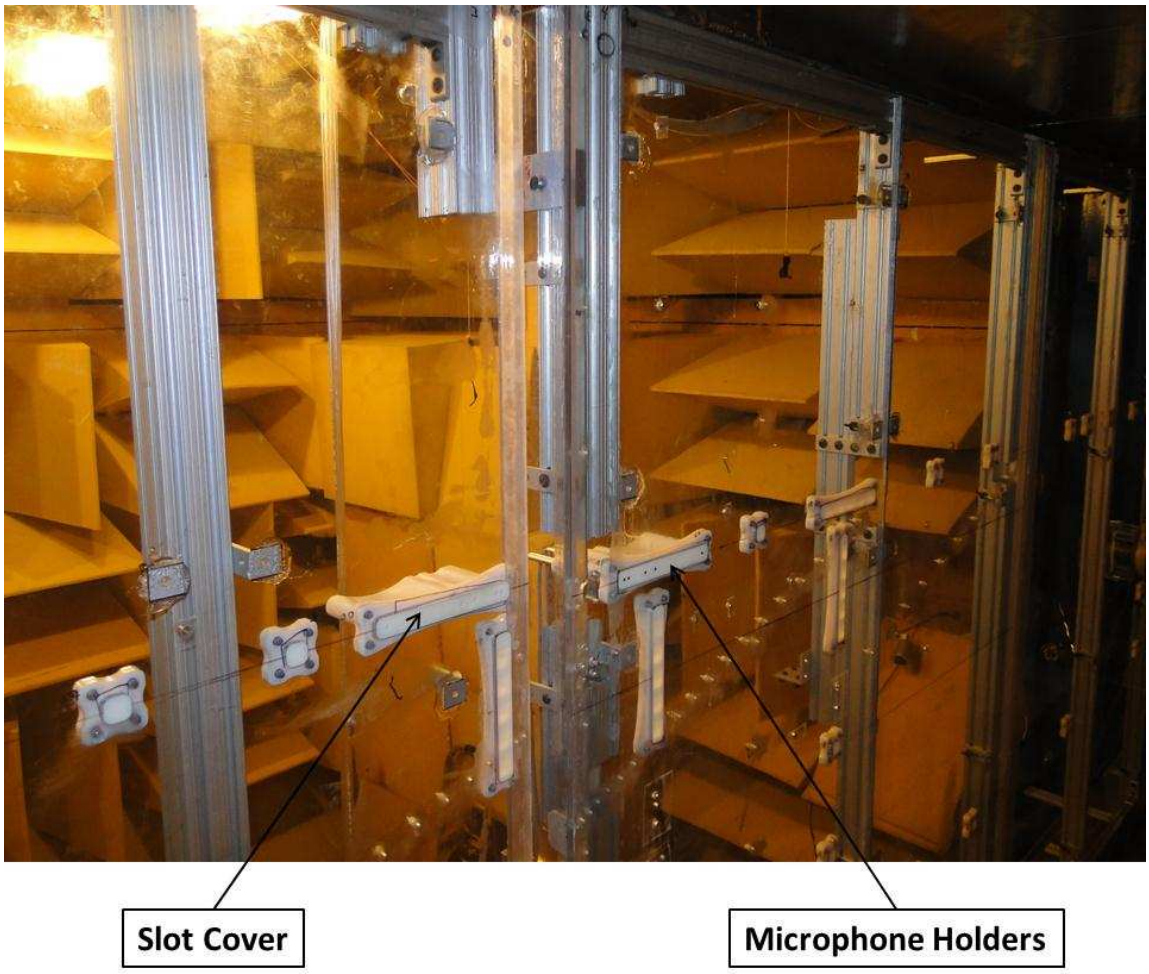

Figure 14. B&K Microphone holders and slot covers inserted into the test wall

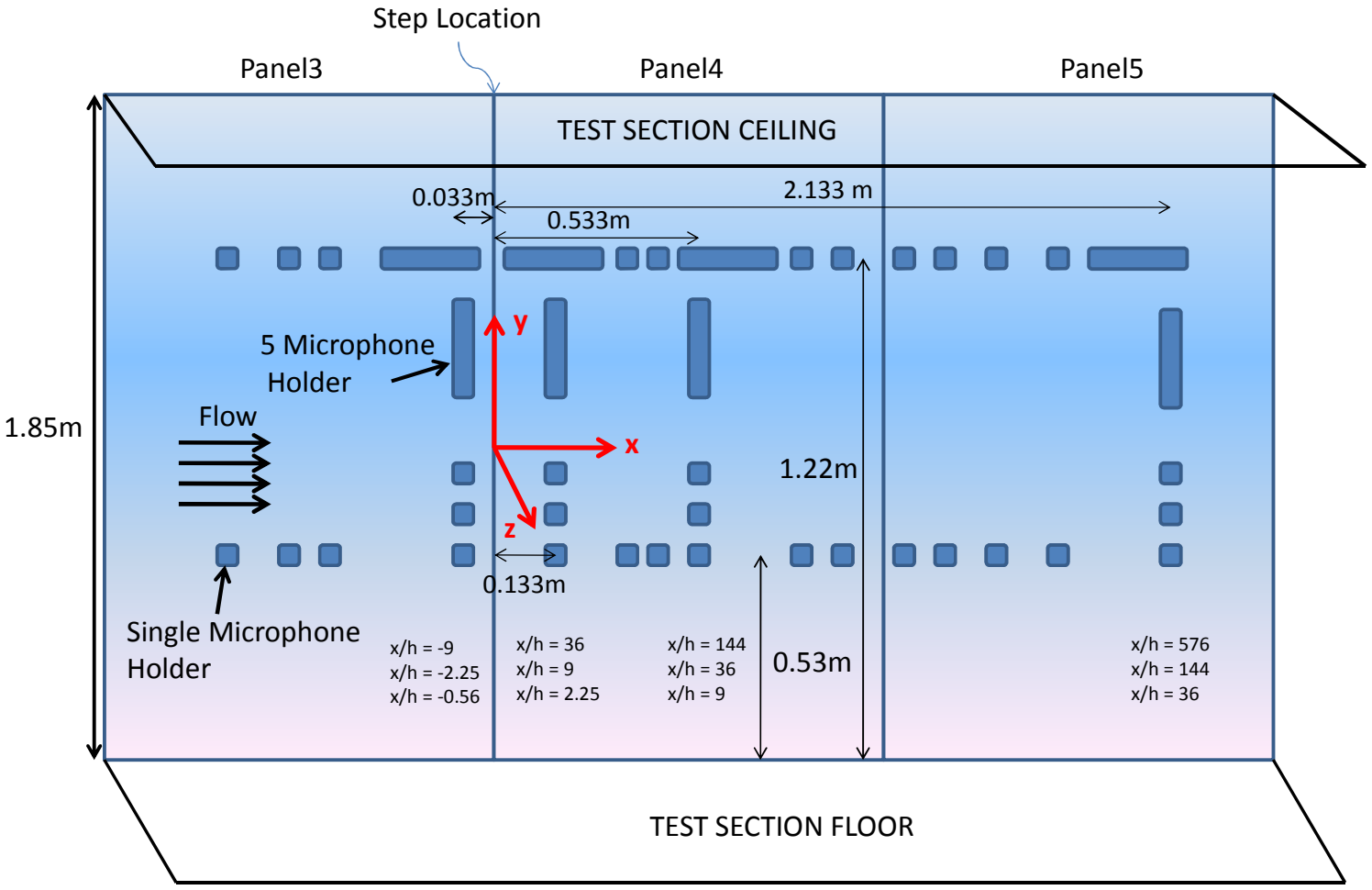

Figure 15. Wall pressure fluctuation measurement locations along the test wall

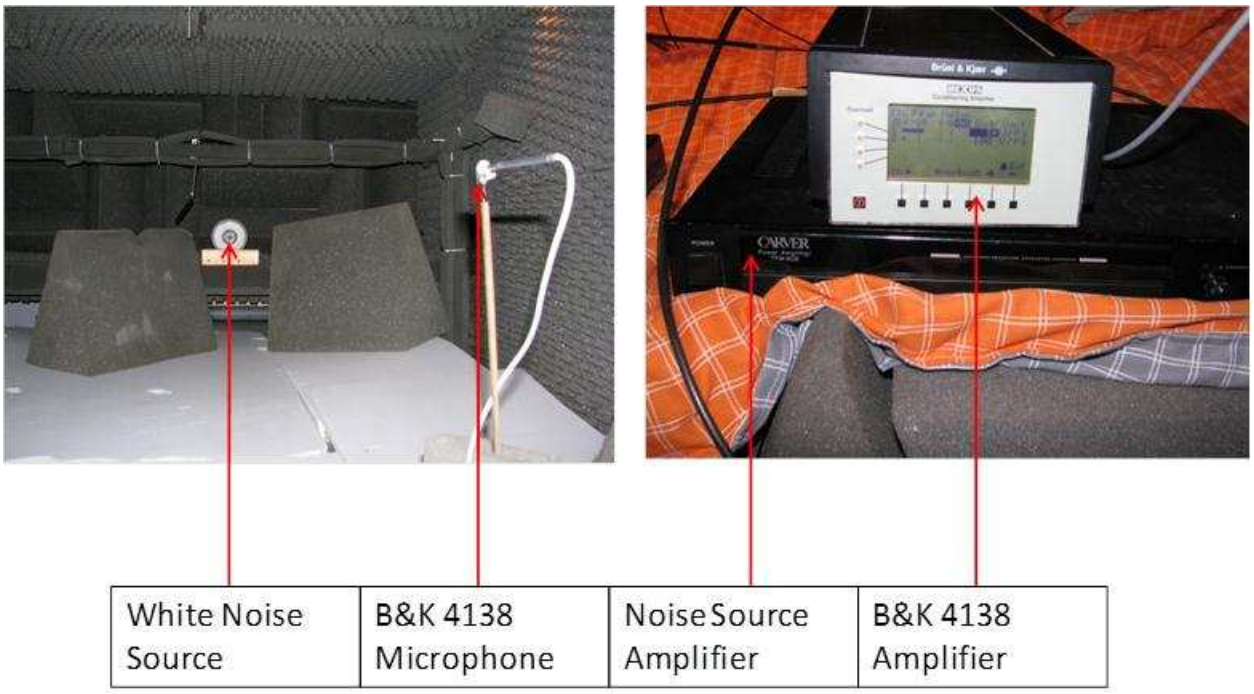

Figure 16. B&K Microphone calibration setup inside acoustic chamber (Used with permission of Jonathan B. Forest (2012))

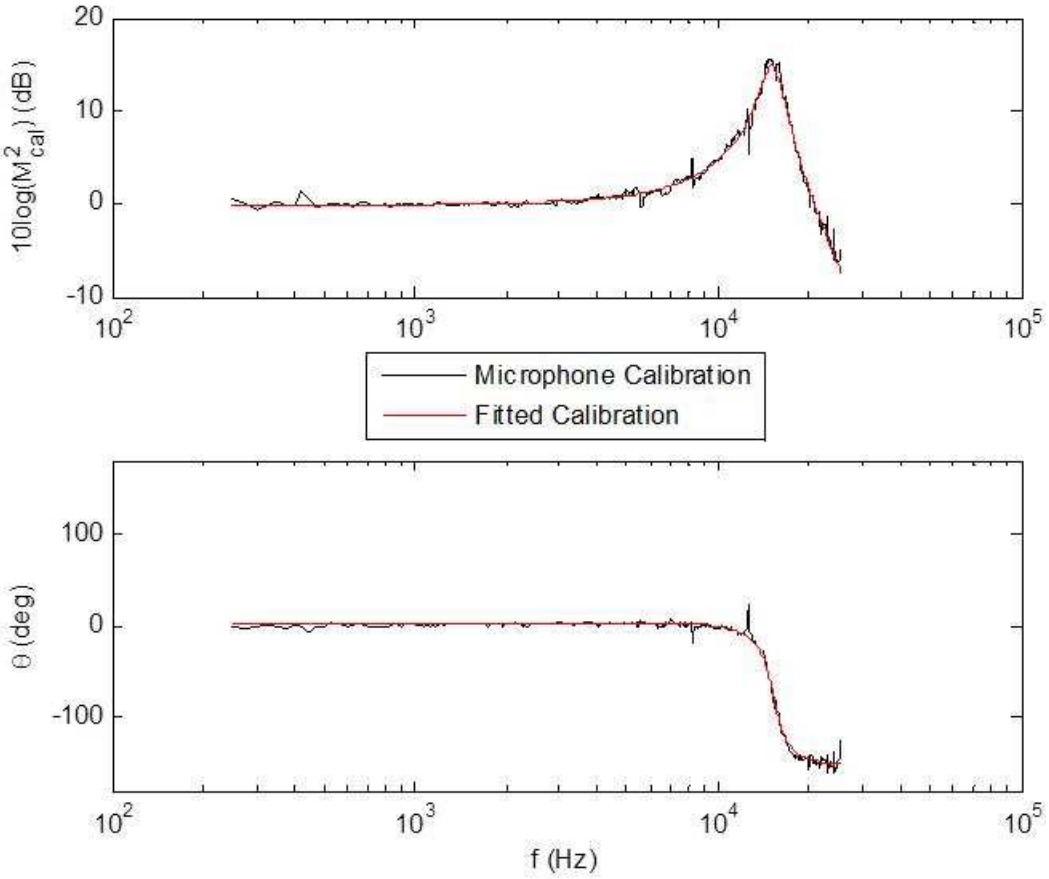

Figure 17. B&K Microphone calibration magnitude and phase curves (Used with permission of Jonathan B. Forest (2012))

Figure 18. LAN XI data acquisition hardware

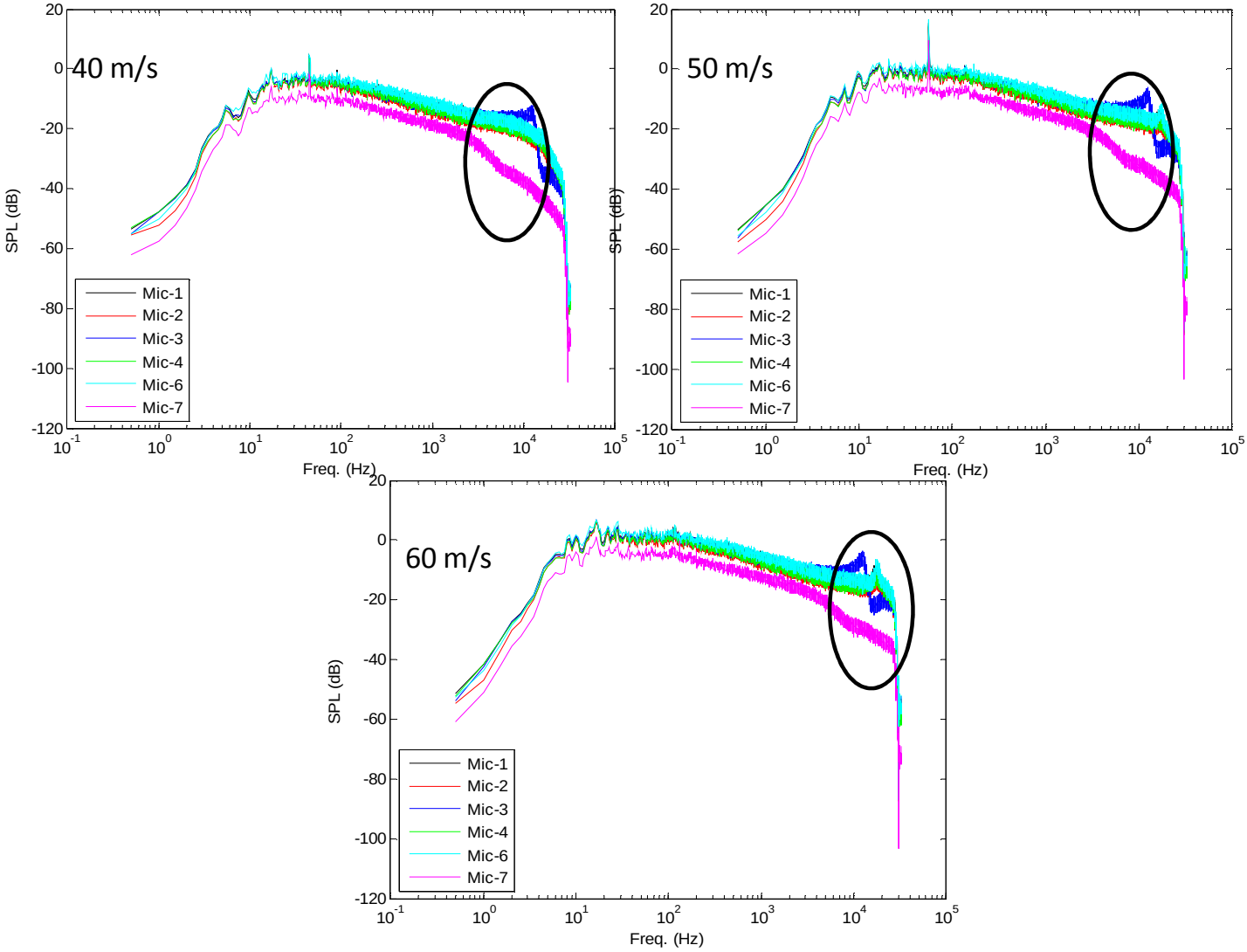

Figure 19. Residual effects of microphone resonant peak on measured spectra

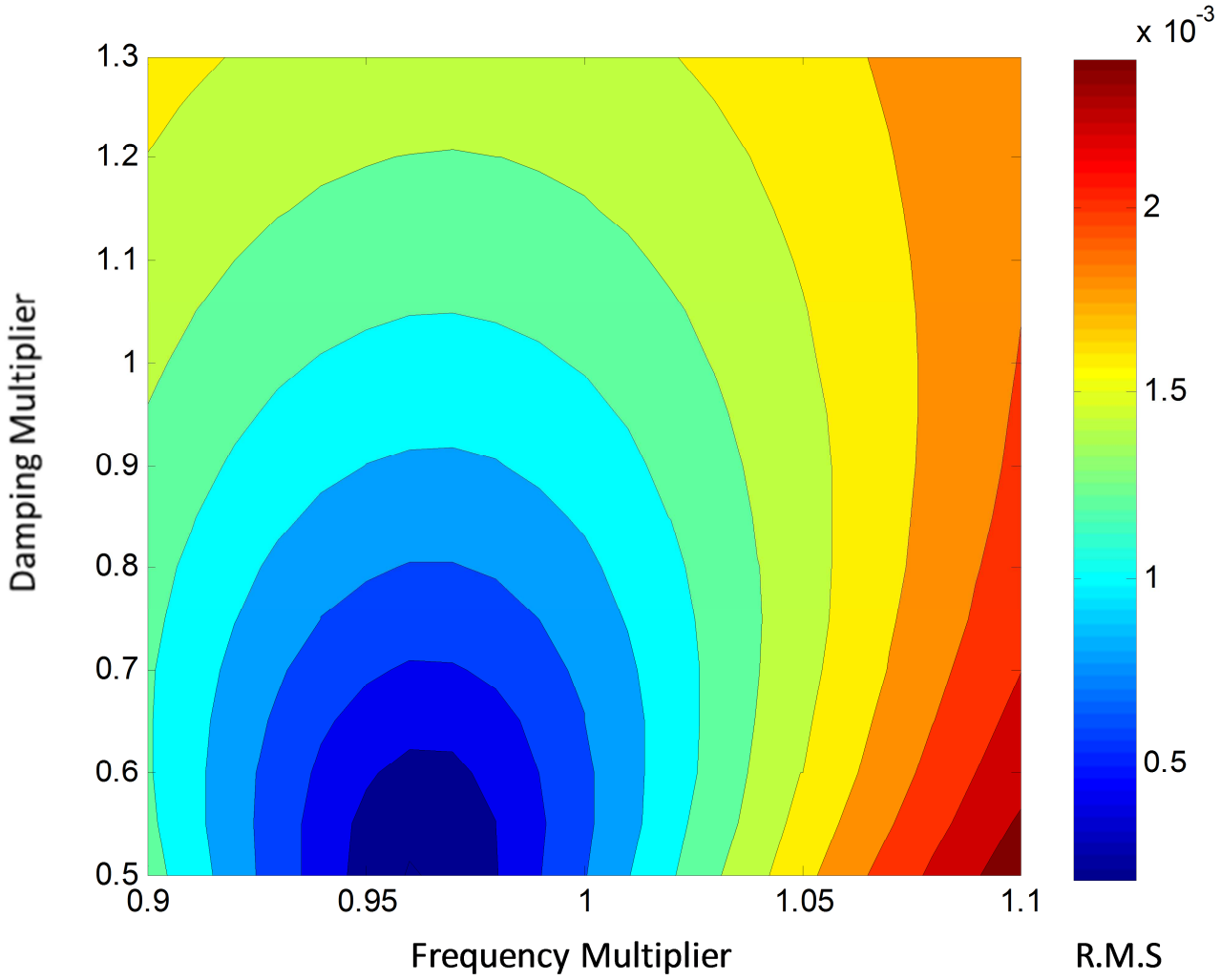

Figure 20. R.M.S level of derivative of calibrated spectra used for optimization

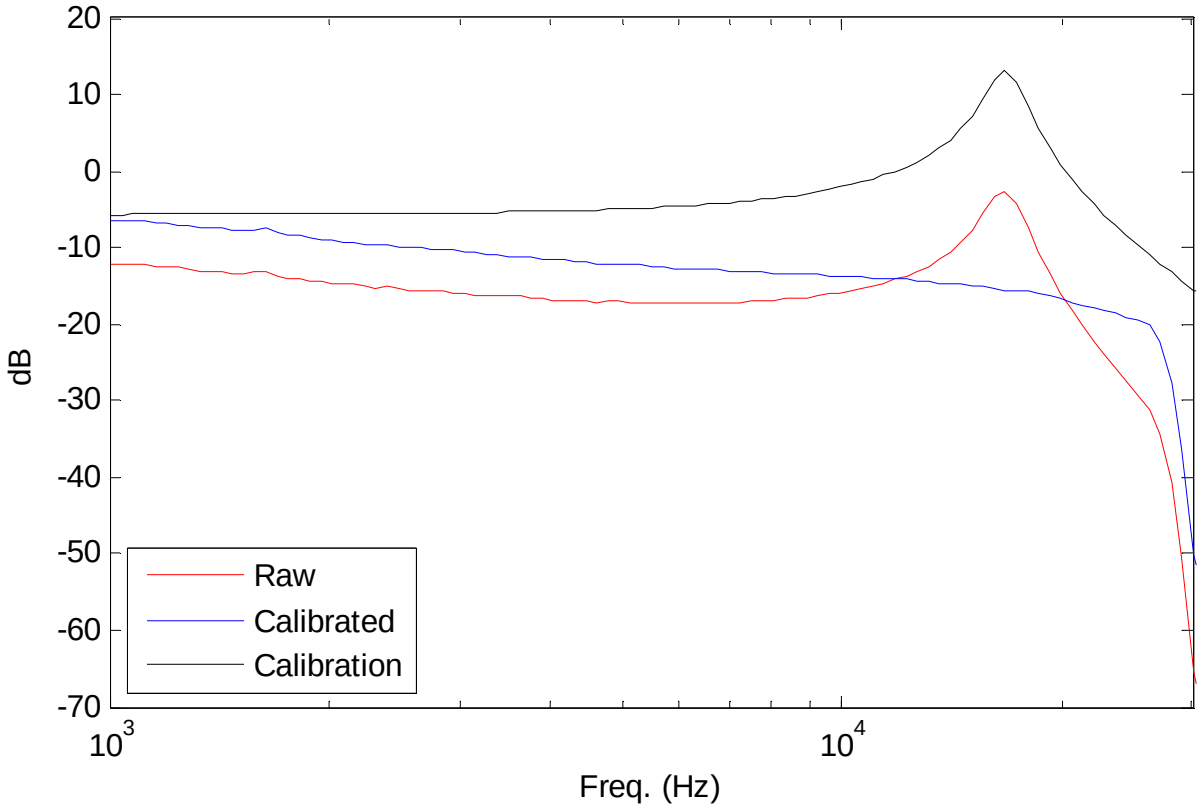

Figure 21. Calibrated microphone-pinhole system spectrum. (Also shown are the uncalibrated (raw) spectrum and the magnitude of calibration itself)

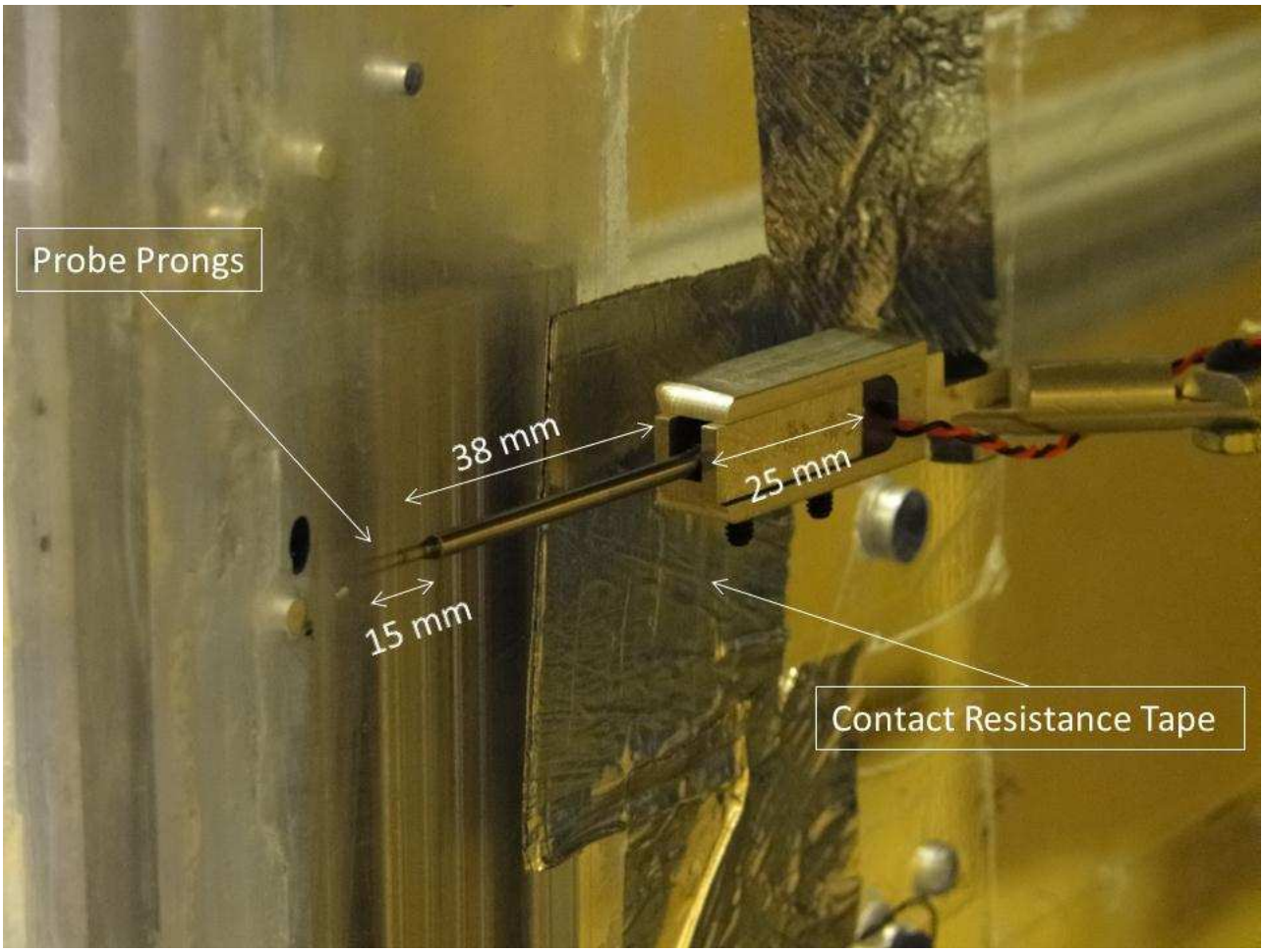

Figure 22. Single hotwire positioned against the wall using contact resistance method

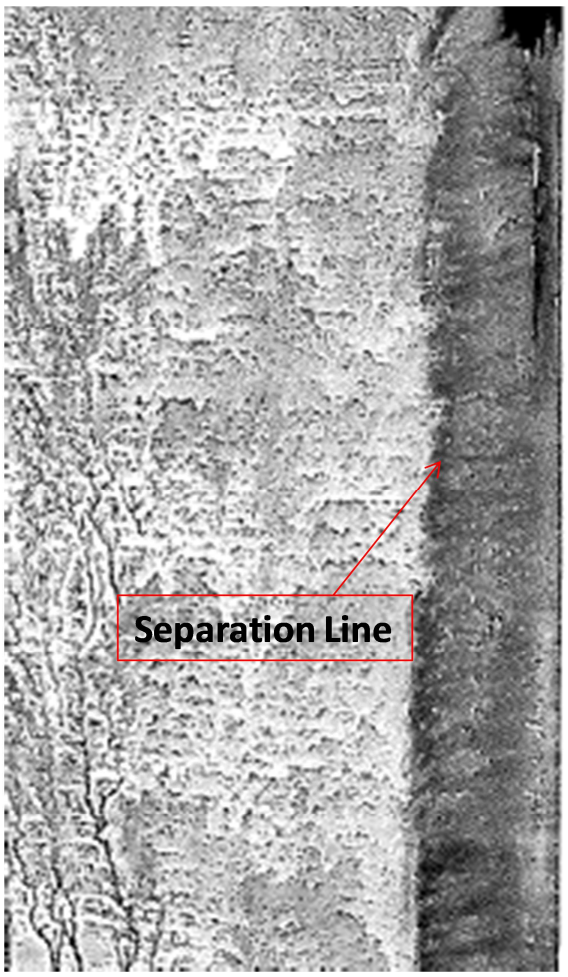

Figure 23. Upstream separation oil flow visualization for largest step size

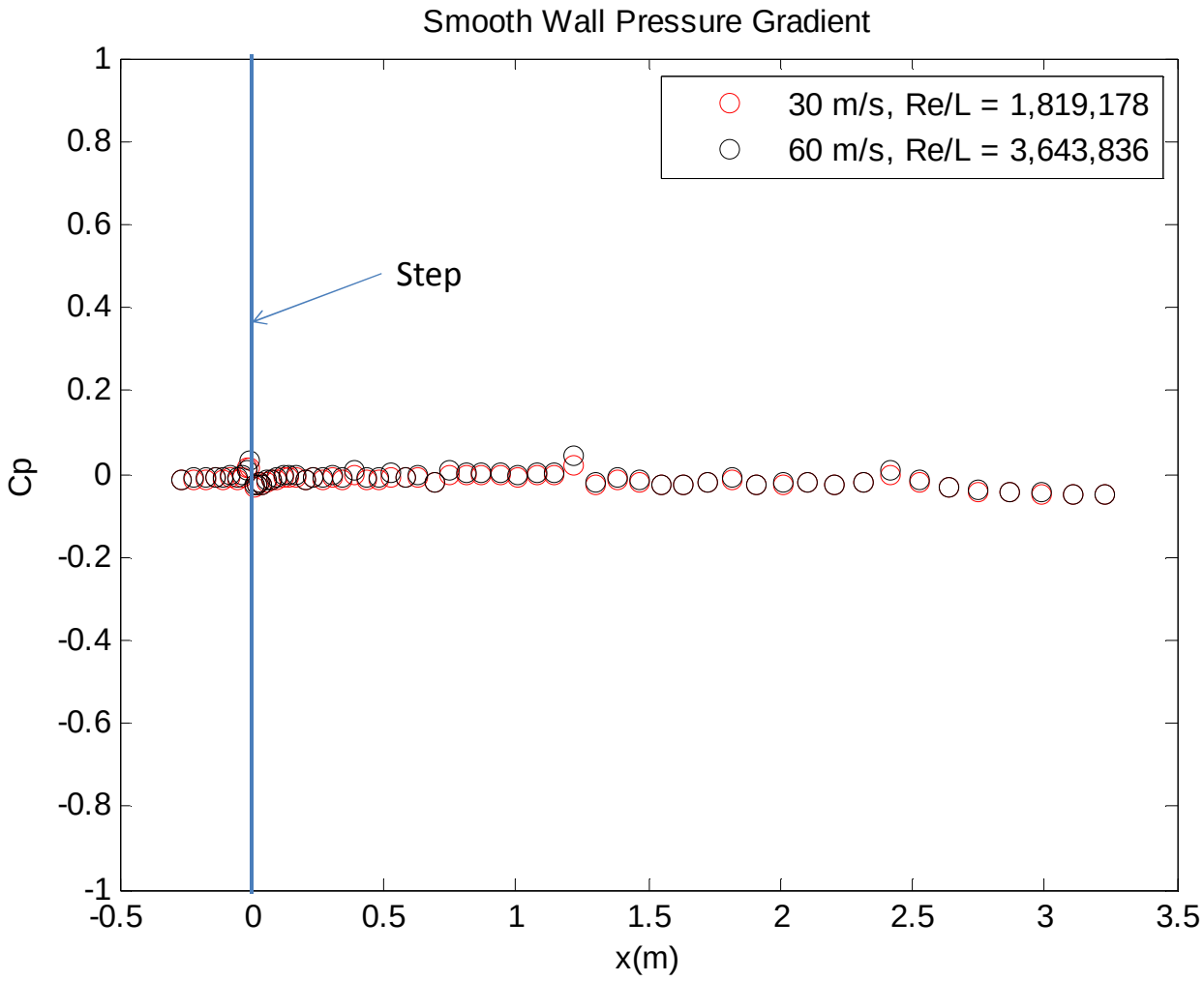

Figure 24. Streamwise mean wall pressure gradient for smooth wall

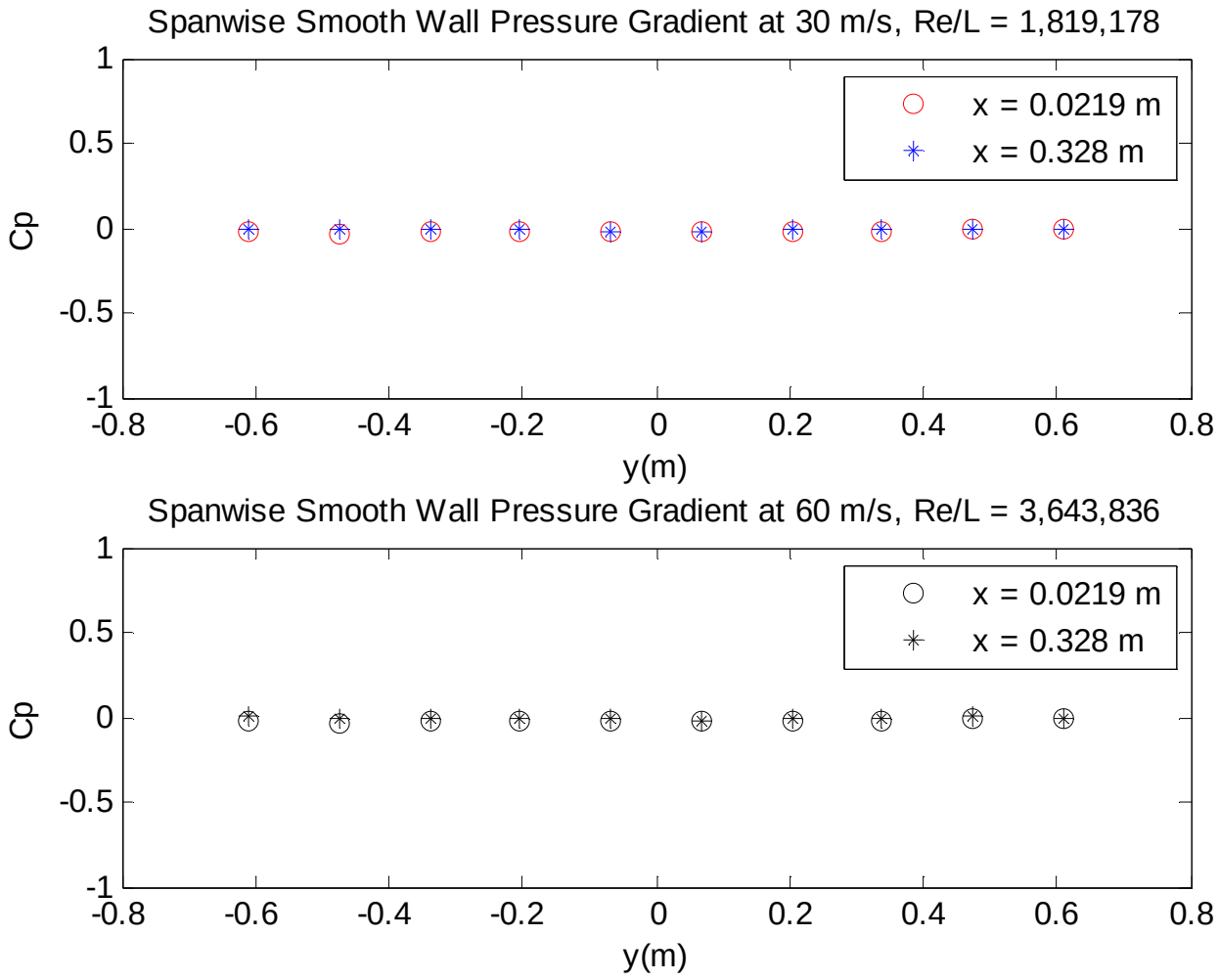

Figure 25. Spanwise mean wall pressure gradient for smooth wall

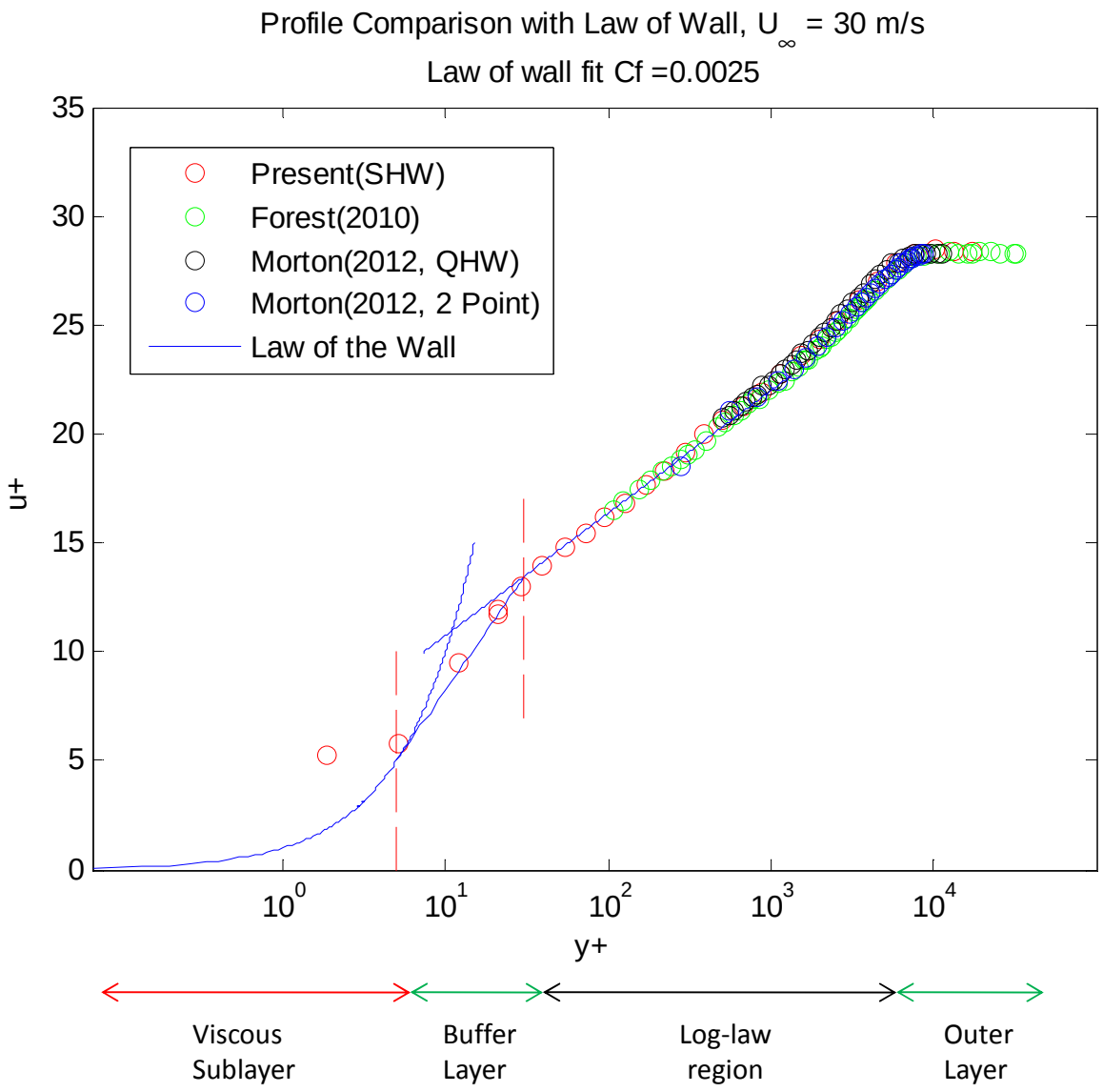

Figure 26. BL profile comparisons with law of the wall at 30 m/s

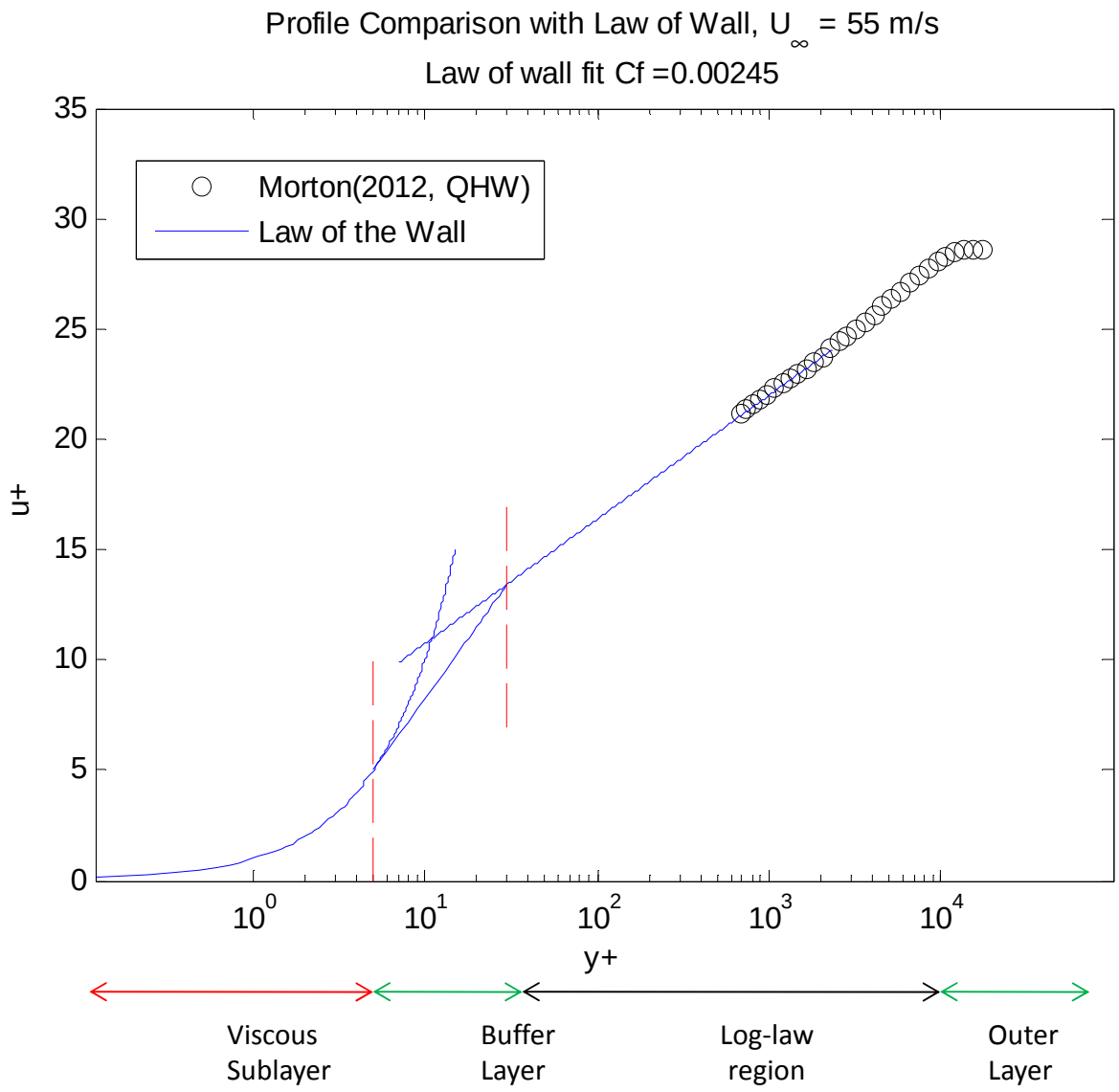

Figure 27. BL comparison with law of the wall at 55 m/s

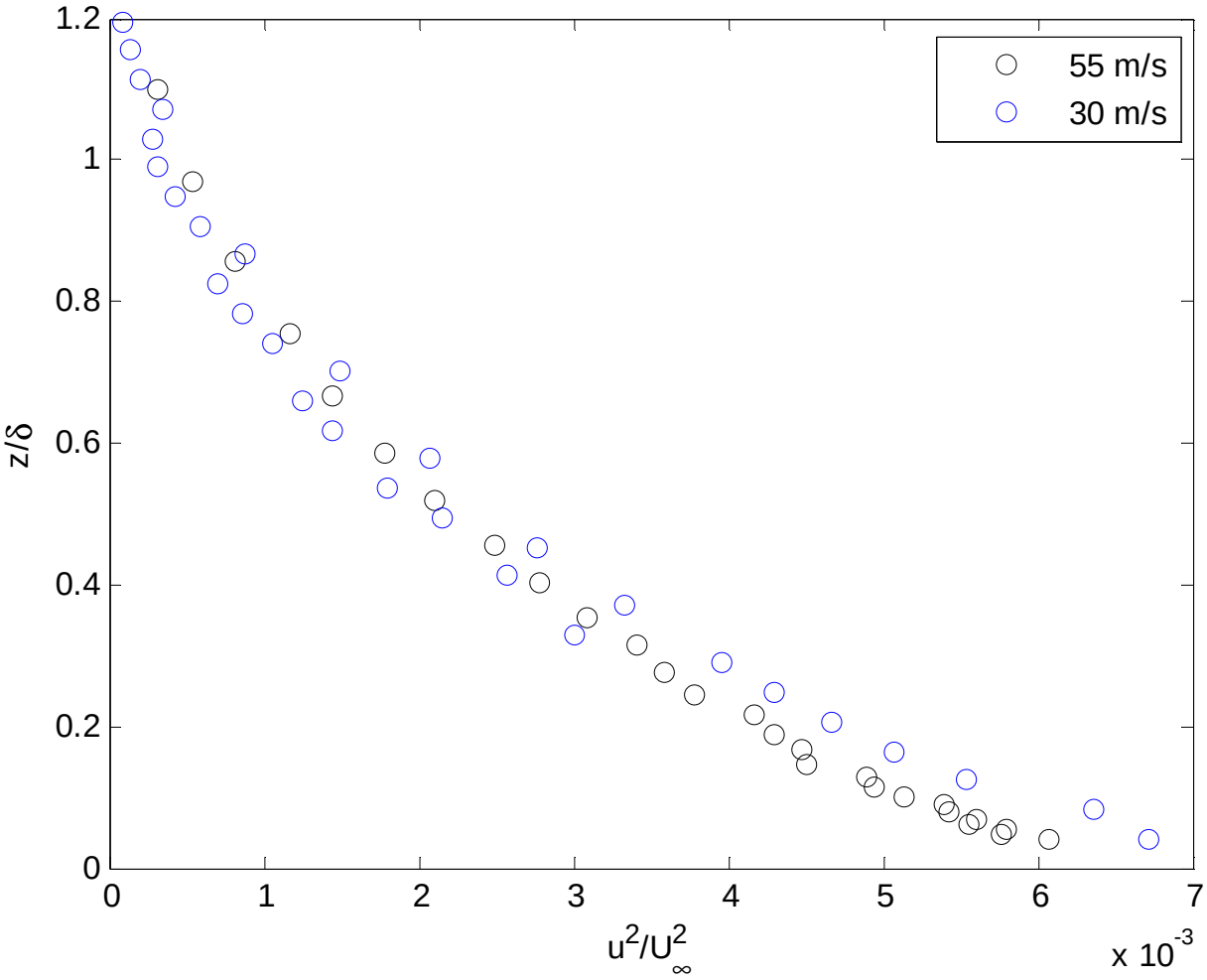

Figure 28. Streamwise turbulent intensity for smooth wall

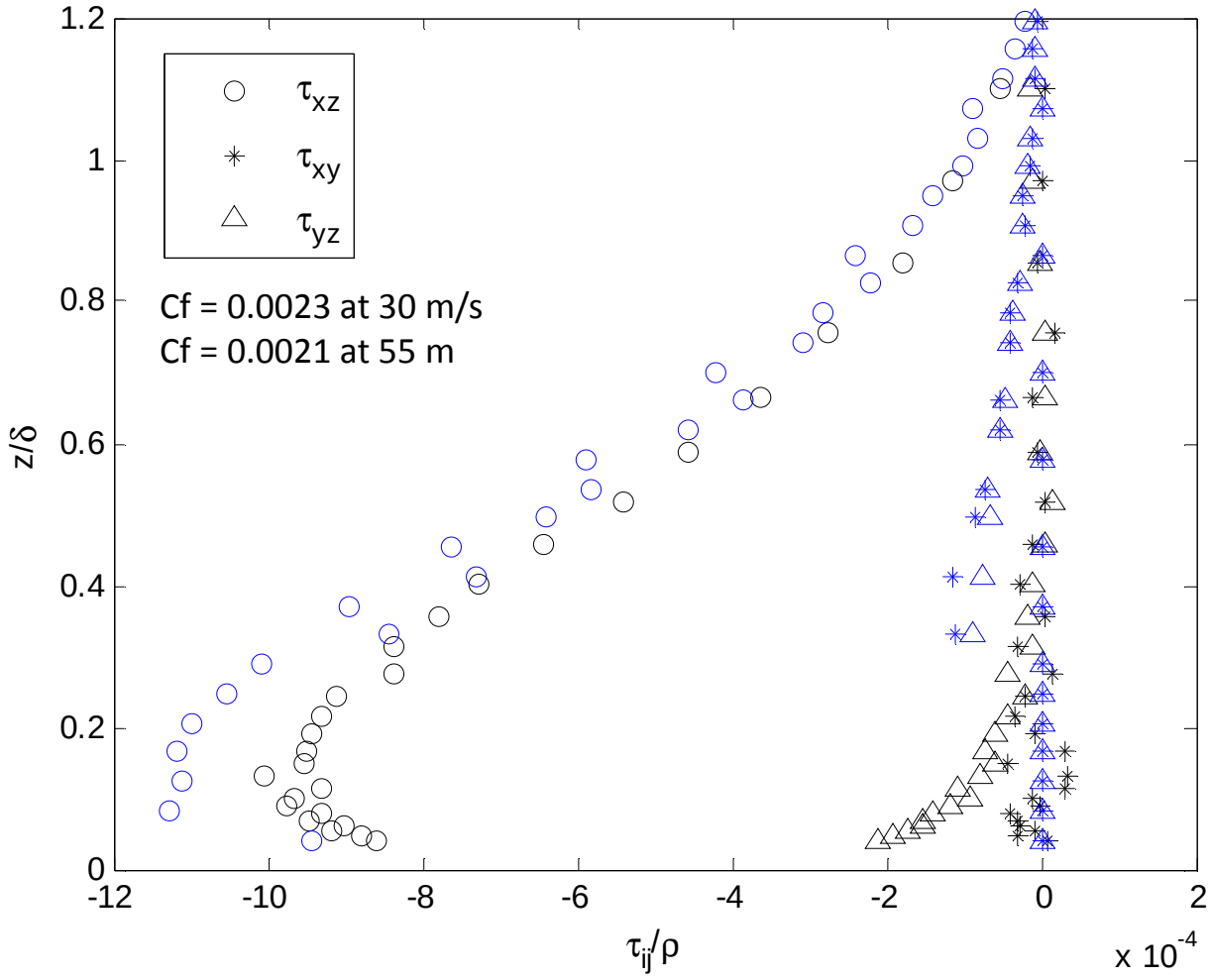

Figure 29. Reynolds shear stress for smooth wall, blue symbols represent 30m/s, black symbols represent 55 m/s

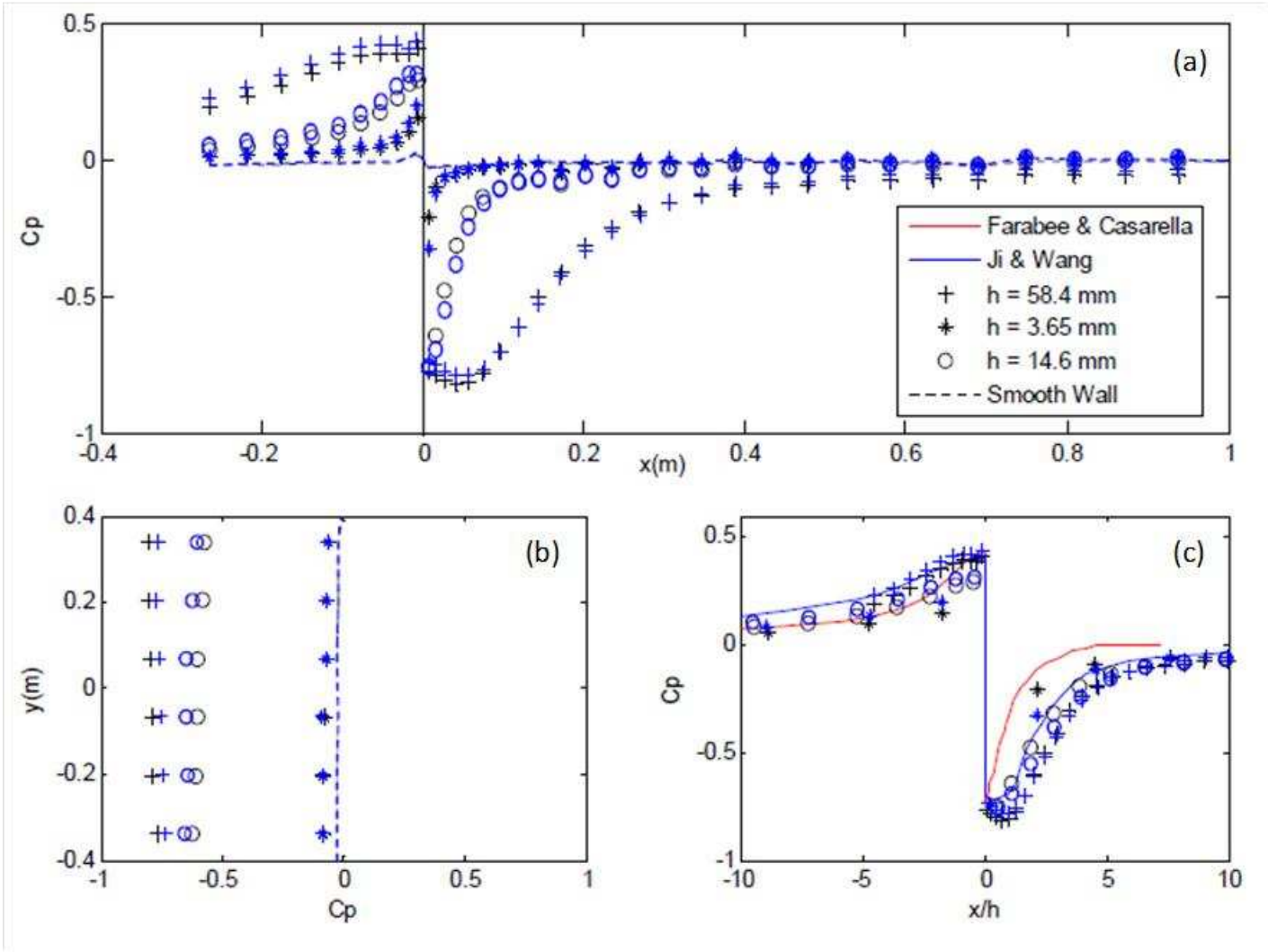

Figure 30. (a) Mean wall pressure comparisons for all steps and smooth wall at both 30 and 60 m/s. (b) Spanwise mean pressure for the steps and smooth wall. (c) Mean wall pressure for all steps with Farabee and Casarella and Ji and Wang's results. Black Symbols represent 30 m/s and Blue symbols represent 60 m/s.

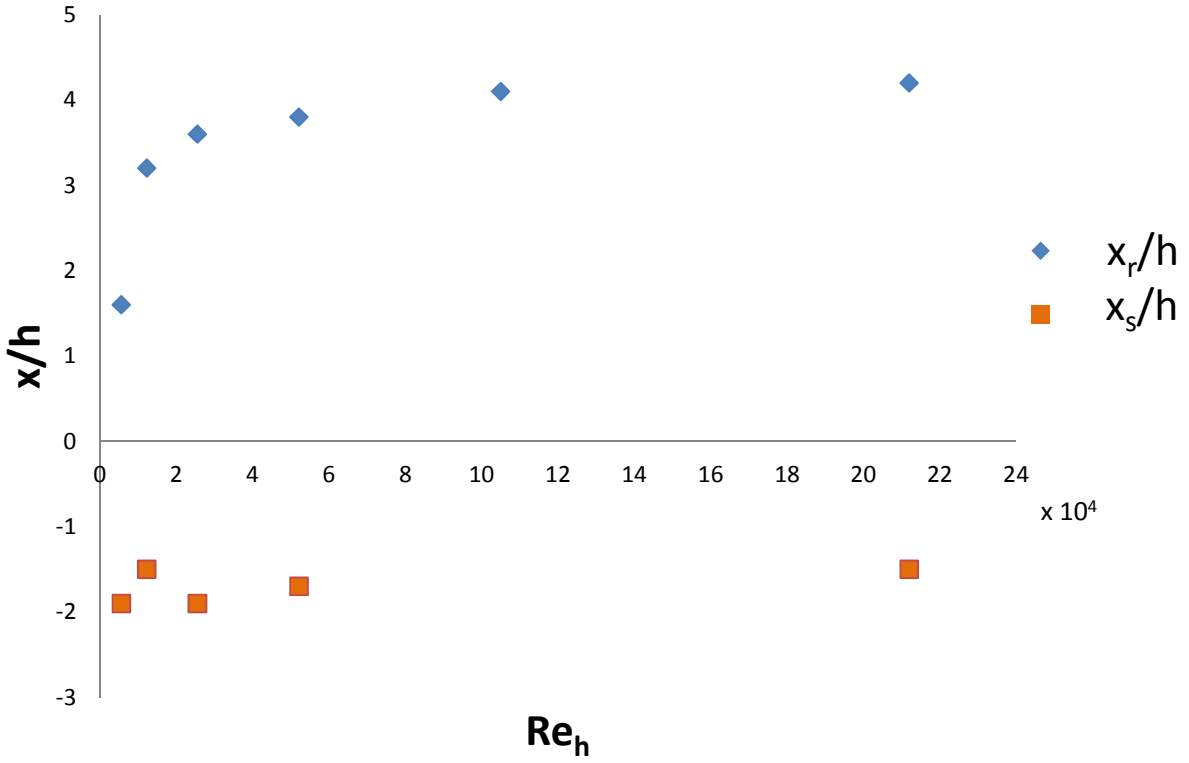

Figure 31. Reattachment and separation lengths as a function of step Reynolds number

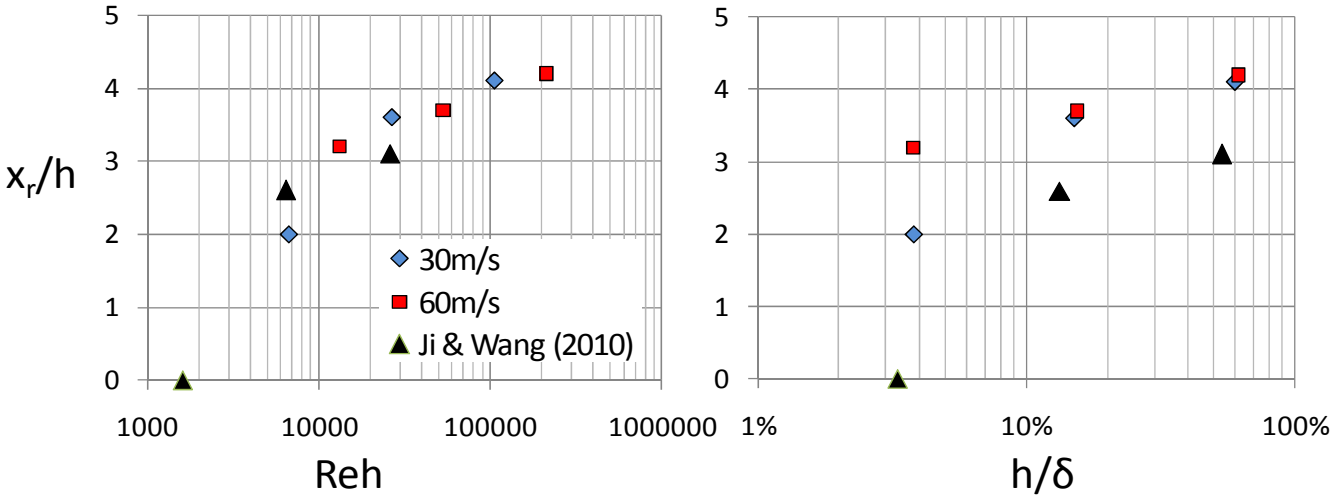

Figure 32. Reattachment lengths as a function of Reynolds number and step height

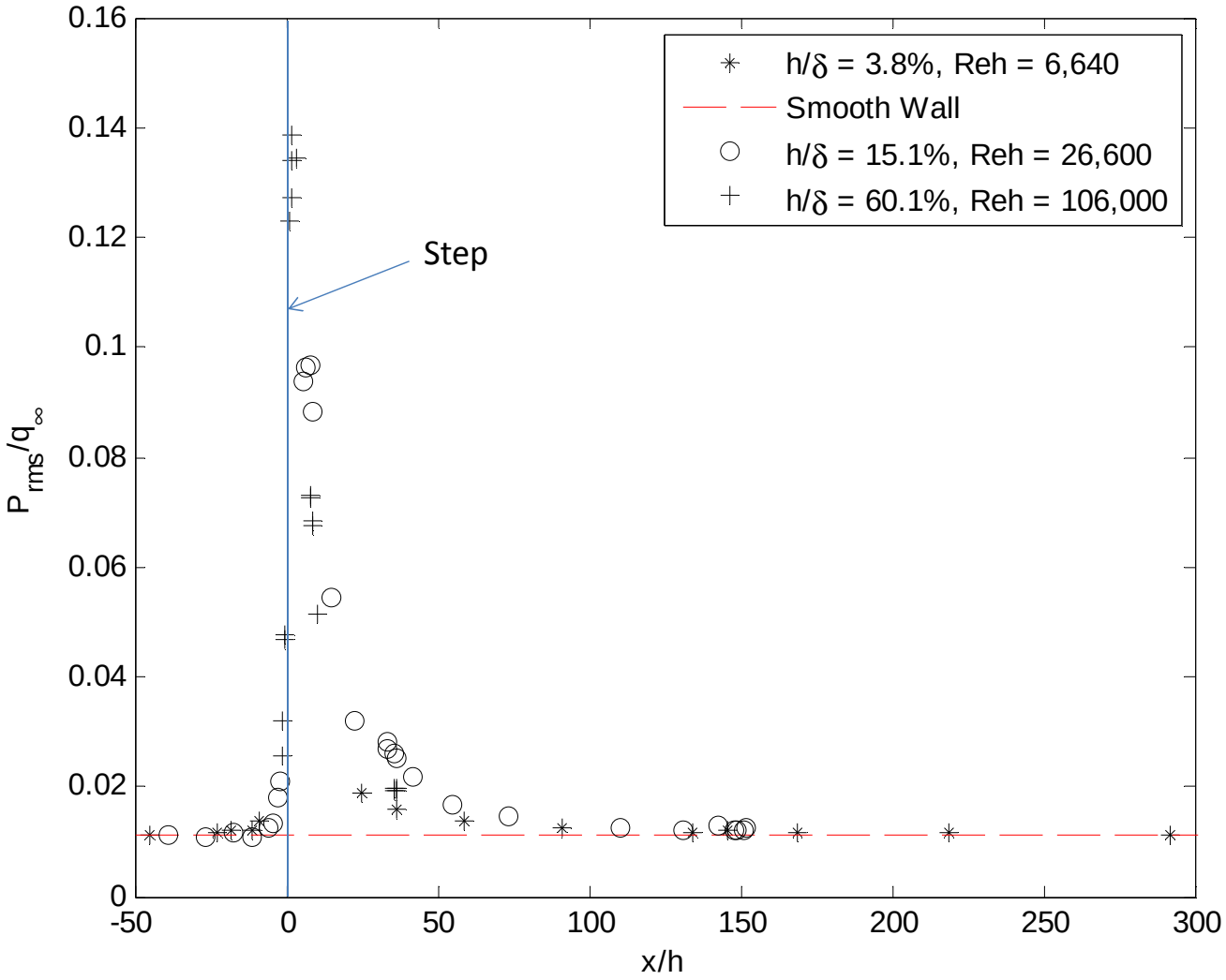

Figure 33. Forward steps root mean square wall pressure fluctuation values at 30 m/s

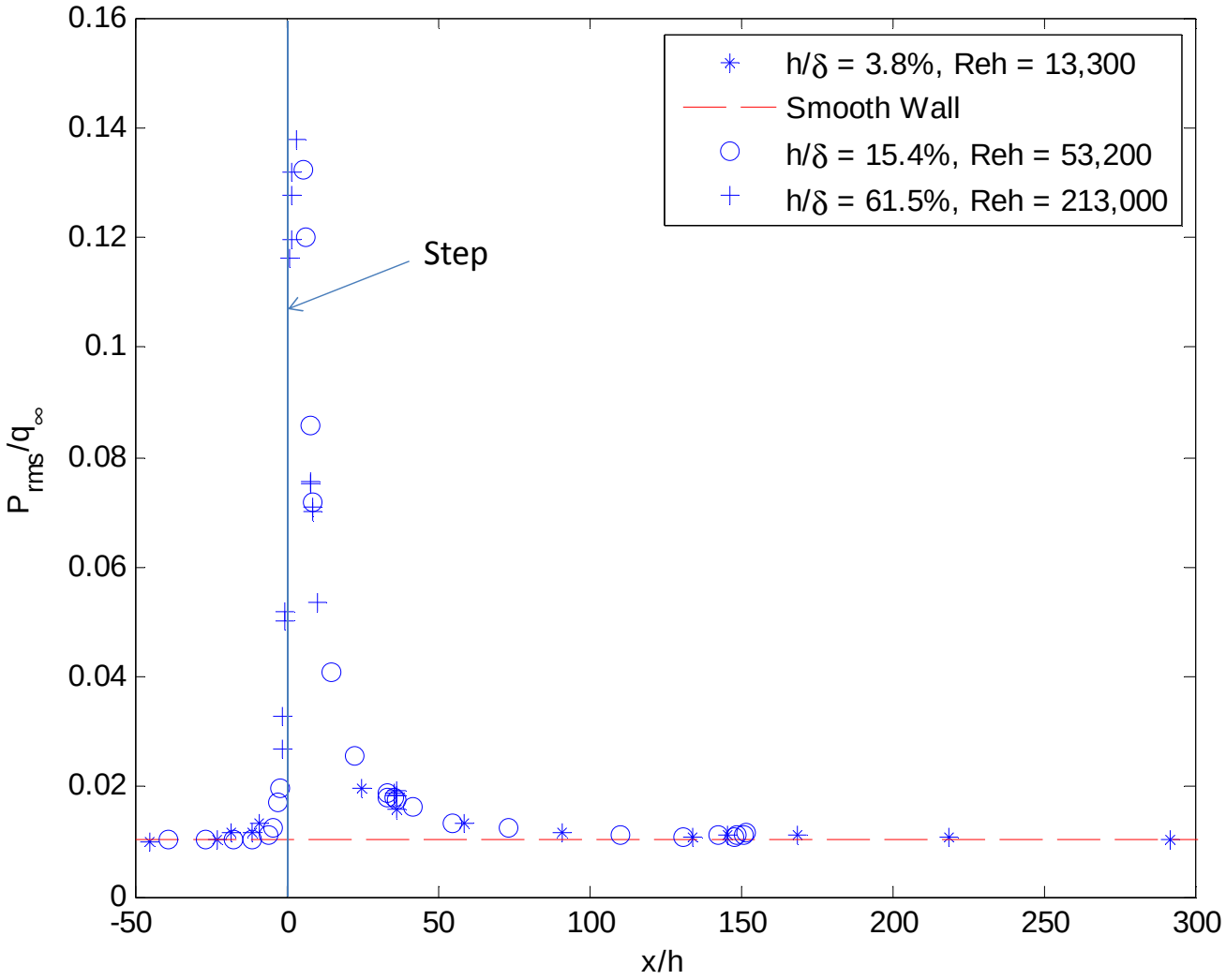

Figure 34. Forward steps root mean square wall pressure fluctuation values at 60 m/s

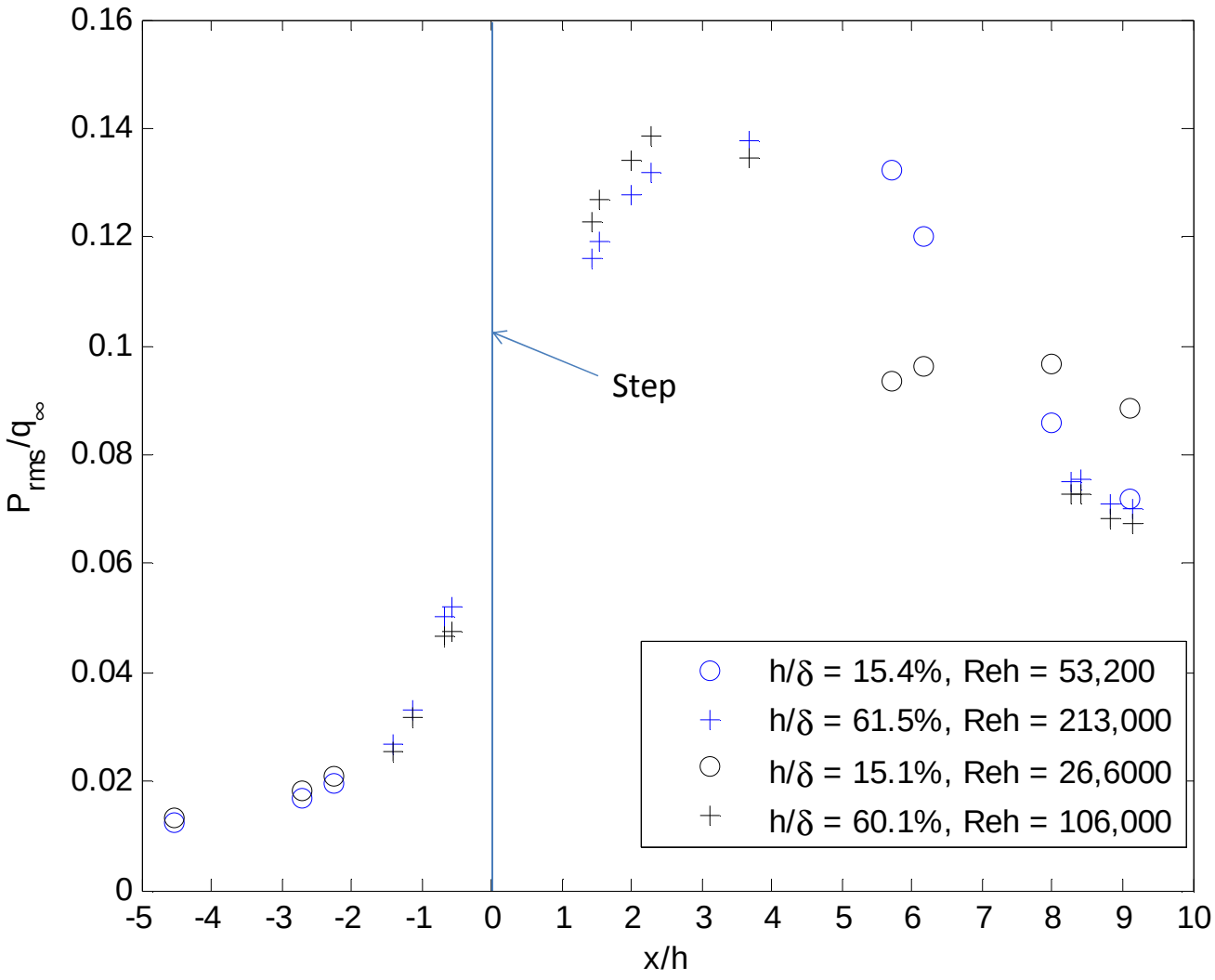

Figure 35. Root mean square values of pressure fluctuations for medium and large step near the step

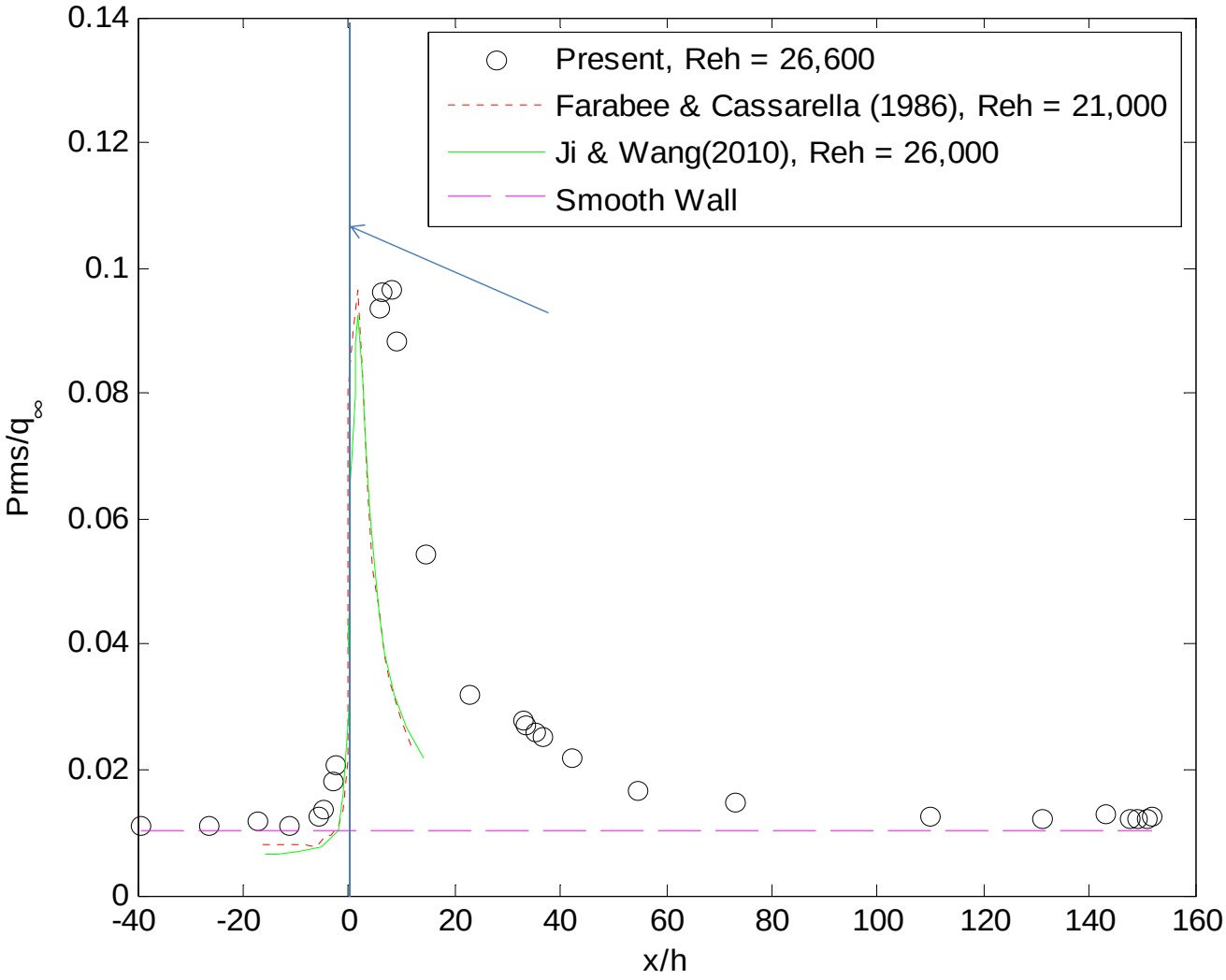

Figure 36. Root mean square pressure comparison with Farabee and Casarella, Ji and Wang

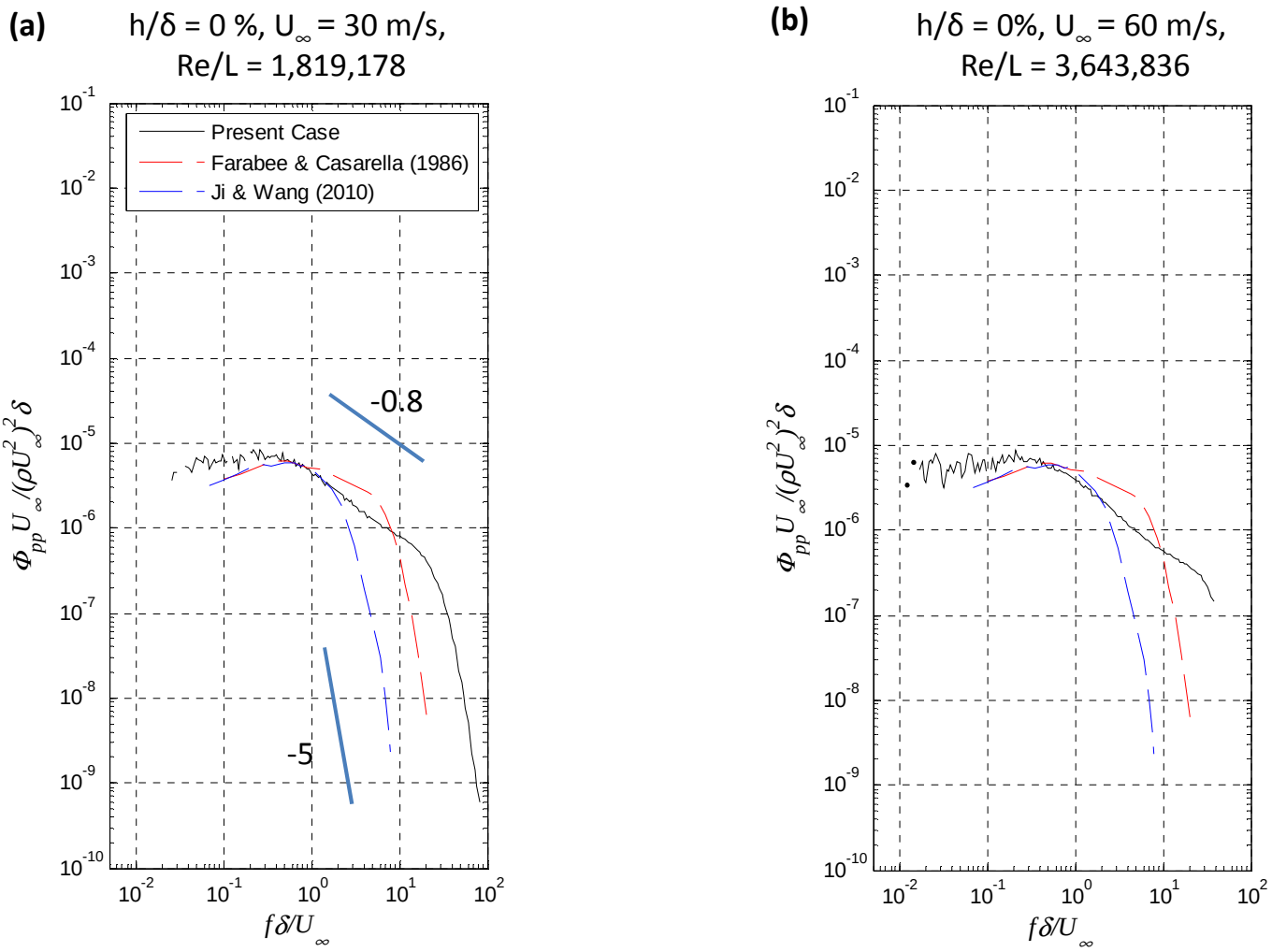

Figure 37. Smooth wall pressure spectra, (a) Low Reynolds Number, (b) High Reynolds Number

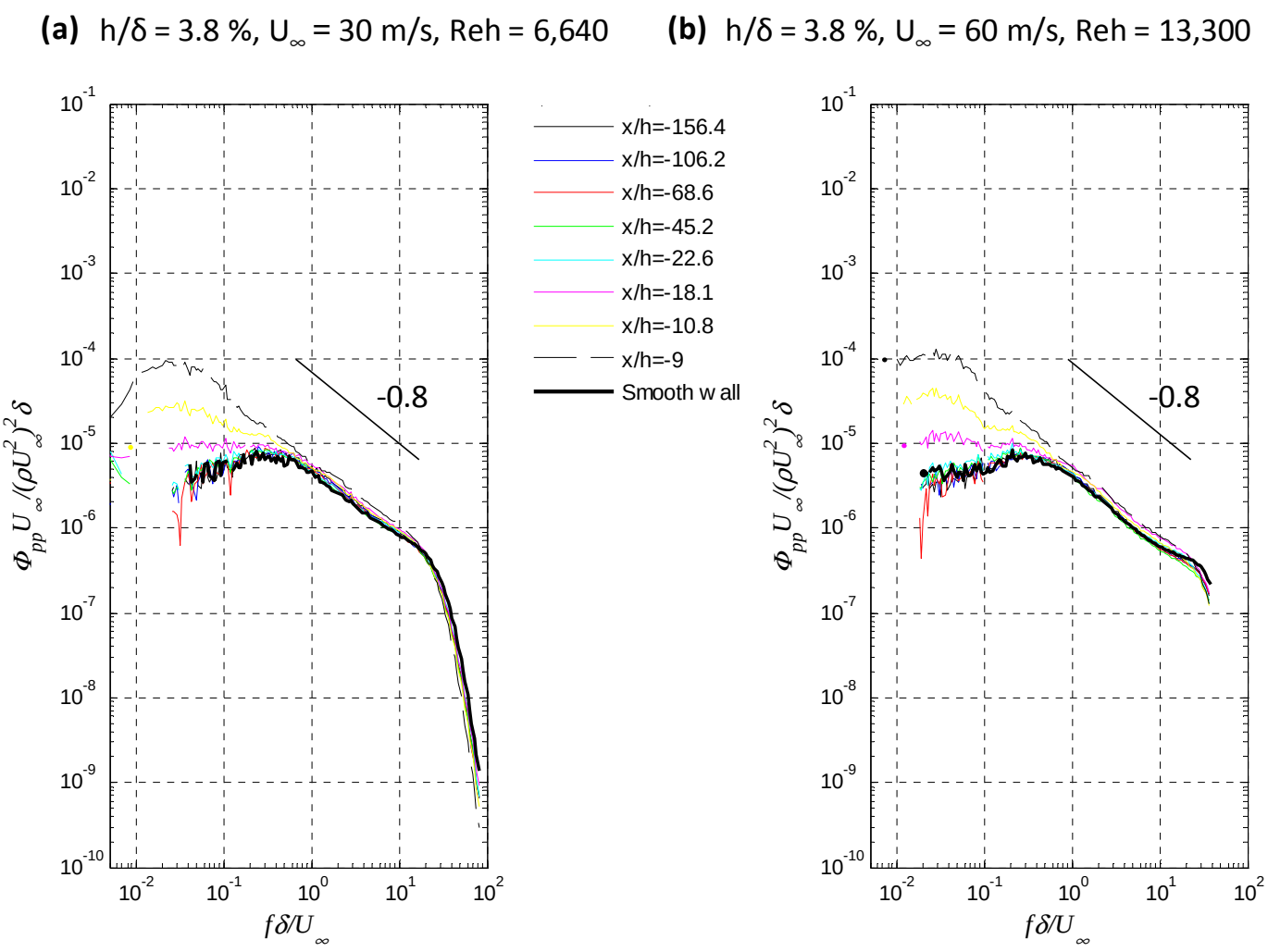

Figure 38. Upstream pressure spectra for small step (a) Low Reynolds Number, (b) High Reynolds Number

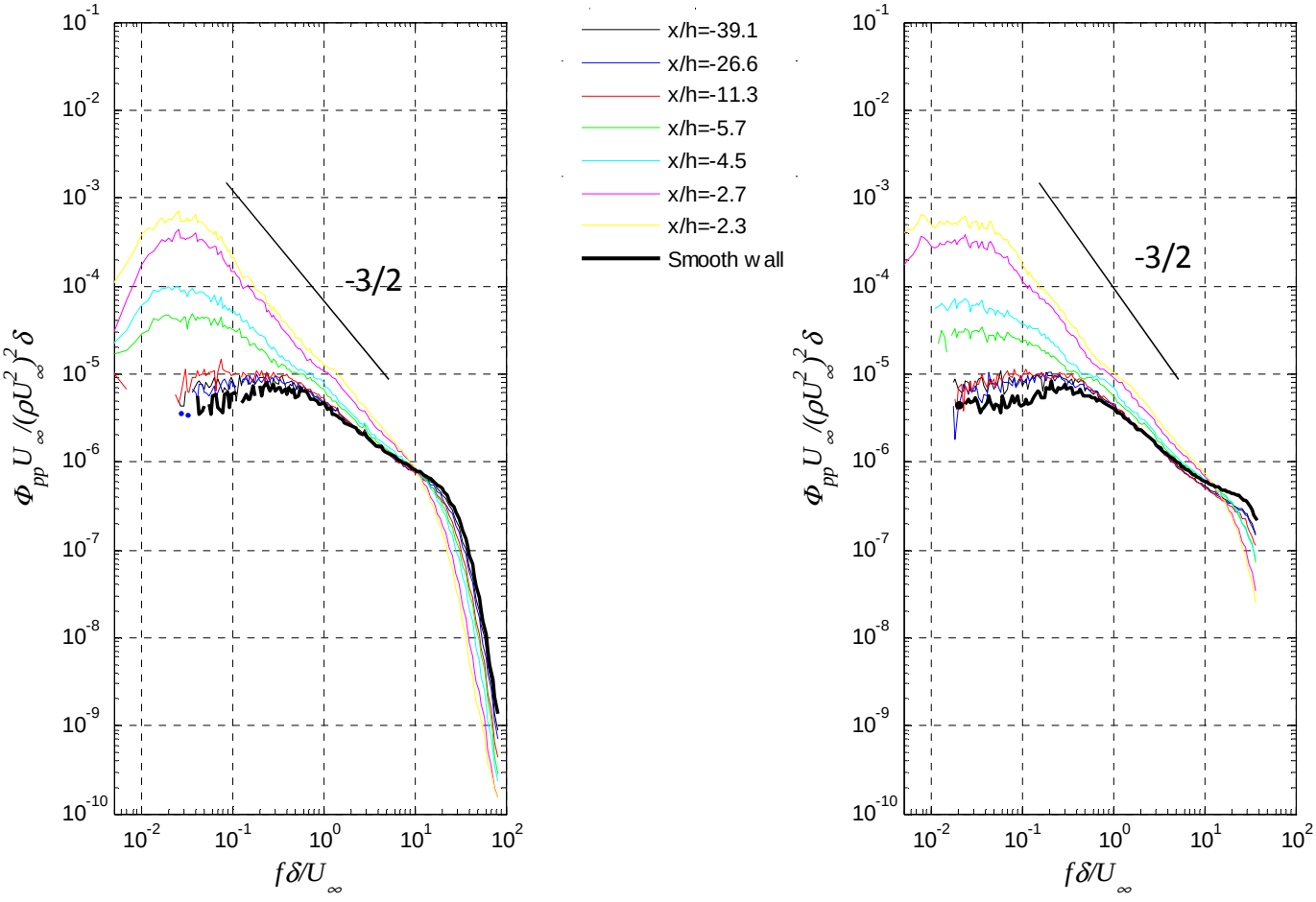

Figure 39. Upstream pressure spectra for medium step (a) Low Reynolds Number, (b) High Reynolds Number

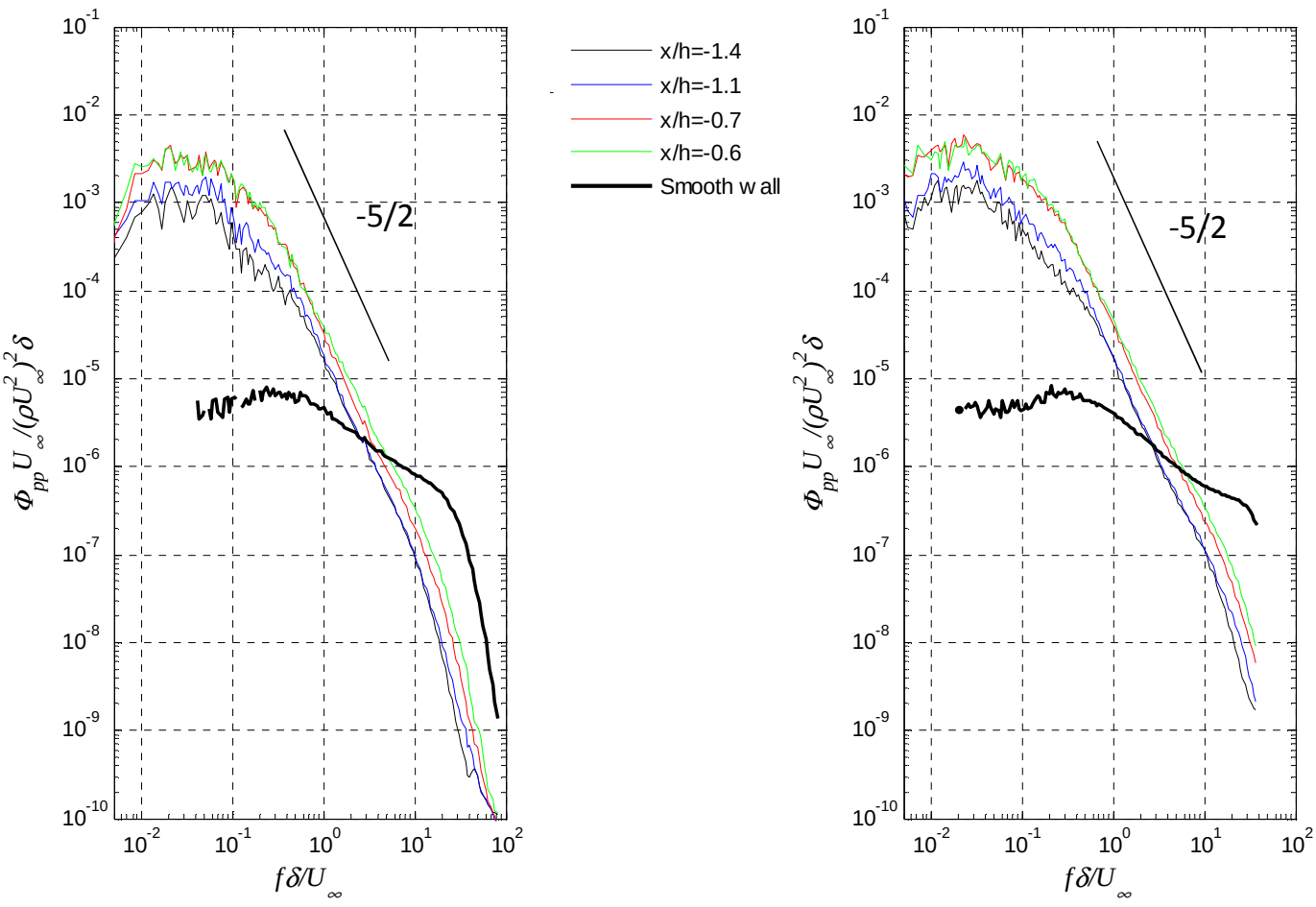

Figure 40. Upstream pressure spectra for large step (a) Low Reynolds number, (b) High Reynolds number

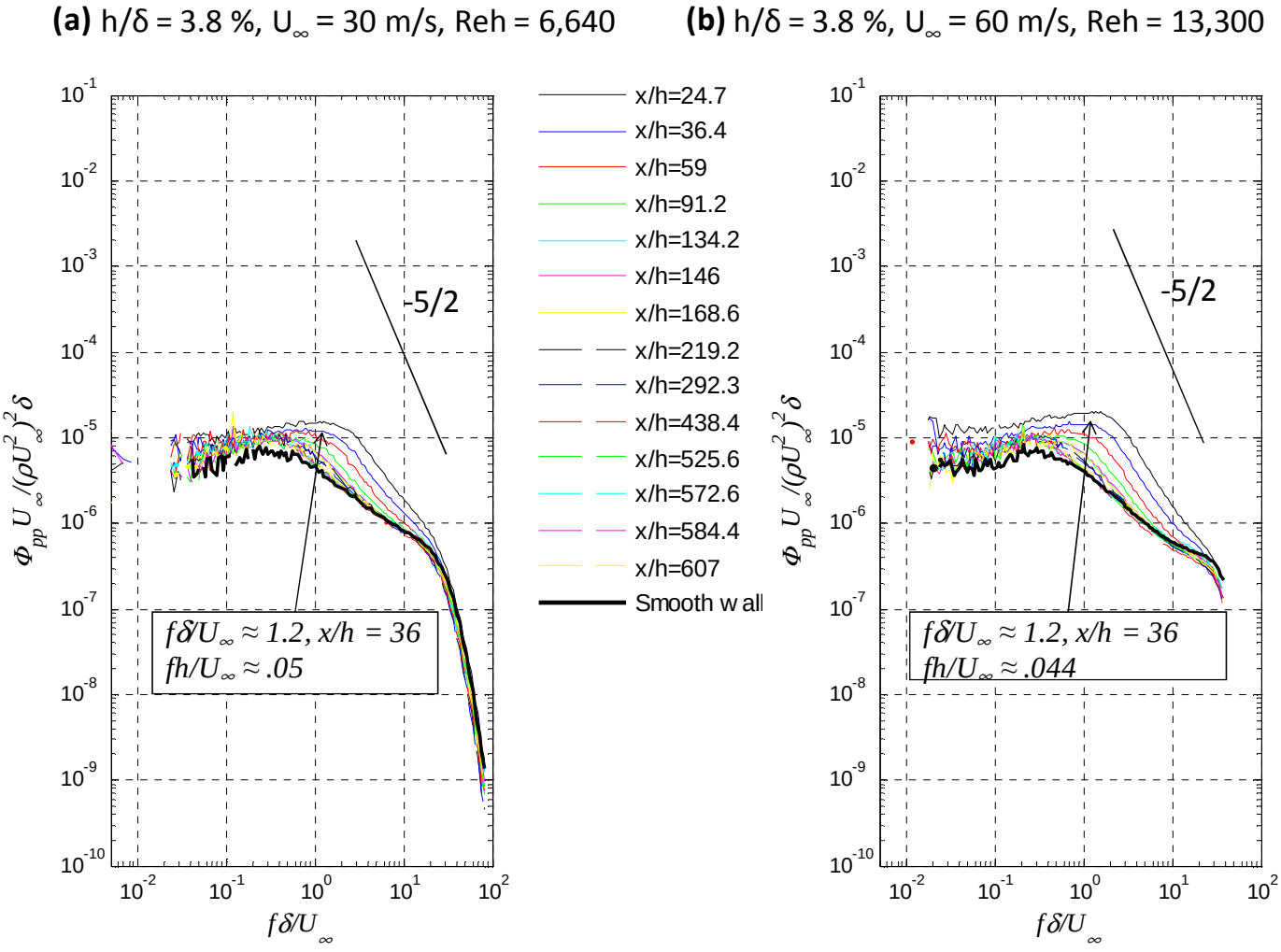

Figure 41. Downstream pressure spectra for small step (a) Low Reynolds Number, (b) High Reynolds Number

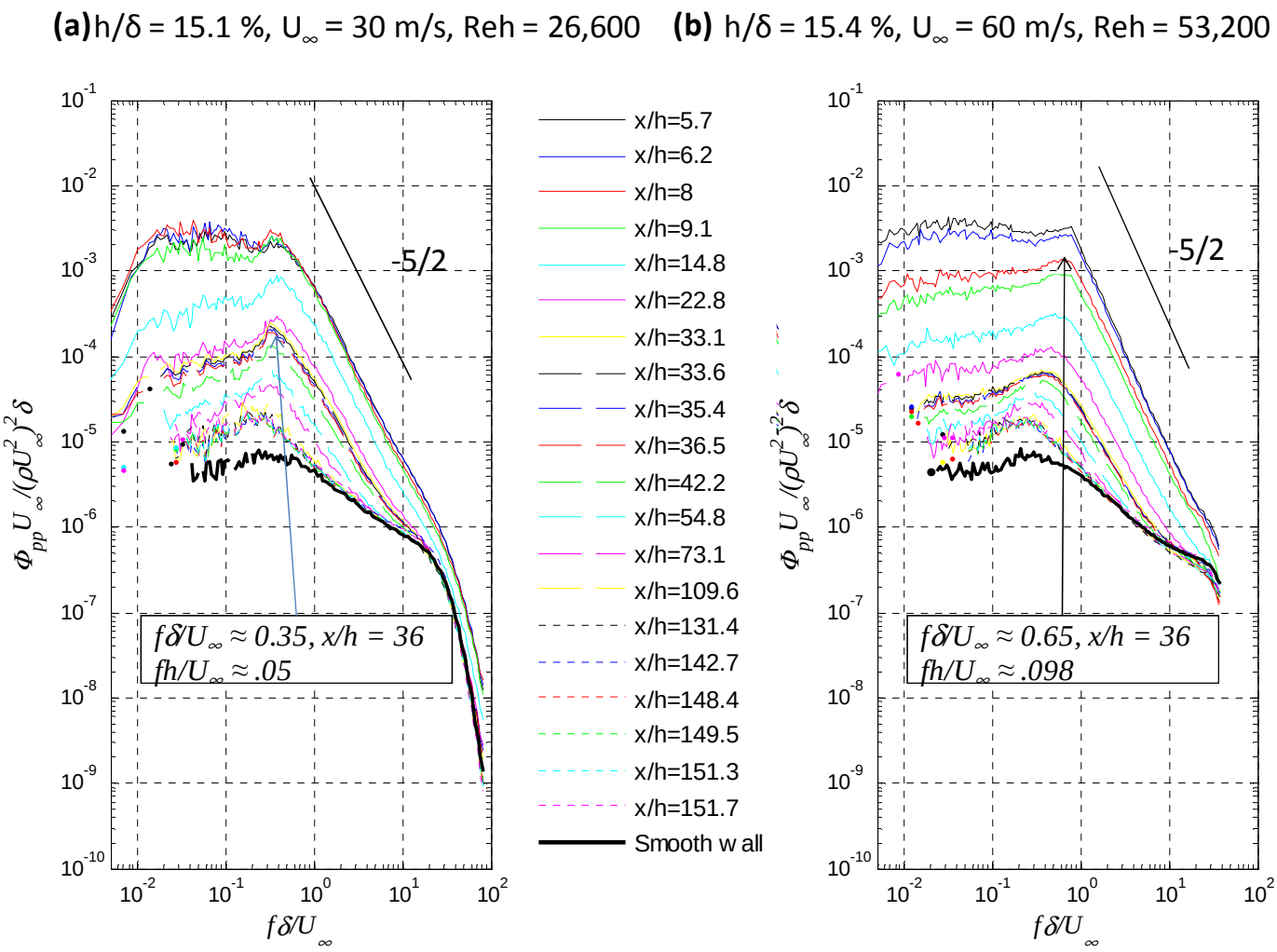

Figure 42. Downstream pressure spectra for medium step (a) Low Reynolds number, (b) High Reynolds number

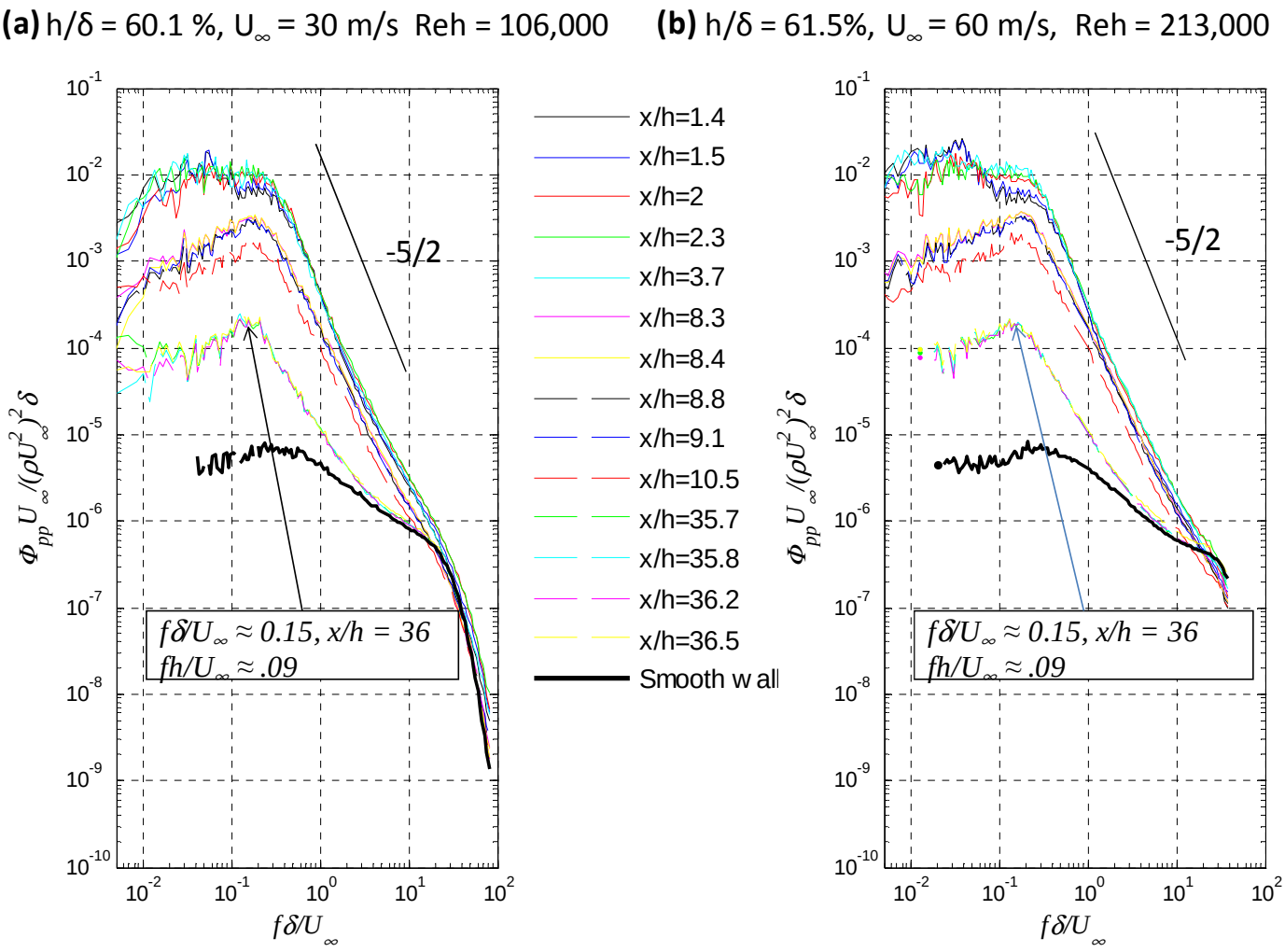

Figure 43. Downstream pressure spectra for large step (a) Low Reynolds number, (b) High Reynolds number

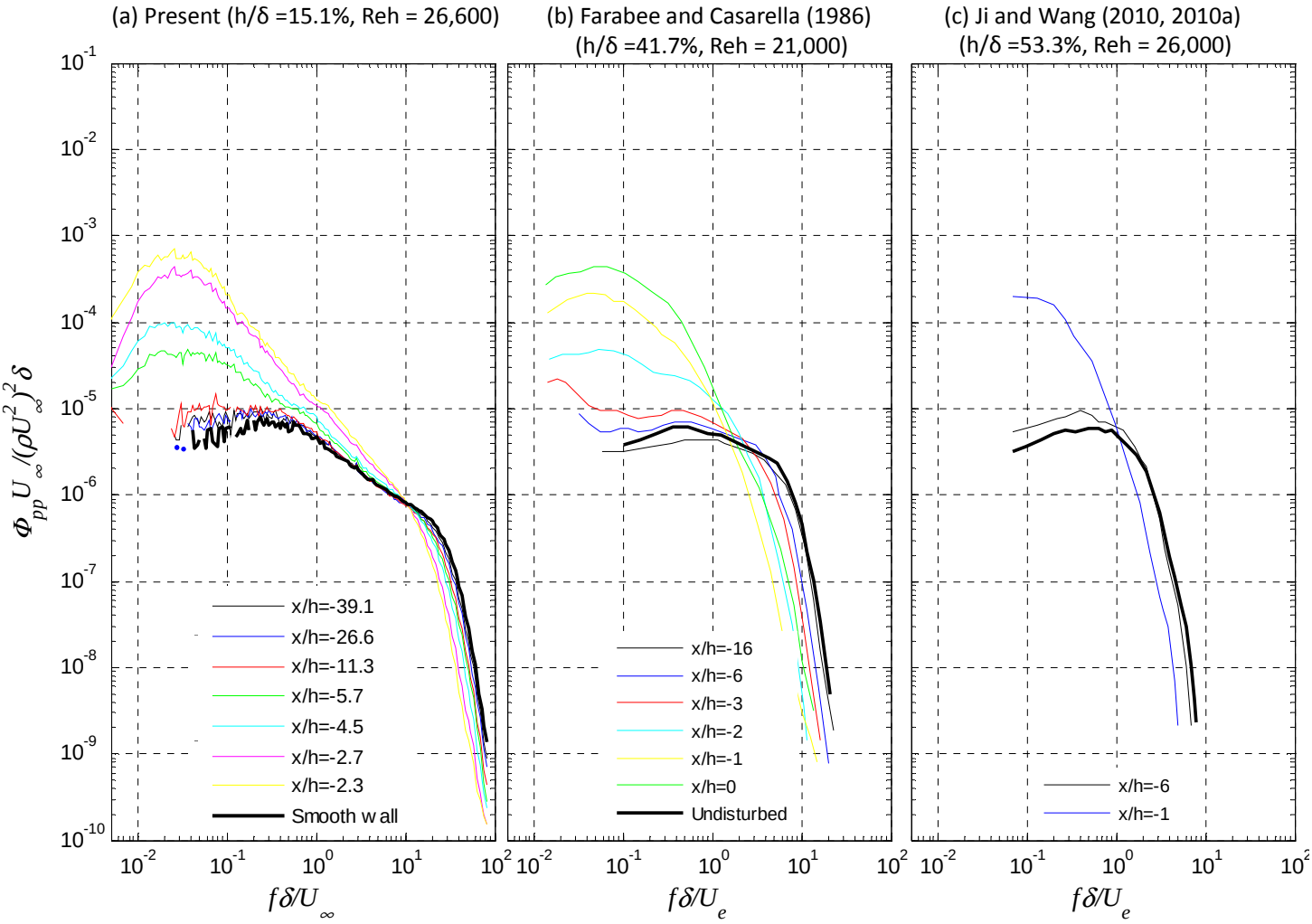

Figure 44. Upstream pressure spectra comparison with past experiment and LES calculation for similar Reynolds number cases

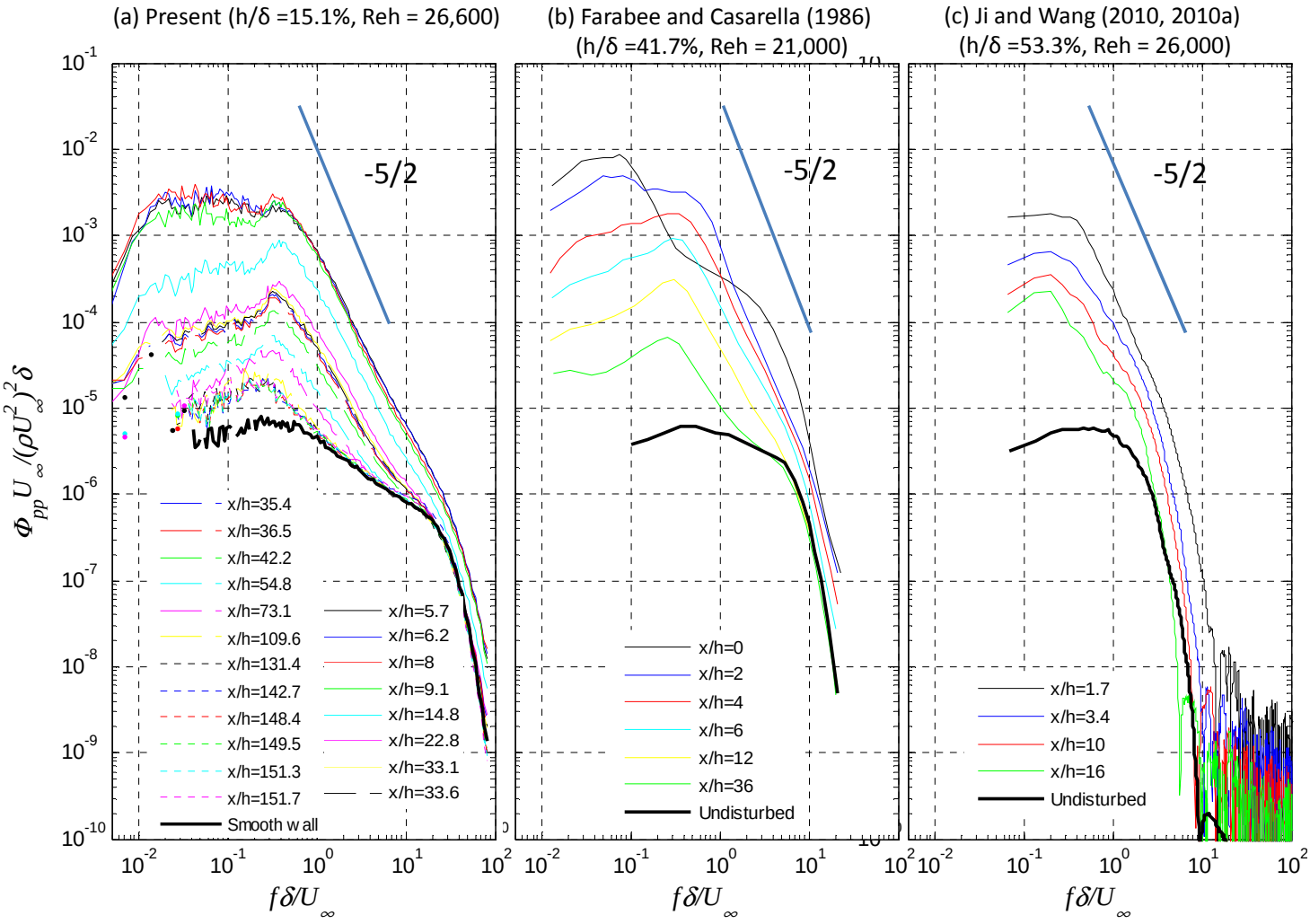

Figure 45. Downstream pressure spectra comparison with past experiment and LES calculation for similar Reynolds number cases

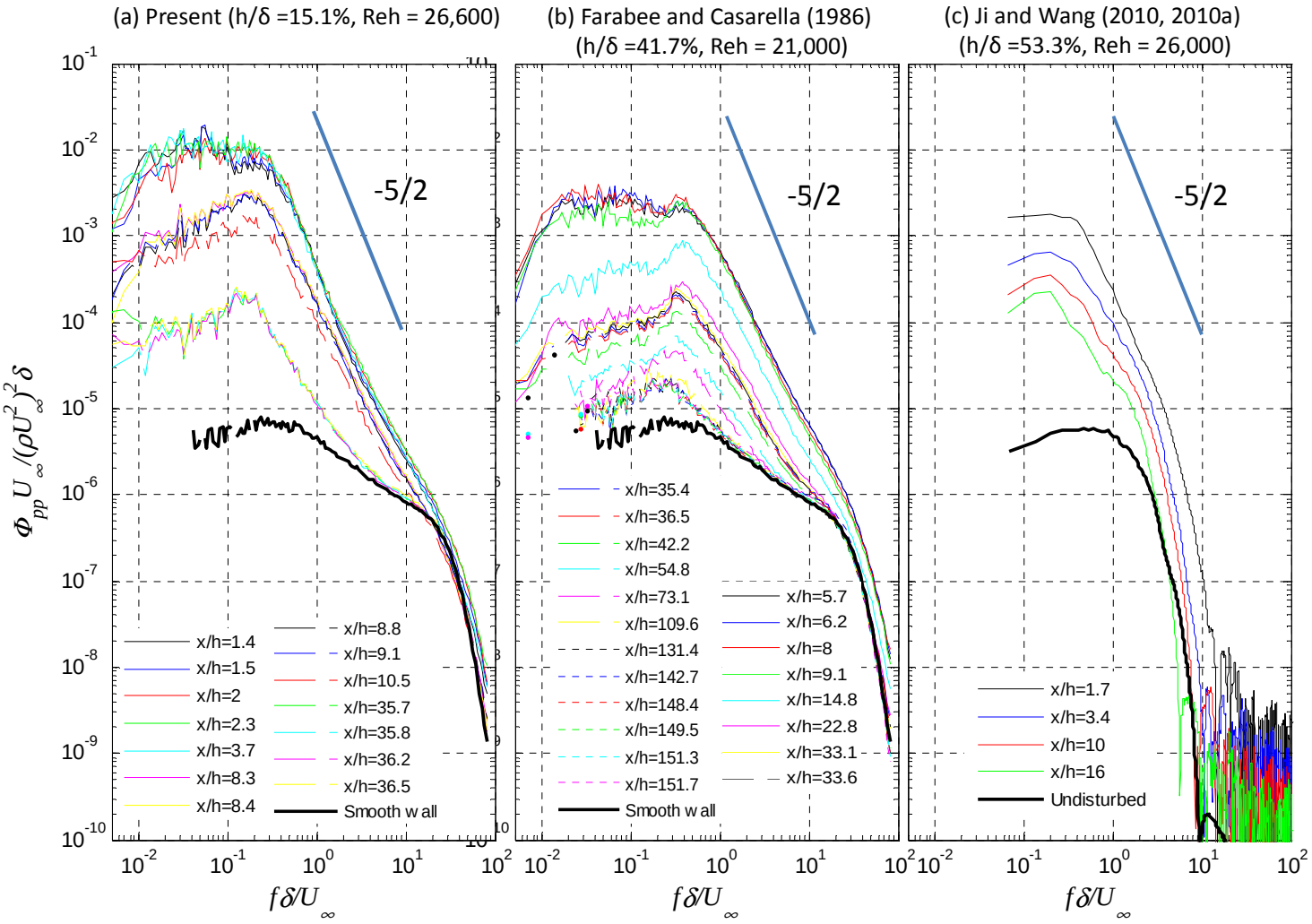

Figure 46. Downstream pressure spectra for current work and LES calculation for comparable step size and Reynolds number

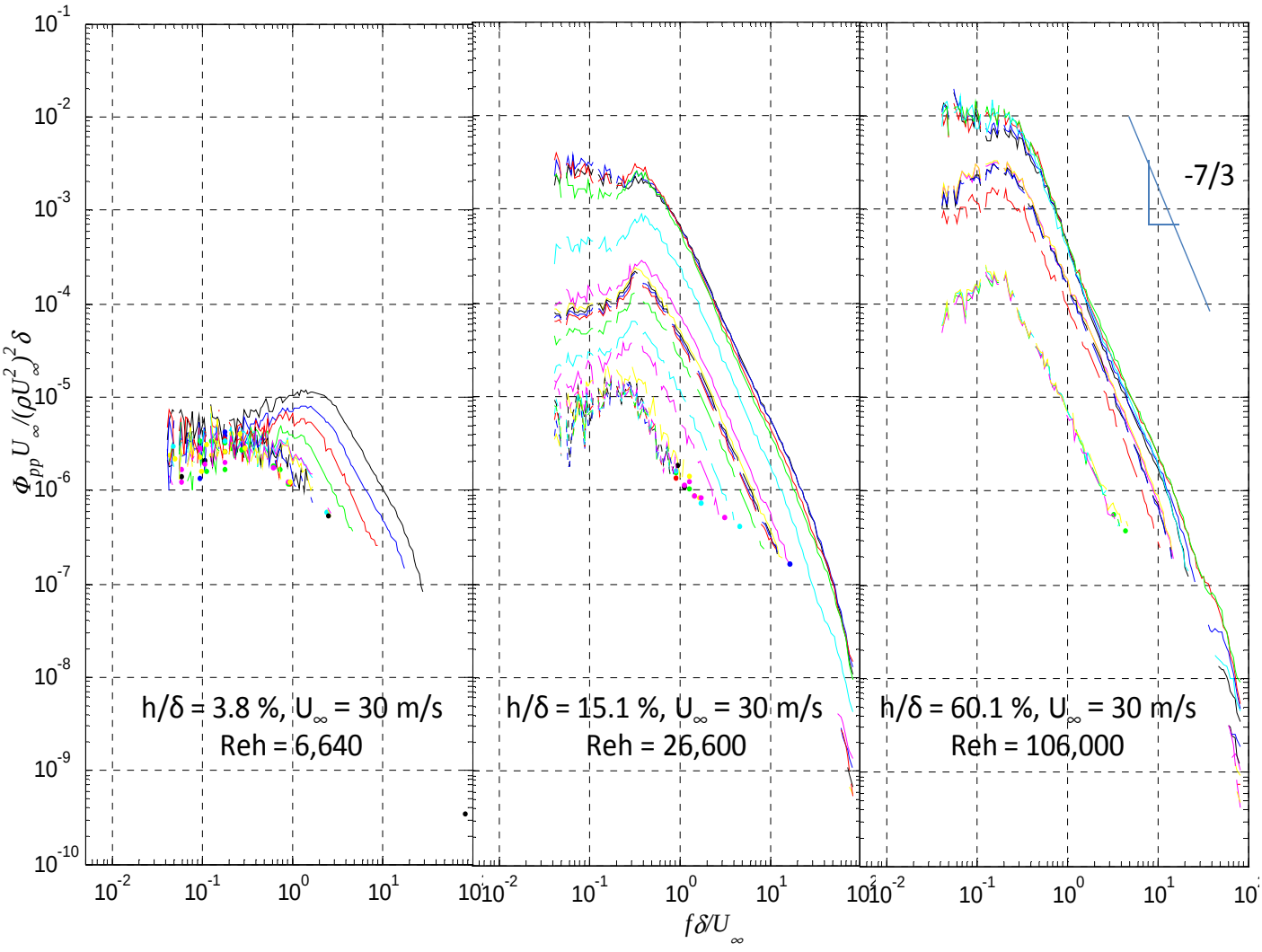
h/δ = 3.8 %, U∞ = 30 m/s
Reh = 6,640
h/δ = 15.1 %, U∞ = 30 m/s
Reh = 26,600
h/δ = 60.1 %, U∞ = 30 m/s
Reh = 106,000
-7/3
Φpp U∞ /(ρU∞²)² δ
fδ/U∞

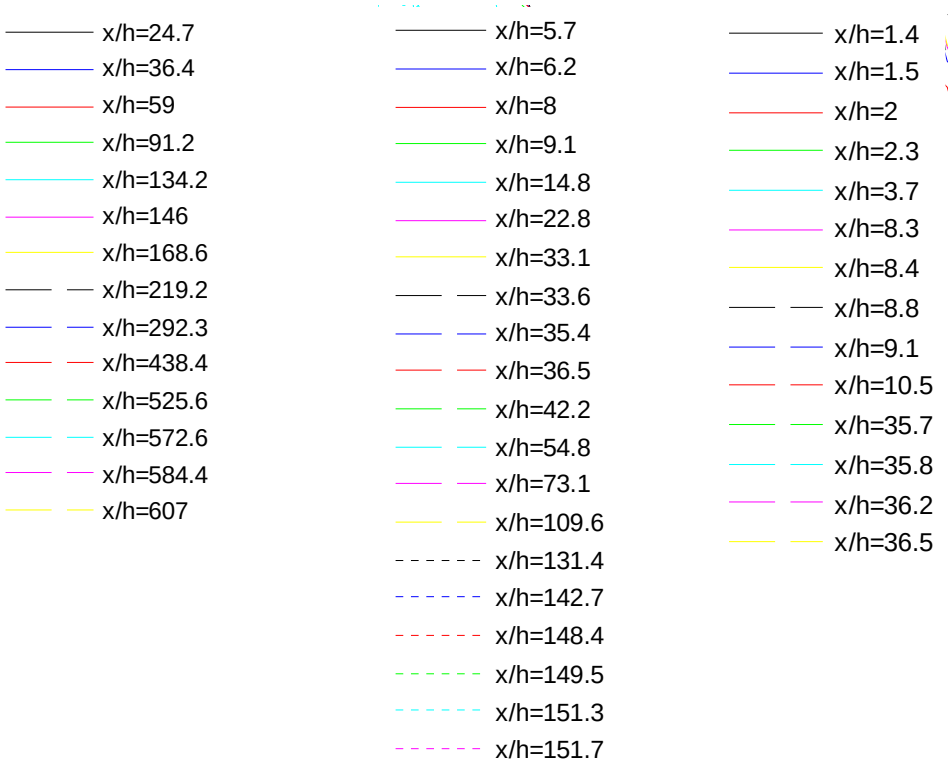

Figure 47. Subtracted pressure spectra for all steps at 30 m/s

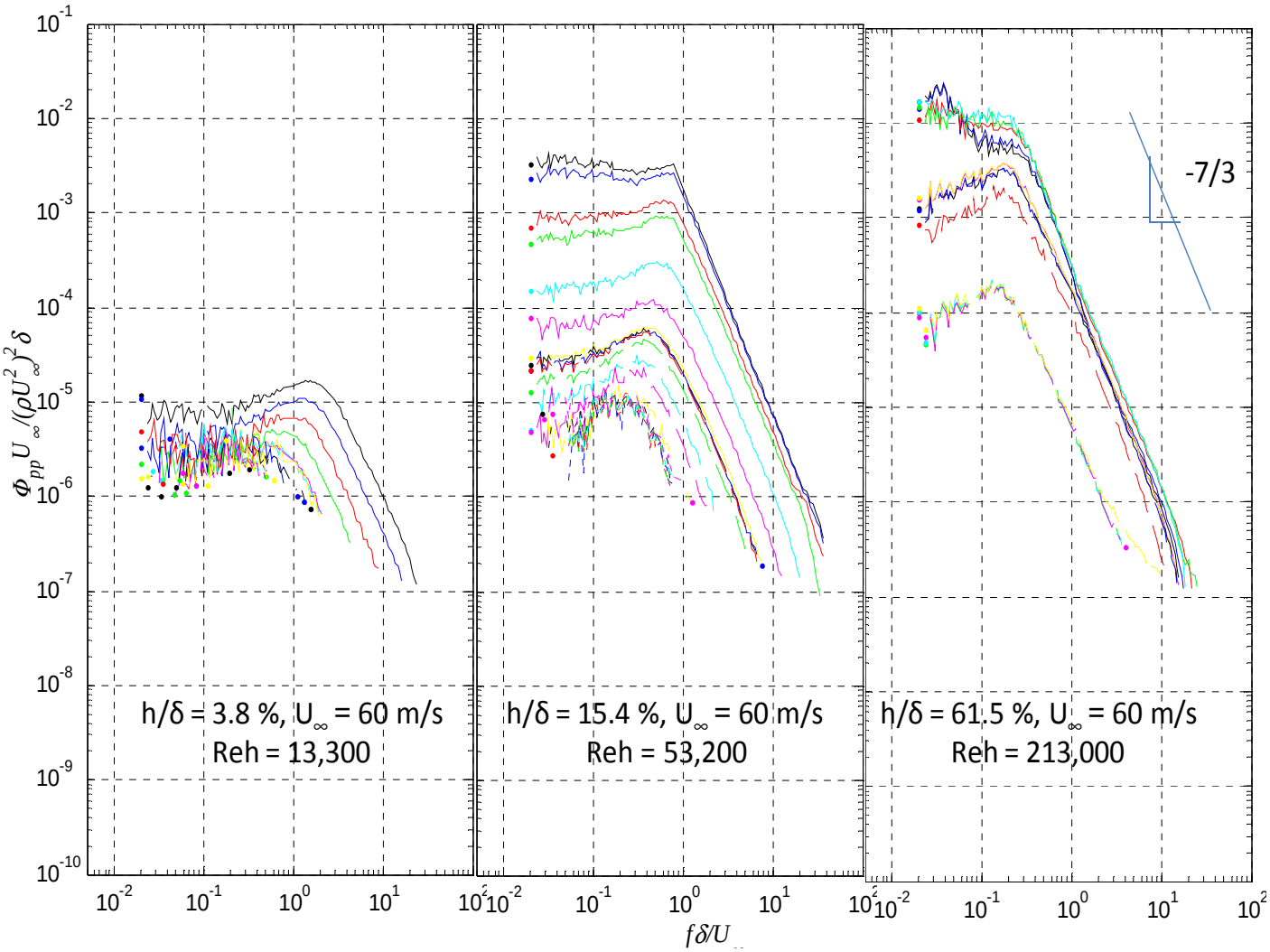

Figure 48. Subtracted pressure spectra for all steps at 60 m/s. (Legend same as that for Figure 47)

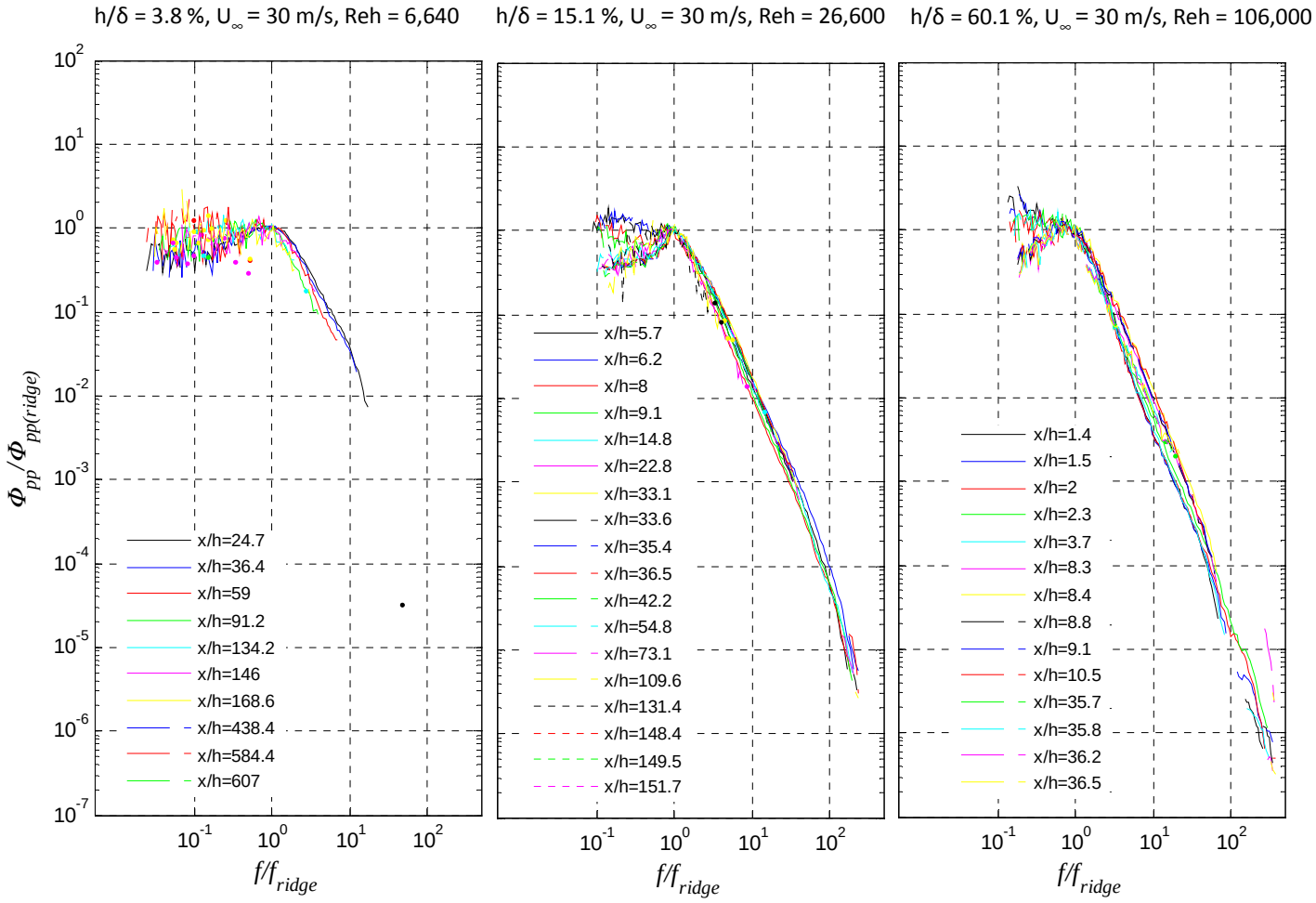

Figure 49. Pressure spectra normalized with ridge frequency and magnitude for all downstream locations at 30 m/s

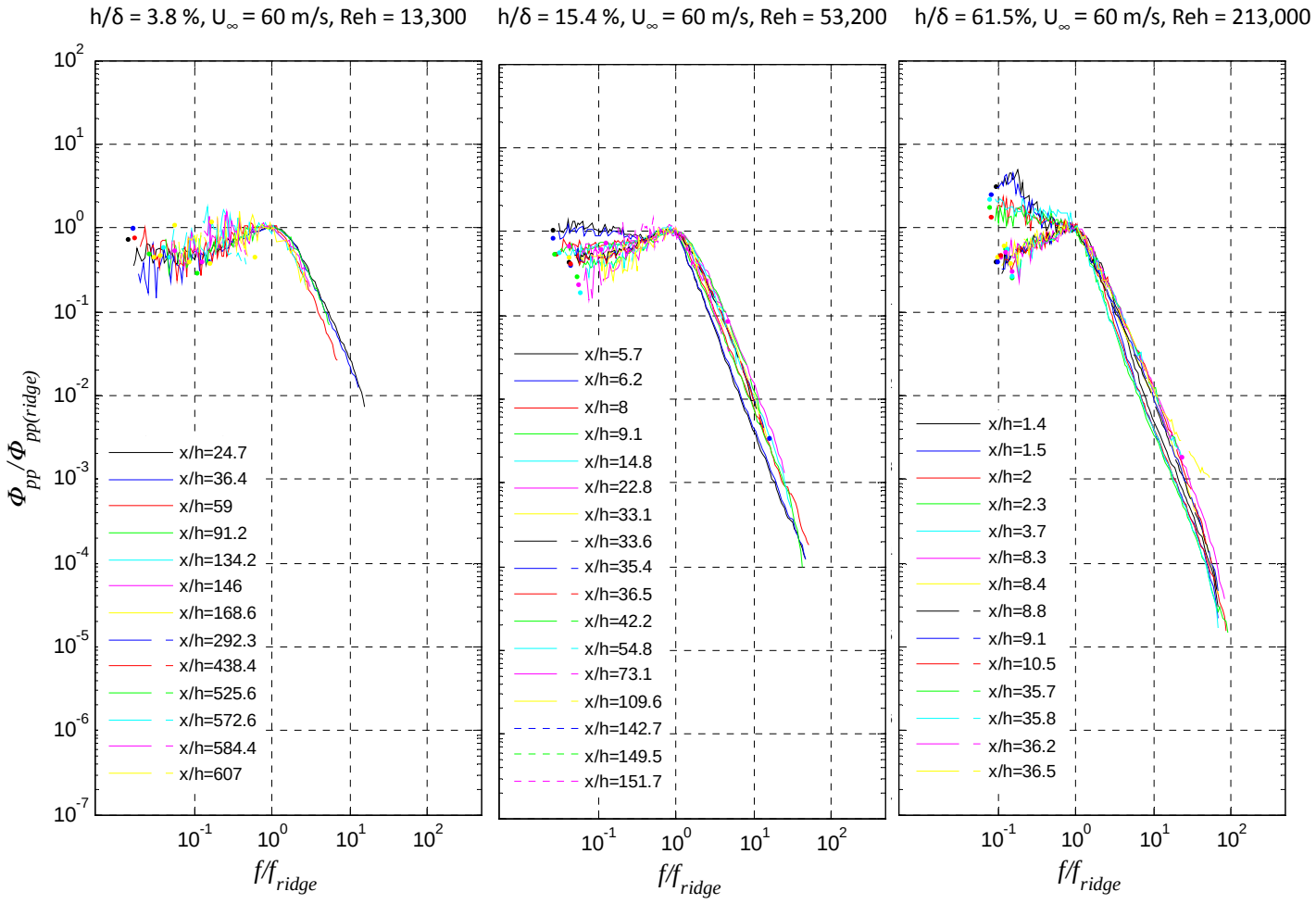

Figure 50. Pressure spectra normalized with ridge frequency and magnitude for all downstream locations at 60 m/s

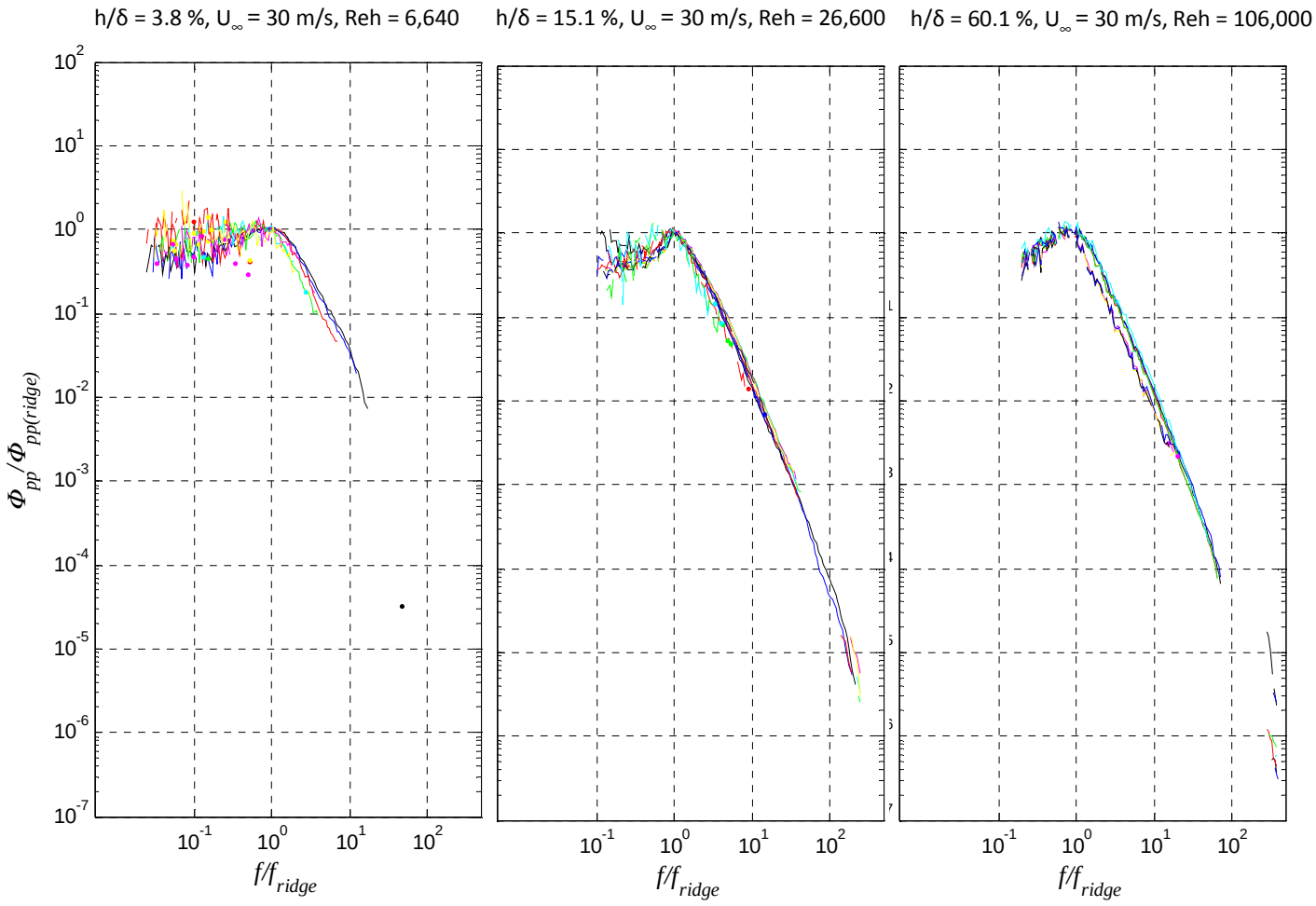

Figure 51. Pressure spectra normalized with ridge frequency and magnitude for x/h>8 at 30 m/s

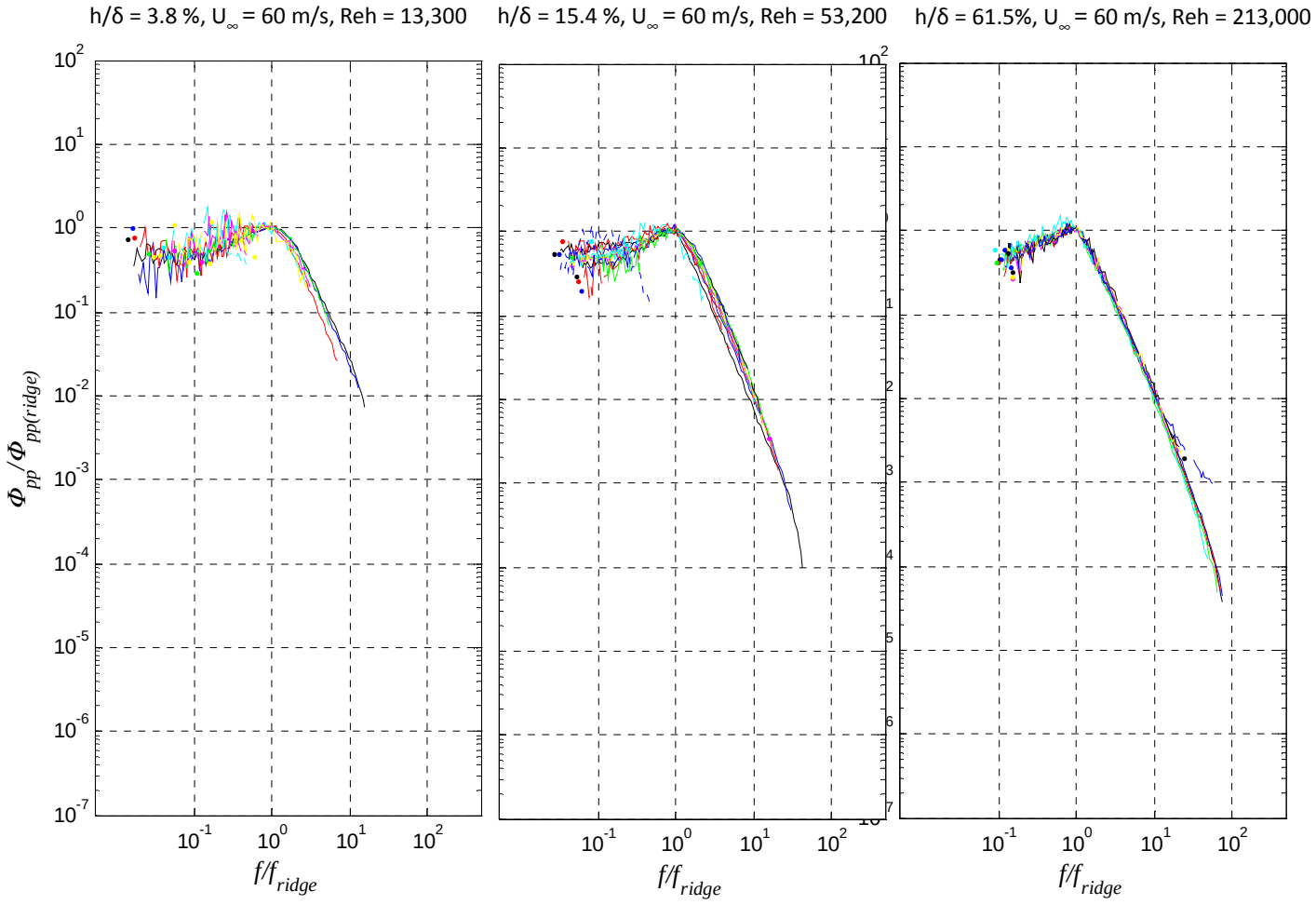

Figure 52. Pressure spectra normalized with ridge frequency and magnitude for x/h>8 at 30 m/s

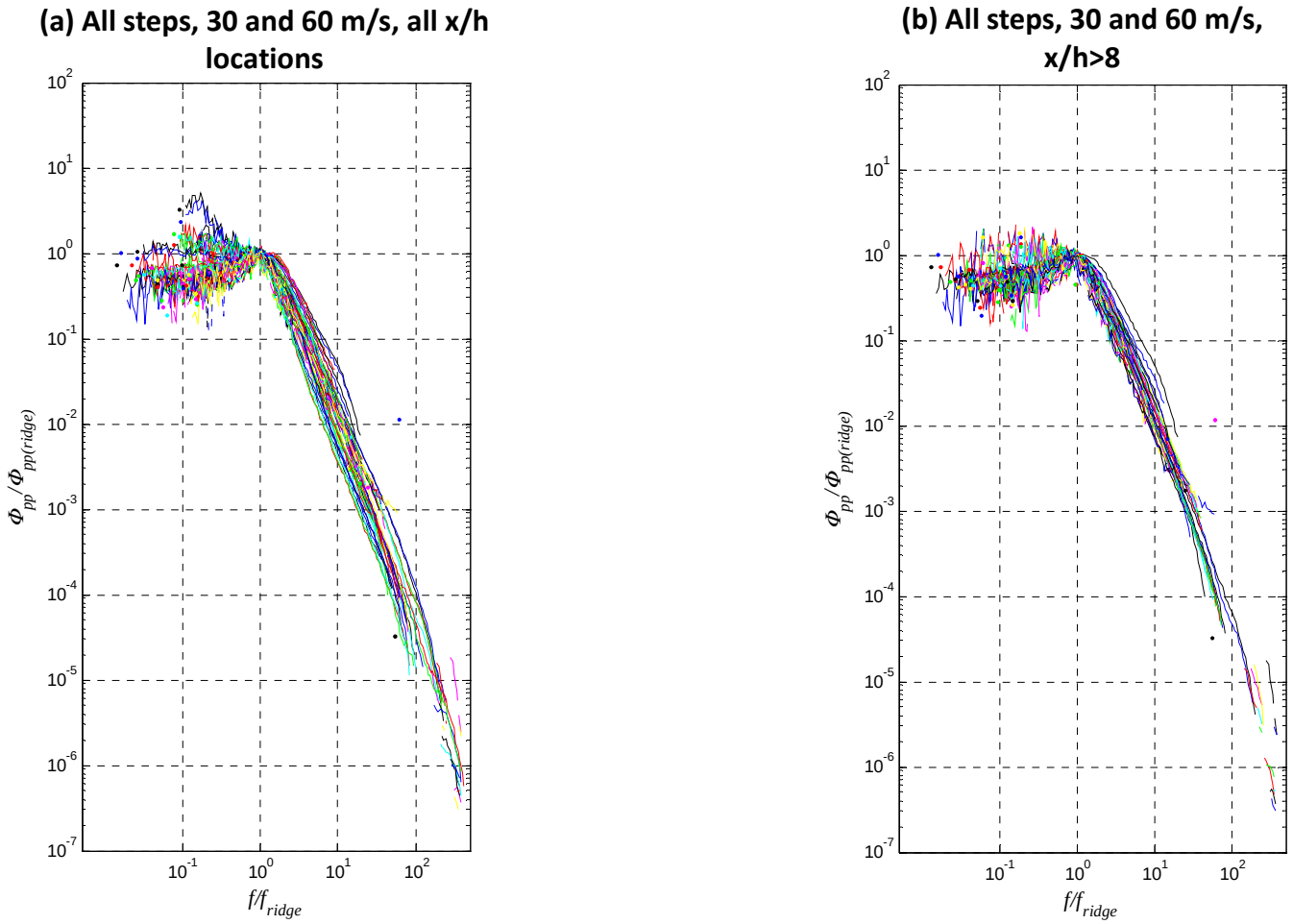

Figure 53. Pressure spectra for all steps sizes and both Reynolds number normalized with ridge frequency and magnitude. (a) All downstream *x/h* locations, (b) Downstream *x/h*>8 locations

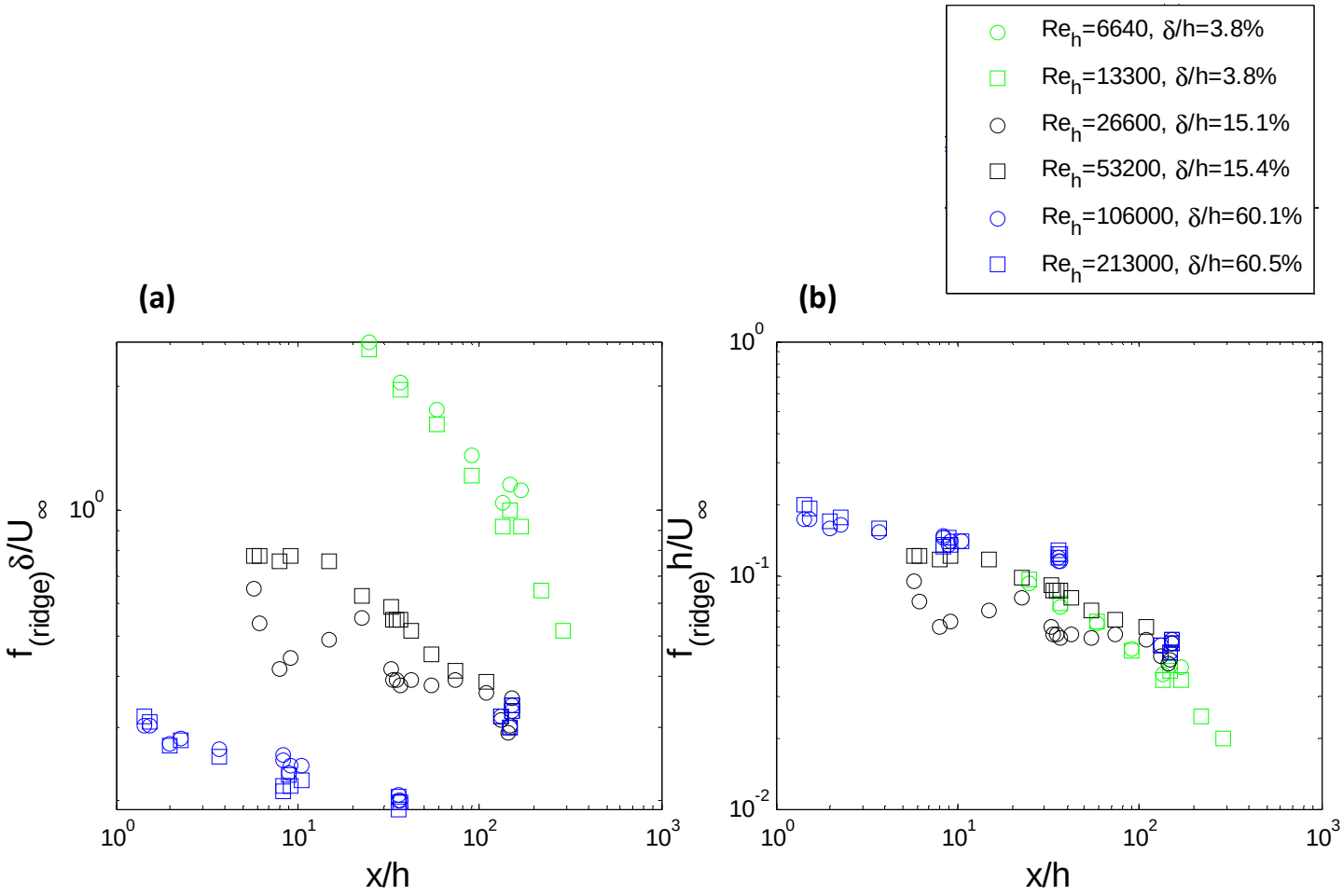

Figure 54. Ridge frequencies for downstream pressure spectra as a function of streamwise distance (*x/h*), (a) Normalized on boundary layer thickness, (b) Normalized on step height

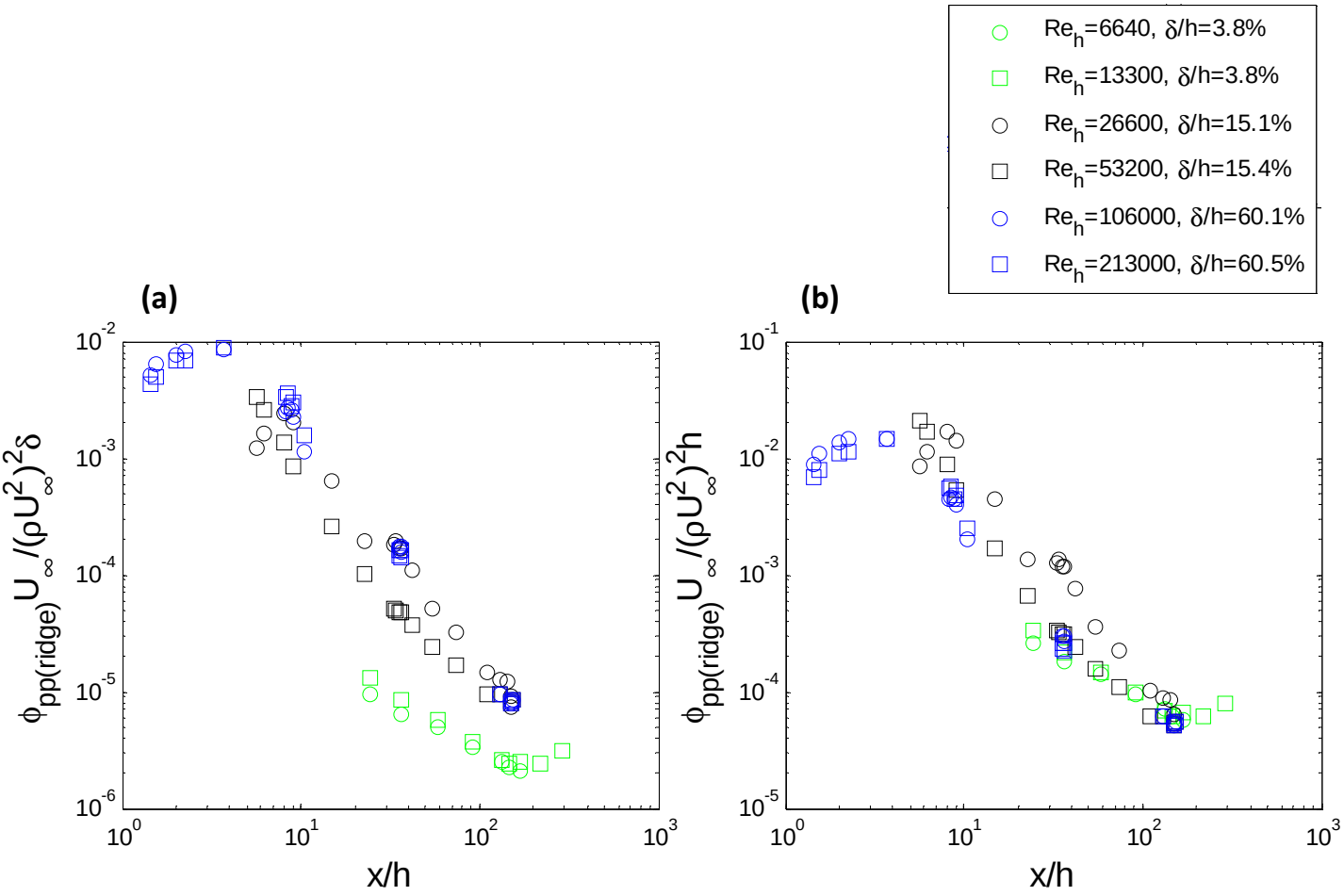

Figure 55. Ridge spectral levels for downstream pressure spectra as a function of streamwise distance (*x/h*), (a) Normalized on boundary layer thickness (b) Normalized on step height

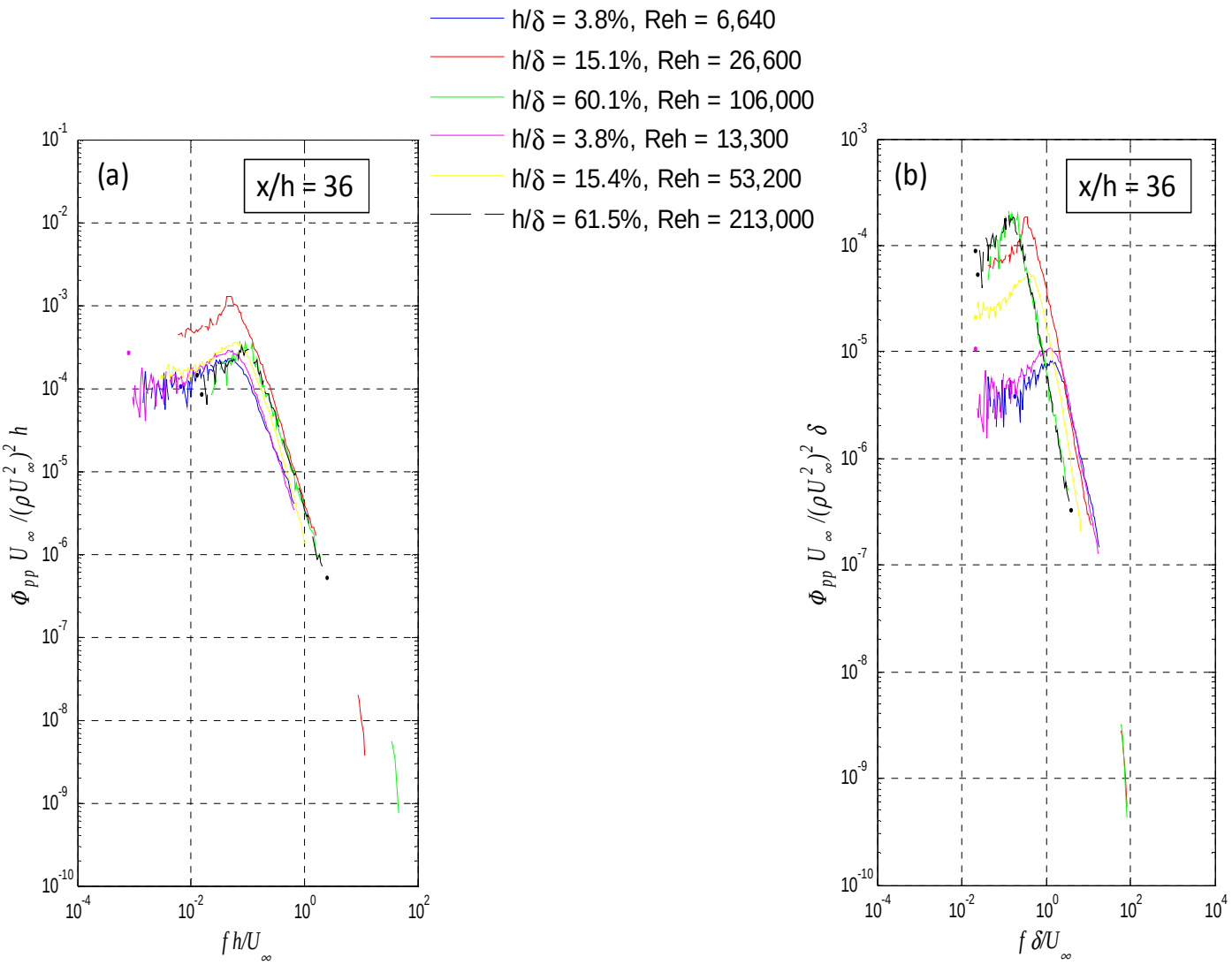

Figure 56. Subtracted Spectra for all 3 steps at 30 and 60 m/s, *x/h* = 36.

(a) Normalized with step height, (b) Normalized with boundary layer thickness

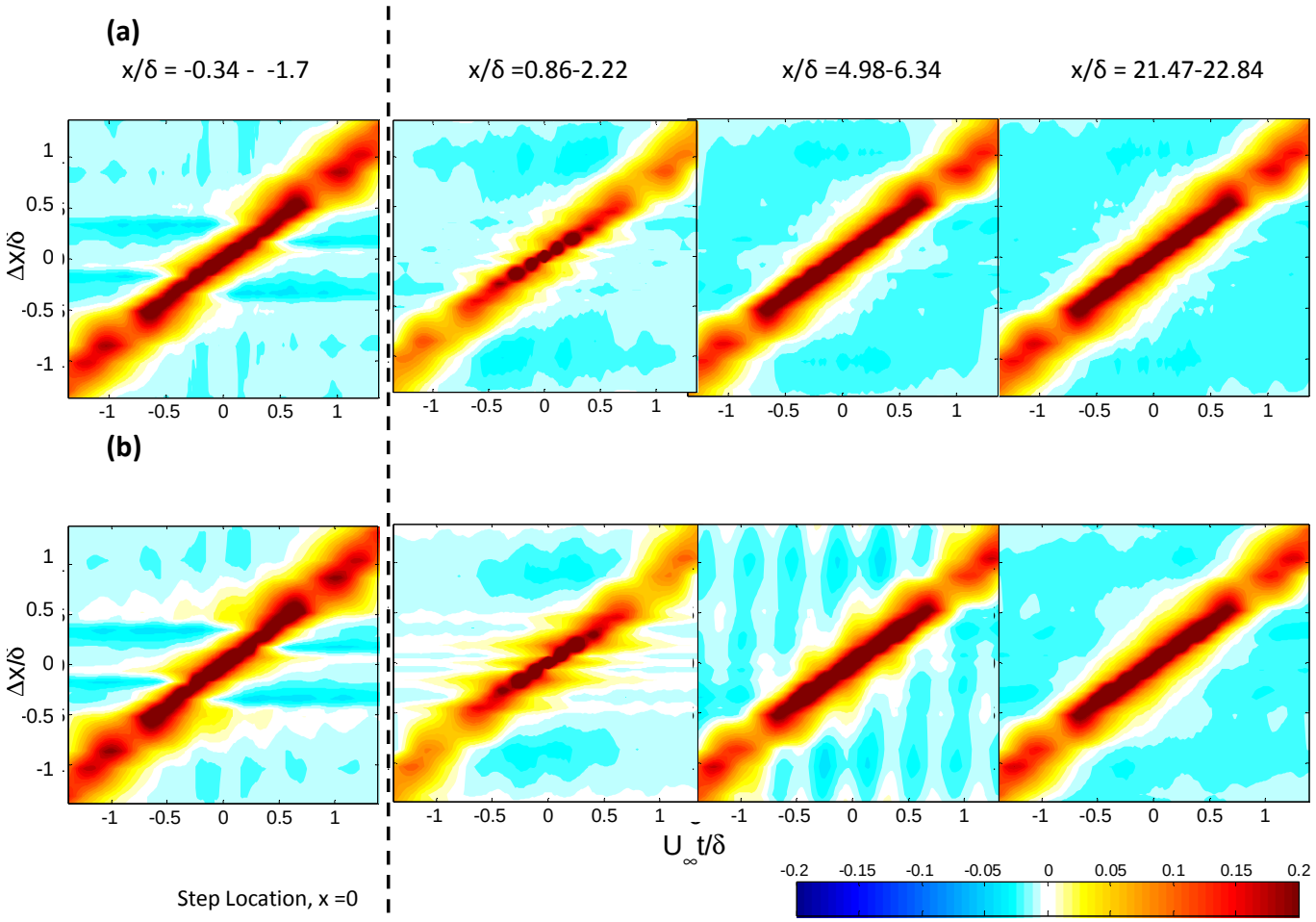

Figure 57. Streamwise pressure space time correlation coefficient for smooth wall. (a) 30 m/s (b) 60 m/s

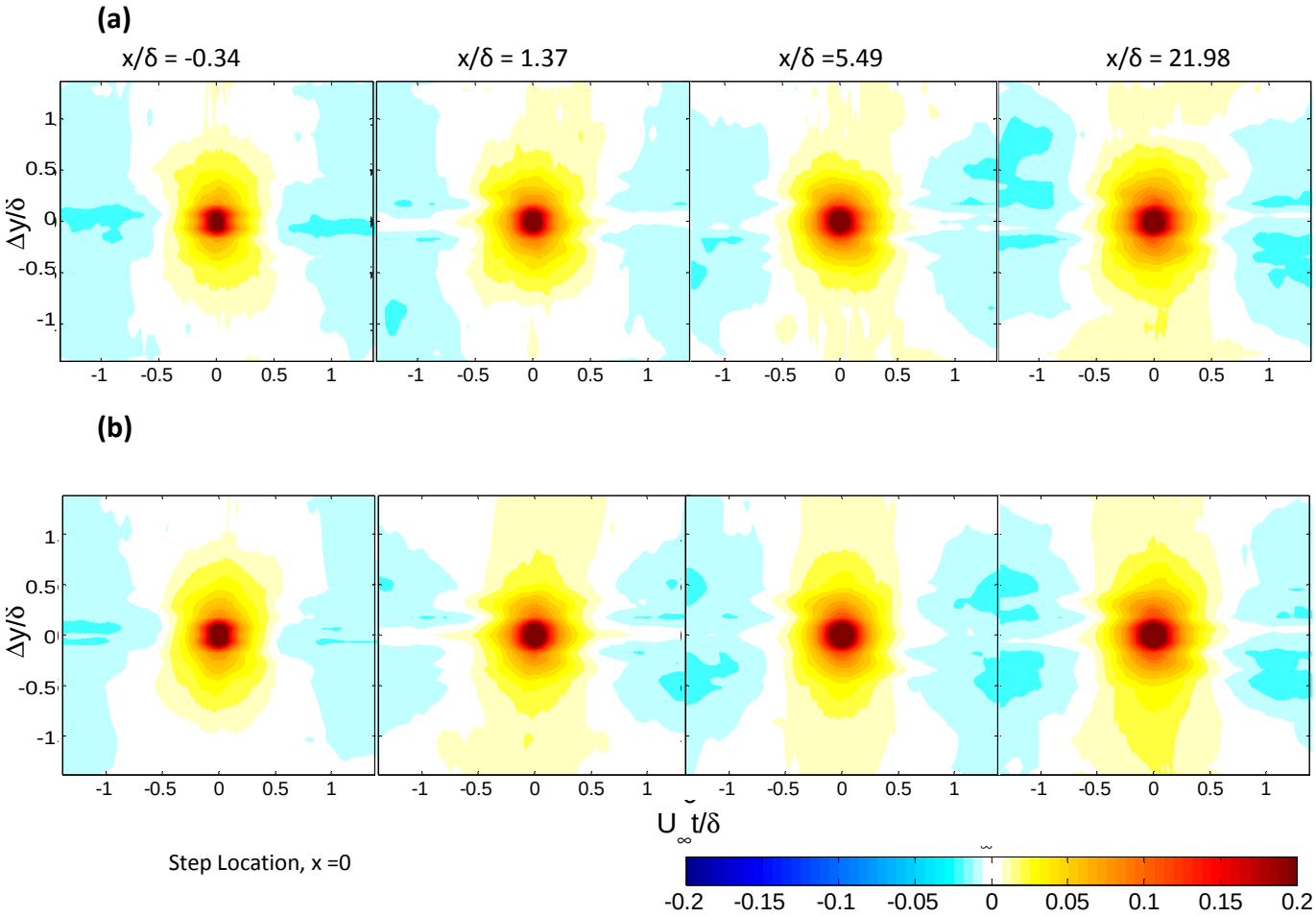

Figure 58. Spanwise pressure space time correlation coefficient for smooth wall. (a) 30 m/s (b) 60 m/s

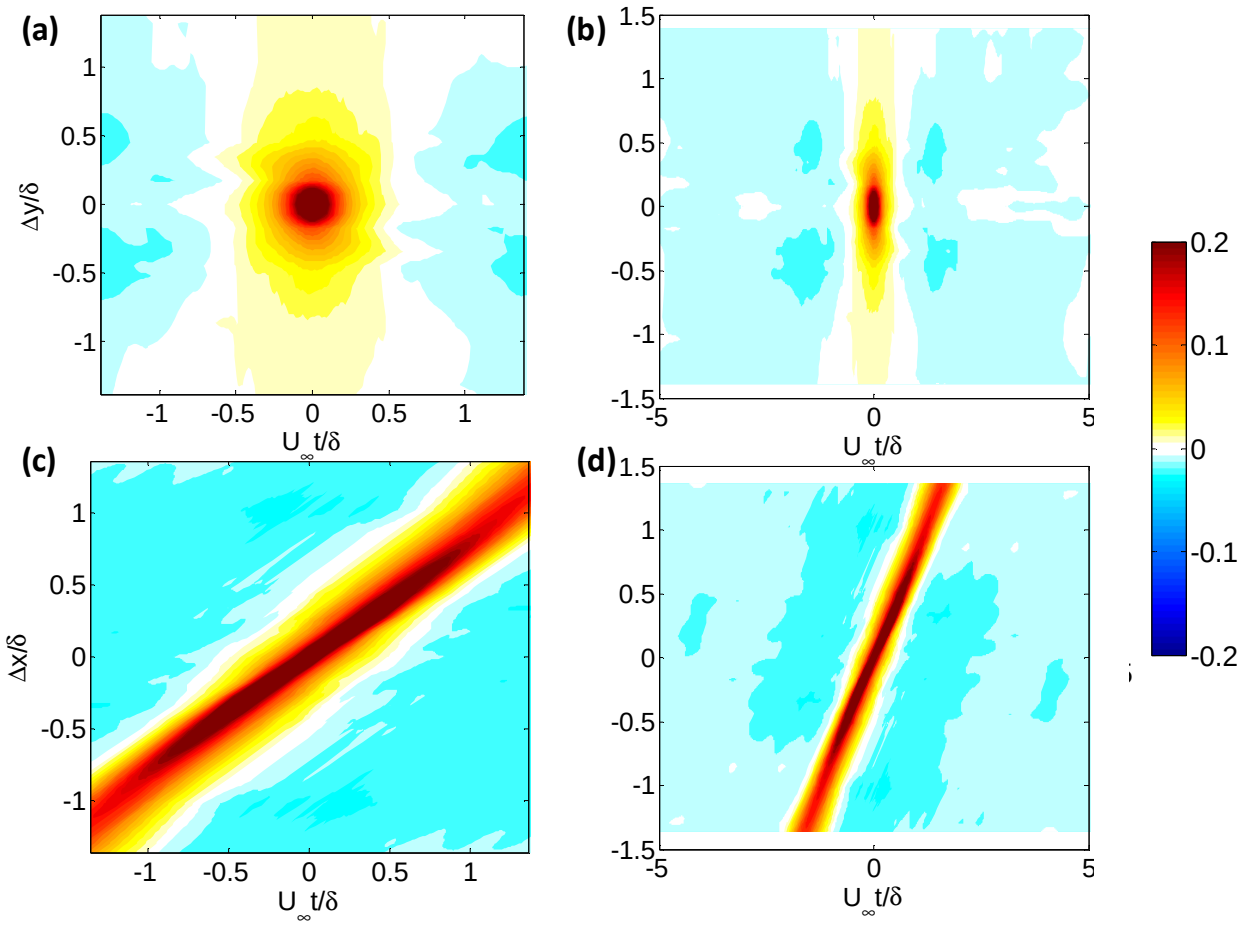

Figure 59. Smooth wall correlations. (a)Undistorted spanwise (b)Distorted spanwise (c)Undistorted streamwise (d)Distorted streamwise

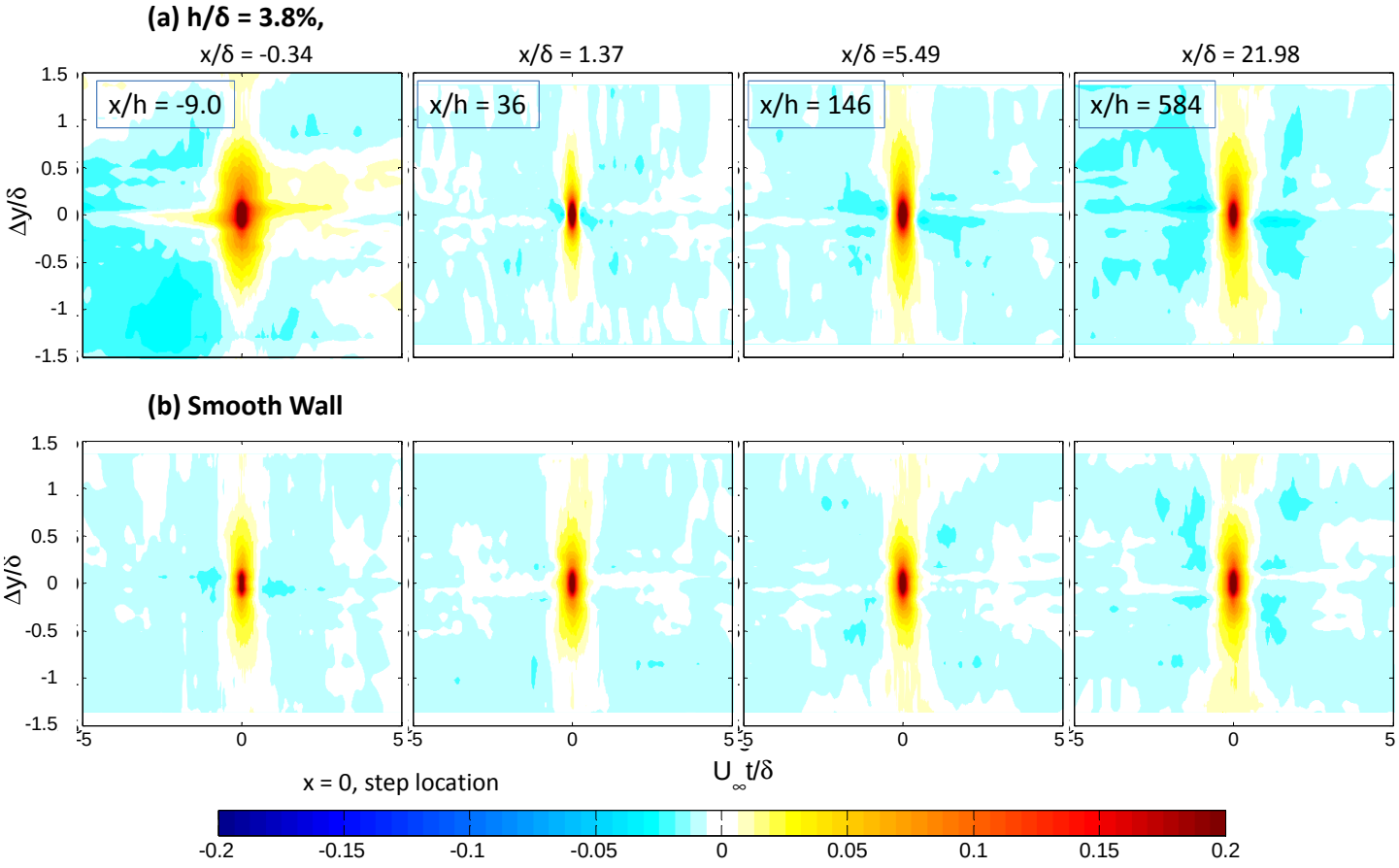

Figure 60. Spanwise pressure space time correlations. (a) Small step, 30m/s. (b) Smooth wall, 30m/s

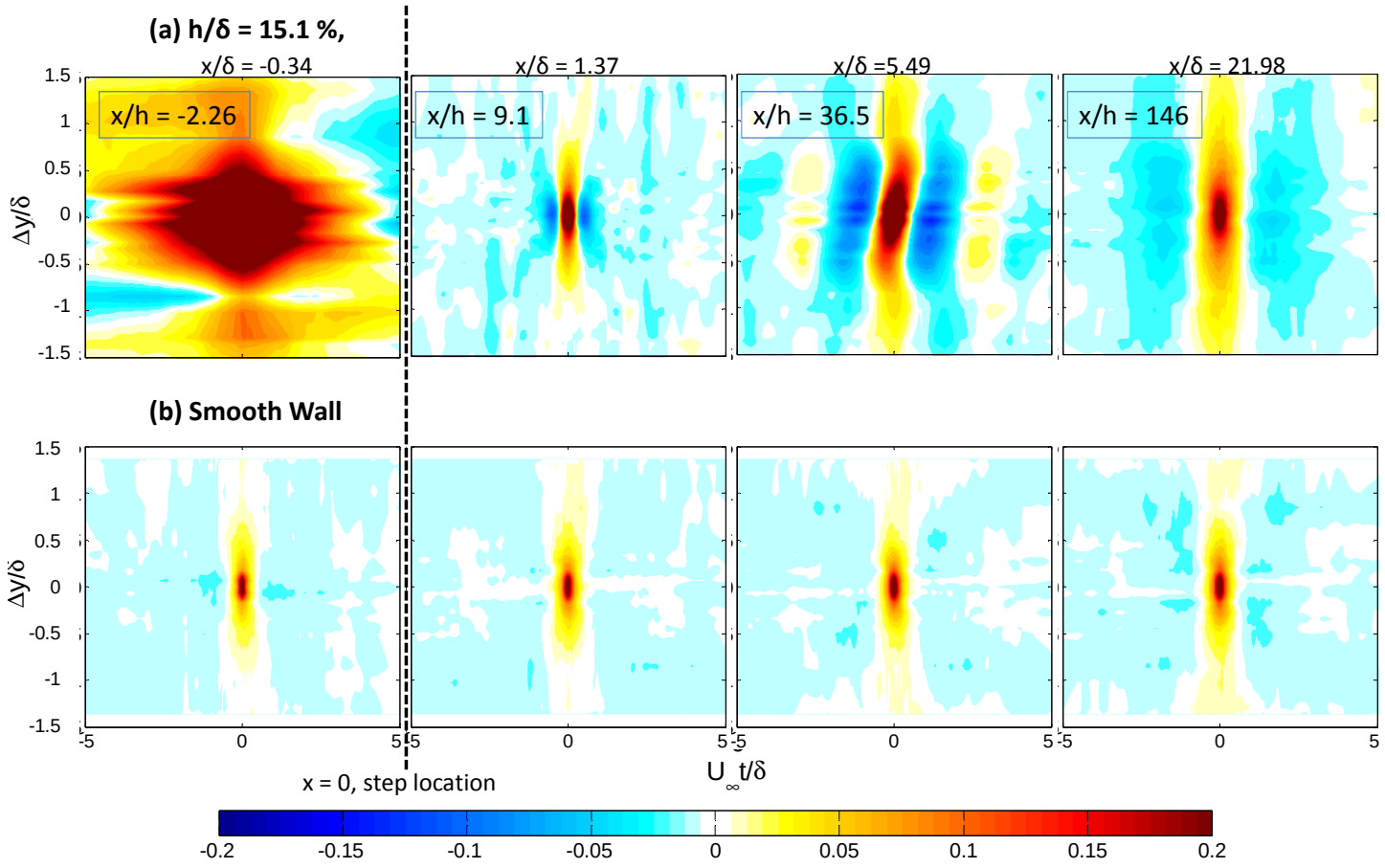

Figure 61. Spanwise pressure space time correlations. (a) Medium step, 30 m/s. (b) Smooth wall, 30 m/s

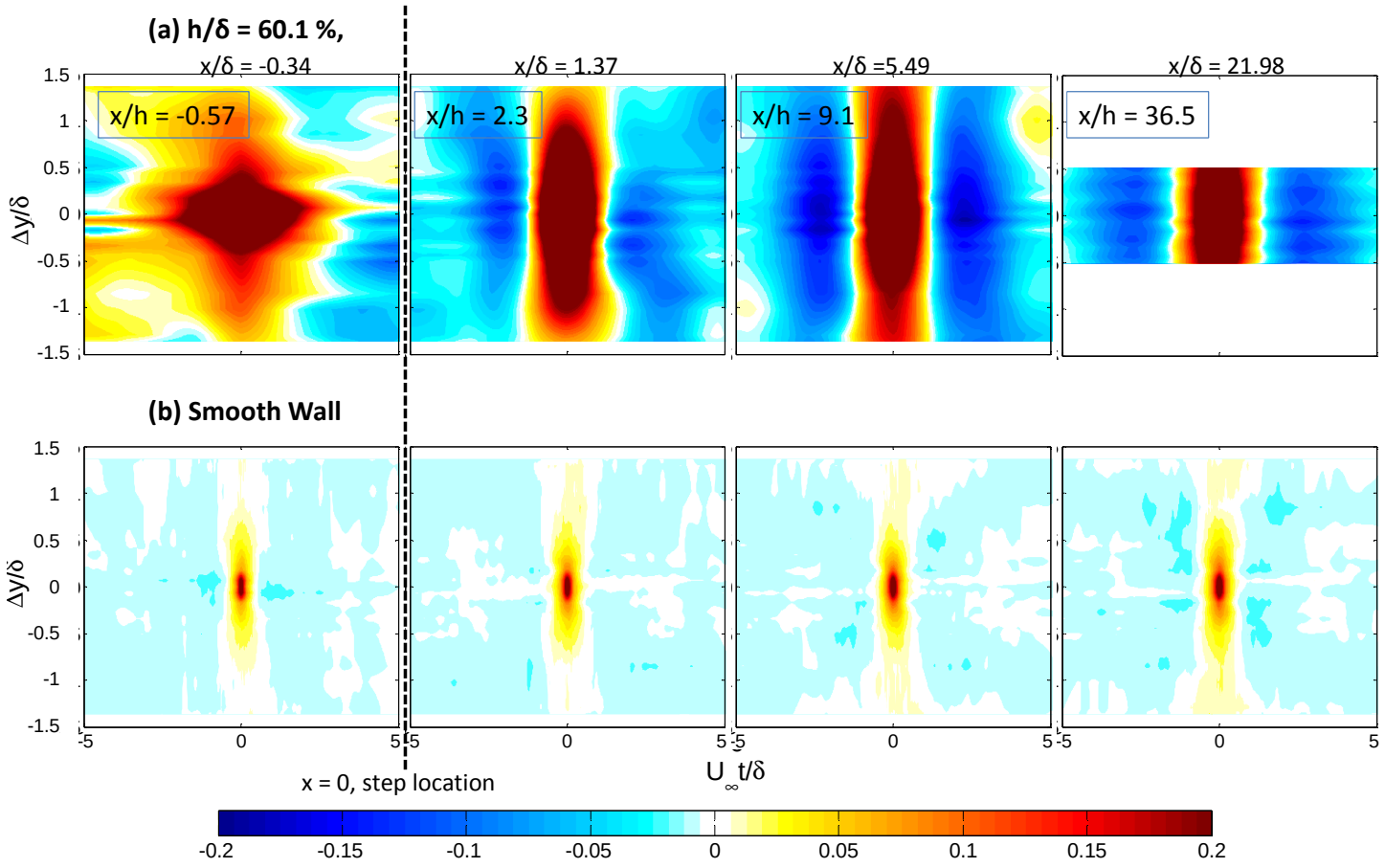

Figure 62. Spanwise pressure space time correlation. (a) Large step, 30 m/s. (b) Smooth wall, 30 m/s

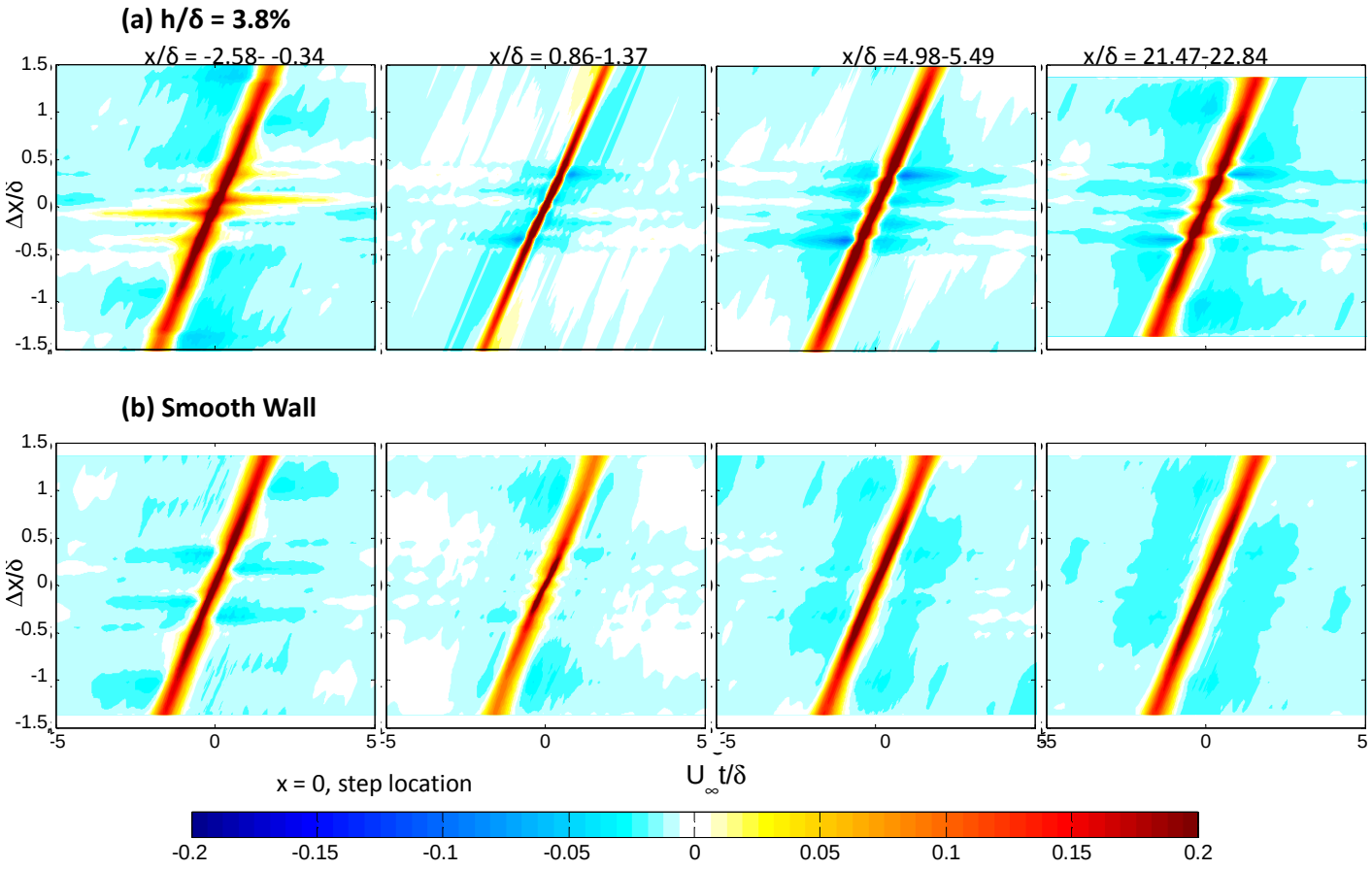

Figure 63. Streamwise pressure space time correlation. (a) Small step, 30 m/s. (b) Smooth wall, 30 m/s

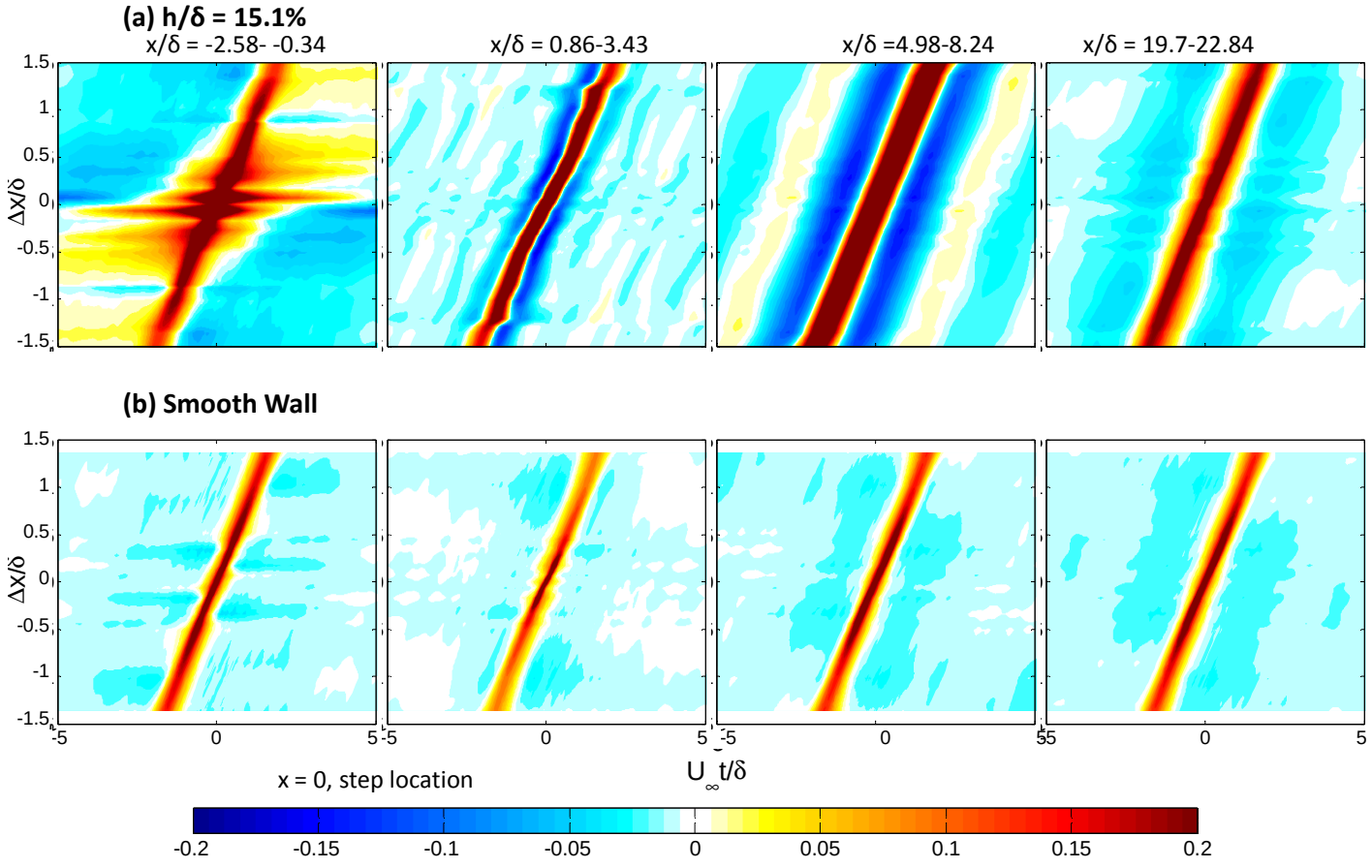

Figure 64. Streamwise pressure space time correlation. (a) Medium step, 30 m/s. (b) Smooth wall, 30 m/s

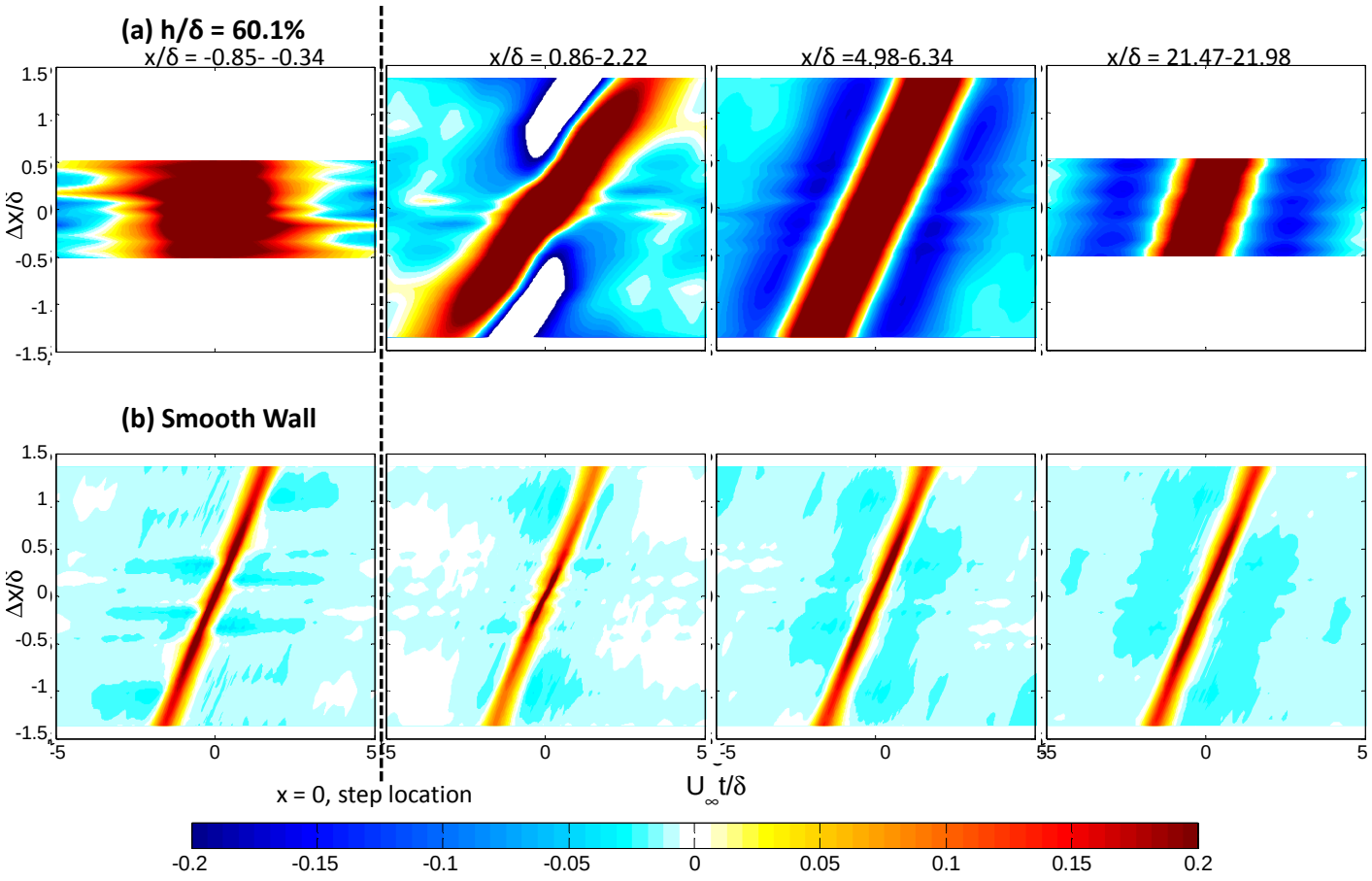

Figure 65. Streamwise pressure space time correlation. (a) Large step, 30 m/s. (b) Smooth wall, 30 m/s

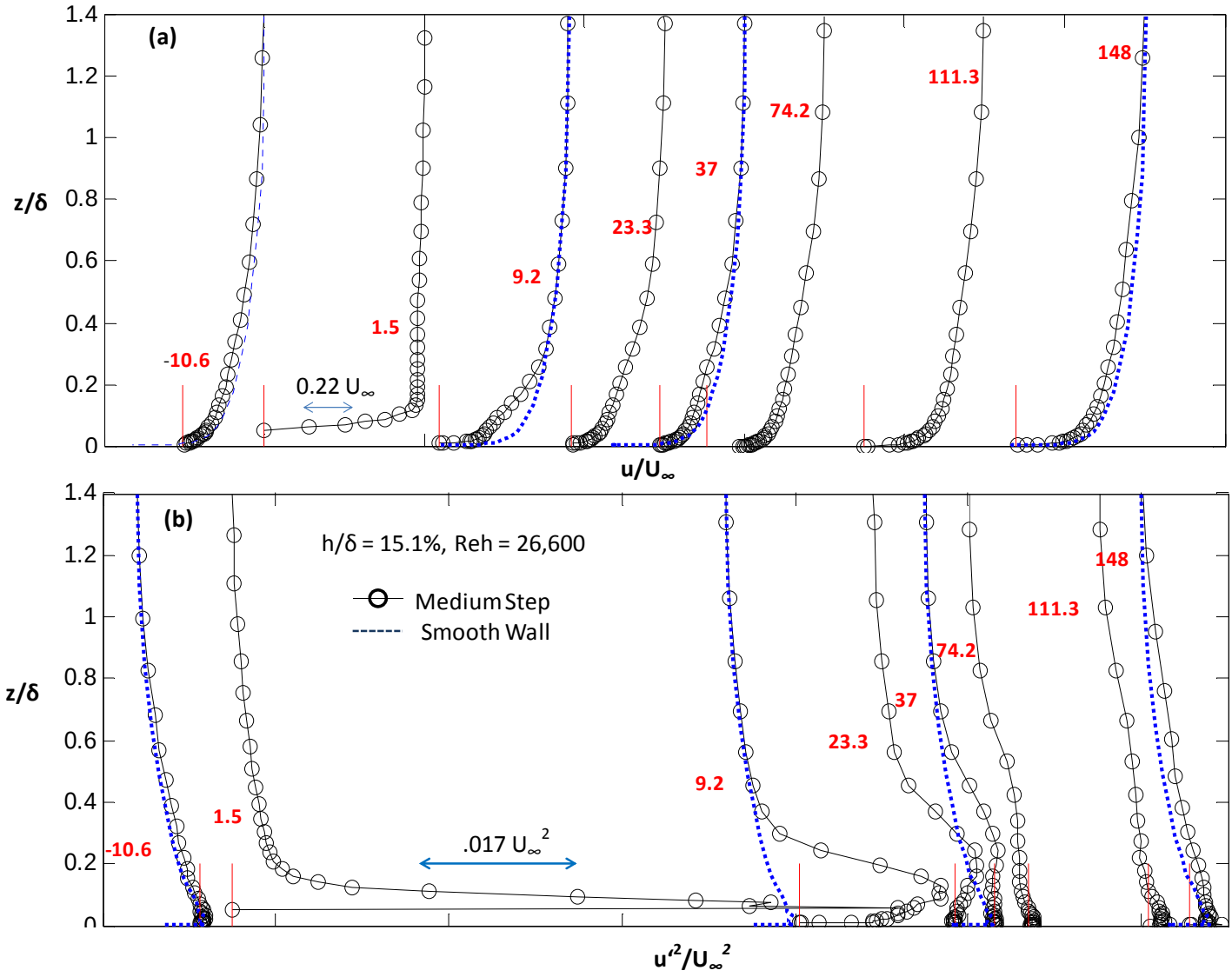

Figure 66. Mean velocity and turbulence profiles for medium step. (a) Mean velocity. (b) Turbulence intensities

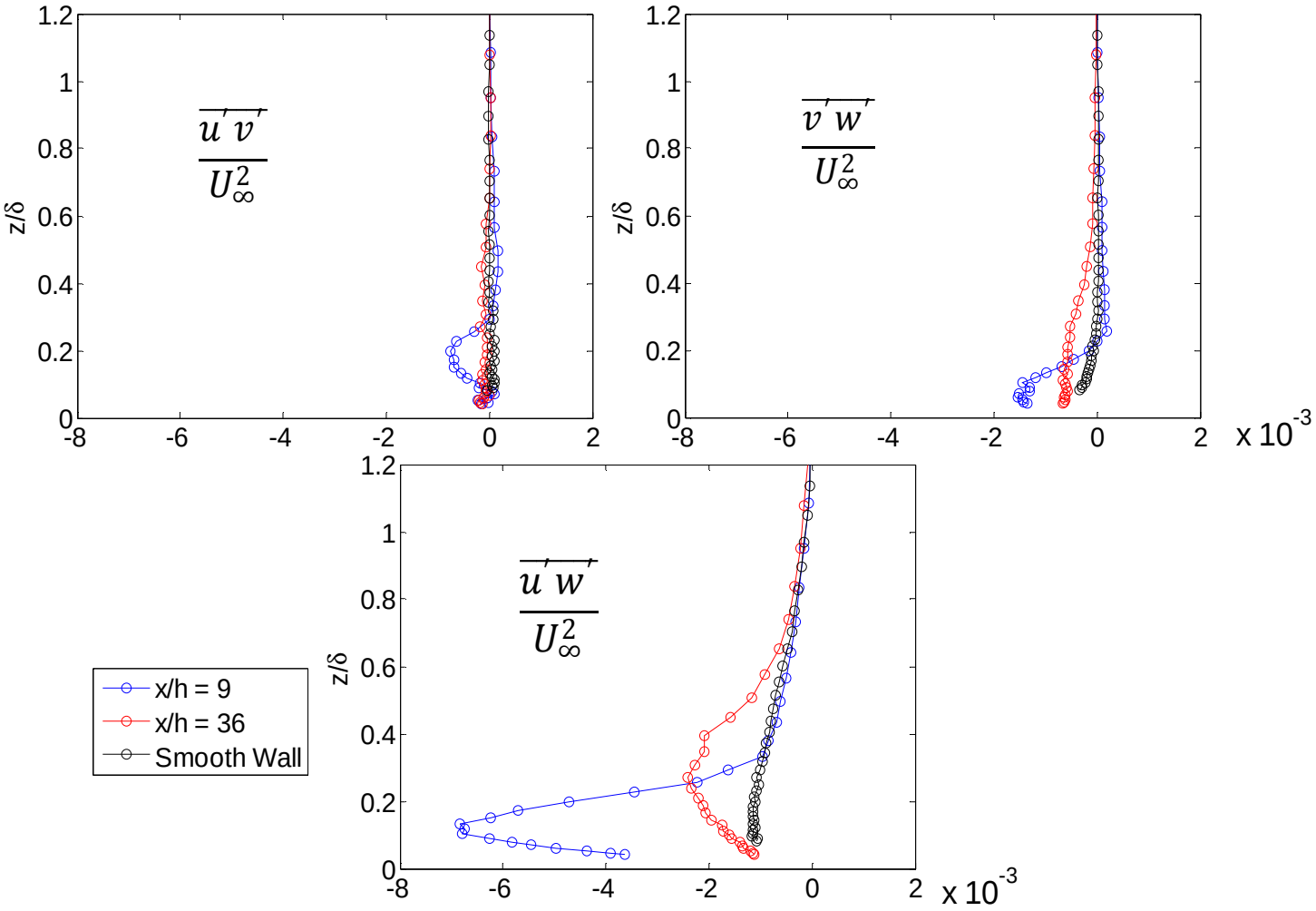

Figure 67. Reynolds shear stress components at 9 and 36 step heights downstream of the medium step. (Based on quad hotwire measurements made on medium step size by Mr. Michael Morton and Dr. Aurelien Borgoltz)

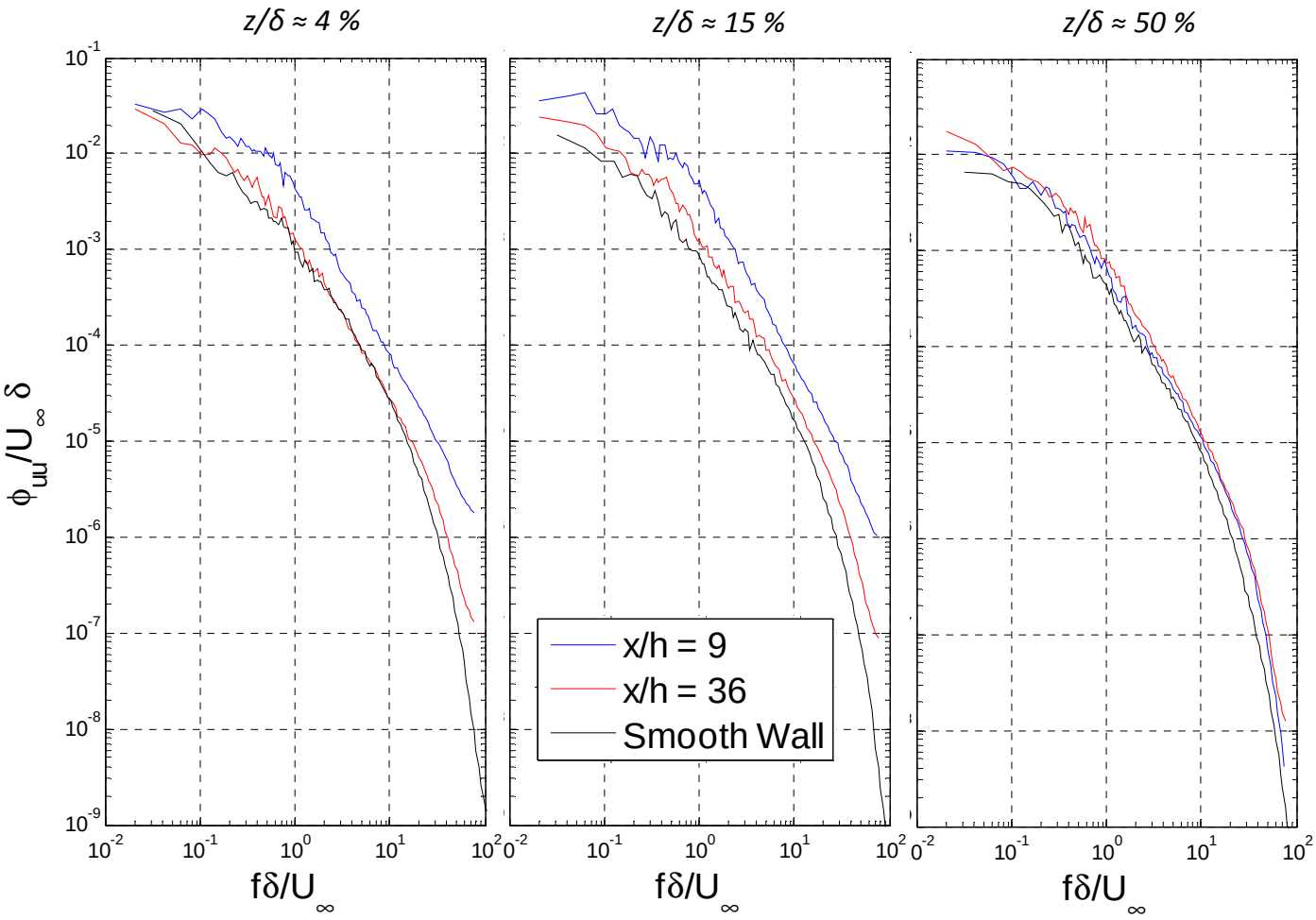

Figure 68. Streamwise velocity fluctuation spectra at 9 and 36 step heights downstream of medium step. (Based on quad hotwire measurements made on medium step size by Mr. Michael Morton and Dr. Aurelien Borgoltz)

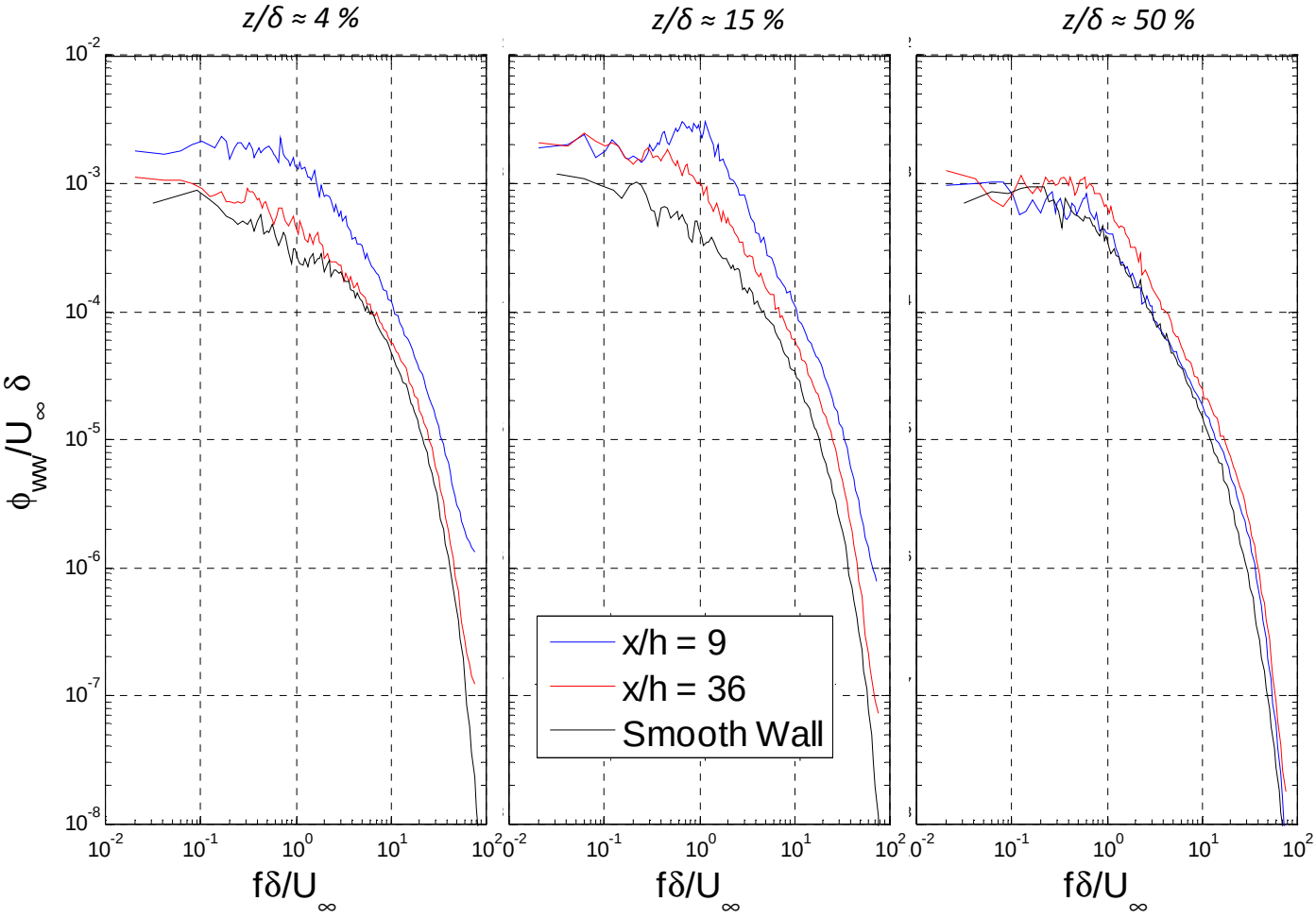

Figure 69. Normal to wall velocity fluctuation spectra at 9 and 36 step heights downstream of medium step. (Based on quad hotwire measurements made on medium step size by Mr. Michael Morton and Dr. Aurelien Borgoltz)

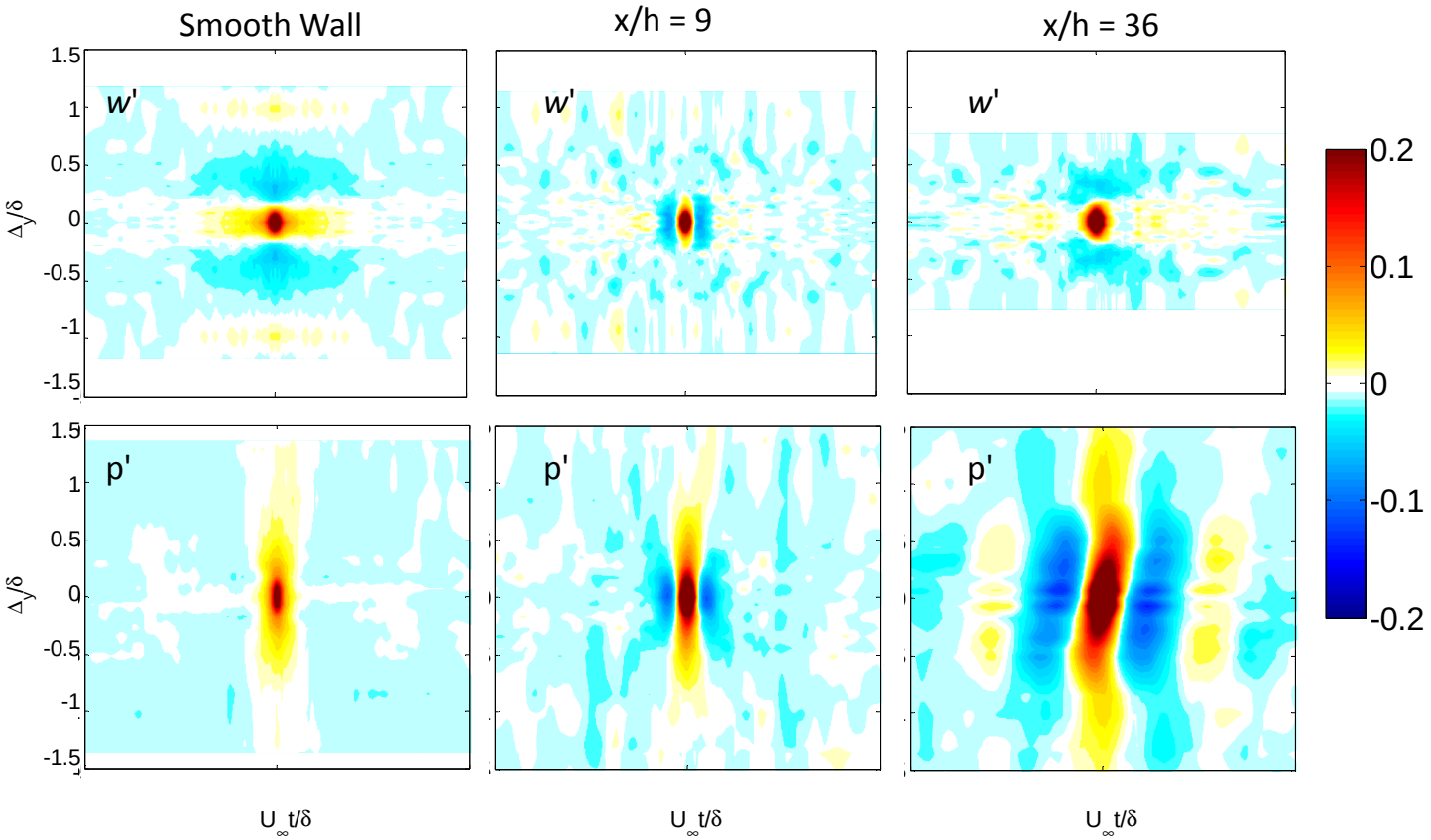

Figure 70. Spanwise space-time correlation of normal to wall velocity fluctuation component at z/δ = 15% and spanwise pressure space-time correlations at x/h =9 and x/h =36 for medium step (h/δ = 15.1%). (Based on quad hotwire measurements made on medium step size by Mr. Michael Morton and Dr. Aurelien Borgoltz)

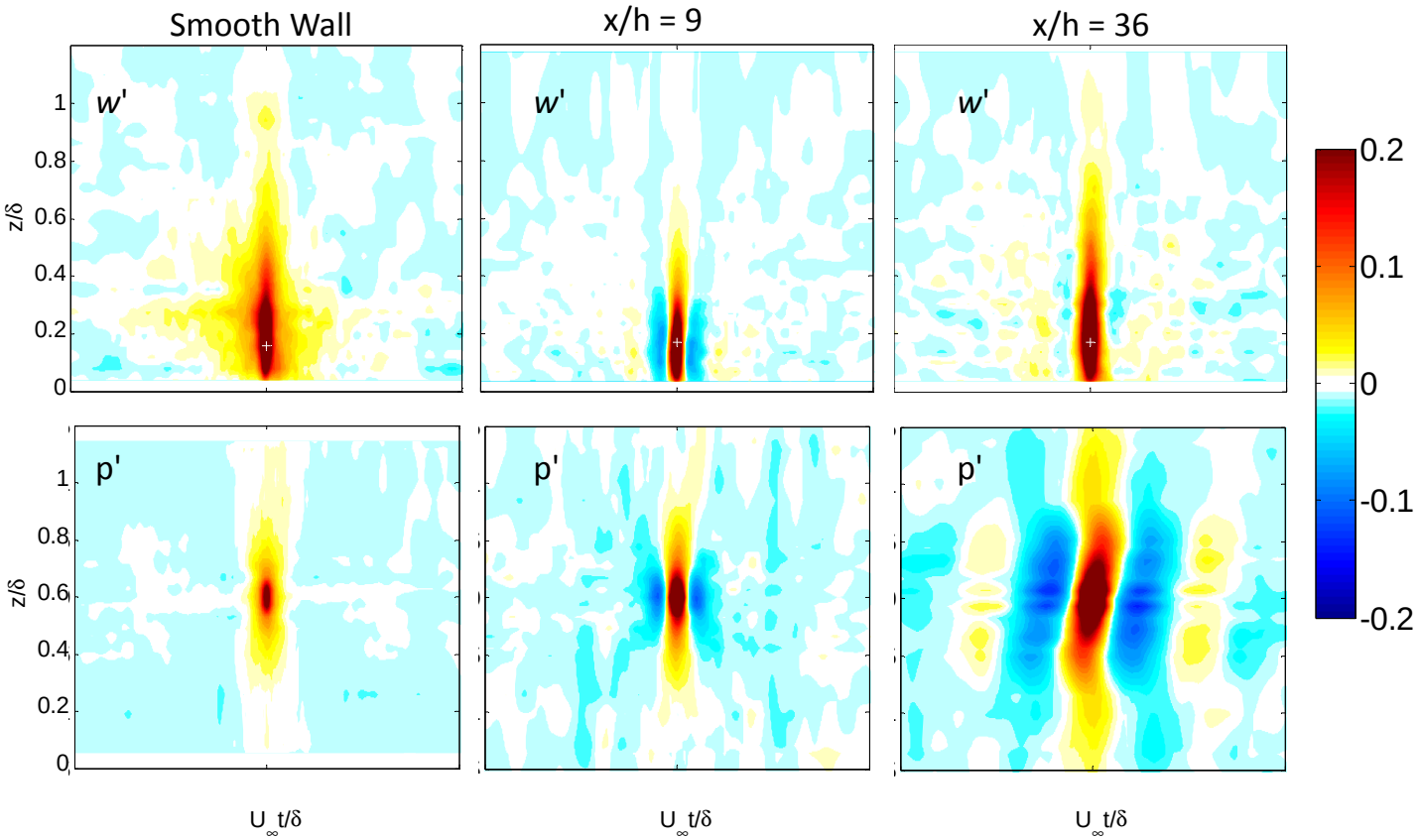

Figure 71. Normal to wall space-time correlation of normal to wall velocity fluctuation component at *z/δ* = 15% and spanwise pressure space-time correlations at *x/h* =9 and *x/h* =36 for medium step (h/δ = 15.1%). (Based on quad hotwire measurements made on medium step size by Mr. Michael Morton and Dr. Aurelien Borgoltz)

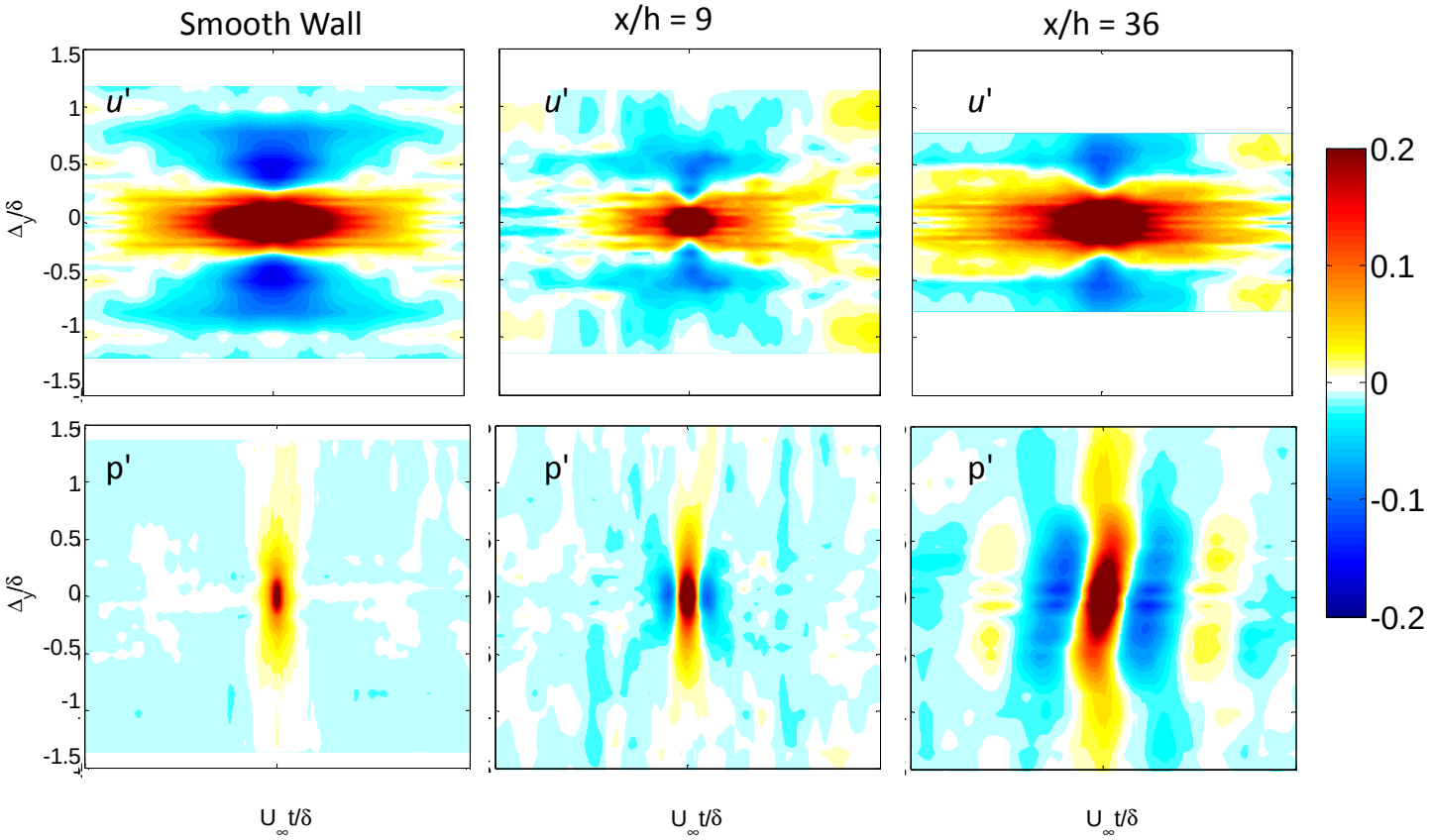

Figure 72. Spanwise space-time correlation of streamwise velocity fluctuation component at z/δ = 15% and spanwise pressure space-time correlations at x/h =9 and x/h =36 for medium step (h/δ = 15.1%). (Based on quad hotwire measurements made on medium step size by Mr. Michael Morton and Dr. Aurelien Borgoltz)

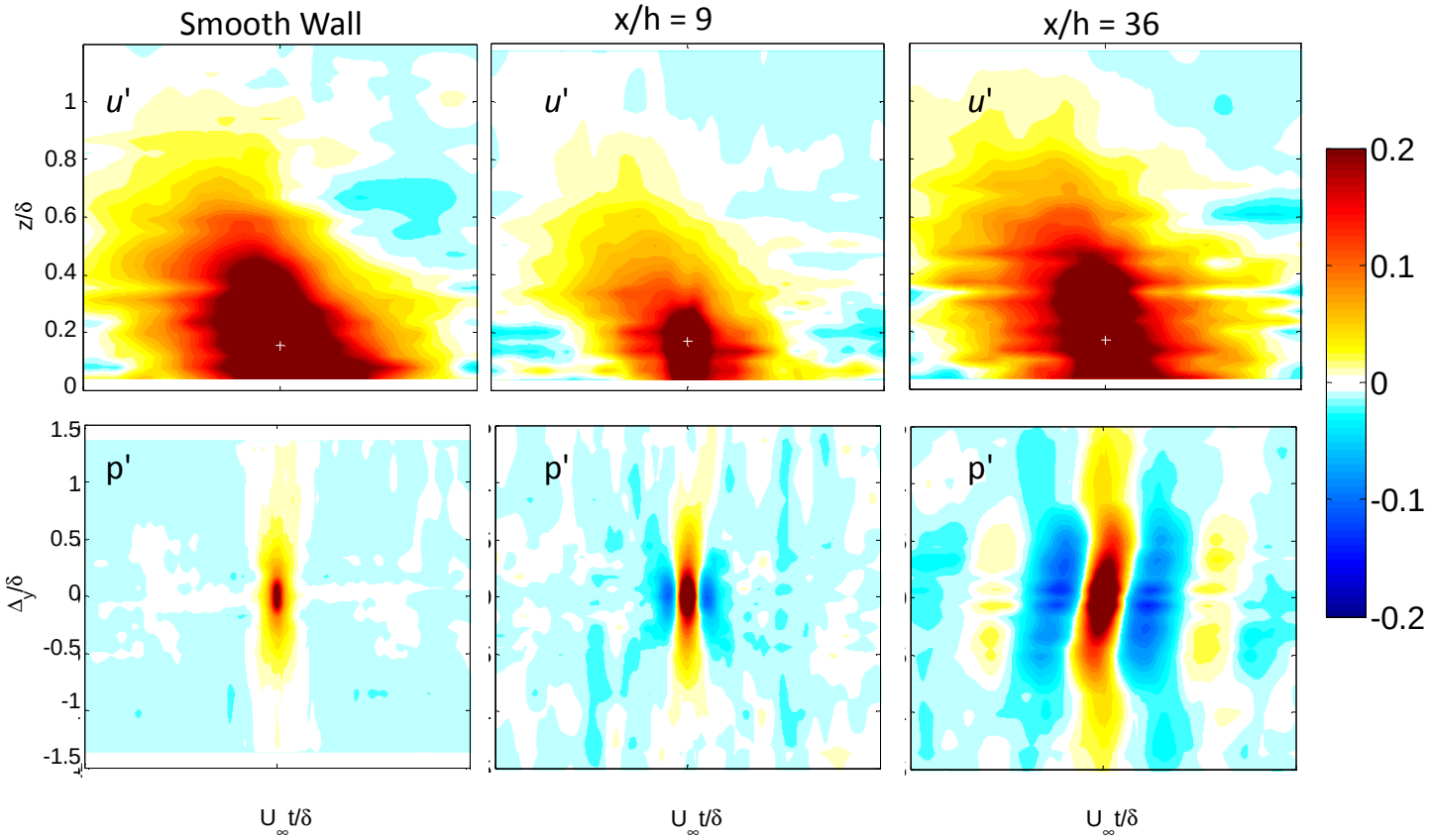

Figure 73. Normal to wall space-time correlation of streamwise velocity fluctuation component at z/δ = 15% and spanwise pressure space-time correlations at x/h =9 and x/h =36 for medium step (h/δ = 15.1%). (Based on quad hotwire measurements made on medium step size by Mr. Michael Morton and Dr. Aurelien Borgoltz)

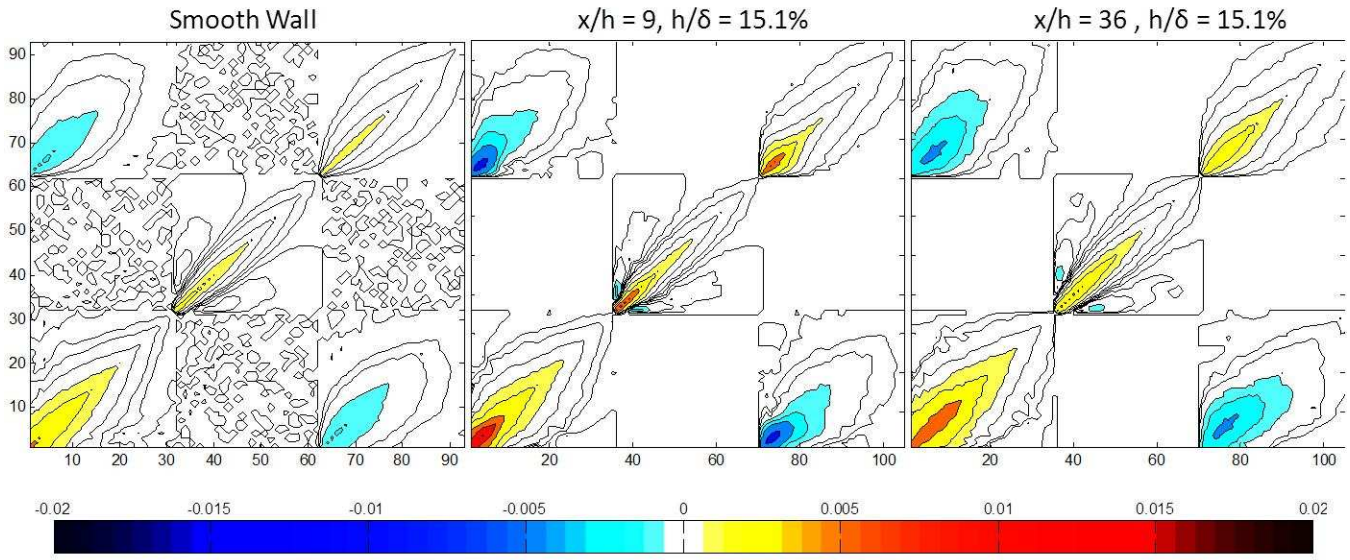

Figure 74. Zero time delay normal to wall correlation coefficients of shear stresses for smooth wall. (Based on quad hotwire measurements made on medium step size by Mr. Michael Morton and Dr. Aurelien Borgoltz)

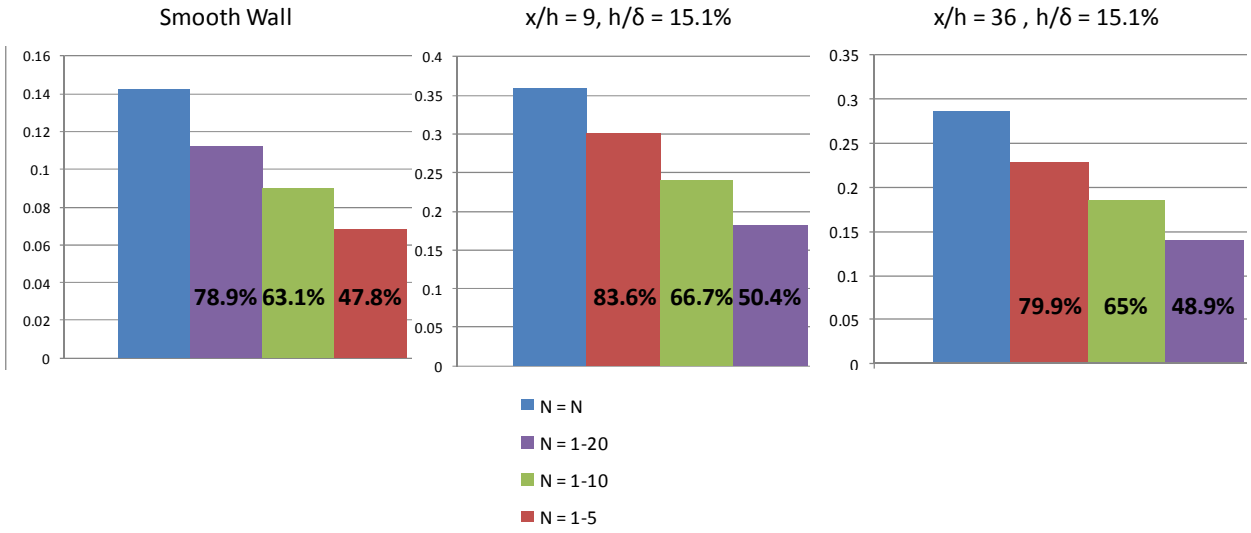

Figure 75. Distribution of mean turbulent energy within different modes. (Based on quad hotwire measurements made on medium step size by Mr. Michael Morton and Dr. Aurelien Borgoltz)

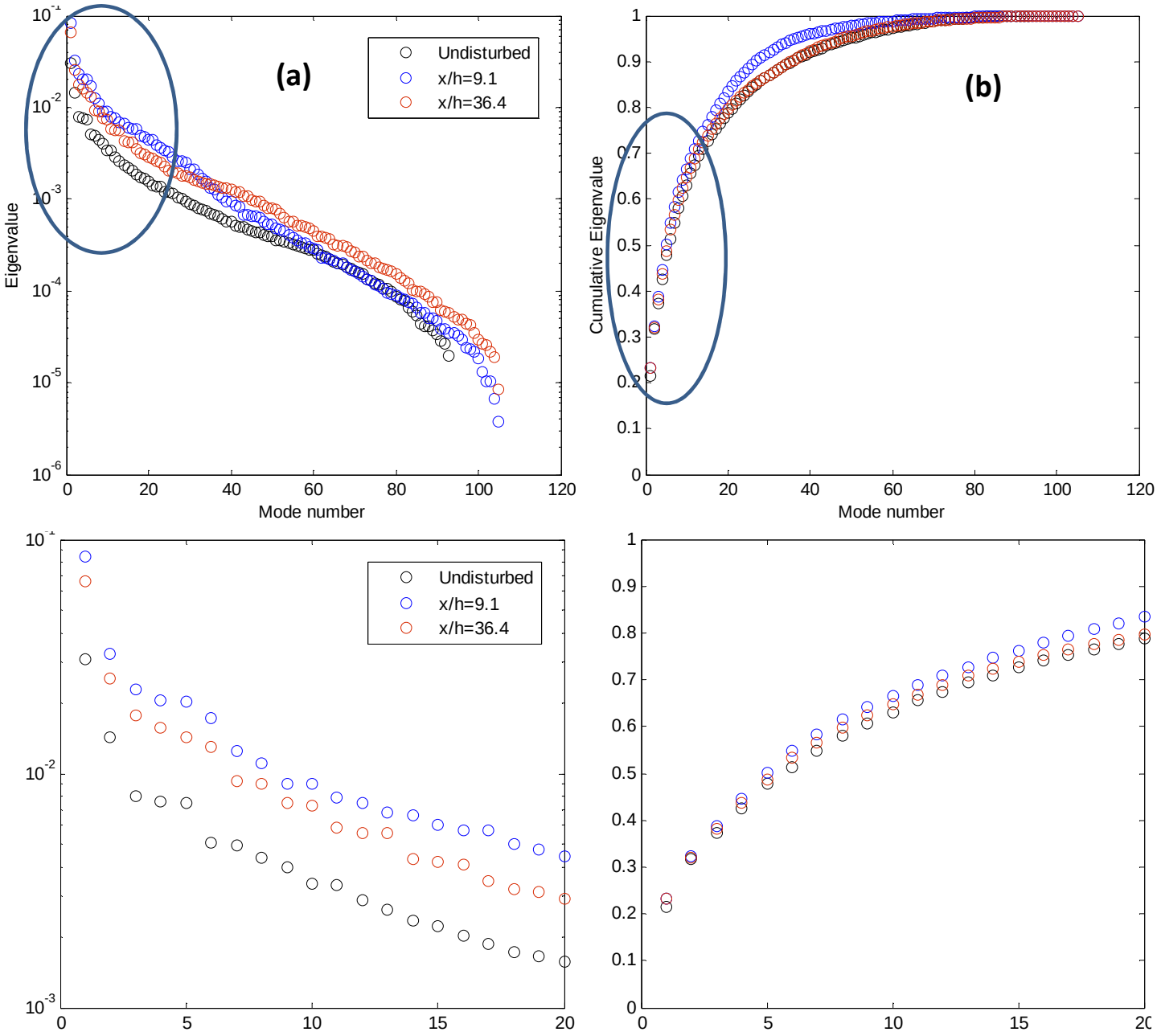

Figure 76. Eigenvalue spectrum for smooth wall and medium step. (a) Eigenvalue spectrum. (b) Cumulative eigenvalue spectrum. (Based on quad hotwire measurements made on medium step size by Mr. Michael Morton and Dr. Aurelien Borgoltz)

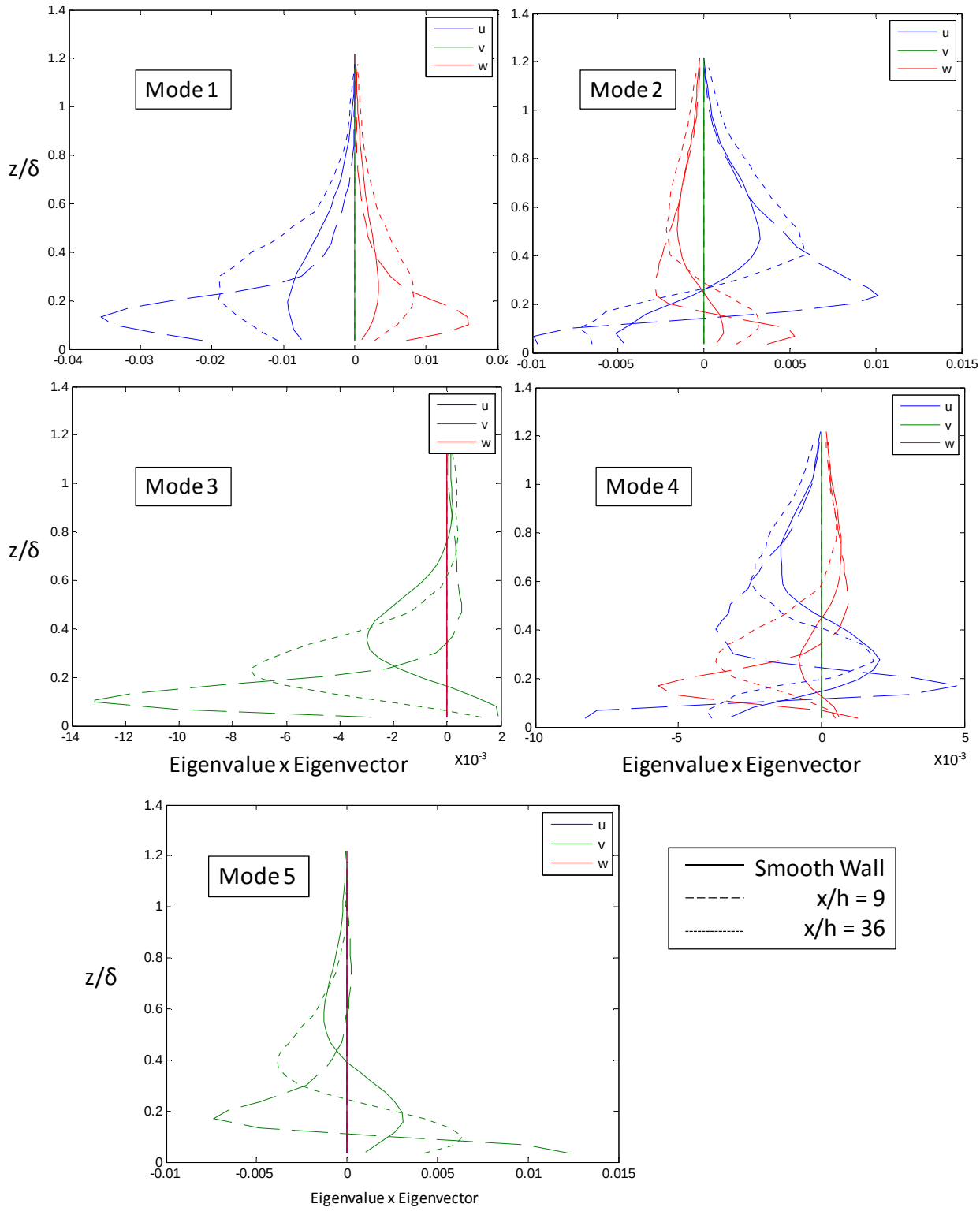

Figure 77. Mode Shapes and amplitude for the first 5 modes. (Based on quad hotwire measurements made on medium step size by Mr. Michael Morton and Dr. Aurelien Borgoltz)

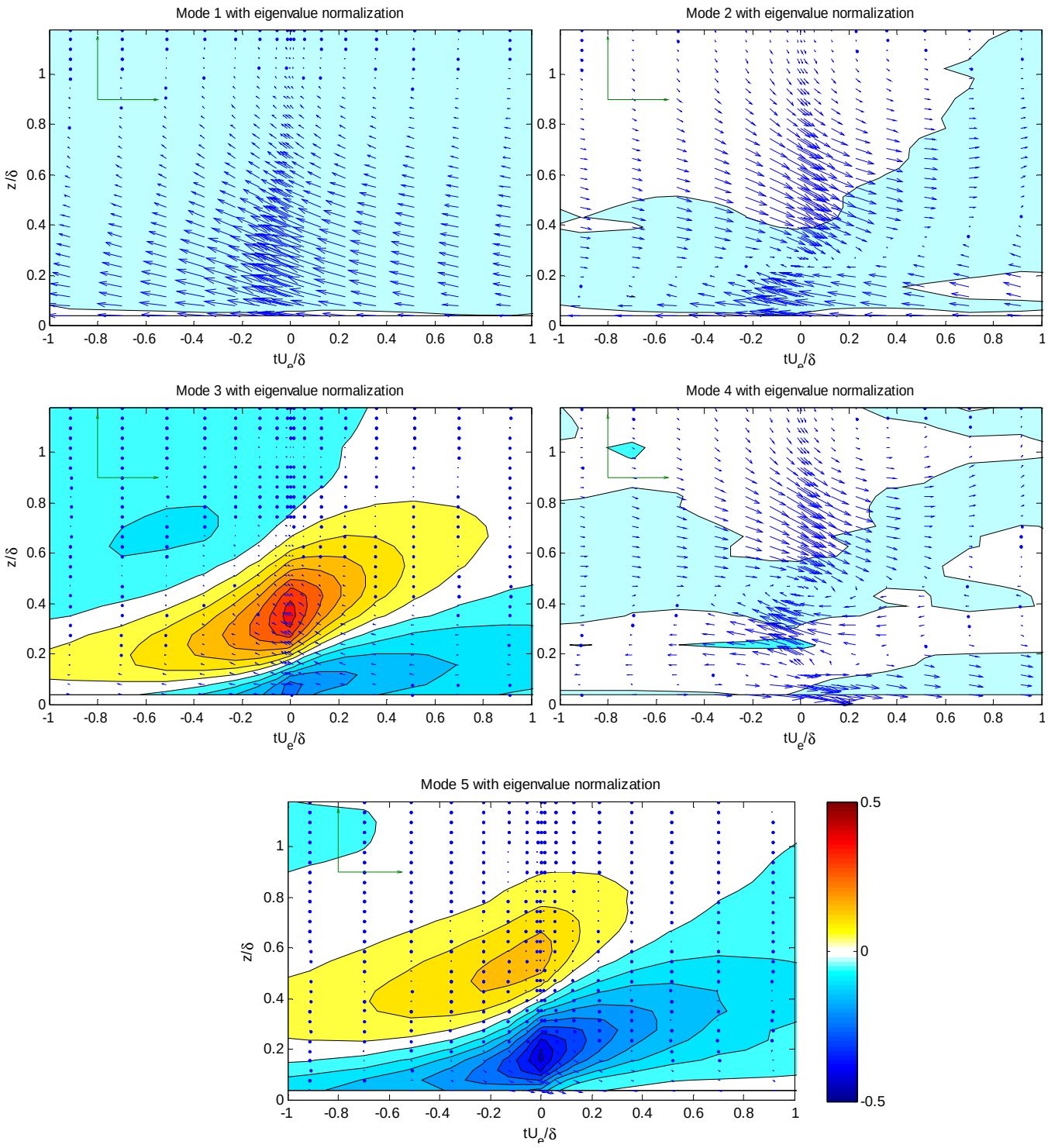

Figure 78. Smooth wall normal to wall Compact Eddy Structure. (Based on quad hotwire measurements made on medium step size by Mr. Michael Morton and Dr. Aurelien Borgoltz)

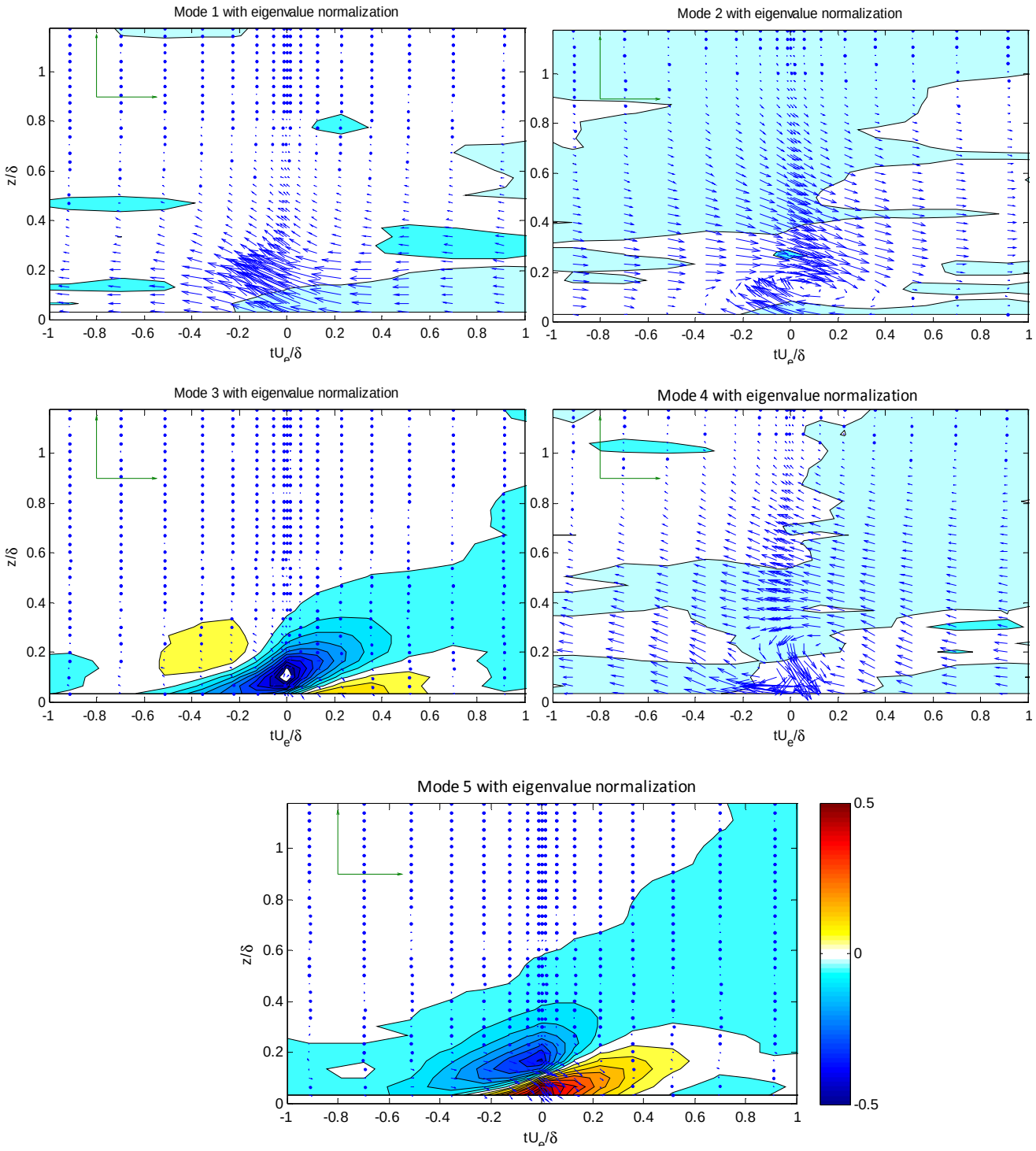

Figure 79. Normal to wall Compact Eddy Structure for medium step (h/δ=15.1%) at *x/h* = 9. (Based on quad hotwire measurements made on medium step size by Mr. Michael Morton and Dr. Aurelien Borgoltz)

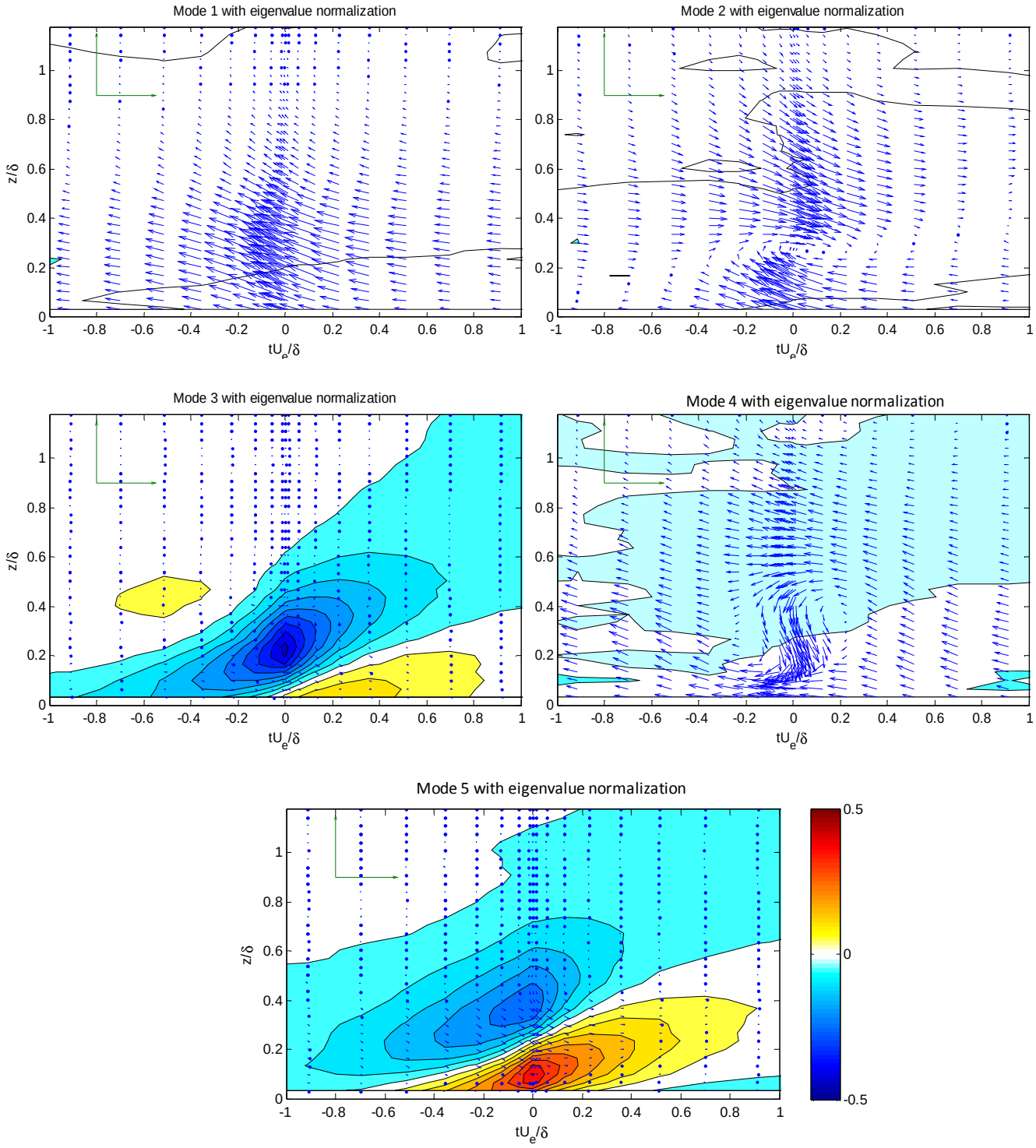

Figure 80. Normal to wall Compact Eddy Structure for medium step (h/δ=15.1%) at *x/h* = 36. (Based on quad hotwire measurements made on medium step size by Mr. Michael Morton and Dr. Aurelien Borgoltz)

Appendix A. Statistical Representation of Turbulent Flow

The purpose of this section is to provide a brief overview of the mathematical processes that were used to obtain and process the data from the experiment. Since turbulence is a stochastic process i.e. non deterministic in nature a framework of statistics must be adopted to study the physical characteristics (pressure and velocity) of such a flow. The study of fluctuating quantities through statistics help to identify the scales of turbulent structures (also known as eddies). For the present work the statistical manipulation of the wall pressure fluctuations helps to understand and identify the source of the elevated pressure fluctuations upstream and downstream of the step. The velocity fluctuations help to understand the turbulence added to the flow by the presence of the step. The pressure and velocity signals are acquired using data acquisition systems (microphones and anemometers) in real time. However, the real time statistics render the determination of any periodicities associated with the flow and are not helpful in determining the nature of the flow. Thus, to better understand the flow one has to turn to the frequency domain representation of the pressure (and velocity). The most useful tool in performing this transformation from time domain to frequency domain of a time dependent signal *f(t)* is the Fourier transform which is defined as

$$F(\omega) \equiv \int_{-\infty}^{\infty} f(t) e^{-2\pi i \omega t} dt \qquad (Eq.A1)$$

ω are the frequencies of interest over which the transform is performed. The Fourier transform of stochastic processes is important because it helps to create a frequency domain representation of a signal and helps identify hidden properties of a particular signal which would be very difficult to do in time domain. The inverse Fourier transform is an operation that helps to transform a signal in frequency domain into time domain. For the present work, this transform was used to create the space time pressure and velocity correlation maps. The inverse Fourier transform of a signal $F(\omega)$is defined as

$$f(t) \equiv \int_{-\infty}^{\infty} F(\omega) e^{2\pi i \omega t} d\,\omega \qquad (Eq.A2)$$

Since the limits of integration on the Fourier transform and inverse Fourier transform are infinite these transforms have to be appropriately done in a discrete manner for finite signals. For some discrete signal *x(n)* with length N the discrete Fourier transform used in the current work is defined as

$$X(k) = \sum_{n=1}^{N} x(t)\, e^{-2\pi i (k-1)(n-1)/N} \; for\; 1 \le k \le N \qquad (Eq.A3)$$

And, the inverse discrete Fourier transform is defined as

$$X(k) = \frac{1}{N} \sum_{n=1}^{N} X(k)\, e^{2\pi i (k-1)(n-1)/N} \; for\; 1 \le n \le N \qquad (Eq.A4)$$

The above definitions of discrete Fourier transforms were used in the present work to obtain the results shown in the chapter 3 of this text.

Another important statistical operation which will be used again and again in this text is the cross correlation of two signals also known as convolution of two signals and is defined for two signals *f(t)* and *g(t)* delayed by time τ as

$$(f * g)(t) \equiv \int_{-\infty}^{\infty} f^*(t)g(t+\tau)d\tau \qquad (Eq.A5)$$

Cross correlation in time domain is difficult to calculate and hence we turn to the frequency domain solution of the above equation and the cross correlation simply becomes

$$(F * G)(\omega) \equiv E[F^*(\omega)G(\omega)] \qquad (Eq.A6)$$

Where $F^*(\omega)$ denotes the complex conjugate of the Fourier transform of signal f(t) and the operator E[] denotes the expected value. Thus, in frequency domain the cross correlation of two signals is simply the expected value of the product of the conjugate of Fourier transform of one signal with Fourier transform of another. The cross correlation or in spectral form the cross spectra between the two signals helps to identify the existence of relationship between two signals. The cross correlation is calculated in such a way that its value lies between -1 and 1. This is done by normalizing the cross correlations with the square of the dynamic head ($1/2\rho U_\infty^2$). A value of 1 indicates a complete dependence of one signal on the other and for a stochastic process means cross correlation of a signal with itself at zero time lag. A value of 0 indicates no dependence or relation between the two signals.

A special case of cross correlation of a signal with itself at a time delay, this case is called autocorrelation and when calculated as a frequency spectrum shows the amount of signal strength in a particular frequency band. The autocorrelation of a signal is given by

$$[f(t) * f(t+\tau)] = \int_{-\infty}^{\infty} f^*(t)f(t+\tau)dt \qquad (Eq.A7)$$

Then in frequency domain the expression for autocorrelation follows from the cross correlation defined above as

$$Gpp = \frac{1}{T}E[F^*(\omega)F(\omega)] \qquad (Eq.A8)$$

Where the term *Gpp* has been used to designate the frequency spectrum of the autocorrelation of a signal *f(t)* and *E[ ]* denotes the expected value of the term inside the bracket obtained by time averaging.

Appendix B. Acoustic Subtraction of Pressure Fluctuations

As pointed in instrumentation and apparatus section, a reference B&K 4138 microphone without a ½ mm pinhole was used as a reference microphone to decontaminate the pressure data. This microphone was always placed about 0.35 m below the test section centerline. Figure B1 shows a front view of the test wall with the measurement microphone locations and the reference microphone in relation to them. The figure also shows the positions of the 5 microphone blocs that were used and the single microphone blocs.

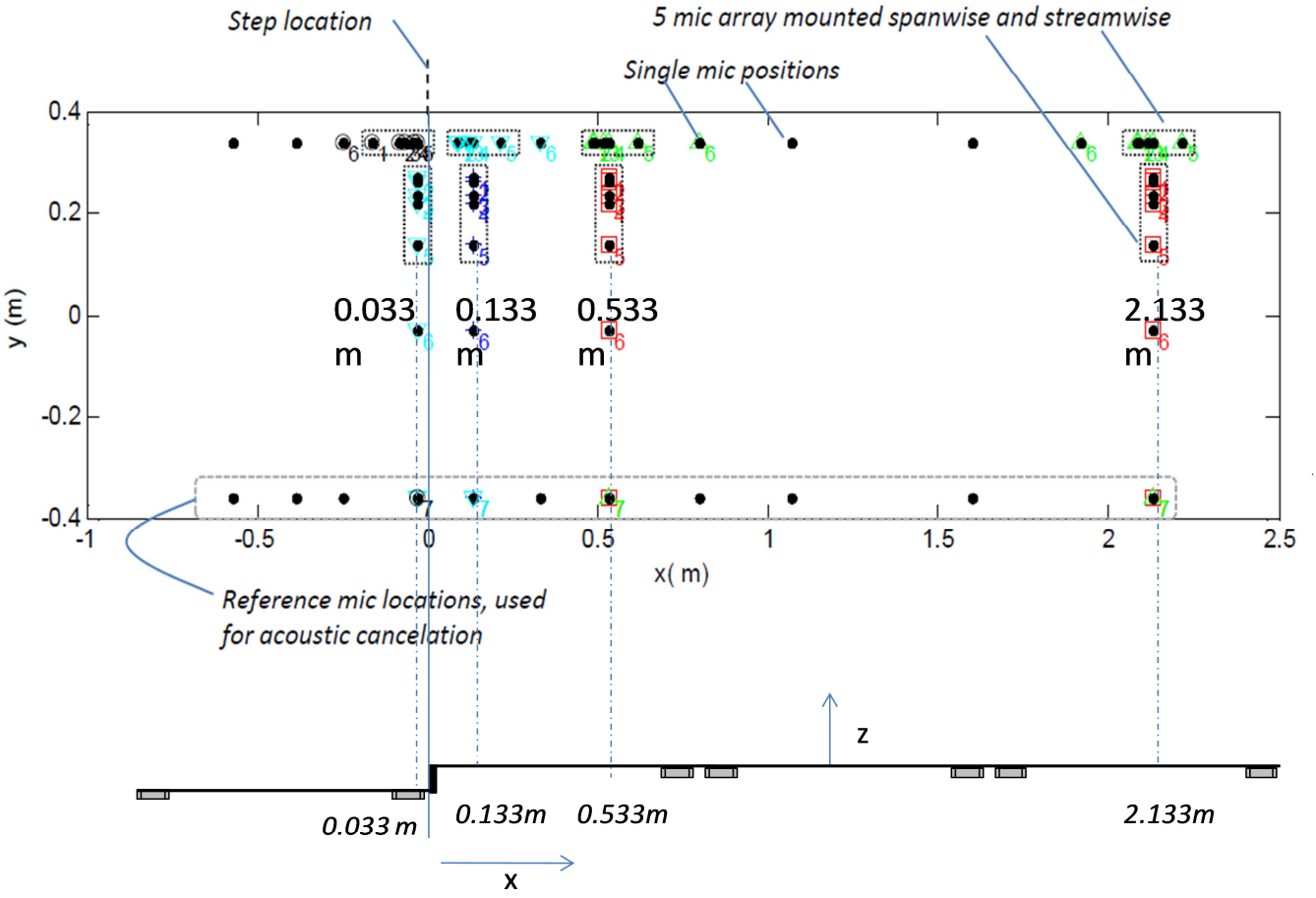

Figure B 1. Measurement and reference microphone locations on the test wall

The pressure fluctuation data from the reference microphone was used to perform acoustic subtraction on the data from the measurement microphone. The data from the measurement and reference microphone was first binned using 12 frequency bins per octave. Acoustic subtraction was performed following the method of Horne (1990). The method uses the

acoustically contaminated pressure data and the cross correlation between the measurement and reference microphone. The procedure is outlined in the following paragraph.

The measured wall pressure Autospectra through measurement microphones consists of two parts: Autospectra due to turbulence and Autospectra due to the presence of background noise or acoustic contamination. The measured autospectra can thus be written as the sum of these two components

$$G_{pp}^{(M)} = G_{pp}^{(T)} + G_{pp}^{(N)} \qquad (Eq.B1)$$

The measured cross spectra of pressure fluctuations between two measurements points 'a' and 'b' is similarly given by

$$R_{ab}^{(M)} = R_{ab}^{(T)} + R_{ab}^{(N)} \qquad (Eq.B2)$$

Now consider a reference point 'c' which is sufficiently far from the measurement point 'a' so that the pressure signal due to turbulence is uncorrelated i.e. $R_{ac}^{(T)} = 0$. Thus, the cross correlation between the points 'a' and 'c' can then be written simply as

$$R_{ac}^{(M)} = R_{ab}^{(N)} \qquad (Eq.B3)$$

The acoustically subtracted Autospectra at point 'a' can then be obtained by subtracting the measured spectra at 'a' with the cross spectra between points 'a' and reference point 'c'.

$$G_{pp}^{(S)}\Big|_a = G_{pp}^{(M)}\Big|_a - R_{ac}^{(M)} = G_{pp}^{(T)}\Big|_a + G_{pp}^{(N)}\Big|_a - R_{ab}^{(N)} \qquad (Eq.B4)$$

Now, considering the expression above, the last two terms effectively cancel each other out since the only correlation between points 'a' and 'c' is the background noise. The above expression thus gives the subtracted Autospectra at point 'a'.

Figure B2 shows the application of this acoustic subtraction methodology for a spanwise array of microphones. Figure B2 (a) shows the Autospectra without cancellation, Figure B2 (b) shows the spectra with acoustic cancellation applied and Figure B2 (c) and Figure B2 (d) show the coherence coefficient and phase difference respectively between the measurement and reference microphones. It can be seen that the background from the tunnel seems to be limited to the lower frequencies between about 1 and 100 Hz where the coherence between the signals is high. There is also a phase difference between the signals at these frequencies. These differences are clearly reflected in the two spectra where the lower frequencies are much more smooth with the cancellation applied and do not display the spikes seen in the spectra without cancellation.

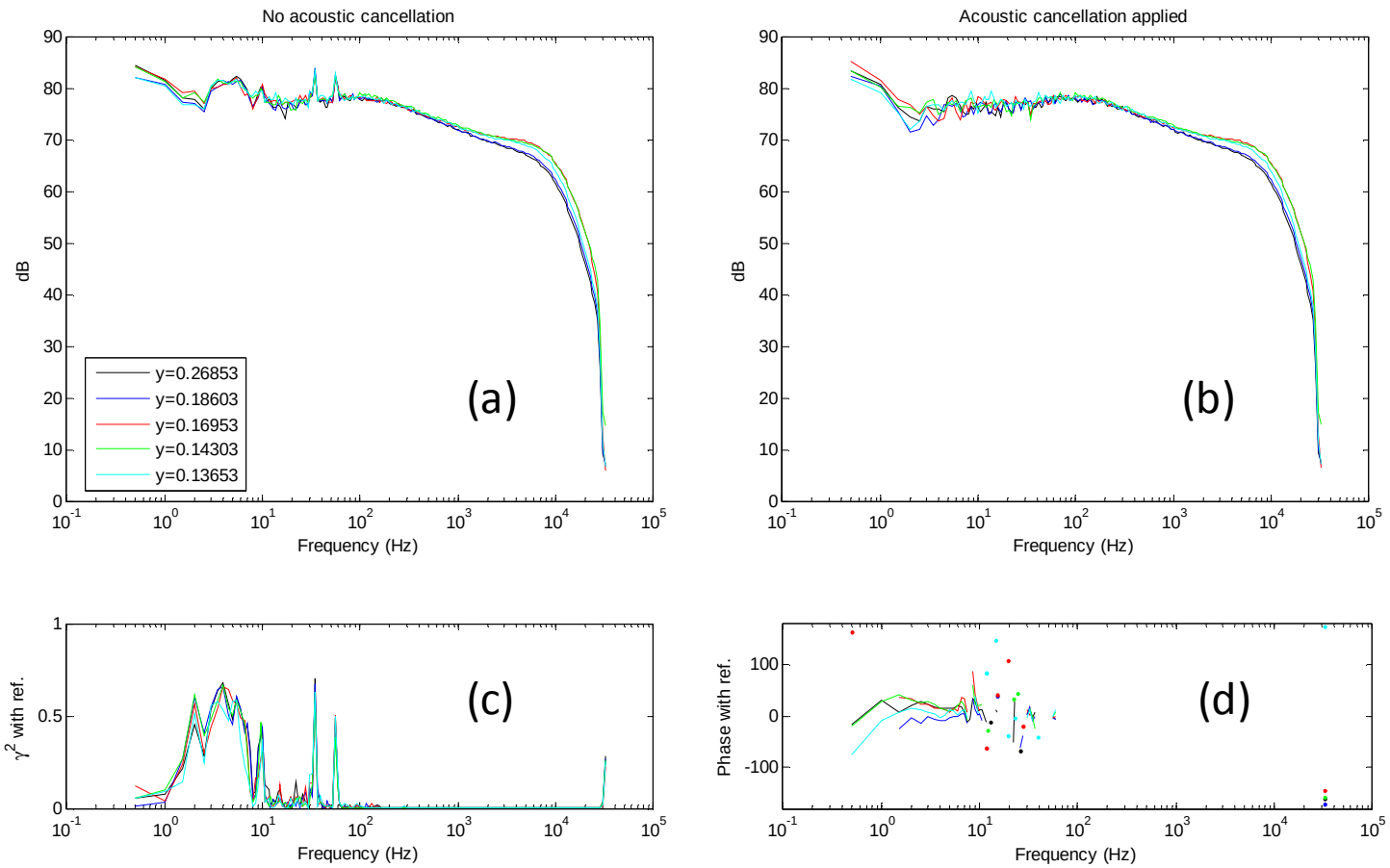

Figure B 2. a) Pressure Autospectra without cancellation. (b) Pressure Autospectra with cancellation applied. (c) Coherence between the measurement and reference microphones. (d) Phase difference between measurement and reference microphones